L-Università ta' Malta

Development of Monoclonal ScFv Antibodies Targeting the T-cell co-Inhibitory Molecules VISTA and PD-L1.

June 2025

Jasmine Spiteri

Submitted to the Faculty of Health Sciences of the University of Malta in Partial Fulfilment of the Requirements for the Master of Science in Applied Biomedical Science.

Supervisor: Prof. David Saliba B.Sc (Hons) Ph.D. (Edin).

L-Università ta' Malta

FACULTY/~~INSTITUTE/CENTRE/SCHOOL~~ of Health Sciences

DECLARATIONS BY POSTGRADUATE STUDENTS

(a) Authenticity of Dissertation

I hereby declare that I am the legitimate author of this Dissertation and that it is my original work.

No portion of this work has been submitted in support of an application for another degree or qualification of this or any other university or institution of higher education.

I hold the University of Malta harmless against any third party claims with regard to copyright violation, breach of confidentiality, defamation and any other third party right infringement.

(b) Research Code of Practice and Ethics Review Procedures

I declare that I have abided by the University's Research Ethics Review Procedures. Research Ethics & Data Protection form code FHS-2022-00428.

As a Master's student, as per Regulation 77 of the General Regulations for University Postgraduate Awards 2021, I accept that should my dissertation be awarded a Grade A, it will be made publicly available on the University of Malta Institutional Repository.

To my family, my partner, my dearest friend and my beloved pets whose unwavering support and patience carried me through every step of this journey.

Acknowledgments

My deepest gratitude goes to my supervisor Prof. David Saliba, for his knowledge, expertise, patience and motivation to guide and teach me throughout this research study.

I would like to express my sincere gratitude to the International Centre for Cancer Vaccine Science (ICCVS) especially Prof. Ted Hupp for their kind donation to provide us with the canine scFv phage display library and other resources.

I would like to express my sincere gratitude to my colleagues, Ms Mariana Grima and Ms. Giuseppina Monda, for providing me with endless support and encouragement throughout this project.

A special thank you goes to Prof. Jean Paul Ebejer for his expertise in bioinformatics, and Ms. Francesca Chircop for developing and providing training on the dendrogram software used during this research project.

I would also like to thank Prof. Godfrey Grech for granting us access to the laboratory and facilities at the Centre for Molecular Medicine and Biobanking, University of Malta.

Finally, I gratefully acknowledge the Tertiary Education Scholarship Scheme (TESS) for funding this research project.

Abstract

Tumour development is a multistep process characterized by aberrant monoclonal cell proliferation. Immune cells exert selective pressure on tumour populations, promoting the survival of low-immunogenic variants that can evade immune detection. One such mechanism involves the recruitment of immunosuppressive cells expressing inhibitory receptors and ligands that suppress T-cell activation. Currently, inhibitory receptors and ligands are being extensively studied as therapeutic targets. The food and drug administration (FDA) has approved several immune checkpoint inhibitors (ICIs) targeting Cytotoxic T-Lymphocyte-Associated Protein 4 (CTLA-4), Programmed Cell Death Protein 1 (PD-1), and its ligand Programmed Cell Death-Ligand 1 (PD-L1). These treatments have shown efficacy in limiting tumour progression and extending patient survival. However, due to dynamic intrinsic and extrinsic changes in the tumour microenvironment (TME), a high rate of acquired resistance to ICIs remains a major challenge. To address this, alternative co-inhibitory molecules are being explored for therapeutic targeting, either as standalone agents or in combination therapies. In this study, recombinant single-chain variable fragment (scFv) antibodies with high affinity for the co-inhibitory molecules V-domain Immunoglobulin Suppressor of T-cell Activation (VISTA) and PD-L1 were initially targeted. These co-inhibitory molecules play a critical role in immune regulation by inhibiting T-cell proliferation and cytokine production when interacting with their respective ligands. Both VISTA and PD-L1 have been shown to be overexpressed in various solid tumours including melanoma, non-small cell lung carcinoma (NSCLC) and ovarian cancer. The generation of recombinant scFv antibodies against these co-inhibitory molecules were pursued using the phage display biopanning technique. Due to technical challenges encountered during the biopanning phage display process, a statistically significant increase in binding towards

either bait protein was not achieved after four rounds. As a result the project's focus shifted toward characterizing 60 monoclonal antibodies derived from a previously successful VISTA-directed biopanning experiment conducted in a separate study. These clones were evaluated for specificity against VISTA and control bait proteins, and their binding affinities were analysed using the Enzyme-Linked Immunosorbent Assay (ELISA). ELISA analysis revealed that most of the clones exhibited strong binding affinity to VISTA with minimal cross-reactivity to control proteins. Notably, most clones demonstrated statistically significant preferential binding to their target bait, with p-values <0.000001. To assess sequence diversity, Sanger sequencing was performed on all clones. The results of Sanger sequencing showed that full-length sequencing was completed only on half of the, most of which had an identical sequence, suggesting potential amplification bias during phage display. Thus, in this project, 60 monoclonal scFvs with a high binding affinity towards VISTA and minimal cross-reactivity towards control bait proteins was achieved. Sanger sequencing of these clones showed minimal diversity indicating an amplification bias during biopanning phage display. Further confirmatory and validation techniques are required to validate the functional activity of the scFv binders. Future efforts should focus on optimizing the biopanning phage display protocol to enhance target-specific library generation and minimize bias.

Table of contents

List of figures

List of tables

List of abbreviations:

Amp LB broth	LB broth containing 100mg/mL of Ampicillin
APCs	Antigen Presenting Cells
AUC	Area Under the Curve
Bcl2	B-cell lymphoma 2
Bcl-xL	B-cell lymphoma-extra large
BLAST®	Basic Local Alignment Tool®
BSA	Bovine Serum Albumin
Btg	B-cell translocation gene
CAFs	Cancer-Associated Fibroblasts
Carb	Carbenicillin
CCL2	CC motif chemokine Ligand 2
CDR3	Complementary Determining Region
CDR3-VH	CDR3 of the Variable Heavy hain
CDR3-VL	CDR3 of the Variable Light chain
CSV	Comma-Separated Values
Cnn2	Calponin 2

Co-NTA MagBeads	Cobalt based NTA ligands present on Superparamagnetic Beads
cSMAC	Central Supramolecular Activation Clusters
CTLA-4	Cytotoxic T-Lymphocyte Associated protein-4
DNA	Deoxyribonucleic Acid
dNTPs	DeoxyNucleotide Triphosphates
EBV	Epstein–Barr virus
ECD	Extracellular Domain
ECM	Extracellular Matrix
EGFR	Epidermal Growth Factor Receptor
EMT	Epithelial Mesenchymal Transition
ELISA	Enzyme-Linked Immunosorbent Assay
EOMES	Eomesodermin
ERK	Extracellular signal Regulated Kinase
Fab	Fragment antigen-binding
FDA	Food and Drug Administration
Foxp3	Forkhead box p3
FSC	Forward scatter
GMQE	Global Model Quality Estimate

HT	Poly-Histidine Tag
ICIs	Immune Checkpoint Inhibitors
IDO	2,3-Dioxygenase
IFN	Interferon
II	Instability Index
Ifngr1	IFN-γ receptor 1
IgC	Immunoglobulin Constant
IGHV	Immunoglobulin Heavy chain Variable region
Ig-V domain	Immunoglobulin Variable domain
IgV	Immunoglobulin Variable
IL	Interleukin
IMGT®	International ImMunoGeneTics information system®
IPRES	Innate anti-PD-1 Resistance
irAEs	Immune-related Adverse Events
ITIM	Tyrosine-based Inhibitory Motif
ITSM	Tyrosine-based Switch Motif
JAK1/JAK2	Janus Kinase 1/2
Kan	Kanamycin

Klf	Kruppel like factor
mAbs	monoclonal Antibodies
MDSC	Myeloid-Derived Suppressor Cells
MFI	Median Fluorescent intensity
mTOR	Mammalian Target of Rapamycin
NCBI	National Center for Biotechnology Information
NFAT	Nuclear Factor of Activated T-cells
NF-κB	Nuclear Factor-κB
NGS	Next Generations sequencing
NK cells	Natural Killer cells
NPC	Non-Protein Control
NSCLC	Non-Small Cell Lung Carcinoma
NTA	Nitrilotriacetic acid
OD	Optical Density
PD-1	Programmed Death-1
PD-L1	Programmed cell Death-Ligand1
PE	phycoerythrin
PEG/NaCl	Polyethylene glycol with Sodium chloride

pI	Isoelectric point
PI 3-K	Phosphoinositide 3-OH Kinase
PI3K	Phosphoinositide 3-Kinase
PMT	Photomultiplier tube
pSMAC	Peripheral Supramolecular Activation Clusters
PTEN	Phosphatase and Tensin Homolog
QMEANDisCo	QMEAN Distance Constraint Score
R	Round
ScFv	Single Chain Variable Fragment
SHP-2	SH-2 domain containing tyrosine phosphatase-2
Slamf6	Signalling lymphocyte activation molecules 6
SPR	Surface Plasmon Resonance
SSC	Side scatter
ssDNA	Single stranded DNA
STAT	Signal Transducer and Activator of Transcription
Tcf7	T-cell factor7
Tet LB agar	Luria Bertani agar containing 100mg/mL Tetracycline
Tet LB broth	Luria Bertani broth containing 100mg/mL Tetracycline

TGF-β	Transforming Growth Factor-β
Th	T helper
TIM-3	T-cell Immunoglobulin and Mucin-3
TLR	Toll-Like Receptors
TME	Tumour Microenvironment
TNFRSF	Tumour Necrosis Factor Receptor Superfamily
Tregs	Regulatory T-cells
VEGF	Vascular Endothelial Growth Factor

Chapter 1:

Introduction

1.1. Development of tumours

Tumour development is a multistep process involving multiple genetic and epigenetic changes that lead to aberrant monoclonal growth. A benign tumour is one that does not penetrate the tissues around it, whereas, a malignant tumour, or cancer, invades and spreads throughout the body by the lymphatic or circulatory system (Cooper 2000). For tumour cells to have a selective advantage in their survival and growth, these cells undergo eight hallmarks. These hallmarks include the ability to acquire new mutations, primarily by activating oncogenes and repressing tumour suppressor genes, evade death, reprogramming cellular metabolism, induce angiogenesis, prevent an immunological response, invade and metastasize (Hanahan 2022).

Tumour cells are surrounded in a Tumour Microenvironment (TME) rich in activated stroma, Cancer-Associated Fibroblasts (CAFs), and inflammatory cells as shown in figure 1.1 (Coussens & Werb 2010, Visser et al. 2005, Wiseman & Werb 2002). This environment plays a role in the genesis and metastatic spread of tumour as well as the disruption of homeostatic mechanisms related to tissue architecture (Baghban et al. 2020). Communication between tumour cells and TME is facilitated through direct contact or by the release of growth factors (Asif et al. 2021). Growth factors stimulate angiogenesis to develop blood and lymphatic vessels to nourish this complex environment (Ishii et al., 2003, Visser et al., 2005). Additionally, CAFs serve as the primary mediators for synthesis of Extracellular Matrix (ECM) proteins such as collagen and laminin. These proteins function as a physical scaffold to promote tumour dissemination (Baghban et al. 2020 and Zhu et al. 2015).

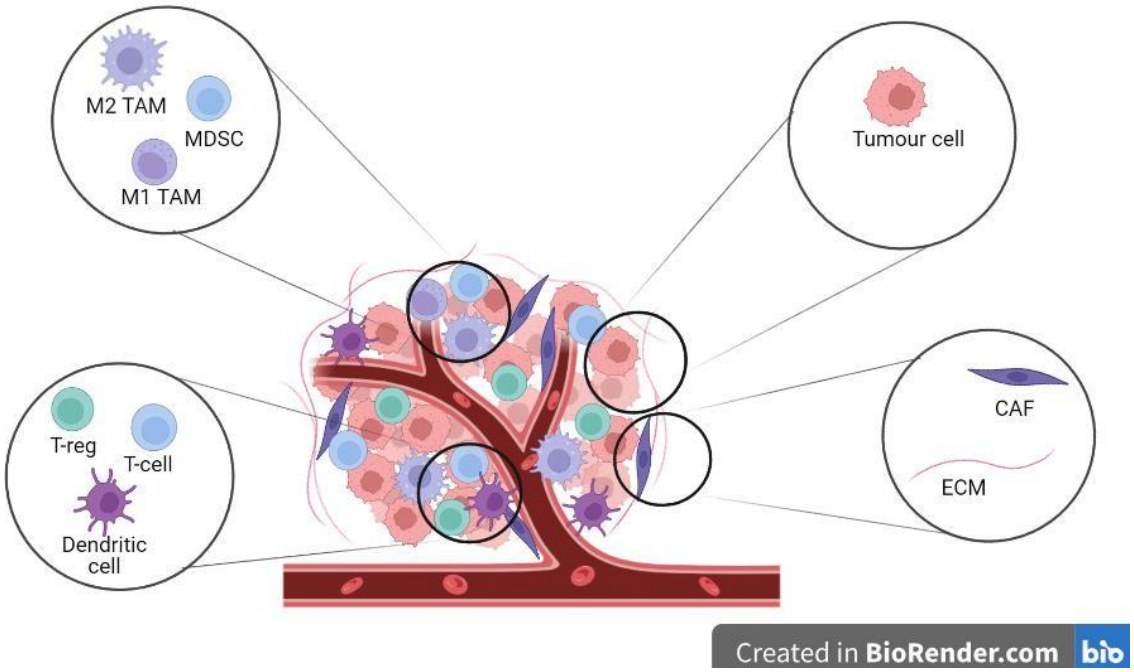

Figure 1.1: A schematic representation of the environment surrounding tumour cells. For the formation of TME, Tumour cells become surrounded with inflammatory cells, blood vessels and fibroblasts supported by the ECM. These cells aid in tumour progression and metastasis.

1.2. Anti-tumorigenic immune response

Initially immunosurveillance present in the TME interacts with tumour cells to initiate an anti-tumorigenic immune response (Marcus et al. 2014). Natural Killer cells (NK cells) are potent mediators as they can detect tumour cells without prior sensitization (Herberman et al. 1975) and directly lyse these cells by the release of cytotoxic granules such as perforin and granzyme b (Davis et al. 2001). In the TME, macrophages are differentiated into M1 macrophages to increase the expression of major histocompatibility complex-II (MHC-II), phagocytose malignant cells and secrete pro-inflammatory cytokines such as interleukin (IL)-23 and IL‑2 to further activate an immune response (Aras & Zaidi 2017). Dendritic cells are present to act as critical tumour Antigen Presenting Cells (APCs) as they acquire antigens from apoptotic tumour cells or soluble antigens that have drained from tumour lymphatics to initiate T-cell priming and cause tumour cells to become infiltrated

with CD4+

and CD8+ T-cells (Broz et al. 2014, Fu et al. 2018, Roberts et al.2016). The action of these innate immune cells against tumour cells is depicted in figure 1.2.

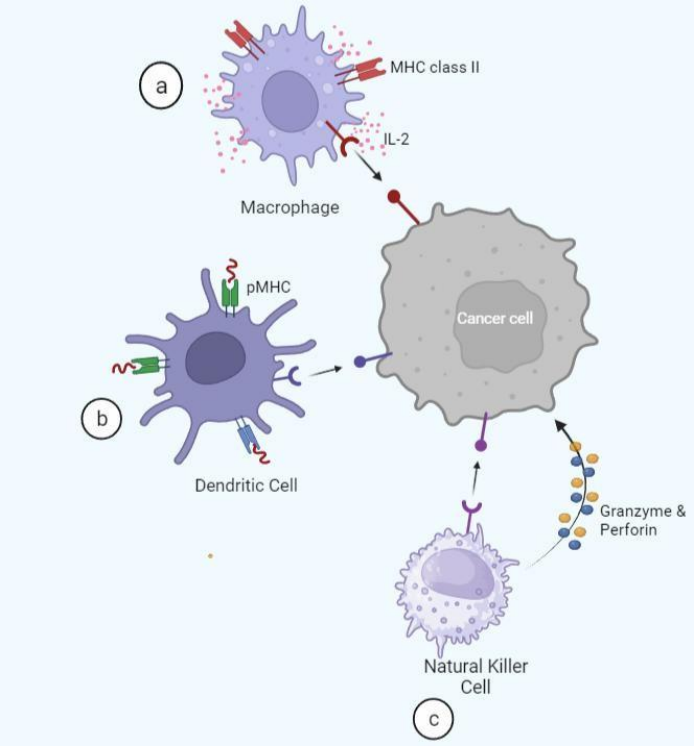

Figure 1.2: An illustration showing anti-tumorigenic immune cells in the TME. Mature dendritic cells and macrophages suppress tumour development by increasing the expression of MCH-II and secreting inflammatory cytokines. Natural killer cells can directly lyse tumour cells by the release of granzymes, perforin.

1.3. T-cell response against tumour cells

Tumours highly infiltrated with T-cells act as "hot" tumours and have better survival outcomes since T-cells have a crucial role in preventing tumour outgrowth (Dahlin et al. 2011). The distinctive interaction of the T-cell receptor (TCR) with peptides attached to MHC (pMHC) on activated innate cells and tumour cells allows T-cells to detect altered or overexpressed tumour antigens. Cluster of Differentiation (CD)8+ T-cells bind to pMHC class-I expressed on nucleated cells to increase the cytotoxic activity of T-cells to directly

lyse tumour cells (Hanson et al. 2000). Alternatively, CD4+ T-cells bind to pMHC class-II expressed on APCs to undergo T-helper subtype differentiation (Gao & Jakobsen 2000). When T-cells differentiate into T helper 1 (Th1) subtypes, proinflammatory cytokines are released such as interferon-gamma IFN-γ to further activate the immune response (Sandick et al. 2003). The release of these proinflammatory cytokines along with a second co-stimulatory signal are required for T-cells to differentiate into their effector subtype and infiltrate the TME to eliminate tumour cells (Chen & Flies 2013, Hwang et al. 2020) as illustrated in figure 1.3. below.

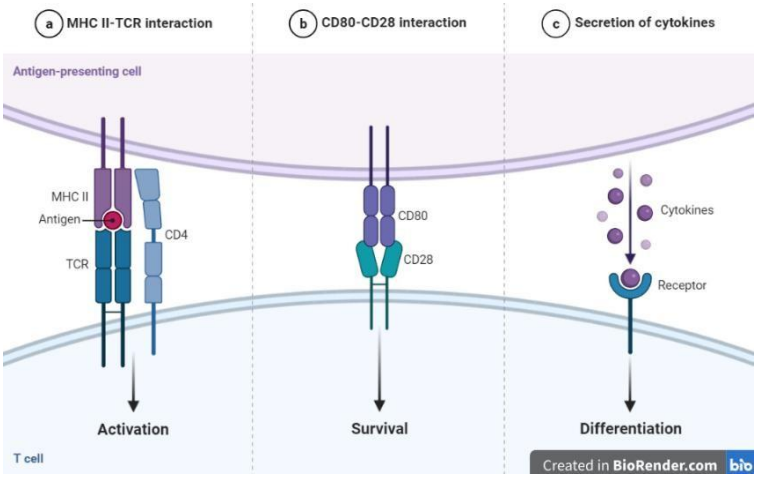

Figure 1.3: T-cell Activation. For a complete T-cell activation, following the interaction between TCR and pMHC, a second signal is required between co-stimulatory molecules and their ligands for example CD28 and CD80 interaction along with the release of pro-inflammatory cytokines.

Co-stimulatory molecules are spread throughout the surface of T-cells and following the interaction between MHC and TCR, the cytoskeleton is re-orientated to form an immunological synapse to sustain TCR activation and to facilitate and amplify signalling (Tskvitaria-Fuller et al. 2003). The immunological synapse consists of central Supramolecular Activation Clusters (cSMAC) which contains an abundance of TCRs bound to MHC to recruit signalling molecules that have a high affinity to their respective ligands

(Saito et al. 2010). Whereas the peripheral SMAC (pSMAC) contains integrins to aid in adhesion (Čemersk & Shaw 2006). Depending on the type of ligand-receptor interaction, different signalling pathways are initiated (Dower et al. 2000).

On naive T-cells, CD28 is the major co-stimulatory signalling molecule that interacts with CD80/86 to activate the T-cell to migrate toward that specific antigen (Riha & Rudd 2010). The intracellular pathways involved in activated T-cells are incompletely defined however studies have shown that CD28 interaction with CD80/86 increases the Phosphoinositide 3-OH Kinase (PI3-K) which in turn activates Protein kinase B (AKT) to increase cytokine production such as IL-2 and aid in T-cell survival, proliferation and migration (Kane et al. 2001, Woods et al. 2000). This signalling pathway can be observed in figure 1.4.

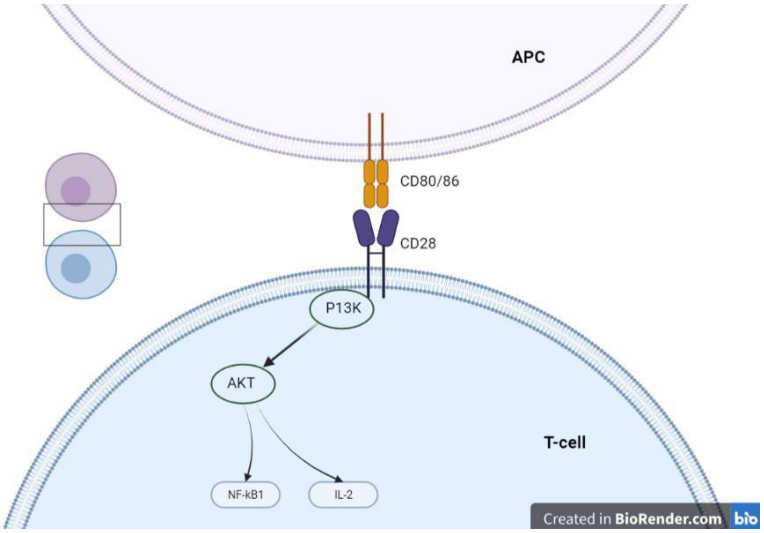

Figure1.4: CD28 signalling pathway. Following CD28 interaction with CD80/86, CD28 stimulates P13K to upregulate PDK1 which in turn activates AKT. PDK1 + AKT phosphorylate and regulate multiple pathways including IL-2 and Nuclear Factor-κB (NF-κB).

1.4. Immune evasion

Following the elimination of tumour cells by immunosurveillance, some tumour subclones may acquire further mutations to escape the immune response. This causes tumour

development to be stalled and reach an equilibrium phase. However, selective pressure imposed by the immune system results in immunoediting to promote low immunogenic subclones with a high tumorigenic potential to continue to proliferate and induce T-cell tolerance (Shankaran et al 2001 & Schreiber et al. 2002). This subclone causes an outgrowth of tumour and eventually cancer.

Tumour cells and its surrounding environment comprise various mechanisms that promote tumour proliferation while suppressing effector immune cells response. The acidic environment of tumours impairs the production of TCRs, secretion of cytokines and CD8+ cytolytic activity to induce a state of T-cell anergy in which the T-cell remains alive but functionally inactive. (Calcinotto et al. 2012). Due to the rapid proliferation of tumour cells, areas distal from vasculature are unable to have proper blood perfusion causing a hypoxic state (Goel et al. 2011). Tumour cells in these areas are better adapted to a limited supply of oxygen, nutrients and can promote further growth by stimulating angiogenesis (Vaupel et al. 2007). However, effector T-cells are less equipped to adapt to the hypoxic environment and instead immunosuppressive cells (Ostrand- Rosenberg et al. 2012) such as Regulatory T-cells (Tregs) (Facciabene et al. 2011) and Myeloid-Derived Suppressor Cells (MDSCs) (Corzo et al. 2010) start to accumulate. The immunosuppressive cells inhibit dendritic cell maturation, release of co-stimulatory factors and reduce the expression of MHC to prevent activation of CD8+ and CD4+ T-cells (Novitskiy et al. 2008). Cancer cells are further able to evade the immune response by directly releasing cytokines such as IL-10 (Dennis et al. 2013) and prostaglandin E2 (Benefield et al. 1996) to prevent maturation of dendritic cells (Ma et al. 2013) and upregulate the expression of immune checkpoint ligands to suppress activation of effector T-cells (Dennis et al. 2013, Lao et al. 2022). Furthermore, macrophages differentiate into M2 macrophages to secrete anti-

inflammatory cytokines such as IL-10 to inhibit T-cell activation (Qian et al. 2011). Macrophages may also express immune checkpoints such as programmed cell death ligand-1 (PDL-1) to further suppress T-cell activation (Kuang et al. 2009). Lack of APC, effector T-cells and an increase in inhibitory cells such as Tregs and MDSCs results in "cold" tumours which are associated with a poor prognosis (Tu et al. 2016).

1.5. Immune checkpoints

Immune checkpoints are co-inhibitory molecules present on the surface of APCs to regulate TCR signalling. Immune checkpoint expression is extremely dynamic, strictly controlled transcriptionally and post-transcriptionally, and greatly impacted by alterations in the environment (Liechtenstein et al. 2012). The type of co-inhibitory molecules and ligands present depend on changes within cellular activation, the tissue and cell type (Ravetech & Lainer 2000).

Co-inhibitory molecules can fine-tune the immune response by acting as threshold receptors or as negative feedback receptors (Rumpert et al. 2020). Threshold receptors and their accompanying ligands are present prior to T-cell activation, thus for a T-cell to become completely activated, co-stimulatory receptors that send a signal greater than the threshold inhibitory signal are required (Rumpert et al. 2020). This is done to distinguish between mild disturbances and avoid an unnecessary immunological reaction. Following cell activation certain inhibitory receptors can be disinhibited to ensure a continuation of the immune response to clear any pathogen present more effectively (Rumpert et al. 2020). On the contrary, inhibitory receptors and the expression of Forkhead box p3 (Foxp3)+ T-cells are upregulated following T-cell activation to act as a negative feedback response to

prevent surrounding tissue damage and an autoimmune response due to an overactive immune system (Jordan et al. 2001, Schnell et al. 2020, Zhu et al. 2012).

In 2012, Zhu et al. developed a tide model to explain the interaction between co-inhibitors and co-stimulators. This is initiated by the interaction between the TCR and the corresponding MHC molecule to trigger a cascade of signalling events that is only partially adequate to activate T-cells. The outcome and magnitude of the signalling cascade are determined by the spatiotemporal expression of antigen-independent interactions between T-cell co-stimulatory and co-inhibitory receptors and their associated ligands (Chen & Flies 2013). The outcome of the signalling cascade leads to either activation or differentiation of naive T-cells, deactivation of T-cells or a state of anergy (Zhu et al. 2012). Naive T-cells have an abundance of co-stimulatory receptors to induce activation and regulate cytokine production for T-cell differentiation into its helper or cytotoxic subtype. However, during peak immune response, co-inhibitors are often expressed along with co-stimulators and the outcome of T-cell activation depends on the type of receptors and ligands present, the ligand-receptor interaction and the affinity of the opposing receptors (Ravetch & Lainer 2000).

Some co-stimulators and co-inhibitors compete with one another to bind to the same ligands, for example, the Cytotoxic T-Lymphocyte Associated protein-4 (CTLA-4) co-inhibitor is a homologue of CD28 and hence competes with CD28 to bind with CD80/86. The CD28 interaction with CD80/86 promotes T-cell proliferation and immune cell migration to that location. Contrarily, when CTLA-4 interacts with CD80/86, it suppresses subsequent T-cell activation as shown in 1.5 below. When CD28 and CTLA-4 are both expressed on the same cell, they compete with one another for the same ligands' binding. If both are expressed, CTLA-4 outcompetes CD28 since it has a higher binding affinity for the ligands.

To further block the interaction with CD28, CTLA-4 may actively remove CD80/86 from APCs by trans-endocytosis (Pardoll 2015).

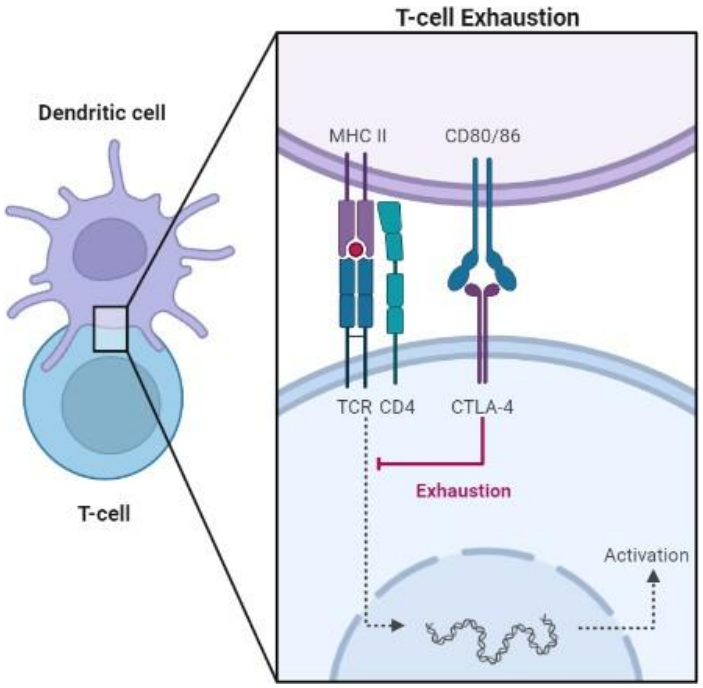

Figure 1.5: Schematic representation of T-cell exhaustion. If Co-inhibitory receptors interact with their ligands following TCR-pMHC interaction as depicted by CTLA-4-CD80/86 interaction, the T-cell becomes exhausted and loses its ability to generate cytokines and proliferate.

The role of co-signalling molecules is to tightly regulate the balance between eliminating pathogens and tumour cells while maintaining peripheral self-tolerance (Pardoll 2012). Co-inhibitory and co-stimulatory signaling mechanisms mutually regulate Tregs along with effector T-cells to maintain homeostasis. This mechanism of peripheral tolerance is present biologically to avoid excessive tissue damage due to the inflammatory response. On the contrary, in TME, there is an imbalance between the expression of co-inhibitors to co-stimulatory molecules to allow tumour cells to evade immune-mediated elimination.

1.6. Overexpression of inhibitory molecules in TME

Depending on the type of signalling pathway that these co-inhibitors generate, upregulation

of inhibitory molecules causes either T-cell exhaustion, anergy, or death. In the TME, T-cells progress from T-cells with co-stimulators capable of exhibiting effector function to partially exhausted T-cells, where T-cells begin to lose their ability to produce inflammatory cytokines such as IFN-γ. Finally, T-cells become fully exhausted which lack the ability to produce cytokines and proliferation (Wherry et al. 2003 & Zajac et al. 1998). This occurs due to the prolonged antigen stimulation from immunogenic tumour cells due to continual TCR and co-stimulatory engagement (Ahmadzadeh et al. 2009 & Schietinger et al. 2016). Furthermore, the presence of inflammatory cytokines such as IFN-α initially aids in control of tumour progression. Nonetheless continuous exposure causes T-cell exhaustion by inducing the production of inhibitory cytokines and inhibitory molecules such as IL-10 and CTLA-4 (Schietinger et al. 2016).

T-cells become anergic when they develop a tolerance mechanism that inhibits them from being activated in the presence of tumour cells. This is achieved as cells surrounding tumours overexpress co-inhibitory molecules and express suboptimal co-stimulatory molecules to prevent activation in the presence of an antigen (Crespo et al. 2013). Certain inhibitory molecules, such as T-cell Immunoglobulin and Mucin-3 (TIM-3) and Programmed Death-1 (PD-1), cause the death of tumour-infiltrating T-cells when they interact with their respective ligands (Shi et al. 2010, Kang et al. 2015).

1.7. Immune checkpoint inhibitors

These dysfunctional T-cells still retain some residual function to target tumour cells and reversal into the activated form is currently being thoroughly studied as a potential immunotherapeutic treatment (Xiao et al. 2020). Immunotherapy which was pioneered by Dr William B. Coley in 1890 was developed by studying the mechanism of tumour evasion

(Jia et al. 2020). It is a form of treatment that stimulates the body's immune system to recognize and respond to tumour associated antigens for degradation and to control tumour growth (Boyero et al. 2020). The overexpression of inhibitory molecules causing dysfunctional T-cells and an increase in Tregs can be targeted by a form of immunotherapeutic agent known as Immune Checkpoint Inhibitors (ICIs) (Sethi et al. 2013). The first immune checkpoint inhibitor licensed by the food and drug administration (FDA) was ipilimumab which consists of monoclonal antibodies targeting CTLA-4 shown in figure 1.6 (Leach et al. 1996). Expression of CTLA-4 results in downregulation of CD4+ T- cells and an increase in the expression of FOXP3 to upregulate Tregs (Lenschow et al. 1996, Wing K. et al. 2008). Therefore, targeting this inhibitor in tumours results in inhibition of Treg dependent immunosuppression and enhances the antitumor immune response (Peggs et al.2009). These CTLA-4 inhibitors were first licensed for the treatment of metastatic melanoma (He et al. 2017) and studies on the effectiveness of ipilimumab in stage III and stage IV melanoma have shown that patients administered ipilimumab have the highest response rate and disease control rates in comparison to patients administered conventional treatment (Fellner 2012 & Schadendorf et al. 2015). Thus, ipilimumab has a great potential to improve the survival rate of patients with metastatic melanoma.

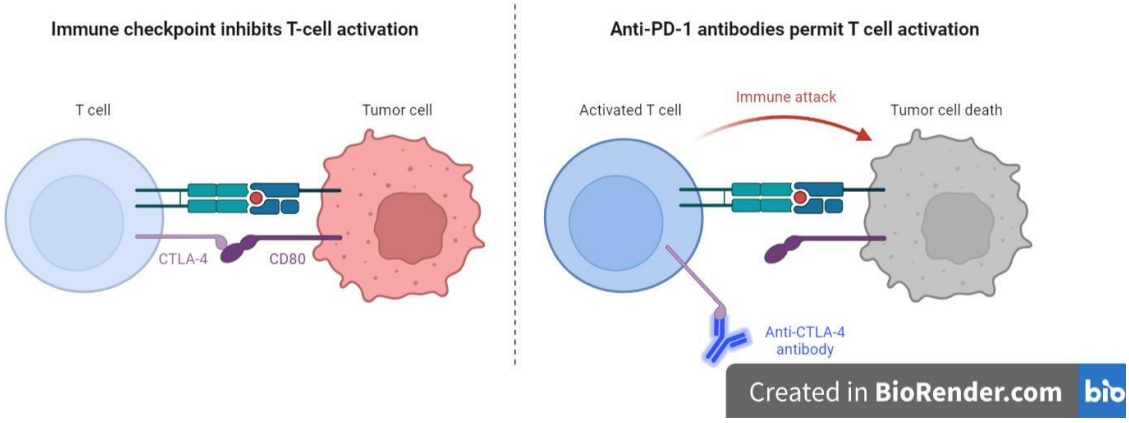

Figure 1.6 The mechanism of action of anti-CTLA-4 therapy. The interaction between CTLA-4 and CD80/86 results in deactivation of T-cells. However, monoclonal antibodies targeting CTLA-4 allows the T-cell to be re-activated and initiate anti-tumour response.

Following the approval of ipilimumab other ICIs have been FDA-approved including pembrolizumab which target PD-1 in various tumours including classical Hodgkin's lymphoma and non-small cell lung cancer (NSCLC) (Stewart 2021), and atezolizumab which target Programmed cell Death-Ligand1 (PD-L1) in liver cancer and lung cancer (National cancer institute 2022). Studies on administration of anti-PD-1 and anti-PD-L1 have also shown that the use of these ICIs have drastically increased the survival rate of high-grade tumours (Topalian et al. 2014, Lynch et al. 2012, Postow et al. 2015).

1.8. Statement of the problem

During treatment with ICIs, patients may develop immune-related Adverse Events (irAEs) that have the potential to cause a severe reaction. These irAEs include nausea, diarrhoea, gastrointestinal disorders, abdominal pain and hypothyroidism and a small subset of patients also experience grade III or grade IV drug-related adverse events. In anti-PD-1/PD-L1 treatment, low grade generalised symptoms were reported in 95% of patients whereas 6% experienced irAEs of a severe grade (Hamid et al. 2013).

There are various causes of these adverse events which may be due to an imbalance in immunologic homeostasis following treatment, which result in a lack of T-cell tolerance (Postow et al. 2018). This is because therapeutic antibodies can target immune checkpoints expressed on normal tissue to trigger an inflammatory response (Baban et al. 2015). Since tumour cells may express antigens corresponding to antigens present on normal tissue, the immune response against tumour cells may cross-react and target normal tissue (Byrne & Fisher 2017) and lastly ICIs may also upregulate the levels of autoantibodies present prior to treatment (Kimbara et al. 2018).

Even though most patients experience some form irAEs, only a small subset of patients

respond to ICIs. Approximately, 15-30% of patients with solid tumours respond to treatment with other individuals either having primary resistance towards the treatment or relapse after the initial response to form acquired resistance. The cause of resistance towards ICIs are highly complex and not completely understood however certain mechanisms have been characterised.

Resistance to ICIs may be caused by the immune inhibitory environment of tumours containing an increased level of inhibitory cells such as MDSCs, Tregs, inhibitory cytokines and various co-inhibitory receptors not targeted by the treatment. Resistance may confer in tumours with a low tumour mutational burden (TMB) and neoantigen expression as they prevent T-cell recognition of tumour specific antigens (Rizvi et al. 2015). Alterations in genes involved in the antigen-presenting machinery cause immunoresistance. These include defects in genes expressing the MHC molecules such as deletions in the beta-2-microglobulin protein which prevent proper folding of the MHC-I molecule. This would result in tumour cells being unable to present antigens on their surface and impair the CD8+ T-cells from causing its cytotoxic function (Restifo et al. 1996). Defects in T-cells effector pathways such as loss of Janus Kinase 1 and 2 (JAK1/JAK2) genes confer resistance to anti-PD-1 therapy. These defects prevent the transcription of genes involved in anti-tumour activity from being activated (Shin et al, 2016).

Immunoresistance is also affected by oncogenic signalling pathways. Loss of Phosphatase and Tensin Homolog (PTEN) tumour suppressor genes during tumour development are associated with anti-PD-1 resistance. This is because the PTEN pathway dampens Phosphoinositide 3-Kinase (PI3K) signalling which is critical for cell survival and proliferation. Loss of PTEN pathway is associated with upregulation of PI3K signalling along with overexpression of CC motif chemokine ligand 2 (CCL2) and Vascular Endothelial

Growth Factor (VEGF) which are inhibitory cytokines of T-cells (Peng et al. 2016). Certain transcriptomic changes known as Innate anti-PD-1 Resistance (IPRES) also confer resistance in patients administered anti-PD-1. These include genes involved in angiogenesis, ECM remodeling, adhesion of cells, mesenchymal transition and wound healing that are found overexpressed in patients of different tumour types not responding to anti-PD-1 treatment (Hugo et al. 2016).

1.9. Improving the effectiveness of ICIs

To improve the efficacy of ICIs, predictive biomarkers may be investigated prior to treatment. This is due to the variability of each tumour, which makes it difficult to determine the response rate of an individual towards treatment. As predictive biomarkers for anti-PD-1/PD-L1 therapy, the National Comprehensive Cancer Network (NCCN) advises assessing PD-1 and PD-L1 expression as anti-PD-1/PD-L1 therapy is associated with a greater response when more than 10% of cancer cells express PD-L1. As a matter of fact, in cases of NSCLCs, pembrolizumab can be used as a primary treatment in patients that have over 50% of the proportion of PD-L1 positive cancer cells over total tumour cells since this treatment has the highest rate of progression-free survival (Herbst et al., 2016). Analysis of Tumour Mutational Burden (TMB) as a companion predictive biomarker can be performed as it has been linked to a better overall survival benefit (Fuchs et al. 2022). Investigating genetic variations in signalling pathways which can either improve or reduce efficacy can be performed. For example, microsatellite instability (MSI), which is brought on by genetic changes in the Deoxyribonucleic Acid (DNA) mismatch repair pathway, increases the amount of neoantigens presented to CD8+ T lymphocytes. Thus, their presence in tumours has been associated with a higher response rate and overall survival

benefit in patients receiving nivolumab and ipilimumab (Overman et al. 2018).

Immune status in the TME can be investigated. The adaptive immune response in TME can be categorised as inflamed, immune-excluded and immune-desert phenotypes (Galli et al. 2020). The immune-excluded phenotype arises when TME prevents the release of chemokines that stimulate T-cell recruitment and form physical barriers to surround the TME. Soluble molecules such as VEGF drive the formation of dense collagen fibers to form a physical barrier which contains an increased fibre mass to surround the TME to prevent any immune cells from entering the area. This results in a high cluster of immune cells surrounding the tumour area (Kather et al. in 2018). Immune desert phenotype results from the increase of Tregs, macrophages and MDSC which inhibit T-cell proliferation and activation. (Kather et al. 2018 & Galli et al. 2020). Their presence prevents the infiltration of the CD4+ and CD8+ T-cells from surrounding and infiltrating the TME (Kather et al. 2018). The third type of phenotype is the inflamed type. In the inflamed type, the TME is infiltrated with CD4+ and CD8+ T-cells that can recognize these neoantigens. This type of environment promotes the highest response with ICI treatment (Gajewski et al. in 2017).

In recent years, cancer immunotherapy has significantly developed, and it is being recognized as a key feature in the control of tumour progression (Qin et al. 2019). The use of ICI can be administered in conjunction with radiotherapy and chemotherapy. Radiotherapy in combination with ICIs has been shown to act synergistically by increasing the presentation of tumour antigens, T-cell activation and stimulates the Interferon (IFN) genes to facilitate the adaptive immune response. Combinatory radiotherapy and immunotherapy may increase the likelihood of radiation mediated and immune mediated adverse events (Bang & Schoenfield 2019). In some cancer types, chemotherapy used in

conjunction with ICI is the standard of care. These work in tandem to improve the response rate since chemotherapy aids to transform cancer types that lack CD4+ and CD8+ T-cell infiltration into those that can be infiltrated by these immune cells (Galluzzi et al. 2020).

Nonetheless, a single immunotherapeutic agent is not suitable to treat all individuals with the same tumour type or all tumours present. Therefore, combinatory ICI therapy is generally preferred as it has an increased likelihood of targeting diverse tumour cells and its environment for destruction while preventing resistance (Tan et al 2020). Thus, other ICIs that target different co-inhibitory molecules than those FDA approved and have a lower incidence of irAE are currently being investigated (Qin et al. 2019). In this study antibodies targeting V-domain immunoglobulin suppressor of T-cell activation (VISTA) and PD-L1 immune checkpoints will be generated.

1.10. VISTA

VISTA is a relatively novel co-inhibitory molecule which forms part of the B7-butyrophilin family. VISTA is coded by the VISR gene found on the reverse strand of chromosome 10 in humans whereas in mice it is found on the forward strand of the same chromosome. It is highly conserved as it shares 85.6% sequence similarity between human and mouse VISTA (Flies et al. 2011). It is mainly expressed on haematopoietic cells most commonly on the, FOXP3+ Tregs, CD11+ myeloid-derived cells, dendritic cells and to a lesser extent on the CD4+/CD8+ T-cells and neutrophils (Wang et al. 2011). VISTA was also found to be highly expressed on tissue of the brain, thyroid and stomach (Wang et al. 2020). VISTA is composed of a type 1 transmembrane protein having an Immunoglobulin variable (IgV) region, stalk segment and a cytoplasmic tail containing a conserved Src homology 2 (SH2) binding motif and a C-terminal SH3 binding domains which are required for the

downstream signaling pathway (Yuan et al.2021). Studies on the structure of VISTA by Slater et al. 2020 has found that this molecule contains an abundance of highly conserved histidine residues which form 3 histidine clusters in the extracellular domain. The function of the clustered histidine residues is still mainly undetermined, but these form an FG loop that corresponds with the CDR3 region of the TCR. In addition, these clusters are required to determine the binding affinity to its corresponding antigen.

VISTA acts both as a ligand on APCs and a receptor on naive T-cells as its cytoplasmic tail contains two protein kinase C binding sites to signal VISTA-expressing cells as well as proline residues that can serve as docking sites (Flies et al. 2011). The role of VISTA as a ligand was demonstrated on lymphoma cells expressing VISTA which were interacting with an unidentified receptor on T-cells to inhibit T-cell proliferation and cytokine production (Wang et al. 2011). VISTA exhibits its inhibitory effect to induce T-cell tolerance through various pathways that are still mainly undetermined however VISTA was shown to induce Tregs production and prevent T-cell priming (Flies et al. 2015).

A study done by ElTanbouly et al. 2020 showed that when compared to wild type mice, VISTA deficient mice exhibited an increase in activated CD4+ T-cells. Furthermore, single-cell RNA sequencing performed on wild type and VISTA deficient mice revealed that wild type mice upregulated inhibitory genes such as Kruppel like factor 2 (KLF2), B-cell translocation gene (Btg)1 and Btg2 (ElTanbouly et al. 2020). The KLF2 is expressed in T-cells to prevent proliferation and protein synthesis and maintain T-cell quiescence (Leiden et al. 2001) whereas btg genes have a role to increase T-cell activation threshold by downregulating CD3 signalling to further inhibit T-cell proliferation (Boussiotis et al. 2001). Mice with VISTA deficiency had an increased expression of KLF3, T-cell factor7 (Tcf7), B-cell lymphoma 2 (Bcl2) and interleukin 7 receptor (Il7r). The KLF3 functions as a KFL2 and

KFL4 agonist whereas Tcf7 interacts with Bcl-6 to promote T-cell proliferation and to generate memory T-cells (Liu et al. 2019). The Il7r and Bcl2 also aid to promote T-cell survival by upregulating anti-apoptotic proteins (Lefrançois et al. 2000). Additionally, there was an increased expression of signalling lymphocyte activation molecules 6 (Slamf6) and IFN-γ receptor 1 (Ifngr1) to increase the expression of co-stimulatory receptors along with an upregulation of actin genes and Calponin 2 (Cnn2) to maintain the immunological synapse (ElTanbouly et al. 2020).

Wang et al. in 2019 discovered a ligand, the V-Set and Immunoglobulin domain containing 3 (VSIG-3) that can interact with VISTA. They confirmed this by using small interfering RNA (siRNA) to create CD3+ cells that expressed various quantities of VISTA receptors. They discovered that the quantity of VISTA expression on the CD3+ cells correlated with the inhibitory effect created by the VSIG-3. The IgSF family member VSIG-3 is a co-inhibitory ligand that can prevent the release of cytokines like CCL5, CCL3, CXCL-11, IL-2, IL-17, and IFN-Ɣ to stop T-cell proliferation and to prevent the infiltration of Th1 subtype into the TME. The VSIG-3 is reported to be upregulated in gastric and hepatocellular carcinomas (Wang et al. 2017).

Furthermore, Johnston et al. 2019 hypothesised that VISTA binds with a stronger affinity to other counter-receptors at an acidic environment such as TME. This study revealed that at an acidic-pH, P-selectin glycoprotein ligand-1 (PSGL-1) receptor binds with VISTA. The PSGL-1 exhibits its co-inhibitory effect by releasing cytokines such as IL-10, Transforming Growth Factor-β (TGF-β) and 2,3-dioxygenase (IDO) to stimulate the production of Tregs (Urzainqui et al. 2007). This study further investigated the pH selective binding between the PSG-L1 and the VSIG-3 and found that there was no specific binding between these two

molecules in the cell-based assays. Therefore, VSIG-3 and the PSGL-1 do not compete to bind with VISTA. Recently VISTA was also shown to interact with the ligand; galectin-9. The interaction between VISTA and galectin-9 prevents the release of granzyme B from T- cells and activates caspase-3 pro-apoptotic pathway to induce T-cell apoptosis (Yasinska et al. 2020). The interaction between VISTA and its inhibitory ligands can be observed in figure 1.7 below.

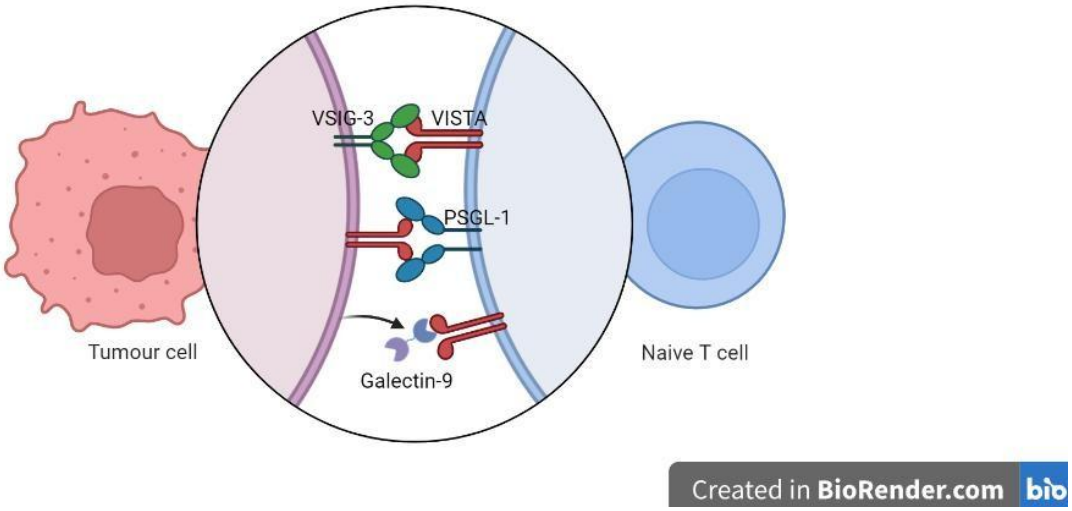

Figure 1.7: The interaction of VISTA with its respective receptor and ligands. VISTA functions as a receptor for VSIG-3 and galectin-9 as well as a ligand for PSGL-1. Illustration adapted from Yum & Hong 2021.

VISTA is a homologue to programmed cell death ligand-1 (PD-L1) and to a lesser extent to PD-1. A blast sequence done by Altschul et al. 1990 found that VISTA has a sequence identity of 24% with PD-L1, which was further confirmed computationally by analysing the IgV domain of all other known structures. VISTA was also found to have some sequence similarities to PD-1 during a National Center for Biotechnology Information (NCBI) database search on the similarity of IgV regions to known co-signalling molecules, Flies et al. 2011 found that VISTA had similarities with CD28 and B7 families however full-length VISTA and PD-1 had several identical residues in the IgV domain. Hence following this

study, VISTA was also referred as PD-1 homologue (PD- 1H).

VISTA is overexpressed on various tumours including ovarian, NSCLC, prostate and melanoma (ElTanbouly et al. 2019). In gastric tumours VISTA is expressed mainly on the infiltrating immune cells with only a small subset of gastric tumours having VISTA expressed in the cytoplasm. The expression of VISTA is strongly associated with PD-L1 expression, and these inhibitors are upregulated on a subgroup of gastric tumours (Böger et al. 2017). Hence, targeting both VISTA and PD-L1 in this gastric tumour subgroup may have a synergistic treatment effect. Furthermore, other studies on different tumours have also found that VISTA and PD-L1 expression are strongly associated. A study performed by Gao et al. 2017 showed that VISTA, PD-L1 and PD-1 were upregulated following ipilimumab treatment in metastatic prostate cancer on CD4+, CD8+ T-cells and macrophages. The expression of these inhibitors reduced IFN-Ɣ and TNF-α production. Overexpression of VISTA following anti-PD-1 therapy may be a mechanism of acquired resistance in endometrial and ovarian tumours therefore, the use of anti-VISTA following anti-PD-1 resistance can be done to activate the anti-tumour response (Mulati et al. 2019).

1.11. The interaction of PD-L1 with PD-1

PD-L1 is a protein receptor coded by the CD274 gene present on chromosome 9. It is composed of 2 extracellular domains made up of Immunoglobulin constant (IgC)-like domain and IgV-like domain along with a transmembrane and cytoplasmic domain (Akinleye & Rasool 2019). This is upregulated after stimulation by IFNs mainly mediated by the MEK/ Extracellular signal Regulated Kinase (ERK) dependent pathway and MyD88/TRAF6-dependent pathway (Liu et al. 2007). It is biologically expressed on T-cells,

B-cells, certain APCs including dendritic cells, macrophages, mast cells derived from bone marrow (Yamazaki et al. 2002) and on tissue such as the heart, lung and kidney to limit an autoimmune reaction towards this tissue (Freeman et al. 2000). However, it has been shown to be overexpressed on different types of solid tumour cells including tumours of kidney, pancreas, uterus, skeletal muscle and colon (Chen et al. 2002) and certain chronic infections to evade an immune response by reducing TCR and CD28 signalling, reducing cytokine production and inhibiting T-cell proliferation and survival (Sheppard et al. 2004, Hui et al. 2017). Overexpression of PD-L1 is associated with a poor overall survival rate (Hino et al. 2010, Thompson et al. 2006) because tumours expressing PD-L1 act as oncogenes promoting tumour development and metastasis. PD-L1 can interact with PD-1 and given that PD-1/PD-L1 pathway has an active role on tumour cells and its surrounding environment, ICIs targeting this interaction have a great potential to mediate an antitumor immune response.

PD-1 is a type I transmembrane protein made up of an immunoglobulin domain, a transmembrane domain and an intracellular domain containing a Tyrosine-based Inhibitory Motif (ITIM) and a Tyrosine-based Switch Motif (ITSM) immunoreceptors found on the Pdcd1 gene on chromosome 2 in humans. PD-1 forms part of the CD28 family and acts as an immune checkpoint on activated T-cells, B cells and on other APCs such as myeloid cells and dendritic cells. However, their function on APCs is yet to be determined (Keir et al. 2008).

The mechanism of action on how PD-1 can exert its inhibitory effect is not completely understood however different inhibitory pathways have been proposed to be initiated by PD-1. PD-1 effect can be TCR-dependent where a low TCR stimulation promotes inhibition

by PD-1 whereas an increase in TCR or CD28 signalling can circumvent the inhibitory signals of PD-1 (Freeman et al. 2000). In the immunological synapse, PD-1 is phosphorylated once it binds with the ligand. Following this, SH-2 domain containing tyrosine phosphatase-2 (SHP-2) and possibly SHP-1 interacts with ITIM and ITISM motifs to dephosphorylate signalling pathways such as mammalian target of rapamycin (mTOR) and RAS-ERK pathways. In addition, it upregulates the PTEN pathway to antagonise PI3K and reduce antigen receptor signalling of CD3 and CD28. PD-1 inhibitory signalling pathway is depicted in figure 1.8 below.

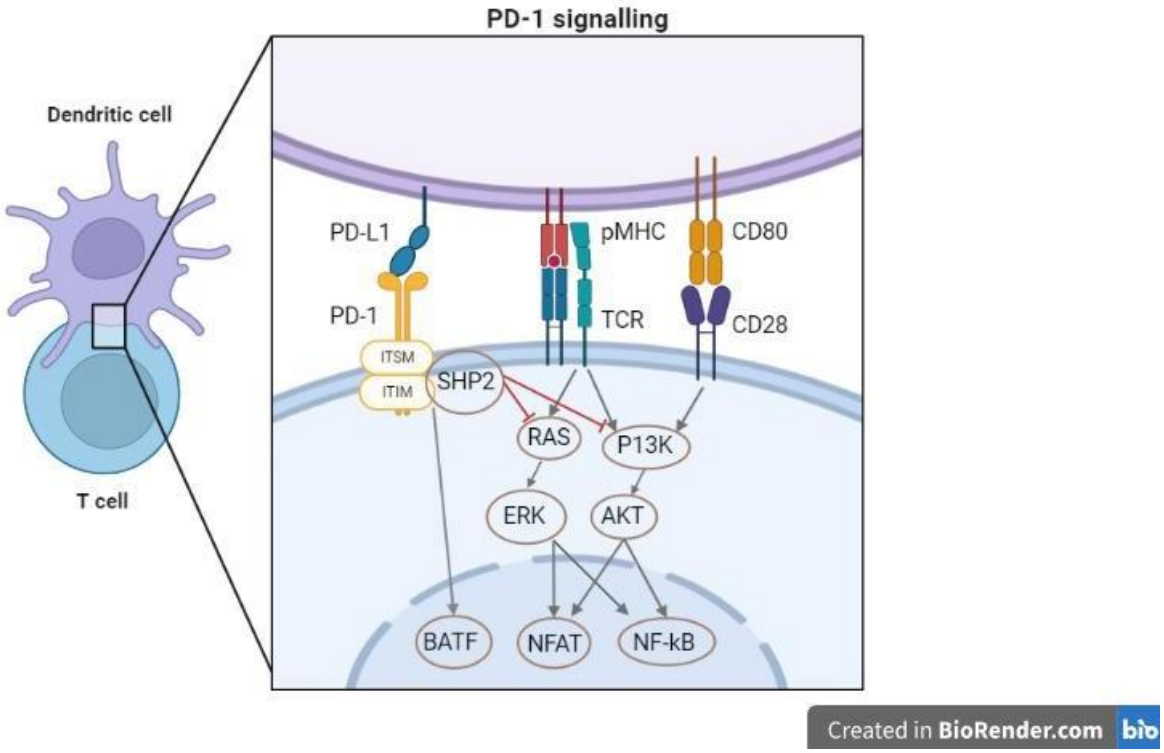

Figure 1.8: PD-1 signalling in T-cells. For PD-1 to exert its function, SHP2 phosphorylates the ITSM domain in the PD-1 tail. This phosphorylation results in inhibition of TCR signalling and its signalling pathways including P13K-AKT and RAS pathways to reduce the activation of transcription factors NF-κB and Nuclear Factor of Activated T-cells (NFAT). This phosphorylation also results in increased expression of BATF to further inhibit the expression of transcription factors. Adapted from Sharpe et al. 2017.

PD-L1 has the ability of reverse signalling. This occurs when PD-L1 expressed on dendritic cells interact with PD-1 to inhibit dendritic cell activation and upregulate IL-10 and IDO

production (Kuipers et al.2006). PD-1 increases the expression of basic leucine zipper transcriptional factor ATF-like (BATF) to suppress the expression of Transcription factors such as FOX 01, IFN and Nuclear Factor of Activated T-cells (NFAT). This also induces further PD-1 production on T-cells in TME causing T-cells to be highly expressed with PD-1 (Staron et al. 2014).

The FDA has approved 6 ICIs targeting the PD-1/PD-L1 pathway: pembrolizumab, nivolumab and cemiplimab for PD-1 and atezolizumab, avelumab and durvalumab to target PD-L1. Pembrolizumab and nivolumab were approved for the treatment of melanoma whereas cempilimab was approved for the treatment of cutaneous squamous cell carcinoma. Atezolizumab was developed to target urothelial carcinoma and NSCLC whereas durvalumab was approved to be administered in unresectable NSCLC following chemoradiation and urothelial carcinoma. Avelumab was approved to target metastatic merkel cell carcinoma (Ai et al. 2020). Treatment with these ICIs has been shown to considerably increase overall survival, which can vary from 13.8 months to 36.9 months, which is significantly longer than previous standard chemotherapy, which ranged from 5.3 months to 18.4 months (Ardizzoni et al. 2022, Averbuch et al. 2023, Garon et al. 2019, Sandru et al. 2014, Sezer et al. 2021, Wolchok et al. 2022, Wolf et al. 2023).

1.12. Biopanning phage display technique

In this project, monoclonal single chain variable Fragment (scFv) part of antibodies will be generated to target VISTA and its homologue PD-L1 using the biopanning phage display technique. The Phage Display technique involves expressing several scFv antibodies on the surface of M13 phages. This is accomplished using modified M13 phages that can fuse short protein DNA sequences to the N-terminus of the minor coat protein PIII, allowing the

scFv to be expressed on the surface fused with the PIII protein. This fused protein can interact with the F-pilus of the bacteria that is infected by the phage (*Ph.D. Phage Display Libraries* n.d). The library of bacteriophages will be used to competitively bind to a target immobilized on a solid surface by the biopanning technique. The unbound phages will be washed off whereas the bound phages will be eluted. A schematic representation of biopanning phage display technique can be observed in figure 1.9. This cycle will be repeated four times for amplification so only the phages that contain proteins with a high affinity towards the target are selected. (Bazan et al 2012).

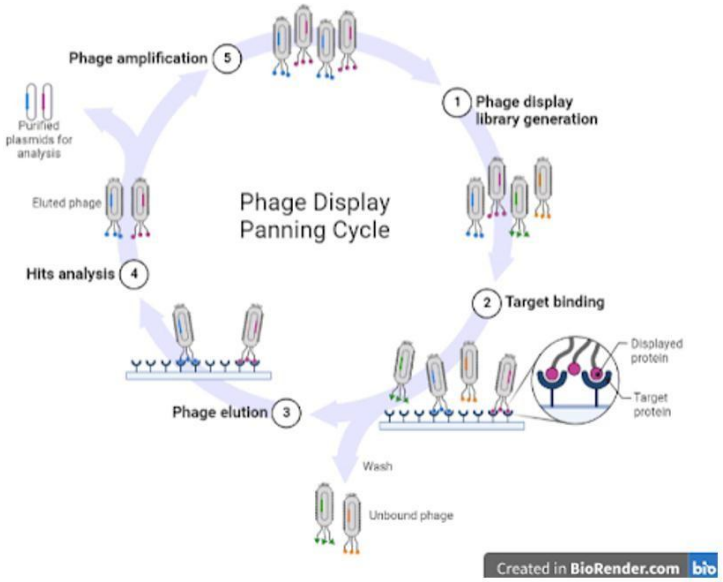

Figure 1.9: Schematic representation of the biopanning phage display technique. Canine scFv antibodies will be extracted and expressed on the surface of M13 phages. These phages will compete to bind to the respective targets; VISTA and PD-L1. The bound phages will be eluted and amplified and used for the subsequent round.

1.13. Aims & objectives

The main aims and objectives of this project will be to generate two monoclonal scFv antibody libraries that will respectively have a strong affinity towards VISTA and PD-L1. These will be generated from two polyclonal libraries that have undergone 4 rounds of biopanning phage display technique to produce phages which have a high affinity towards

their respective targets. Binding analysis of the phage pools following each round will be assessed using Enzyme-Linked Immunosorbent Assay (ELISA). In addition, 30 monoclines from each library will be picked at random to assess the affinity against their target protein and unrelated proteins using ELISA. Following this, the scFv amino acid sequence of each monoclone will also be analysed by Sanger sequencing. This will be done to determine which clones have the highest affinity towards VISTA and PD-L1 and are ultimately ideal as immune checkpoint targets.

Chapter 2:

Method

Ethics approval

- This research project was acknowledged by the Faculty of Health Science Research Ethics Committee (Frec) and has a unique application ID of FHS-2022-00428

2.1.1. Biopanning phage display

The research was carried out at the Centre for Molecular Medicine and Biobanking using a Class 2 laminar flow hood. The scFv phage library for biopanning was kindly provided by the International Centre for Cancer Vaccine Sciences (ICCVS). This library was made up of various combinations of antibody kappa or lambda light chains with heavy chains ligated with the pIII protein of phagemid vectors. These engineered phagemids transfected *E.coli* and with the aid of helper phages produced a pool of M13 phages, which can bind to a vast range of antigens with a high binding affinity (Bashir & Paeshuyse 2020, Liu et al. 2024).

The procedure for biopanning was carried out following our in-house standard operating procedure based on *Ph.D. Phage Display Biopanning Manual of New England Biolabs.* Four rounds of biopanning were performed against PD-L1, VISTA and a non-protein control (NPC) to ensure that there was no non-specific binding. Successful biopanning against VISTA had previously been performed (Spiteri 2022) thus biopanning of VISTA during this project was done as a positive control. However, for this biopanning a different protein tag was utilised as the VISTA bait protein for Spiteri 2022 project was a chimera protein containing an FC region to bind with protein G paramagnetic beads. Protein G originate from streptococcal species, and although it has a strong affinity towards the Fc region of immunoglobulins, it has also been found to bind weakly with the Fragment antigen-binding (Fab) region of immunoglobulins. Certain strains may interact with serum albumin

(Boström et al. 2011). Thus, for this project, the proteins were fused with a poly-histidine tag (HT) which was specifically designed for protein purification to elute proteins by binding with transition metals present on the dynabeads (Malhotra A. 2009). The VISTA and PD-L1 bait proteins with a stock concentration of 100µg/mL [Sino Biological, Bejing, China] contained a HT on the C-terminus. These have a high affinity towards nitrilotriacetic acid (NTA)-cobalt based ligands present on superparamagnetic beads (Co-NTA MagBeads) [Thermo Fisher Scientific Inc., Waltham, Massachusetts, U.S.A]. Superparamagnetic beads were used as Spiteri & Grima 2022 undergraduate projects showed that bead-bound immobilisation was found to generate higher affinity antibodies when compared to proteins immobilised on an ELISA plate.

For biopanning phage display, VISTA and PD-L1 target proteins fused with a HT were diluted 1:10 to create a working concentration of 10µg/mL. These were respectively immobilised on Co-NTA Magbeads with a working concentration of 4mg/mL to act as baits. Immobilisation was achieved through the interaction between the polyhistidine residues of the HT and the cobalt ions chelated to the NTA on the Magbead surface. These bait proteins were incubated with Co-NTA MagBeads for 30 minutes with rotation. To block non-specific binding sites, the bead-protein complexes were incubated for 1 hour with 150 µL of blocking buffer containing 3% Bovine Serum Albumin (BSA) [Sigma Aldrich, Missouri, USA] and 0.1% Tween 20 in PBS. For the first round, the scFv library, with a titre of 10^{12} PFU/mL and a diversity of 1×10^9 (Lisowska et al., 2025), was diluted 1:75 in blocking buffer. This dilution was calculated to represent approximately two copies of each clone, assuming equal representation. The diluted library was then incubated with the different bait proteins and the NPC for 1 hour with gentle rotation. The bound phages were captured using a magnetic separation rack that attracts the Co-NTA Magbeads. Elution of the bound

phages was performed by incubating with 150µl of 100mM triethylamine (TEA) solution with a pH of 11.3 for 10 minutes with rotation. The eluate was transferred to fresh low retention tubes and neutralised using 1M TRIS with a pH of 6.8 and these were stored at 4ºC.

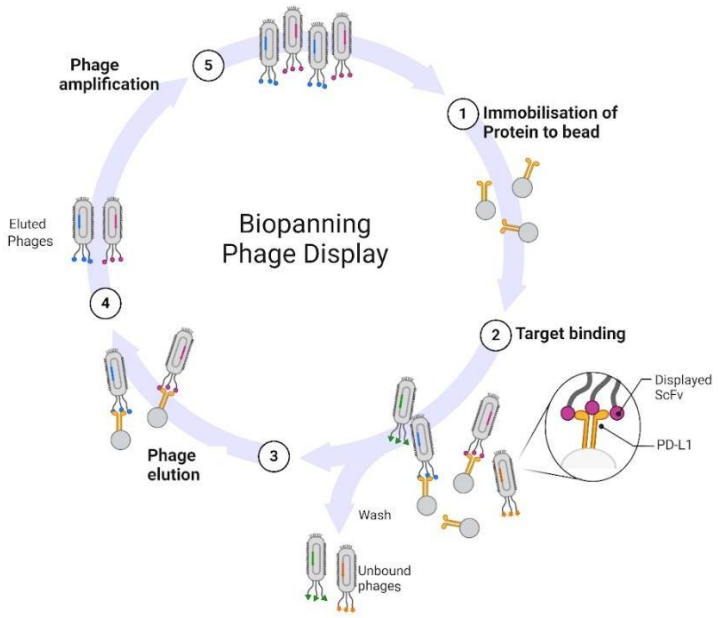

Figure 2.1: Schematic representation of biopanning phage display technique. Initially the PD-L1 protein was immobilised onto paramagnetic beads and the phages competed with each other to bind to PD-L1. The bound phages were eluted and amplified and used for the subsequent rounds.

2.1.2. Mid-log phase of the liquid culture

Amplification of phage eluates was performed by culturing mid-log phase *E.coli* ER2738 which are Tetracycline (Tet) resistant. Mid-log phase *E.coli* were required as adsorption of the bacteriophage to the bacteria occurs through the F-pilus which is broken down during the stationary phase of *E.coli.* (Ready-To-Use Phage Display Library Manual n.d. & Nilsson et al. 2000).

To culture mid-log phase *E.coli,* initially a primary plate was prepared by streaking *E.coli* ER2738 on Luria-Bertani Agar containing 100mg/mL Tetracycline (Tet LB agar) using the

Streak Plate Method illustrated in figure 2.2. The Streak Plate Method was achieved by spreading 10µL of the *E.coli* ER2738 to streak 1⁄4 of the plate using back and forth motion (Sanders 2012). The streaks produced on the 1st quadrant acted as the pool. The side of a new loop was used to spread the inoculum from the area that was streaked last to the adjacent quarter of the plate, streaking in the same motion as the pool. The same technique was used to streak the 3rd quarter; 4th quarter and the center of the plate (Sanders 2012). The streaked plate was incubated overnight at 37°C.

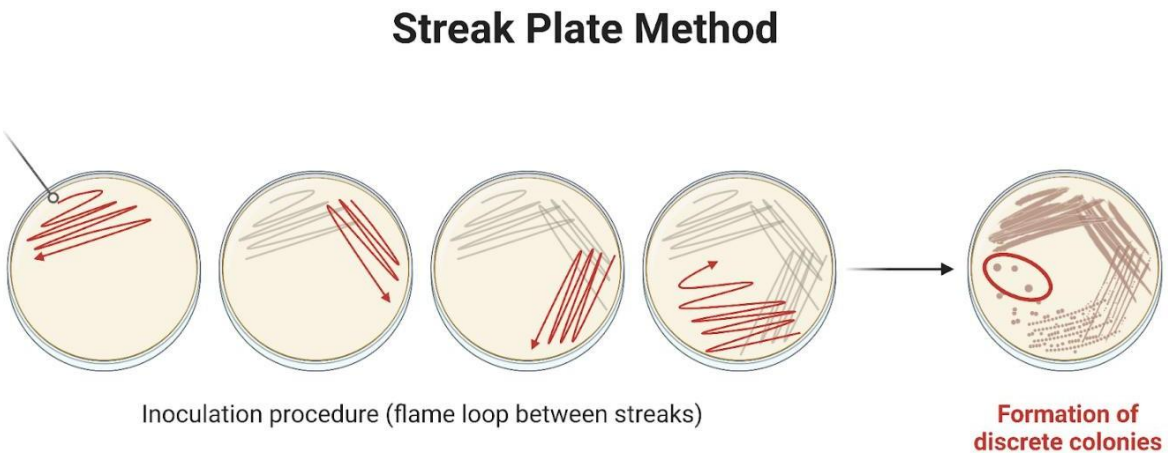

Figure 2.2: The Streak Plate Method. A sterile loop was used to streak the culture plates in a back-and-forth motion to streak 1/4th of the plate. This inoculum was spread in the same motion on the adjacent quarter and this was repeated to streak all 4 quarters of the plate. This streaked plate was incubated at 37°C overnight and the following day single colonies were picked to inoculate the LB broth.

A single colony grown on the primary plate was used as a source of fresh colony to inoculate 25mLs of LB broth containing 100mg/mL Tet (Tet LB broth). This was incubated for 16 hours at 220rpm (Ready-To-Use Phage Display Library Manual n.d.). Following this, 250µL of the incubated liquid culture was transferred into 25mLs of fresh Tet LB broth and incubated at 37°C at 250rpm. After a 1.5-hour incubation, the Optical Density (OD) of the culture was checked using a spectrophotometer set with LD600 [Eppendorf, Hamburg, Germany] as mid-log phase culture produces an OD reading between 0.4-0.6 (Ready-To-

Use Phage Display Library Manual n.d.). Prior to testing OD reading of the culture, the blank was set up using Tet LB broth only. If the OD reading was lower than 0.4, the broth was re-incubated, and the OD reading was checked at 15-minute or 30-minute intervals. Once the liquid culture reached the required OD reading it was immediately chilled at 4^{o}C.

2.1.3. Amplification of phage eluates

To amplify the phage eluate produced from biopanning explained in 2.1.1, 90µL of the neutralised eluate was added to 1mL of mid-log phase culture and incubated for 15 minutes at 37^{o}C. The M13 phages used during biopanning carry the ampicillin resistance gene. Thus, to ensure that only *E.coli* infected with M13 phages are amplified, the neutralised phage eluate with mid-log phase culture is diluted in LB broth containing 100mg/mL of ampicillin (amp LB broth). These were incubated at 37^{o}C for 1.5 hours while shaking at 250rpm. Helper phages M13KO7 which were made in-house with a stock titre of 6.9x10^{12} PFU/mL were then added to the culture and incubated further at 37^{o}C for 1.5 hours while shaking at 250rpm.

Helper phages were required as the phages only insert phagemid vectors containing the scFv-G3P fusion protein and the phage origin of replication to synthesise single stranded DNA (ssDNA). This ssDNA can be assembled into phages in the presence of helper phages as they provide the complete M13 genome to synthesise coat proteins and enzymes required to produce phages incorporated with phagemid DNA (Hoy 2013, Ledsgaard et al. 2018). The helper phages added also contain kanamycin (kan) resistance gene thus to select only the culture cells superinfected with helper phages, 50mg/mL of Kan was added, and the culture was incubated overnight at 30^{o}C while shaking at 250rpm.

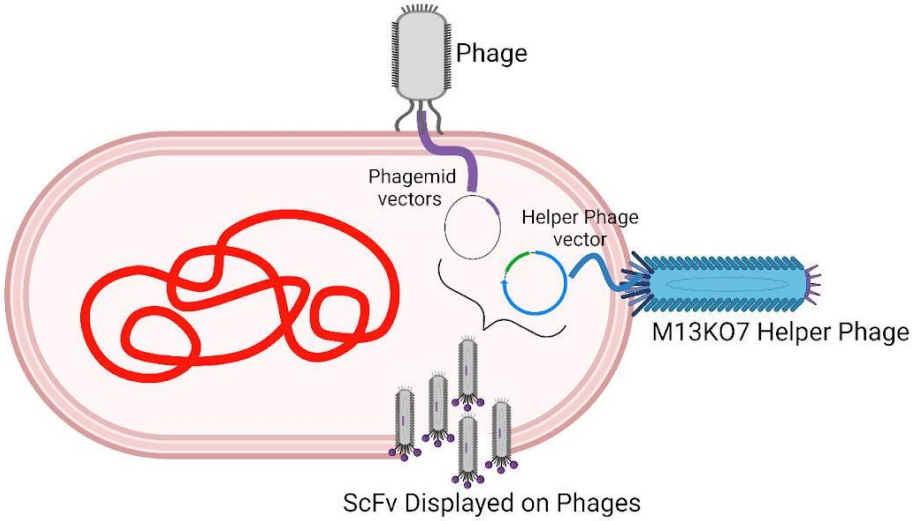

Figure 2.3: Assembly of Phages displaying the scFv protein. The eluted phages insert phagemid vectors which do not contain the whole M13 genome thus M13KO7 helper phages were added containing the whole M13 genome to synthesise structural and functional proteins required to convert the amplified phagemids into phages.

2.1.4. Precipitation of phage eluates

The following day, the mid-log phase culture with phage eluate and helper phages were centrifuged at 4000rpm for 10 minutes. The supernatant was transferred to clean falcon tubes and sterile 20% Polyethylene glycol with 2.5M Sodium chloride (PEG/NaCl) [Thermo Fisher Scientific Inc., Waltham, Massachusetts, U.S.A.] was added to the supernatant of the centrifuged sample. These were incubated on ice for 2 hours to precipitate the phages. PEG is an inert hygroscopic polymer that effectively precipitates phages following centrifugation (Fahie-Wilson & Halsall, Yamamoto & Alberts). Centrifugation was done twice at 4000rpm for 20 minutes at 4°C, removing the supernatant after each centrifugation. The phage pellet was resuspended in 200µL of sterile PBS and centrifuged at 4°C at 10,000rpm for 10 minutes. The supernatant of this centrifuged sample contained the purified phages, and these were transferred to low retention tubes and stored at 4°C. For long term storage, sterile glycerol [Thermo Fisher Scientific Inc., Waltham,

Massachusetts, U.S.A.] was added to produce 50% glycerol stocks which were stored at -20^{o}C.

2.1.5. Subsequent rounds

This biopanning, amplification and precipitation procedure was repeated three times. However, for the subsequent rounds a 1:30 dilution of the enriched scFv elute from the previous round was used instead of the 1:75 dilution of the scFv library to further enrich the pool towards the bait proteins.

2.1.6. Phage titration

To ensure there was no contamination, and a high phage titre was produced following each biopanning round, phage titration on the eluate was performed. Phage titration was initially done by preparing ten-fold serial dilutions of the enriched phages as can be observed in the table 2.1. below.

Volume of Phage Library	LB Broth (µL)	Dilution Factor
2µL of phage library stock solution	198	10^2
20µL of 10^2 dilution	180	10^3
20µL of 10^3 dilution	180	10^4
20µL of 10^4 dilution	180	10^5
20µL of 10^5 dilution	180	10^6
20µL of 10^6 dilution	180	10^7
20µL of 10^7 dilution	180	10^8
20µL of 10^8 dilution	180	10^9
20µL of 10^9 dilution	180	10^{10}
20µL of 10^{10} dilution	180	10^{11}
20µL of 10^{11} dilution	180	10^{12}

Table 2.1: Titres of the phage library stock solution. Dilution of the 10^2 was prepared by adding 2µl of the phage library in 198µl of LB broth. Serial dilutions of 10^9-10^{11} were done by transferring 20µl of the previous dilution into another microfuge tube containing 180µl LB broth.

From 10^9- 10^{11} phage dilutions, 100µl were respectively transferred to a separate labelled microfuge tube. From the Tet LB broth containing the mid-log phase *E.coli*, 100µL were transferred into the respective tubes containing the 10^9-10^{11} phage library dilutions. These were incubated together for 5 minutes to allow enough time for a single bacteriophage to infect a single *E.coli* cell. After 5-minute incubation, the bacteriophages mixed with the *E.coli* were immediately spread by a 'hockey stick' on amp LB agar plates. The inoculum on the amp LB agar plates were allowed to dry with the lid slightly ajar and after drying they were incubated at 37°C overnight. The following day, the culture plates were observed and the phage dilution that had between 30-300 colonies was used to calculate the colony forming unit (CFU)/mL which was equivalent to titre of the phages (Ready-To-Use Phage Display Library Manual n.d.). The equation to measure the CFU/mL is expressed below;

Colony forming units (CFU)/mL = (number of colonies X dilution factor)/ (0.5 X 0.1mL)

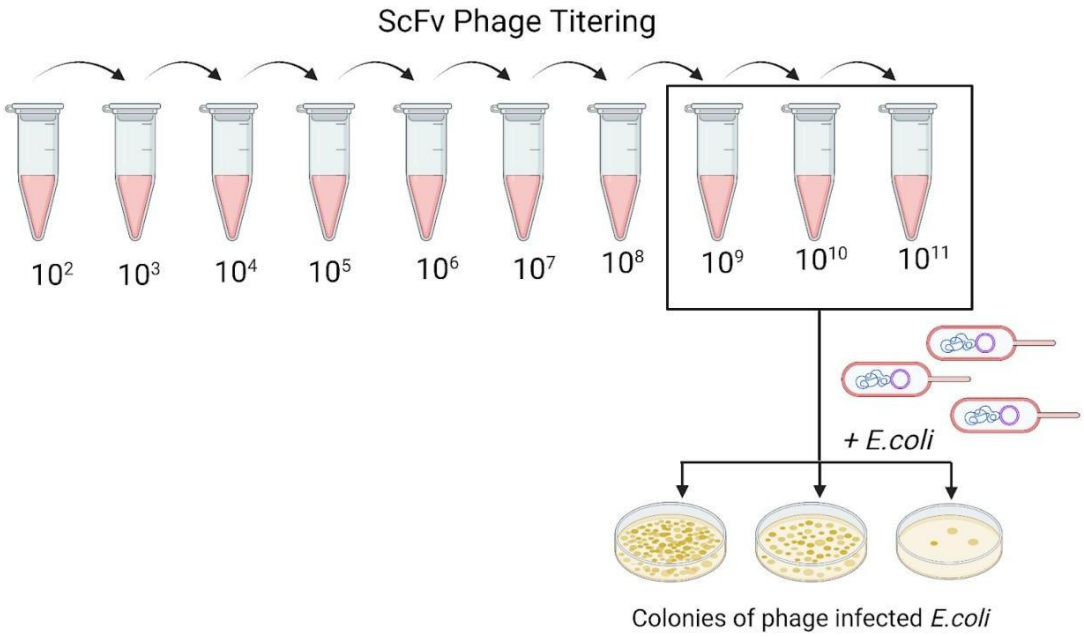

Figure 2.4: Schematic representation of phage titration. A ten-fold serial dilution was prepared of the enriched phages and *E.coli* were added to the 10^9 -10^{11} phage library dilutions. These were allowed to incubate for 5 minutes and following this they were evenly spread onto amp Lb agar plates and incubated overnight at 37°C.

2.1.7. Sterility

It was made sure that during culturing and titering, sterility was maintained to prevent contamination of the bacteria from environmental sources. This was done by wearing disposable gloves and frequently washing hands with soap and water or disinfecting them by using 70% ethanol. Sterile materials such as sterile loops, sterile conical flasks or sterile pipette tips were used to come in contact with the cultures (Coté 1998) which were either autoclaved or discarded in a biohazard bag after single-use. The work was conducted in a laminar flow cabinet and before use, the area was sprayed with 70% ethanol. A laminar-flow cabinet was used as it provides a physical barrier to prevent contamination of the culture used. The horizontal laminar flow of air in the cabinet directs air from the hood and expels it out into the room to prevent any aerosols that may contaminate the culture present (Coté 1998). Following its use of the laminar flow cabinet, Ultraviolet (UV) light was

switched on for 15-20 minutes to sterilise the area. When handling phages and *E.coli*, filtered pipette tips were used to prevent any aerosols and contamination of these in the pipette shaft. To ensure that sterility was maintained during culturing, a culture plate remained un-inoculated and incubated in the same conditions as the inoculated culture plates. The culture plate was checked after 24-hour incubation to ensure no growth was present.

2.2.1. Screening of the enriched phage library using Enzyme- Linked Immunosorbent Assay (ELISA)

The affinity of enriched phage eluates targeting VISTA and PD-L1 was assessed using ELISA. ELISA is a technique which detects the presence of antigens using a labeled primary antibody to measure the presence of biopanned phages. To enable this detection, bait proteins were first immobilized onto ELISA plates. Phages bound to immobilized bait proteins were detected with a phycoerythrin (PE)-conjugated anti-M13 antibody [Sino Biological, Bejing, China]. A no-library control in which bait proteins were incubated without phage, was included as a negative control to assess background signal. As a positive control, a previously validated VISTA-targeting phage library from the 2022 undergraduate project by Spiteri was used.

This was done by respectively adsorbing 250ng of VISTA-HT and PD-L1-HT protein in different wells to act as bait protein for the phages to bind. In one of the wells, VISTA-Fc was added for the positive control library. These were left to incubate overnight at 4^{o}C. Prior to adding the phages, the plate was blocked with 1% BSA, 0.1% Tween 20 in wash buffer for 2hrs at 4^{o}C to saturate any non-specific binding sites. Three serial dilutions of 1:10, 1:100 and 1:1000 in PBS of round 1 to round 4 VISTA and PD-L1 enriched phage eluates were prepared. From these dilutions, 100µLof each was added to specifically bind

to their respective bait proteins. For the negative control, 100µLof PBS was added to both PD-L1- HT and VISTA-HT wells. For the positive control, 100µLof 1:100 dilution in PBS of round 4 VISTA library biopanned during Spiteri 2022 project was added to the well containing VISTA-Fc. These were incubated for 1 hour at room temperature and after this any non- specific binding phages were washed off.

Following this, 70µL of anti-M13 fluorescently labelled to PE with a working concentration of 1.01µg/mL was added to all the wells to quantify the amount of phages bound to the bait protein. The anti-M13 was left to incubate for 1 hour at room temperature in the dark and the fluorescent intensity of each well was analysed by Tecan Spark®.

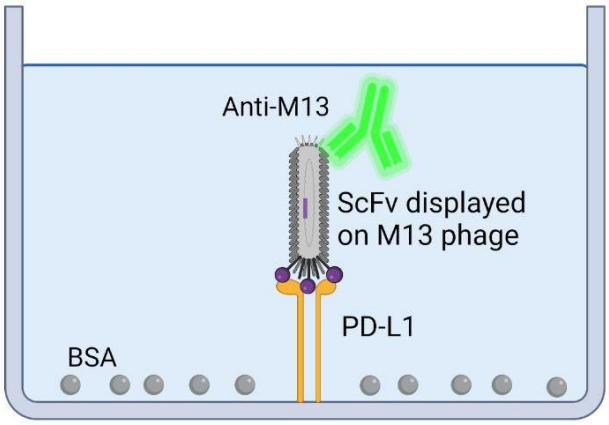

Figure 2.5: ELISA technique to check the affinity of the phage eluates against PD-L1 target. PD-L1 bait proteins were first immobilised to their respective wells and any non-specific binding sites were blocked using BSA. M13 phages from each round and fluorescently labelled anti-M13 were added to detect those phages bound to PD-L1.

The fluorescent intensity of the primary antibody detected is directly proportional with the quantity of phages present in the well. To minimize background fluorescence during the ELISA assay, black ELISA plates were employed. The Tecan Spark® was utilized to measure the fluorescent intensity of the primary antibody bound to the phages, which aids in determining the binding affinity of phages to bait proteins. The fluorescence top module was the method used to analyse the sample. Fluorescence detection was done by guiding

the light from a Xenon-flash lamp through fibre bundles with the use of mirrors. The light was then filtered to allow a specific wavelength of 561nm ± 20nm to pass through to act as the excitation wavelength. This caused the release of emitted light to be guided through a filter and monochromator so that light with an emission wavelength of 606nm ±20nm was detected by a photomultiplier tube (PMT).

2.3.1. Analysis of protein binding

From the ELISA results, four rounds of biopanning phage display towards PD-L1 and VISTA proteins did not produce antibodies which have a strong affinity. Thus, troubleshooting had to be performed before a repeat biopanning was done. Since the method used was already optimised and in-house successful biopannings have already been achieved, one possible reason why biopanning was not successful might have been due to HT protein not being exposed for binding with the cobalt-based ligands found on the paramagnetic beads. Therefore, analysis on the binding of VISTA-HT with the Co-NTA Magbeads was performed by flow cytometry. This was done by assessing 6 different titres of VISTA-HT by diluting 100µg/mL of stock concentration in binding buffer to produce 0, 0.0005, 0.005, 0.05, 0.5 and 5µg/mL of VISTA-HT. These dilutions were prepared in duplicates so that one set acted as the negative control as no antibody was added to it. Additionally, the same concentrations were used to prepare trimer-HT [Sino Biological, Bejing, China]. This was done to act as a positive control for the Co-NTA Magbeads, as biopanning with this protein was successfully conducted in previous studies (unpublished). The trimeric spike protein (S), located on the surface of the SARS-COV-2 virus, consists of two subunits: S1 and S2. These subunits are critical for the virus, as they mediate receptor binding and fusion with the host cell (Juraszek et al., 2021; Xiong et al., 2021). This glycoprotein has been the target of other studies aimed at reducing SARS-COV-2 infectivity.

The VISTA-Fc with Dynabeads™ protein G beads [Thermo Fisher Scientific Inc., Waltham, Massachusetts U.S.A] were also used as a positive control to ensure that any negative results were not due to problems with anti-VISTA. The VISTA-HT and the trimer-HT were each immobilised on Co-NTA Magbeads with a working concentration of 4mg/mL whereas the VISTA-Fc was immobilised on protein G beads with a working concentration of 3mg/mL. These bait proteins with paramagnetic beads were incubated together with rotation for 30 minutes. Non-specific binding sites were blocked using 3% BSA, 0.1% Tween 20 in PBS and were left incubating for 1 hour with rotation. In the case of trimer-HT, anti-trimer-PE was not available thus anti-trimer primary antibodies made in mouse and anti-mouse-PE were used instead. This was done by first incubating trimer-HT with 150µL of 28.2µg/mL of anti-trimer antibody made in mouse [Sino Biological, Bejing, China] for 1 hour with rotation. After 1 hour, PE conjugated anti-mouse [Biolegend, California, USA] with a working concentration of 1µg/mL was added to the different dilutions of trimer bait protein. Whereas 20µL of Anti-VISTA labelled with PE [Thermo Fisher Scientific Inc., Waltham, Massachusetts, U.S.A.] with a working concentration of 2µg/mL was respectively transferred to the dilutions of VISTA-Fc. To one set of dilutions of VISTA-HT anti-VISTA labelled with PE was not added to act as negative controls. The fluorescently labelled antibodies were left incubating for 1hr with rotation in the dark. Following these incubations the proteins were reconstituted in blocking buffers and transferred in flow cytometric tubes for flow cytometry

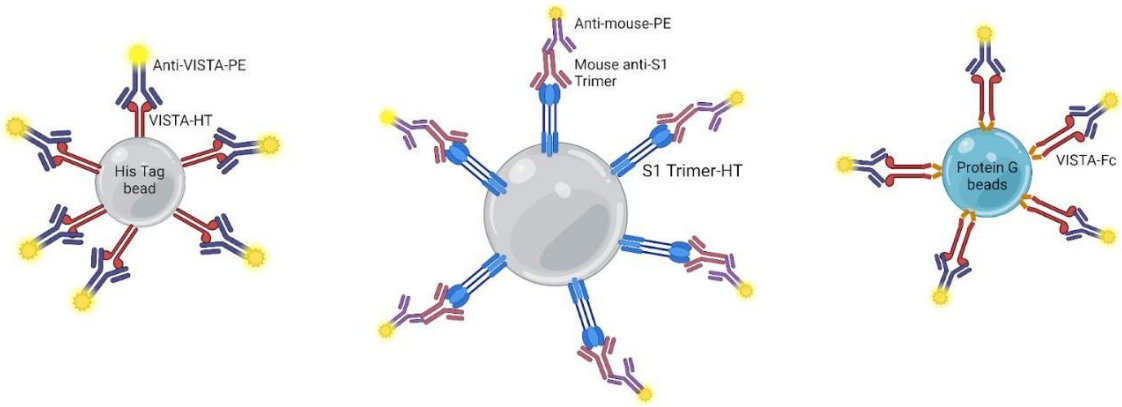

Figure 2.6: Schematic showing analysis of protein binding. The bait proteins were immobilised on their respective beads; VISTA and trimer-HT were immboilised on Co-NTA magnetic beads whereas VISTA-Fc chimera protein was immobilsed to protein G bead. Anti-VISTA-PE was added to bind with the immobilised VISTA. However, in the case of trimer protein, anti-trimer made in mouse was added to bind with trimer and anti-mouse-PE was added to bind with the primary antibody

2.3.2. Flow cytometry

The amount of anti-VISTA and anti-trimer present in the flow cytometry test tubes was determined by The Attune NxT Flow Cytometer [Thermo Fisher Scientific Inc., Waltham, Massachusetts, U.S.A.]. The flow cytometer moves the particles present in a sheath fluid by the process known as hydrodynamic focusing. Hydrodynamic focusing moves the sample from a wide diameter tube to a narrow diameter tube which causes an increase in pressure in the sample stream which becomes greater than the pressure in the sheath fluid. Due to this pressure difference, coaxial flow results which causes the cells to move in a single line (Wilkerson 2012). The particles then flow one by one into a laser beam to be uniformly illuminated by a laser to produce excited electrons which emit light. Depending on the deflection of the light emitted, the forward scatter (FSC) and the side scatter (SSC) can be generated (Wilkerson 2012). The FSC measures the amount of light released in the same axis as the laser beam which is proportional to the size of the paramagnetic beads. The SSC measures the amount of light detected perpendicular to the

laser beam which is proportional to the shape and optical homogeneity of the bead (Su et al. 2020). The flow cytometer also contains multiple parameters used for fluorescence detection which are made of an optical system consisting of an excitation laser and collection optics (McKinnon, K.M. 2018). The NxT Flow cytometer contains 4 excitation lasers which are the 405nm (violet), 488nm (blue), 561nm (yellow) and 637nm (red). The ideal excitation laser that is able to excite the fluorophore in the sample is chosen so the fluorophore can absorb the light of the laser to produce excited electrons (Fluorophores for Flow Cytometry n.d). Once the excited electrons fall back to the ground state, photons of light are emitted with a specific wavelength range known as the emission spectra (Ormerod 2009). The fluorescent light released from the fluorophore are reflected perpendicularly to the laser beam (Adan et al. 2016). With the use of optical lens, bandpass filters and detectors, only the emission spectra is detected and quantified to prevent the detection of background fluorescence with a different wavelength (Reggeti & Bienzle 2010). All of the light signals released are detected by PMTs or photodiodes (PDs) that are able to convert the light signals into electrical signals. General overview on the principle of flow cytometer can be observed in figure 2.7. below. The electrical signal is then amplified by an amplifier to produce a voltage pulse which can be interpreted (Snow 2004).

The fluorophore used in this study was PE. The excitation maximum (Ex-Max) and the emission maximum (Em-Max) of the PE are 496 and 578nm respectively therefore, the ideal excitation laser was the 561nm yellow laser. The yellow laser (YL)-1 parameter was used as it contains a bandpass filter of 585/16nm so that the Em-Max light of the PE was passed through the bandpass filter and detected.

The daily maintenance of the NxT flow cytometer was done before sample analysis. Daily maintenance was performed by checking the wash solution, focusing fluid and the

shutdown fluid to ensure that enough volume was present and if necessary, the waste container was emptied. The software was then switched on and the start-up procedure was initialised which involved pumping and priming of the fluidics systems, temperature checks and daily performance tests. The daily performance tests involved performing analysis on a sample of beads conjugated to different fluorophores which are able to emit light in the different parameters of the flow cytometer. The fluorescence signal detected in all of the different parameters is compared to a set of reference ranges. If the signal produced was within the reference range, it indicated that the flow cytometer can be used for analysis of the samples. Between analysis of the different samples, a wash solution was used to clean the needle to prevent carryover from one sample to another.

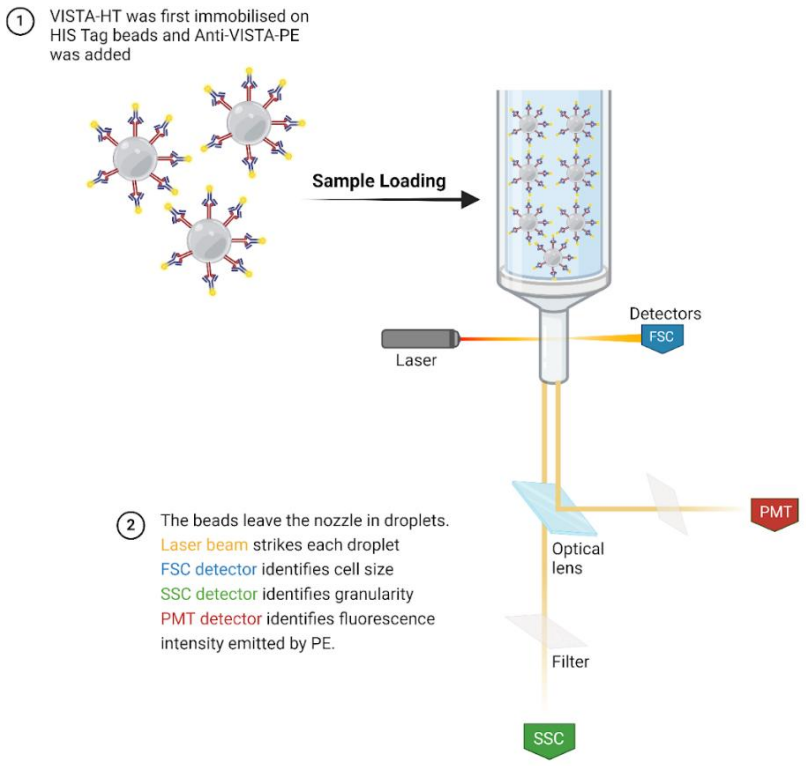

Figure 2.7: Fluorescence detection of anti-VISTA-PE by flow cytometry. The schematic shows 1. VISTA-PE bound to VISTA-HT that was immobilised to beads. 2. The beads that pass through the nozzle one by one are targeted by a laser beam. The light emitted from the bead in the same axis as the laser measures the forward scatter (FSC) which shows the size of the magnetic beads. The light emitted perpendicularly from the beads shows the (SSC) identifies granularity whereas the fluorescent light emitted by the PE- fluorophore was measured perpendicularly using a PMT.

2.3.3. Troubleshooting biopanning

Analysis of VISTA-HT binding showed that there was no binding to paramagnetic beads. This suggests that the tag protein may not have been exposed on the protein surface and the target was being washed off, causing biopanning to be unsuccessful. Thus, it was decided that prior to repeat biopanning of PD-L1, the bait protein binding should be assessed using the same method as 2.3.1 using 20µLof 2.78µg/mL of anti-PD-L1-PE [Sino Biological, Bejing, China] to ensure that the bait is binding to the beads.

Repeat biopanning of PD-L1 was performed using two different baits which were; PD-L1-HT that binds with Co-NTA Magbeads and PD-L1-Fc chimera protein [Sino Biological, Bejing, China] which binds to Dynabeads™ Protein G. This was done to check whether different baits affect biopanning. Furthermore, instead of a VISTA positive control, biopanning against the trimer-HT protein was performed to act as a positive control as successful biopannings have been repeatedly done against this target. A NPC control was also included (which contained only PBS) on both Co-NTA Magbeads and protein G beads to make sure that there was no non-specific binding of the library to the beads.

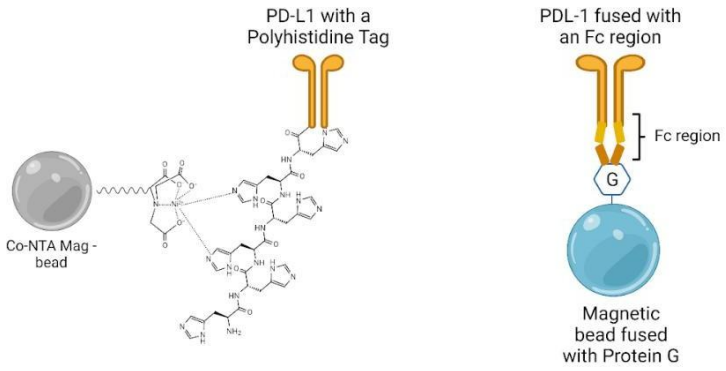

Figure 2.8: Differences between a PD-L1-HT and PD-L1-Fc. The schematic on the left shows the PD-L1 with a polyhistidine tag that binds to Co-NTA magnetic beads whereas the schematic on the right shows PDL-1 fused with an Fc region which binds to protein G present on magnetic beads.

During each round, the target proteins were also assessed by flow cytometry to make sure

that they were bound to their respective beads while using the NPCs as blanks. This was achieved as during biopanning double the volume of PD-L1-HT, PD-L1-Fc, NPCs and respective beads were used and incubated using the same concentrations and incubation steps as 2.1. above. Double the volume of blocking buffer was added and following this incubation, half the volume of the PD-L1-Fc with protein G beads, PD-L1-HT with Co-NTA Magbeads, PBS with Co-NTA Magbeads and PBS with protein G beads were transferred into separate Eppendorf tubes. To each of these tubes 20µLof 2.78µg/mL anti-PD-L1-PE was added and incubated for 1hr in the dark with rotation. Following this, the proteins were reconstituted in 500µL of blocking buffer and transferred into flow cytometric tubes for flow cytometry. The NPC which contained only PBS with the two different bead-types acted as a baseline control for the target proteins. Flow cytometry revealed a fluorescence shift in samples containing PD-L1-HT and PD-L1-Fc relative to the NPCs, confirming successful immobilization of both target proteins. The biopanning procedure was then continued as outlined in Section 2.1.

In the first round of biopanning, a 2:15 dilution of the scFv library in blocking buffer was used instead of the standard 1:75 dilution, to increase clone representation to approximately 20 copies per clone assuming equal representation. In subsequent rounds, a 1:15 dilution of the enriched scFv eluate from the previous round was used, replacing the 1:30 dilution applied during the initial biopanning. Amplification was then performed using a lower stock titre of helper phages (6.9×10^{11} PFU/mL). This adjustment was necessary because higher titres of M13KO7 phages could potentially outcompete the amplification of the phagemid and instead lead to the predominant amplification of M13KO7 phages (Ledsgaard et al., 2018). To mitigate this, a lower titre of helper phages and a higher copy number of phagemids containing the scFv DNA were used to favour the amplification of

scFv-displaying phages. Precipitation and titration were performed for all four rounds following the procedure described in Section 2.1.

2.3.4. Screening of the enriched phage library

Screening of all 4 rounds of biopanning was performed using the same method as 2.2.1 above using ELISA technique. The results of this ELISA showed that biopanning of both PD-L1-HT and PD-L1-Fc were also unsuccessful however biopanning of the positive control (trimer-HT) was successful.

To ensure that this result was not due to an ELISA error, for example PD-L1 was not binding to the ELISA plate, screening of all 4 rounds of biopanning against PD-L1-HT, PD-L1-Fc and trimer was also checked by flow cytometry. More controls were also included to perform flow cytometry. These include a NPC where no bait was added for all rounds of the different libraries to check non-specific binding, a no library control where no phages were added against all targets and a bait control to check whether the PD-L1-HT and PD-L1- Fc were binding to their respective beads.

Flow cytometry was performed by first immobilising 0.5µg/mL of protein bait to their respective beads meaning 0.5µg/mL of trimer and PD-L1-HT were respectively immobilised on Co-NTA Magbeads with a working concentration of 4mg/mL. Whereas 0.5µg/mL of PD-L1-Fc were immobilised on protein G beads with a working concentration of 3mg/mL. For the NPCs, 100µLof binding buffer was respectively added to both Co-NTA Magbeads and protein G beads. These were allowed to incubate for 30 minutes with rotation. Blocking of any non-specific binding sites was performed by incubating with blocking buffer for 1 hour with rotation. Screening of the libraries was performed by preparing a 1:10 dilution of round 1- round 4 biopannings against PD-L1-HT and respectively adding each round to

100µL of the immobilised PD-L1-HT bait, 100µL trimer bait (bait control) and 100µLof binding buffer (NPC). This was repeated for R1-R4 libraries biopanned against trimer and PD-L1-Fc however for the libraries biopanned against PD-L1-Fc, a 1:10 dilution of each round was added to PD-L1-Fc bait instead of PD-L1-HT bait. In conjunction, PBS were respectively added to 100µL of immobilised PD-L1-HT, PD-L1-Fc and trimer bait proteins to act as the no library controls. These were incubated for 1hr with rotation. Following this incubation, 70µLof 1.01µg/mL of anti-M13 fluorescently labelled with PE was added to all wells and incubated for 1 hour in the dark. To check for the immobilisation of the bait proteins to the beads, 20µL of 2.78µg/mL of anti-PD-L1-PE were respectively added to 100µLof immobilised PD-L1-HT and PD-L1-Fc and incubated for 1hr in the dark with rotation. Following these incubations, all tubes were reconstituted in 500µL of blocking buffer and transferred into flow cytometric test tubes for analysis by flow cytometry.

2.4.1. Preparation of candidate phage clones

Since biopanning against both PD-L1-Fc and PD-L1-HT were unsuccessful, candidate phage clones were isolated from the library that had been biopanned against VISTA-Fc. The candidate phage clones were prepared to randomly isolate 30 different strains of scFv antibodies from the round 4 enriched phage eluate. Each clone was then assessed for specificity towards target and control proteins by ELISA. This process aimed to select and amplify strains with high specificity and affinity for the target, while exhibiting low binding affinity to control proteins. These scFv antibodies offer an advantage over the enriched phage eluate, as isolating these strains ensures that the clone consistently binds to a single epitope and reduces non-specific binding. Additionally, the plasmid DNA of all clones were extracted by the plasmid miniprep to determine the DNA sequence of these proteins by Sanger sequencing (Castelli et al., 2019; Lipman et al., 2005).

For Candidate phage clones' preparation, a fresh round 4 titration plate was prepared using the same method as 2.1.6. above to pick 30 well-isolated colonies. Each colony was incubated overnight at 37°C into separate tubes containing 400µL of 100µg/mL of Carbenicillin (Carb) in Lb broth to allow proliferation of *E.coli* containing phagemid vectors. Carbenicillin antibiotic was used instead of ampicillin as the same gene that confers resistance to ampicillin (the β-lactamase gene) also confers resistance to carbenicillin. Carbenicillin was preferred as it is more stable than ampicillin and can grow fewer microsatellite colonies (Oswald 2024).

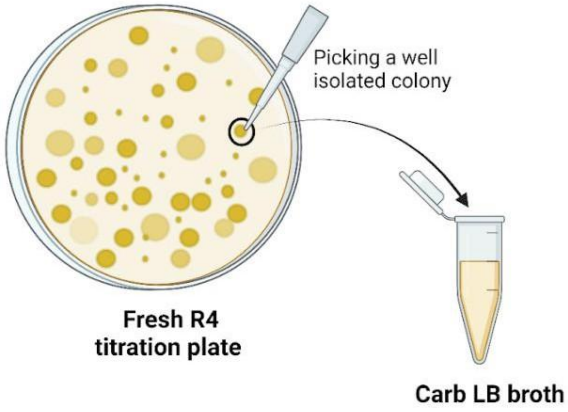

Figure 2.9: An illustration showing how to pick a well-isolated colony. A pipette tip was used to pick a single colony of *E.coli* infected with a specific M13 phage clone and transfer it to Lb broth with Carbenicillin.

From the overnight cultures, 50µL of each clone was transferred into fresh respectively labelled 5mL Eppendorf tubes containing 100µg/mL of Carb in Lb broth and M13KO7 helper phages with a stock titre of $6x10^{11}$ PFU/mL. These were left incubating at 37°C for 1.5 hours with shaking at 250rpm.

From the overnight cultures, another 50µL of each clone were transferred into respectively labelled round bottomed tubes containing 3mLs LB broth with 100µg/mL of Carb and incubated overnight at 37°C with shaking at 250rpm. The following day, these cultures

were centrifuged at 16,000xg for 1 minute to discard the supernatant. The pellet left was stored at -80°C to be used for Monarch® Plasmid extraction

To the remaining overnight culture, 15% glycerol stocks were prepared and stored at -80°C for indefinite long-term storage of the phage infected *E.coli.* Glycerol stabilizes the bacteria and prevents damage, allowing the phage-infected *E.coli* to remain viable for future experiments (Sprouffske et al. 2016).

Following 1.5hours incubation with the M13KO7 helper phages, 5mg/mL of Kan in sterile deionized water was added to the broth so that only *E.coli* infected with phagemids and helper phages proliferate. These were incubated overnight with shaking at 250rpm at 37°C.

The next day, the overnight cultures were centrifuged twice at 4,000×g for 10 minutes at 25°C. After each spin, the supernatant containing the phages were transferred into appropriately labelled low-retention tubes using filter tips. Following the centrifugation, an equal volume of blocking buffer (1% BSA, 0.1% Tween 20 in PBS) was added to the supernatant and incubated on ice at 4°C for 10 minutes. Subsequently 160µL of sterile 20% PEG/NaCl was added to each tube and incubated overnight at 4°C. The following day, each tube was centrifuged at 10,000xg for 20 minutes at 4°C. The supernatant was discarded, and the pellet was resuspended in 100µL of sterile PBS to produce candidate phage clones.

2.4.2. ELISA to assess the binding specificity of the candidate phage clones

ELISA was performed on each candidate phage clone to assess the binding specificity of each monoclone with VISTA and IgG target proteins. A no library control was also added as a negative control, and round 4 polyclonal phages biopanned against VISTA-Fc was used as a known positive control. A 96-well black plate was first coated with 50µL of 1µg/mL of

VISTA or IgG according to the plate layout. VISTA-Fc bait was added into two extra wells to add the positive control which was the round 4 polyclonal library and the negative control. The plate was incubated at room temperature for 2 hours.

Afterwards, all wells were blocked with 1% BSA in PBS with Tween 20 and incubated overnight at 4°C. The following day, 50µL of each candidate phage clone was added to the corresponding wells containing VISTA and IgG baits. For the positive control, a 1:100 dilution of the round 4 polyclonal library was used, and for the negative control, 50µL of PBS was added. These were incubated for 2 hours at room temperature and after this incubation, 70µL of 1.01 µg/mL anti-M13 antibody, fluorescently labelled with PE, was added to all wells. The plate was incubated for 1 hour in the dark and the Fluorescence emitted was then assessed using the TECAN Spark®.

Another ELISA was done to check the binding specificity of all monoclones against another control protein which in this case was the SARS-COV-2 envelope protein-HT [Sino Biological, Bejing, China]. The same procedure as described above was followed, but instead of IgG, the SARS-COV-2 envelope protein was used as the target. Additionally, not all 30 clones were tested simultaneously. ELISA was initially performed on clones 1–15, and after that, clones 16–30 were analysed. Although the same procedure was followed for clones 16–30, the positive control exhibited low relative fluorescence, necessitating a repeat of the experiment. Since the volume of the candidate phage clones used for ELISA had been depleted, the phage clones were retrieved from the stored 15% glycerol stocks of phagemid clones.

2.4.3. Retrieval of phage clones from the glycerol stocks

The 15% glycerol stocks which were stored at -80^{o}C, contained *E.coli* infected with a single phage clone. Retrieval of phage clones was performed on clones 16-30 and 9,10, which were used as controls to check the reproducibility of the clones when retrieved. Clone 9 was a low-binding clone to both VISTA and SARS-COV-2, whereas clone 10 had a high binding affinity with VISTA whereas a low binding affinity to SARS-COV-2. To prevent repeated freeze-thaw cycles, the 15% glycerol stocks were retrieved a few at a time in an ice bucket (Sprouffske et al., 2016). These were spread on Carb LB agar plates using a 20µL loop and incubated overnight at 37°C (*Ready-To-Use Phage Display Library Manual* n.d).

The following day, an isolated colony from each Carb LB agar plate was picked and transferred into appropriately labelled tubes containing 400µL of Crab LB broth and allowed to incubate overnight at 37◦C for 16 hours at 250rpm. From the overnight cultures, 50µL of each clone was transferred into fresh, labelled Eppendorf tubes containing 100µg/mL Carb in LB broth and 1µL of M13KO7 helper phages with a stock titre of 6×10^{11} PFU/mL. These were incubated at 37°C for 2 hours with shaking at 250rpm.

Centrifugation was performed at 13,300 rpm for 6 minutes at 25°C to remove the supernatant. The cells were then resuspended in 500µL of 100µg/mL Carb LB broth with 5mg/mL Kan, and incubated overnight at 37°C with shaking at 250rpm. The following day, the cultures were centrifuged again at 13,300rpm for 6 minutes at 25°C. The supernatant, containing phages, was transferred to freshly labelled low-retention tubes and an equal volume of 1% BSA, 0.1% Tween 20 blocking buffer was added and incubated on ice for 10 minutes. Subsequently, 160µL of sterile 20% PEG/NaCl was added to each tube and incubated overnight in the refrigerator.

The next day, each tube was centrifuged at 10,000×g for 20 minutes at 4°C. The supernatant was discarded, and the pellet was resuspended in 100µL of sterile PBS to produce the candidate phage clones. However, the majority of clones did not form a visible pellet after this centrifugation. The ELISA used to assess the binding specificity of these clones against VISTA and SARS-COV-2 baits showed weak binding to both targets, indicating that retrieval from the glycerol stocks was unsuccessful.

The experiment was repeated, but instead of 1.5mL Eppendorf tubes, 5mL Eppendorf tubes were used to allow more air for *E.coli* growth. Additionally, a higher titre of M13KO7 helper phages (5×10^8 PFU) was used to improve M13 proliferation. However, these adjustments did not improve the phage pellet or ELISA results. It was concluded that further optimization of phage clone retrieval from glycerol stocks was needed, but it was determined that this would be too time-consuming to include in this project.

2.4.4. Preparation of additional candidate phage clones

Since the retrieval of phage clones was unsuccessful, it was decided to select an additional 30 monoclones, labelled 31–60, using the same method outlined in section 2.4.1. However, during this period, other researchers were conducting experiments to prepare candidate phage clones, which were yielding erroneous results. After troubleshooting this experiment, it was determined that the helper phages were not functioning optimally, likely due to suboptimal storage conditions as the aliquot used had exceeded its recommended shelf life. To avoid repeated freeze–thaw cycles, the working aliquot of helper phage had been stored at 4 °C, where stability is limited to approximately six months (Frei & Lai 2017). Therefore, for the preparation of the new candidate phage clones, all 30 clones were prepared using a fresh aliquot of helper phages with the same

phage titre as section 2.3.3. Additionally, 15 of these clones (31, 33, 35, 37, 39, 42, 44, 46, 48, 50, 51, 53, 55, 57, and 59) were tested with this new type of helper phages, known as hyperphages [PROGEN Biotechnik, Heidelberg, Germany]. The key difference between helper phages and hyperphages is that helper phages can display only one scFv on the surface of a phage, whereas hyperphages can display up to five scFvs, resulting in higher avidity (PROGEN, n.d.).

Following the preparation of the candidate phage clones, an ELISA was performed to assess binding to VISTA and SARS-COV-2 using the same procedure as described in section 2.4.2. However, 3% BSA with 0.1% Tween 20 blocking buffer was used instead of 1% BSA with 0.1% Tween 20. A mistake was made in the procedure where, instead of adding 50µL of each clone, a 1:100 dilution of each clone was prepared, and 50µL of this dilution was added to the wells. Despite this error, the results showed that the clones prepared with hyperphages exhibited much higher binding to VISTA compared to those prepared with helper phages.

For the subsequent ELISA, VISTA, SARS-COV-2, and PD-L1 were used as baits, and 50µL of the clones prepared with hyperphages were used for testing.

2.5.1. Re-amplification of R4 VISTA library

Re-amplification of the round 4 enriched phages from the library produced during Spiteri 2022 project was necessary due to the depletion of the volume, as it was being used as a control for various experiments. Re-amplification was carried out by infecting 1mL of *E.coli* ER2738 in mid-log phase with 5µL of the round 4 enriched phages and incubating the mixture at 37°C for 15 minutes. The culture was then diluted in 20mL of LB Carb and incubated for 1.5 hours with shaking at 250rpm at 37°C. After this, 5µL of M13KO7 helper

phage was added to the culture. This mixture was incubated for 10 minutes at 37°C without shaking, followed by an additional 1.5 hours of incubation at 250 rpm at 37°C.

Following this, 10µL of 50mg/mL kan was added to the culture, and the mixture was incubated overnight at 30°C with shaking at 250 rpm. The following day, the culture was centrifuged at 4,000rpm for 10 minutes, and the supernatant was transferred to a fresh falcon tube. To precipitate the phages, 3.5mL of PEG/NaCl was added, and the mixture was incubated overnight at 4°C. The next day, the phages were centrifuged at 4,000rpm for 20 minutes at 4°C. The supernatant was discarded, and the centrifugation step was repeated. The remaining supernatant was carefully removed, and the phages were resuspended in 200µL of sterile PBS.

The phages were then centrifuged at 10,000rpm for 10 minutes at 4°C, and the supernatant was transferred to a low-retention tube. Glycerol stocks of the re-amplified Round 4 phages were prepared by adding sterile glycerol to achieve a final concentration of 50%.

Finally, an ELISA was performed to assess the binding performance of these re-amplified phages in comparison to the original Round 4 enriched phages, using VISTA as the target and a no library control.

2.6.1. Plasmid extraction and sequencing

Plasmid extraction was done on all 60 monoclones of VISTA-Fc to assess each clone by Sanger sequencing. Sanger sequencing of all monoclones was conducted to compare the protein sequences between high-affinity and low-affinity clones towards our target protein.

Plasmid extraction was carried out using Monarch® Plasmid Miniprep Kit [New England Biolabs, Massachusetts, U.S.A.] on the phage-infected *E.coli* pellets that were stored at -80°C (prepared during section 2.4 above). For each clone, the pellet was resuspended in 200µL of resuspension buffer and mixed thoroughly by vortexing. Lysis of the cells to release the plasmids was achieved by adding 200µL of lysis buffer and gently inverting the tube until the solution turned dark pink. Once the solution reached the dark pink colour, it was incubated for one minute. The lysis reaction was neutralized by adding 400µL of neutralizing buffer and gently inverting the tube until the solution turned homogeneous yellow and precipitate formed. The mixture was then incubated for 2 minutes.

Following incubation, the suspension was centrifuged at 16,000xg for 5 minutes. The supernatant was carefully transferred to the appropriately labelled NEB columns, and the columns were centrifuged twice for 1 minute at 16,000xg. The flow-through was discarded after each centrifugation, and 200µL of plasmid wash buffer 1 was added to wash away any RNA and proteins. Centrifugation was repeated, but this time, 400 µL of plasmid wash buffer 2 was added. The columns were then transferred to appropriately labeled Eppendorf tubes and subjected to a 1-minute dry spin at 16,000xg.

The columns were subsequently transferred to fresh Eppendorf tubes, and 30µL of elution buffer was added to the center of the matrix, without puncturing it. These were incubated with elution buffer at room temperature for 1 minute. Following this incubation, a final 1-minute centrifugation at 16,000xg was performed to collect the eluate.

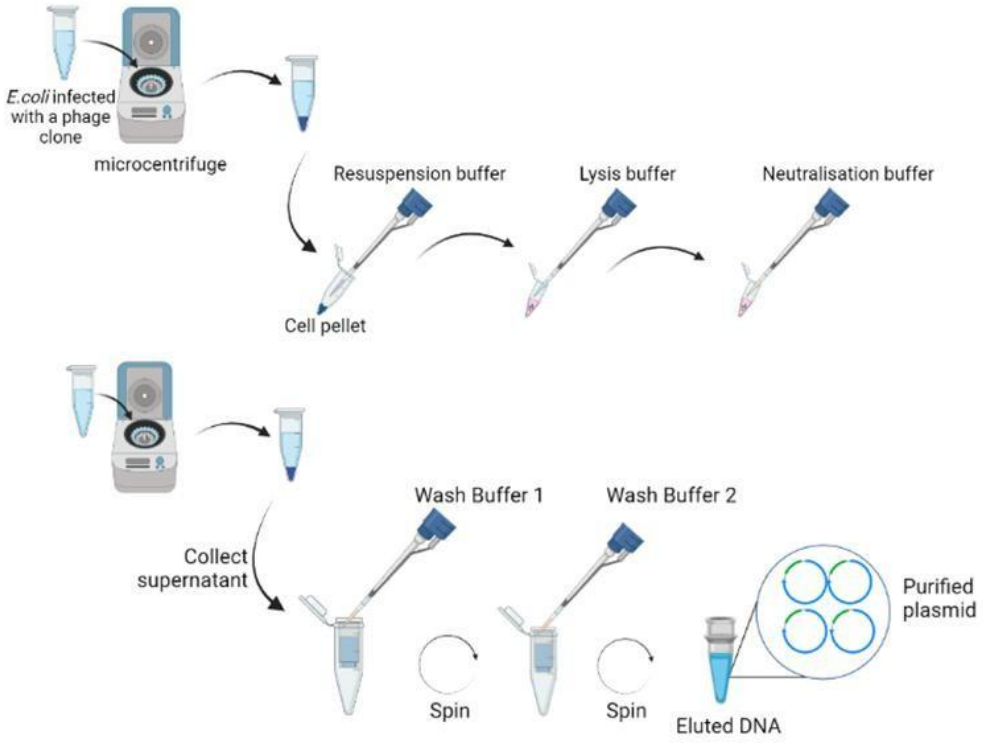

Figure 2.10: Plasmid extraction using Monarch® Plasmid Miniprep Kit. An overview showing how *E.coli* infected with phage clones are first lysed to release a lysate containing plasmid DNA. The neutralised lysate was centrifuged and the supernatant containing the plasmid DNA was collected. This was washed and centrifuged twice to remove any impurities and finally purified plasmid was eluted.

2.6.2. Checking the quality of DNA

The NanoDrop Microvolume Spectrophotometer [Thermo Fisher Scientific Inc., Waltham, Massachusetts, U.S.A.] was used to assess the quality of DNA eluted from each clone. This was done by first wiping the pedestal between each use with a tissue and pipetting 2µL of each clone eluate on the pedestal. The spectrophotometer released a beam of light which diffracts so that only light in the ultraviolet-visible spectrum with a wavelength range of 170-380nm is released. The nucleic acids absorb light at a wavelength of 260nm whereas any other contaminants absorb light at a peak of 230 and 280nm. Thus, a ratio of 260/280 and 260/230 was done to assess the purity of the DNA eluted. To ensure that the DNA does not have many contaminants the ratio of 260/280 need to give a result close to 1.8 and for

the 260/230 ratio need to have a value between 2.0-2.2 (Thermo Scientific n.d). The Nanodrop also quantified the nucleic acids present using the Beer-Lambert equation C= A/L, where C= molar concentration, A- UV absorbance, ε = wavelength-dependent molar coefficient and L= length of light path.

2.6.3. Sanger sequencing

From the eluted plasmids, 15µL of each clone were pipetted into two wells and sent abroad to LGC genomics in Germany for Sanger sequencing. A table was done to keep a record where each clone was pipetted. Sanger sequencing is a technique that incorporates DNA replication along with 2', 3'-dideoxynucleotide phosphates (ddNTPs). These act as fluorescently labelled-chain terminators to produce different length fragments that can determine the nucleotide sequence. DNA replication works by primarily denaturing the DNA by heating at 96°C to expose the DNA template. The temperature was then lowered to 50°C to allow annealing of the primer that acts as the starting point for DNA synthesis. Duplicates of each clone were sent as forward and reverse primers were added to sequence both strands of the DNA. The temperature was raised to 60°C for DNA synthesis using DNA polymerase and deoxynucleotide Triphosphates (dNTPs) which include adenine triphosphate (dATP), cytosine triphosphate (dCTP), guanine triphosphate (dGTP) and thymine triphosphate (dTTP) which binds to their complementary nucleotide; adenine with thymine and cytosine with guanine for chain elongation. To a lesser extent there were also ddNTPs which contain different fluorochrome labels for each nucleotide. These ddNTPs lack a hydroxyl group on the 3' end which was required to form a phosphodiester bond with a new nucleotide. Thus, once a ddNTP bound to the DNA strand, no new nucleotides were incorporated for chain elongation. This was repeated various times so

that chain termination by ddNTPs produced a pool of different length DNA fragments which were complementary to each nucleotide on the template strand. These different length DNA sequences underwent capillary gel electrophoresis which allowed for the separation of DNA strands by their size (Dey 2018). The capillary contained an electrical field so that the negatively charged DNA moved towards the positive electrode with a speed that depends on their molecular weight. The shortest fragment moved the fastest through the capillary and the longest fragment moved the slowest and thus the fragments which had one base difference were separated from each other. These fragments passed one after the other through a laser that excited the fluorescent label to emit light which was detected. The type of light emitted was interpreted and translated into a peak on a graph which corresponds to each nucleotide. The specific peak of each fluorophore was then used to plot a graph of signal intensity against time, known as a chromatogram which was used to interpret each nucleotide that were complementary to the template strand.

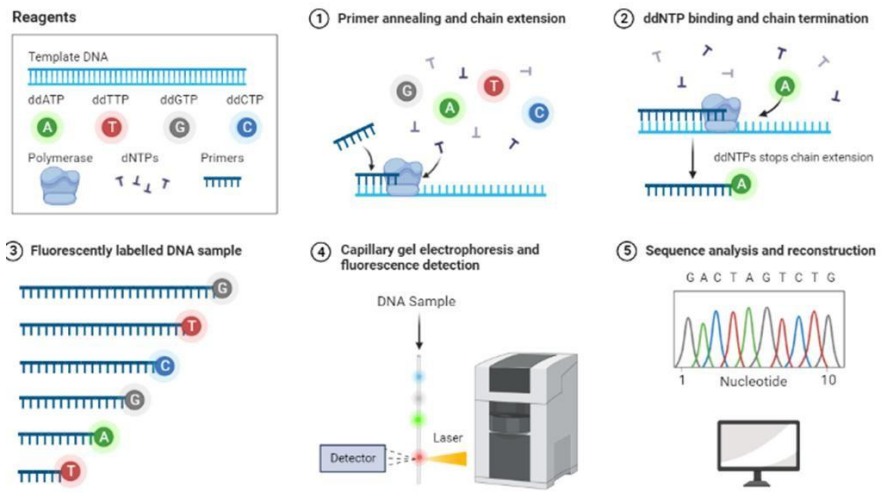

Figure 2.11: Sanger sequencing. The illustrations shows 1. Primer annealing and chain extension using deoxynucleotide triphosphates and polymerases, 2. Binding of fluorescent labelled 2', 3'-dideoxynucleotide phosphates (ddNTPs) which caused chain termination, 3. This was repeated multiple times so that chain termination by ddNTPs produced a pool of different length DNA fragments, 4. Detection of different length DNA fragments and fluorescent labels was done using capillary gel electrophoresis, 5. The result from capillary gel electrophoresis was used to produce a chromatogram to interpret the results.

2.7. Data analysis

The data produced from ELISA was transferred onto GraphPad Prism, Version 10.4.1. (*GraphPad Software*, 1984) for data analysis. For all of ELISA analysis, 12 technical repeats were done. To compare the fluorescence results of rounds 1-4 of biopanning phage display, the Area Under the Curve (AUC) was done from the results of 1:10, 1:100 and 1:1000 of each round. The AUC was made using the trapezoid rule, where the mean was used as the height for the different dilutions. Since two adjacent points were connected by a straight line, the data produced had an approximate normal distribution (Gagnon & Peterson 1998), and the difference in the statistical significance between the AUC was determined by Welch ANOVA with Brown-Forsythe correction were a p-value <0.05 was determined to be statistically significant. Any statistical significant result were shown with an '*' to represent the data and the replicates produced were expressed as the mean with the standard error of the mean (SEM).

Statistical analysis of the ELISA of monoclones was done by first performing the Shapiro-Wilk test for normality where a p-value ≥ 0.05 indicates that the data was normally distributed. Statistical analysis of those clones binding with different baits that were normally distributed were analysed by Multiple Unpaired T-test whereas the Multiple Mann-Whitney test was used for those monoclones that were not normally distributed. Statistically significant results were based on q-value instead of p-value since multiple comparisons were being performed there is an increased risk of false positive statistically significant results. Thus, the False Discovery Rate (FDR) (Q) is used instead to reduce the likelihood of a false positive result from all of the p-values performed. The desired FDR was set to 1% which means that 1% of the discoveries made were false positives. The FDR

calculated from the two-stage method of Benjamini, Krieger and Yekutieli. This method is adapted from Benjamini-Hochberg method and it determines the distribution of p-values and compares the p-values to the threshold set of the FDR level. The p-values that are lower than the set threshold are considered as a discovery (Benjamini & Yekutieli 2001, Benjamini et al. 2006)

DNA sequence data obtained through Sanger sequencing were analysed using SnapGene® software version 8.0.1 (Dotmatics, 2012) to generate the protein sequence of each clone. This program also facilitated the alignment of protein sequences for each clone and enabled the annotation of Complementarity-Determining Regions (CDRs) and framework regions, which were previously defined by Lisowska et al. 2025 by comparing the sequence obtained to international ImMunoGeneTics information system® (IMGT®) database.
The protein sequence of each clone was copied from SnapGene® and used to compute their physicochemical properties including molecular weight, isoelectric point (pI), and instability index (II) using the ExPASy ProtParam tool (Gasteiger et al. 2005).

Variations in the protein sequences of the CDR3 regions of both heavy and light chains were visualized using a custom dendrogram program developed locally by Ms. Francesca Chircop in 2025. The CDR3 protein sequences were extracted from SnapGene® and compiled into a Comma-Separated Values (CSV) file. This file was then uploaded into the dendrogram software to perform hierarchical clustering, enabling visualization of the relationships among different clones. To create this dendrogram, the program first performed pairwise comparisons of every sequence against every other sequence in the CSV file using National Center for Biotechnology Information (NCBI) Basic Local Alignment Tool® (BLAST®) (Altschul et al. 1990) version 2.16.0 specifically the protein version; BLASTP

in short mode (Madden & Camacho 2008). This tool generates e-values which was then used to calculate the distance matrix between clones using the equation below:

$d = -\log_{10}(\max(\text{e-value}, 10^{-300}))$.

Clustering of data was then performed by using Ward's linkage method (Chircop, F. 2025). This method groups data to eventually form a single cluster containing all clones. At each step, the method merges the pair of clusters that results in the smallest increase in the sum of squared differences (sum of squares index), ensuring that similar data points are grouped together (*Ward's Method (Minimum variance method)* n.d).

Additionally, homology modelling was performed using the SWISS-MODEL tool (Waterhouse et al. 2018) to predict the 3D structures of the strongest and weakest binders, based on FASTA sequences exported from SnapGene®. The stereochemical quality of the predicted structures were assessed through Ramachandran plots generated by the same tool.

All tools were used with their default settings and parameters.

Chapter 3:

Results

3.1. Binding analysis of the different phage pools towards bait proteins

Four rounds of biopanning phage display were conducted targeting PD-L1-HT whilst biopanning against VISTA-HT was done as a positive biopanning control since a successful enrichment against this target has been previously achieved. The binding affinity of the phage pools from each round was assessed through ELISA against their respective target proteins (see Figures 3.1A & 3.2A) where an increase in fluorescence with each round culminating in the highest intensity in round (R)4 was expected to show.

The "no-library" control where no phages were added to bait proteins was included in all ELISAs which was shown as the '0' on the x-axis, and anti-M13 was added to measure background fluorescence. Additionally, a dilution series (1:10, 1:100) of a positive control was incorporated from the R4 phage pools of successful biopanning against VISTA-Fc, which had previously demonstrated a high binding affinity for VISTA bait (Spiteri 2022).

During ELISA, to assess non-specific binding, VISTA bait served as a negative control (Figure 3.1B) for the phages biopanned against PD-L1, while PD-L1 bait was used as a negative control for phages biopanned against VISTA (Figure 3.2B). The R4 of the negative bait controls were also shown as a dotted line in the graphs of both R1-R4 phage dilutions with target protein.

The phage pools from each round were diluted to 1:10, 1:100, and 1:1000 before binding to 250ng of the bait proteins. The Median Fluorescent Intensity (MFI) from PE-conjugated anti-M13 bound to each dilution series of phages was measured using absorbance value of 561nm. Twelve measurements were taken from various areas of the wells for repeated measurements and the median values obtained were plotted to determine binding affinity. Statistical analysis was performed by initially generating Area Under the Curve (AUC) of the

different dilutions of each round and the Welch ANOVA with Brown-Forsythe correction was done to compare AUCs across the rounds.

Figure 3.1A shows that R1-R4 of phages biopanned against PD-L1 exhibited low MFIs with PD-L1-HT compared to the positive control, and the expected gradual increase in fluorescent intensity from R1 to R4 was not observed. From R2 to R3 there is a statistically significant higher result in the MFI which was promising, however, R4 had a statistically significant lower MFI than R3. Round 4 phage dilution against PD-L1 has the lowest MFI compared to R1-R3. This suggests that the phage pools did not have a high binding affinity for PD-L1 indicative of a failed biopanning. Even though the R4 phage pools with PD-L1 bait had a very low MFI, these still displayed a statistically significant higher binding affinity towards PD-L1 than with the negative control bait; VISTA shown as a dotted line in figure 3.1.

ELISA analysis of all rounds of phages biopanned against PD-L1 with the VISTA bait (Figure 3.1B) was done as a negative control. There is no statistically significant difference between the MFI R1-R4 and it was significantly lower than the positive control. This indicates that the phages biopanned against PD-L1 bait were not binding with VISTA proteins.

A)

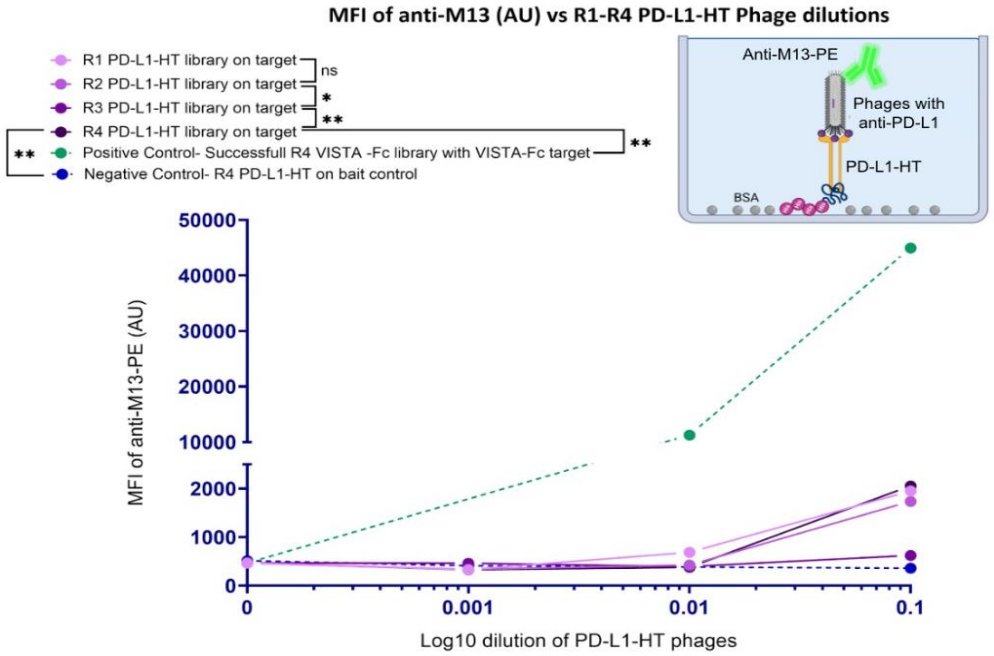

B)

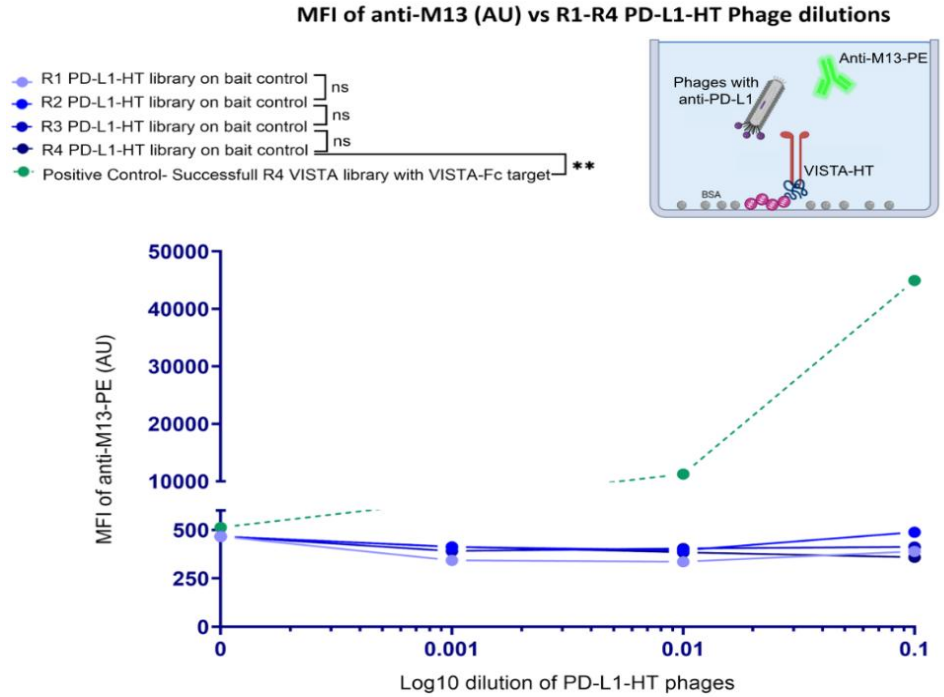

Figure 3.1: Binding Analysis of R1-R4 PD-L1 phage pools with their targets and control baits. The results of 1:10, 1:100, 1:1000 dilutions of phages from all four rounds of biopanning against PD-L1-HT in A) shows a significant increase in fluorescence between R2 and R3 (p = 0.0355), while R4 showed a significantly lower MFI compared to R3 (p = 0.0001), indicating failed biopanning. Whereas the positive controls of R4 phage pools with high affinity for VISTA (shown in green) showed significant binding. A negative control of the R4 PD-L1 phage pool against VISTA-HT bait (shown in blue) showed lower fluorescence compared to R4 phage pool against PD-L1-HT. B) shows R1-R4 PD-L1 phage pools with VISTA-HT negative control bait. The results of the dilutions of phages from all four rounds of biopanning showed no significant result between R1-R4.

Biopanning against the VISTA-HT bait was carried out concurrently as a positive control, as previous phage display biopanning against this bait had been successful in a previous project (Spiteri, 2022). However, as illustrated in Figure 3.2A, there was no statistically significant difference in the results from R1-R4 for phages biopanned against VISTA-HT, indicating a failure of this positive control biopanning. In contrast, the phages from R4 demonstrated a statistically significant higher binding affinity for the negative control PD-L1 bait when compared to VISTA bait. The MFI for R1-R4 was significantly lower than that of the positive control, which consisted of R4 VISTA phages from the successful biopanning against both VISTA-Fc and VISTA-HT baits. The positive control phages for ELISA were tested against both VISTA-Fc and VISTA-HT to assess if the phages exhibited any difference in binding due to different tags. It was observed that there was a significant increase in binding towards VISTA-Fc but nonetheless the R4 successful VISTA phages still had a high MFI with the VISTA-HT bait .

ELISA analysis of all rounds of phages biopanned against VISTA with the PD-L1 bait shown in figure 3.2B was done as a negative control. There was only a statistically significant difference between the MFI of R3-R4 which was significantly lower than the positive control.

A)

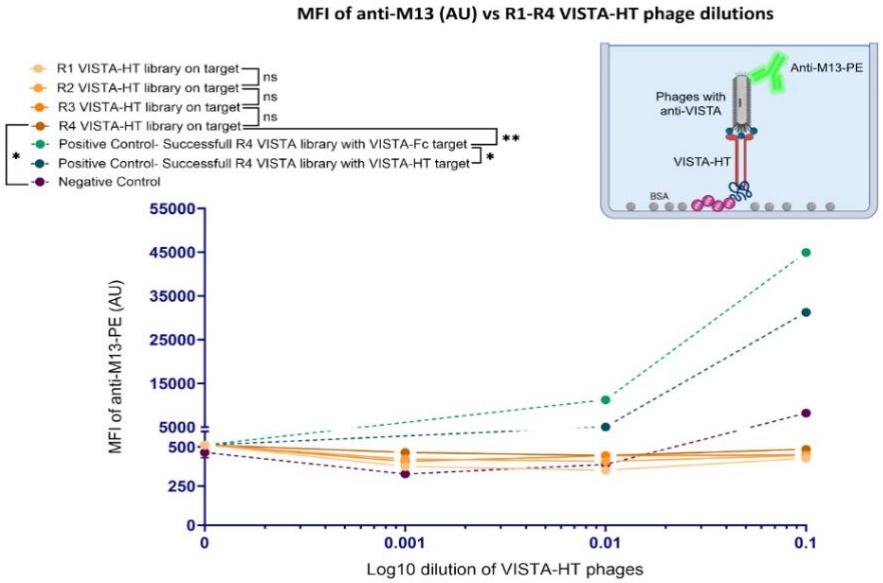

B)

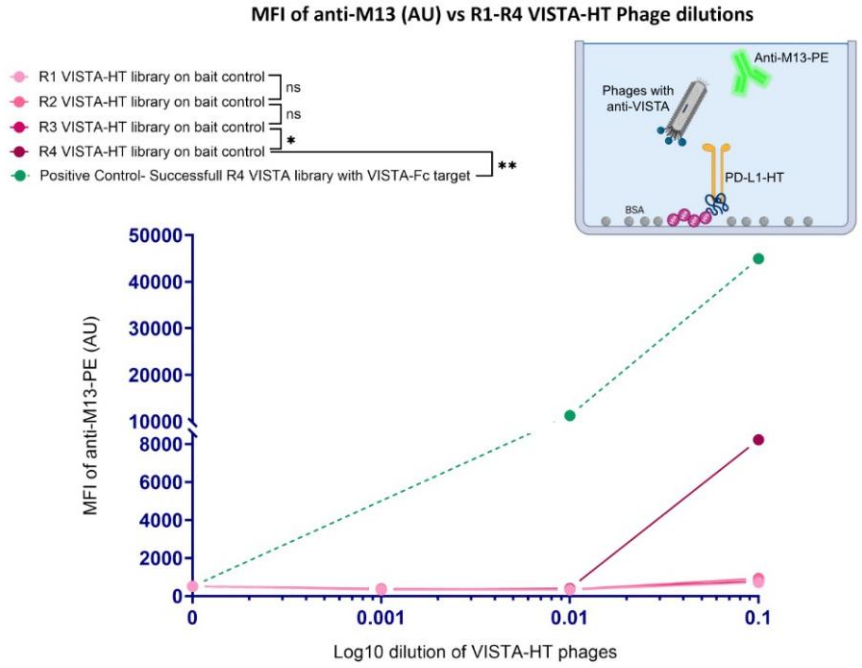

Figure 3.2: Binding Analysis of positive control biopanning. A) shows the results of different dilutions of phages from all four rounds of biopanning against VISTA-HT. There is no significant increase in fluorescence between all rounds indicating failed biopanning. Positive controls of R4 VISTA phage pools with high affinity for VISTA-Fc from Spiteri 2022 research against both VISTA-HT, VISTA-Fc bait showed significant binding. The negative control of the R4 VISTA phage pool against PD-L1 bait (shown in purple) had significantly higher fluorescence compared to the R4 phage pool against VISTA-HT (p-value 0.0131) which may indicate cross- reactivity. B) shows the results of 4 rounds of VISTA-HT phage pools with PD-L1 bait. There is a significant result between R3 & R4 (p-value of 0.0079) however the binding in R4 was still significantly lower than the positive control.

3.2. Troubleshooting VISTA & PD-L1 biopanning

Biopanning was performed using our optimized in-house protocol, adapted from the Ph.D. Phage Display Biopanning Manual by New England Biolabs (n.d). Since biopanning against VISTA was already done successfully, the initial successful biopanning was done using a different immobilisation technique as VISTA bait was fused with an Fc which immobilises to protein G beads. Thus an experiment was conducted to check whether VISTA in this biopanning was being efficiently immobilised. The VISTA bait protein in figure 3.3. was tagged with a HT to enable specific binding to NTA-cobalt-based magnetic beads. To confirm this binding, six different titres of VISTA-HT immobilized on Co-NTA Magbeads were assessed (0, 0.0005, 0.005, 0.05, 0.5, and 5 μ g/ml) and PE-labelled anti-VISTA was added to quantify the amount of VISTA-HT immobilized on beads. Flow cytometry was then employed to measure the fluorescence emitted from each bead, with a proportional increase in fluorescence expected as the bait titre increased.

Control experiments included testing various titres of VISTA-Fc immobilized on protein G beads to ensure that negative results were not caused by issues with the PE-labelled anti-VISTA or the flow cytometry process. Additionally, different titres of trimer-HT immobilized on Co-NTA Magbeads were used as a positive control to confirm that lack of binding was not due to problems with the Co-NTA Magbeads. For detection of trimer-HT binding, a primary anti-trimer antibody derived in mouse was used, followed by a PE-labelled anti-mouse secondary antibody. This bait was used as a control as successful biopanning with the trimer-HT had been previously achieved.

As can be observed from figure 3.3A, different titres of phages biopanned against VISTA-HT with and without VISTA-HT bait produced a negative signal with anti-VISTA-PE. This

shows that VISTA-HT was not immobilized on Co-NTA Magbeads. In contrast, the control experiments in Figures 3.3B and 3.3C demonstrate that increasing titres of both VISTA-Fc and trimer-HT led to higher fluorescence, indicating that these baits were being efficiently immobilised on beads. Since the controls both worked it indicates that lack of fluorescence detection with the VISTA-HT in figure 3.3A is unlikely to be due to issues with anti-VISTA-PE or with the Co-NTA Magbeads. Thus from this experiment it was concluded that one reason why VISTA-HT, used as a positive control during biopanning, yielded negative results was due to the lack of bait immobilisation to beads.

A) Different titres of VISTA-HT target (µg/mL)

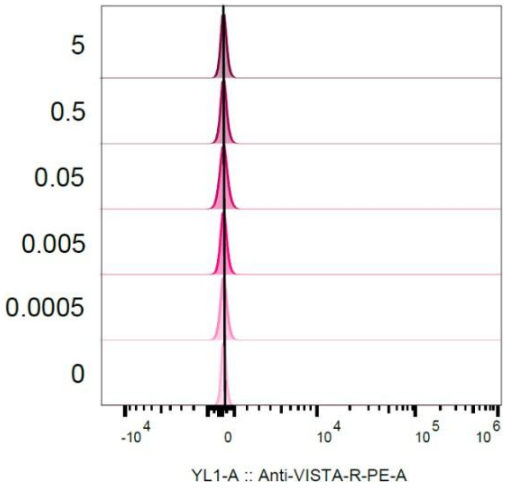

B) Different titres of VISTA-Fc target (µg/mL)

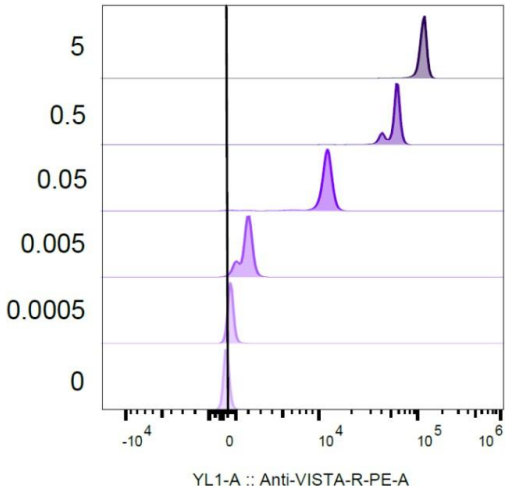

C) Different titres of trimer-HT target (µg/mL)

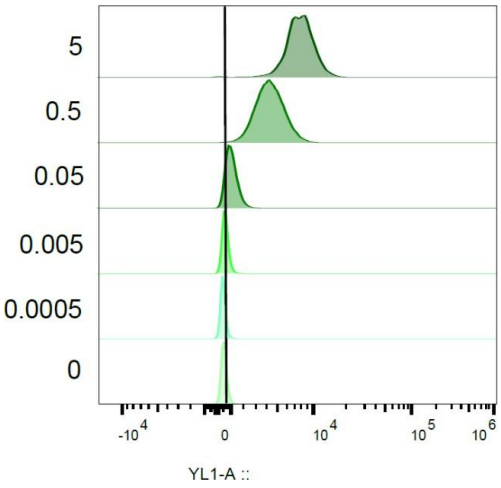

Figure 3.3: Quantification of different titres of bait proteins immobilized on beads by flow cytometry. A) shows histogram plots for various titres of VISTA-HT immobilized on Co-NTA Magbeads, which displayed low fluorescence detection with anti-VISTA-PE. In contrast, B) and C) respectively show histogram plots for varying titres of VISTA-Fc immobilized on protein G beads and trimer-HT immobilized on Co-NTA Magbeads. Both controls exhibited an increase in fluorescence corresponding to higher bait protein quantities, with the highest fluorescence observed at a concentration of 5µg/mL. This shows that VISTA-HT was not being efficiently immobilised to the beads.

Since analysis of protein binding showed that VISTA-HT was not being immobilized onto beads, during repeat biopaning of PD-L1 different immobilization techniques were tested; PD-L1-HT which was used during initial biopanning and PD-L1-Fc chimera protein that immobilizes to protein G beads. Prior to repeat biopanning, binding analysis of different titres of PD-L1-HT immobilized to Co-NTA Mag beads and PD-L1-Fc immobilzed to protein G beads were analysed in figures 3.4a and 3.4c respectively. Quantification of the immobilized proteins was done using anti-PD-L1-PE. Negative controls were used for this analysis which included different titres of both PD-L1-HT and PD-L1-Fc without PE-labelled anti-PD-L1 shown in figures 3.4b and 3.4d respectively to ensure that there was no background fluorescence.

As can be observed, with PD-L1-HT (figure 3.4a) there is a proportional increase in fluorescence detection with the increase in quantity of PD-L1-HT. On the other hand, PD-L1-HT without adding the PE-labelled antibody control did not have an increase in fluorescence. Figure 3.4c shows a proportional increase in fluorescence detection with immobilized PD-L1-Fc however a constant fluorescent result was achieved after 0.05µg/ml of PD-L1-Fc indicating bead saturation. Figure 3.4d showed there was no increase in fluorescence detection without PE-labelled antibodies. This shows that both PD-L1-HT and PD-L1-Fc were efficiently binding to magnetic beads.

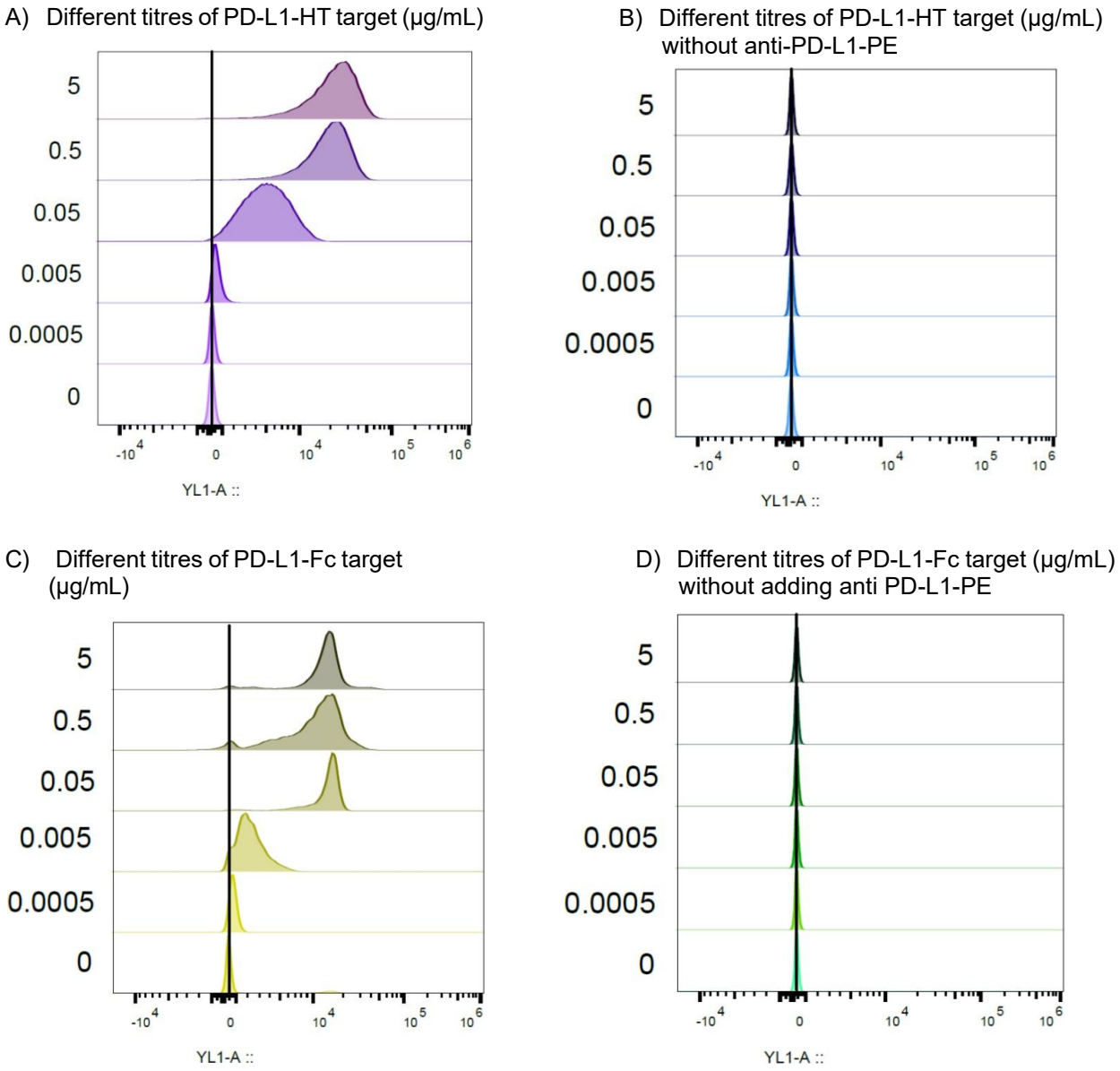

Figure 3.4: Quantification of different titres of immobilized PD-L1 by flow cytometry. A) shows histogram plots for various titres of PD-L1-HT immobilized on Co-NTA Magbeads, which displayed a proportional increase in fluorescence with anti-PD-L1-PE. In contrast, B) shows the control histogram of the same titres of PD-L1-HT without anti-PD-L1-PE which did not show any increase in fluorescence detection. C) contains the histogram plots of PD-L1-Fc immobilized to protein G beads which had an increase in fluorescence detection which remained constant at 0.05µg/ml indicating bead saturation. Whereas D) shows the different titres of PD-L1-Fc without anti- PD-L1-PE which gave the same result as B). This shows that both PD-L1-HT and PD-L1-Fc were immobilized to their respective beads.

3.3. Binding analysis of the repeat biopanning phage pools

Since an issue with immobilisation was identified following the initial biopanning. For the repeat biopanning, prior to adding phages to the immobilised baits, efficient immobilisation was checked during R1-R3 to ensure that the bait was consistently binding. This was done by preparing double the volume of both baits and beads and following immobilisation, anti- PD-L1-PE was added to half of the volume to check binding by flow cytometry. To confirm there was an increase in fluorescence, the fluorescence emitted from the baits binding with the beads was compared to the fluorescence when no bait was added to their respective beads labelled as a NPC. As can be observed from figure 3.5, R1-R3 of both PD-L1-Fc and PD-L1-HT had an increase in fluorescence compared to the NPC. This shift shows that efficient immobilisation was consistently achieved. Once binding was confirmed the rest of biopanning was continued with the remaining volume.

A)

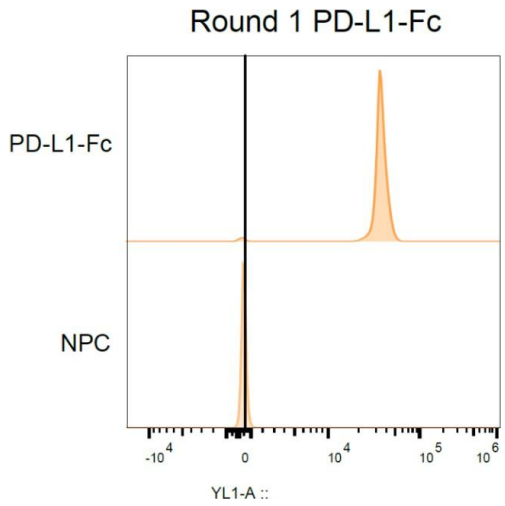

B)

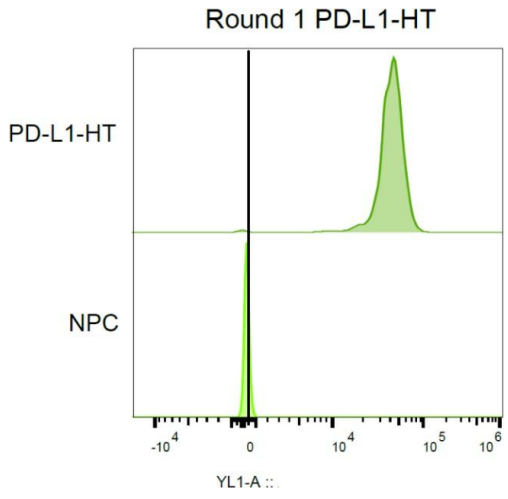

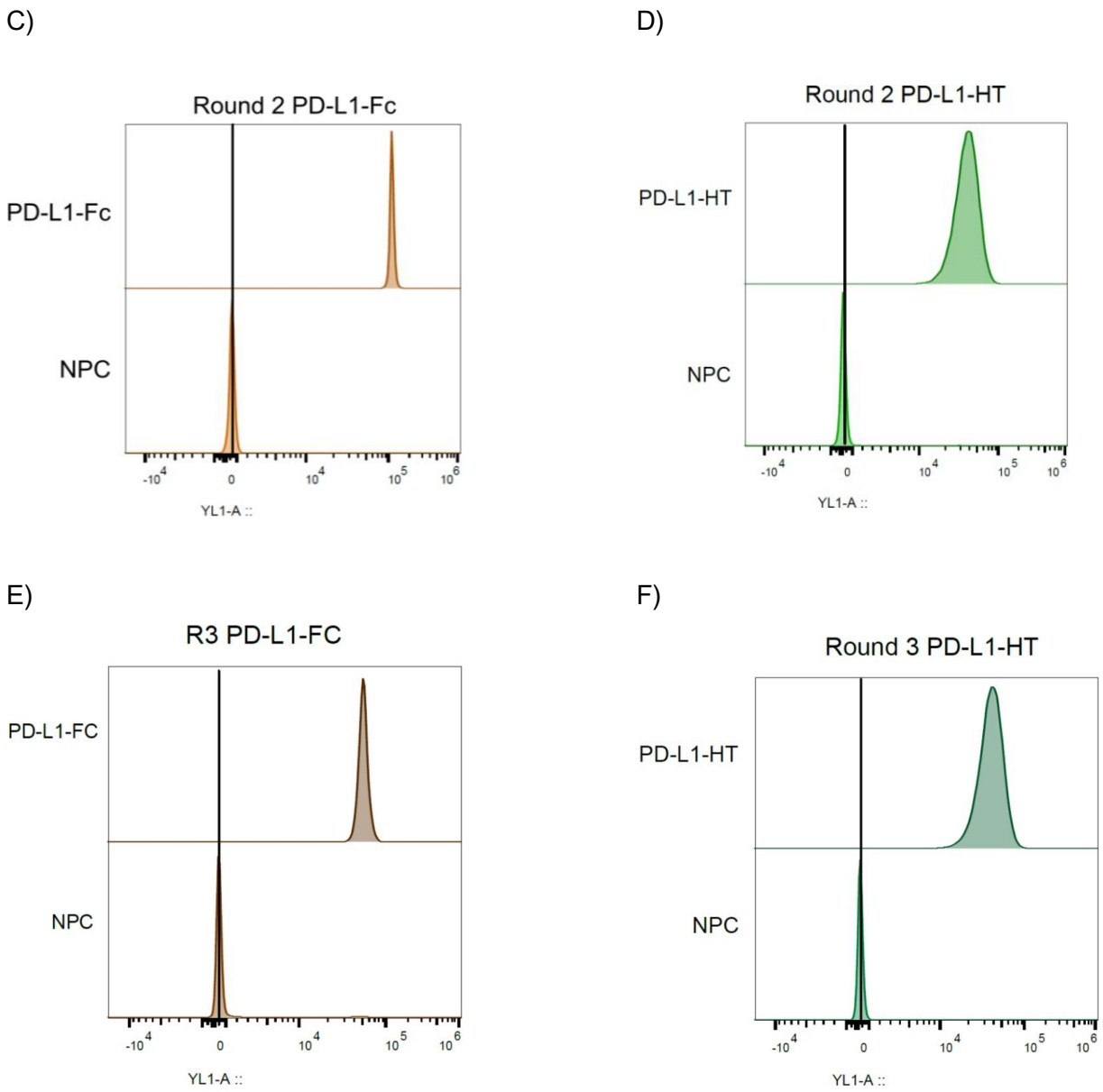

Figure 3.5: Binding analysis of PD-L1-HT and PD-L1-Fc during R1-R3. During biopanning of R1-R3, immobilisation of PD-L1-Fc to protein G beads and PD-L1-HT to Co-NTA beads was checked by adding anti-PD-L1-PE to baits immobilised on beads. The fluorescent result emitted was compared to the fluorescent result emitted with the NPC containing magnetic beads only. As can be observed during these rounds both PD-L1-Fc and PD-L1-HT had an increase in fluorescent result compared to the NPC in all rounds.

During repeat biopanning, several modifications were also implemented to enhance the likelihood of successful selection. In addition to verifying the efficiency of immobilization during R1-R3, trimer-HT was used as a positive control, which had been successful in previous biopanning experiments. Furthermore, a new aliquot of phage library was used and the representation of scFv phages was increased in each round, and a lower stock titre

of helper phages was used. To ensure that a sufficient phage titre remained following elution of phages, a tenfold serial dilution of the enriched phages was performed to obtain phage dilutions ranging from 10^9 to 10^{11}. These dilutions were then used to infect *E.coli* and the infected cultures were evenly spread on ampicillin LB agar plates and incubated overnight at 37° C. The next day, plates containing approximately 30–300 colonies were selected for counting. Using the colony count and corresponding dilution factor, the phage titre was calculated in CFU/mL. The resulting colony numbers and calculated titres are presented in Figure 6.1 and Table 6.1 of the appendices. Overall, phage titres ranged from 6.20×10^{11} to 6.20×10^{12} CFU/mL, indicating that sufficient phage quantities were retained after each round to proceed to subsequent rounds of biopanning.

Despite these adjustments, ELISA results assessing the binding affinity of the different biopanning rounds to the target proteins PD-L1-HT and PD-L1-Fc, shown in Figures 3.6A and 3.6C, showed a negative result. The mean fluorescence intensity (MFI) for all rounds against both PD-L1-Fc and PD-L1-HT was very low, and no statistically significant differences were observed between the rounds. The R4 library biopanned against PD-L1-Fc (in figure 3.6A) had a statistically significant lower result when compared with negative control bait (shown in a purple dotted line in figure 3.6A). The R4 library biopanned against PD-L1-HT produced a similar MFI result to the negative control bait (shown in an orange dotted line in figure 3.6C) as there was no statistical difference.

The positive control for ELISA analysis was the same as the initial ELISA in figures 3.1 & 3.2 although only a 1:100 dilution of R4 library biopanned against VISTA-Fc was used in this case which shows a high MFI result. These rounds were also tested against the trimer-HT negative control bait shown in figures 3.6B and 3.6D to check for cross-reactivity. The R1 PD-L1-Fc library in figure 3.6B produced a higher fluorescent result compared to the

other rounds however it was not statistically significant. On the other hand, phage pools biopanned against PD-L1-HT did not produce any significant result with trimer-HT bait.

A)

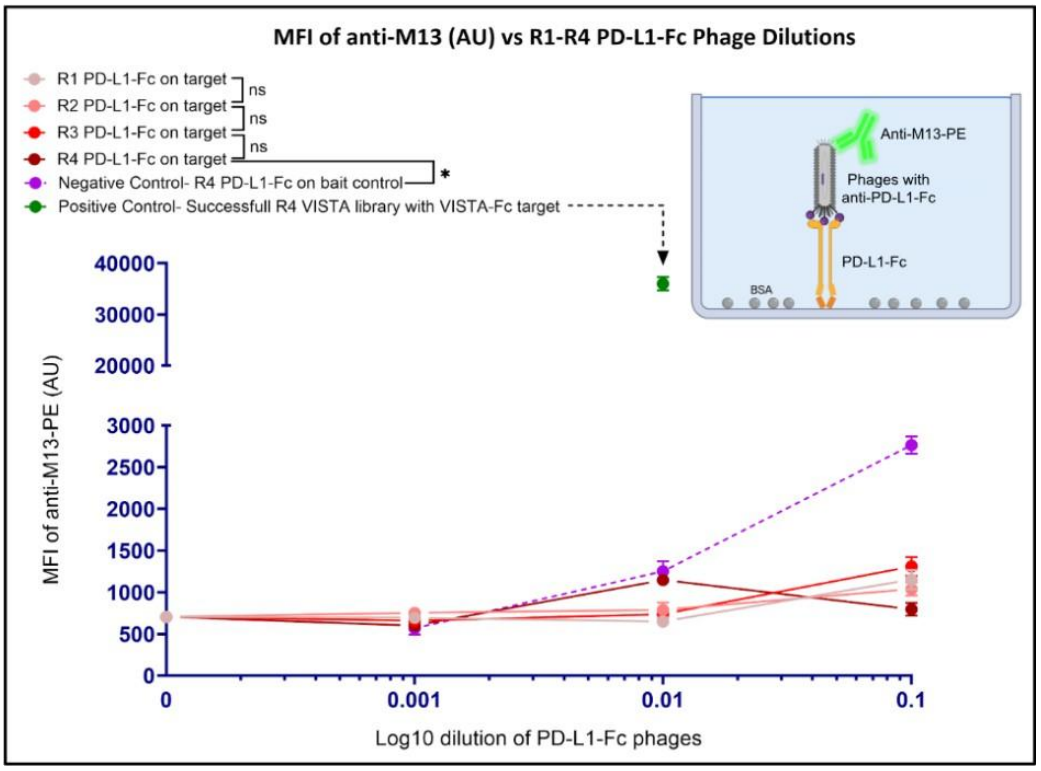

B)

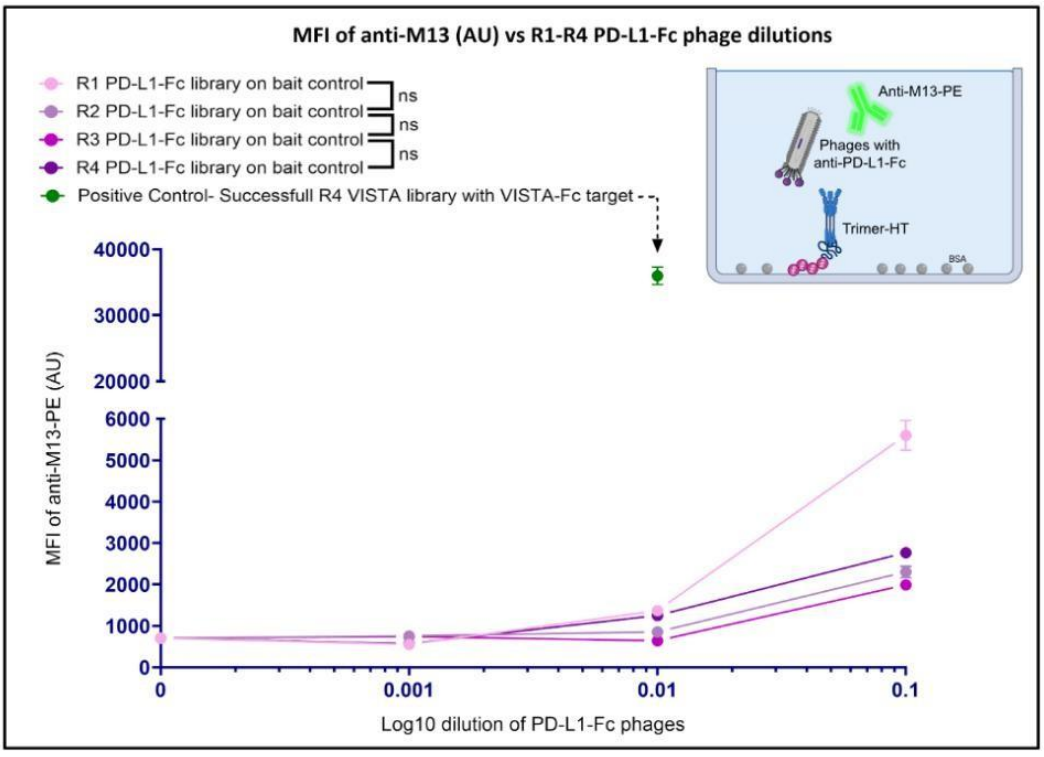

C)

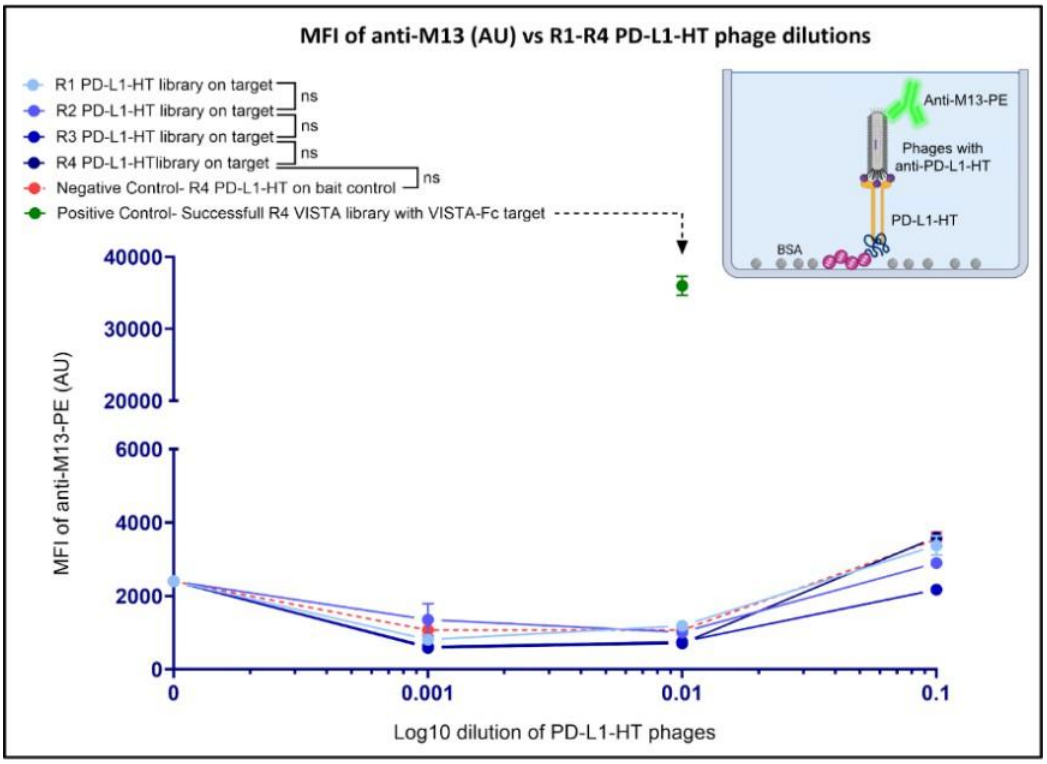

D)

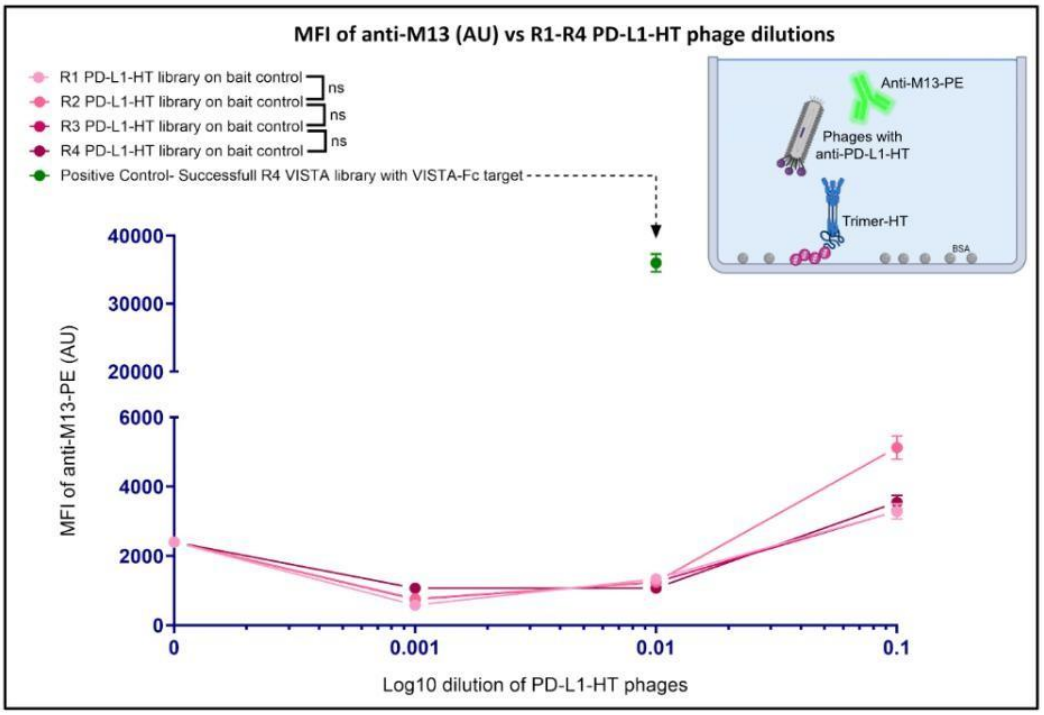

Figure 3.6: Binding Analysis of R1-R4 PD-L1-Fc and PD-L1-HT phages with their target and control baits. Both R1-R4 PD-L1-Fc phage pools A) and PD-L1-HT phage pools C) did not have a significant increase in fluorescence from one round to the other showing that both biopannings failed. The 1:100 positive control library against VISTA-Fc shown in green produced a high fluorescent result indicating high binding affinity towards VISTA bait. The R4 PD-L1-Fc library with the negative control trimer bait (marked as a purple dotted line) was significantly higher than with the target bait. Analysis of different rounds of PD-L1-Fc with trimer bait in B) and R1-R4 PD-L1-HT phage pools with the control trimer bait D) also showed no significant results.

ELISA analysis of the positive control biopanning against trimer-HT (Figure 3.7A) revealed a statistically significant increase in fluorescent intensity between R2 and R3, as well as between R3 and R4. A clear, gradual increase in MFI from R1 to R4 was observed, with the 1:10 dilution of R1 showing an MFI below 5,000 AU, compared to the 1:10 dilution of R4, which exhibited an MFI close to 15,000 AU. The high MFI observed for the 1:10 dilution of R4, was still notably lower than that of the 1:100 dilution of the R4 library biopanned against VISTA-Fc. This suggests that an additional round of biopanning may be necessary to generate antibodies with higher binding affinity. The R4 library with trimer-HT was statistically significantly higher than when the same round was tested with the negative control bait showing that these phages were not cross-reacting.

For the negative control bait both PD-L1-Fc and PD-L1-HT baits were used to check binding with the enriched phages (figure 3.7B below). A statistically significant increase in MFI was observed between R3 and R4 when using the control bait but it was still significantly lower than R4 with the target bait.

A)

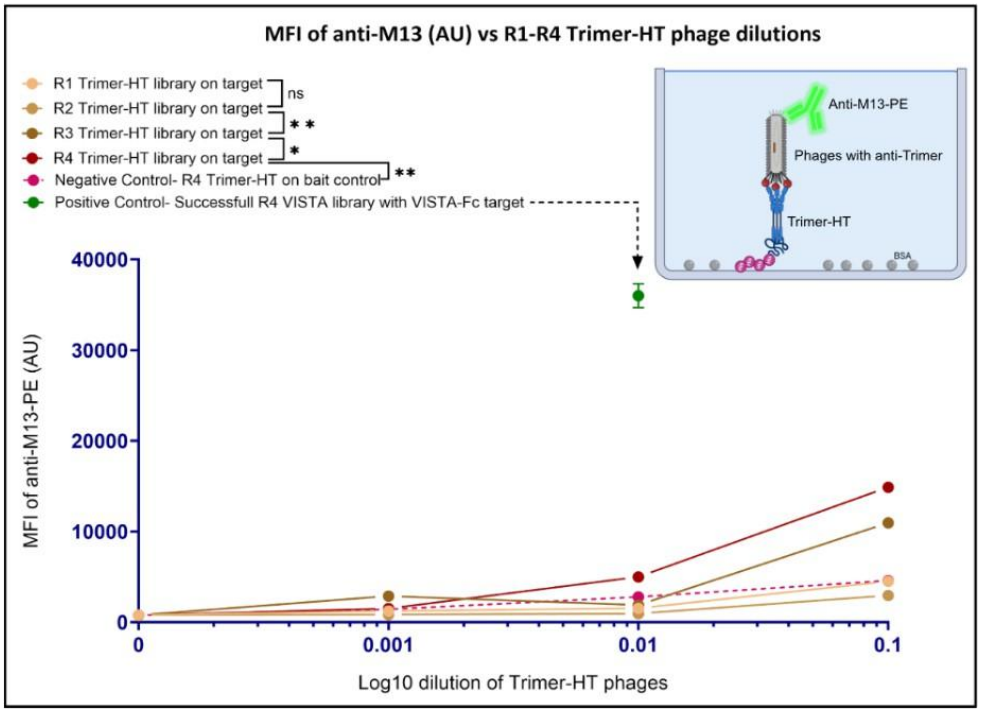

B)

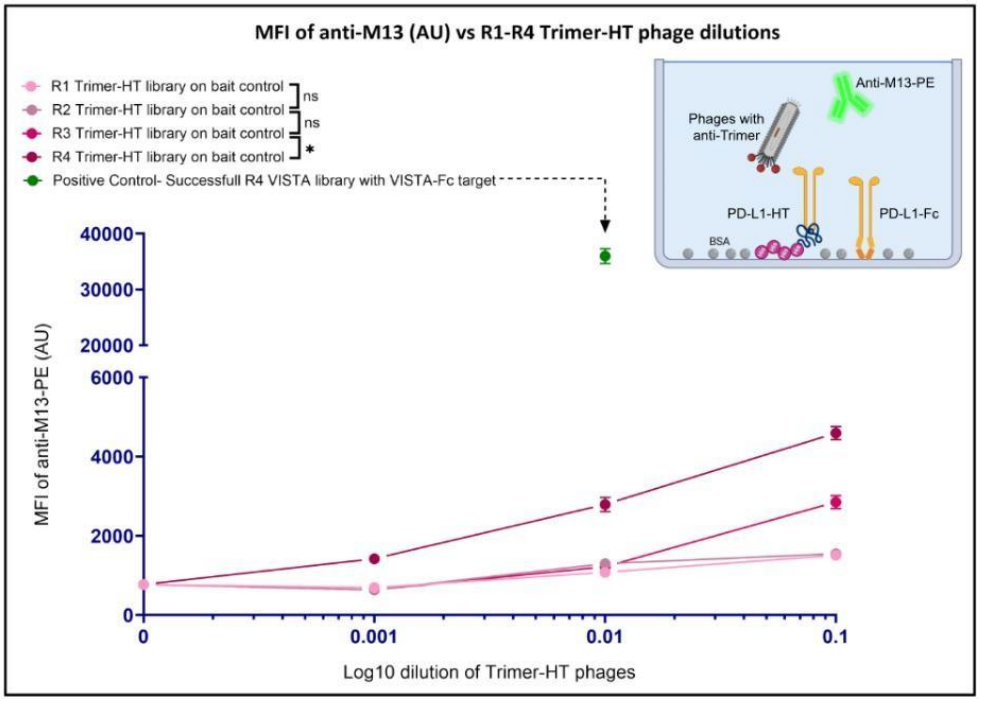

Figure 3.7: Binding analysis of R1-R4 trimer phages with their target and control baits. The different dilutions of R1-R4 trimer phages with trimer bait A) show that there is a gradual increase in fluorescence from R1-R4 indicating that this biopanning was successful. R4 was also statistically significantly higher than the negative control which was R4 trimer phages with both PD-L1-Fc and PD-L1-HT baits. Even though biopanning was successful another round is recommended to produce higher binding phages as R4 was much lower than the positive control marked in green which was 1:100 R4 VISTA phages with VISTA bait. The ELISA of all rounds with the control bait B) also shows a gradual increase between R3 and R4 however it was still markedly lower than R4 with the target bait.

3.4. Testing the binding analysis of different rounds by flow cytometry

Since ELISA analysis of repeat biopanning towards both PD‑L1-Fc and PD-L1-HT produced low fluorescent results, analysis of binding was attempted by flow cytometry. This was done as during ELISA, the baits were randomly oriented on the plate which may have been denatured or displaced during washing (Fegan et al. 2022 & Gibbs et al. n.d). Thus to ensure that any lack of binding with the baits was not due to a lack of exposure of the antigen of interest, binding of phages was assessed by immobilising the PD-L1-Fc, PD-L1- HT and trimer-HT on their respective beads similar to the biopanning procedure. This ensures that the baits are uniformly oriented and the area where biopanning binding occurred was exposed. Following immobilisation, R1-R4 of the different PD-L1 libraries and trimer library were added to their target and control baits. Anti-M13-PE was then added to check the fluorescence released from the bound phages. A no library control was included to detect the background fluorescence and to act as a baseline. To ensure that the PD-L1 baits were immobilised on the beads, a control was included where after immobilisation, anti-PD-L1-PE was added. All four rounds of the libraries were tested against their target, magnetic beads without bait and a negative control bait to check for non-specific binding. As can be observed from figure 3.8 A, B, C, the PD-L1-Fc phage pools did not show a shift in the fluorescent result from one round to other with either PD-L1-Fc, magnetic beads only or trimer-HT phages further confirming that high binding phages were not generated.

A) PD-L1-Fc bait with R1-R4 library biopanned against PD-L1-Fc

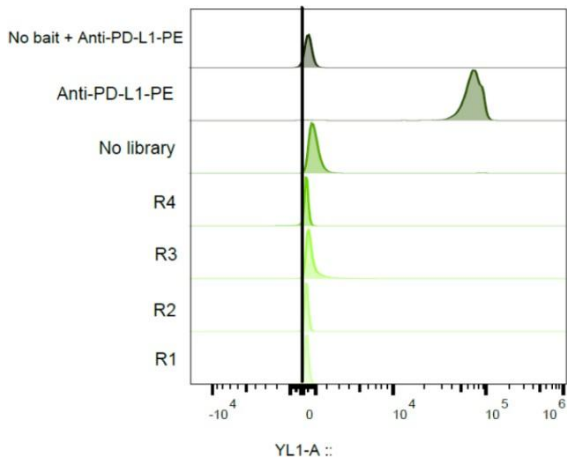

B) No target with R1-R4 library biopanned against PD-L1-Fc

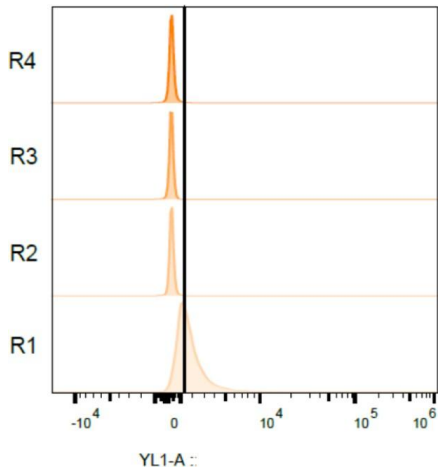

C) Trimer bait with R1-R4 library biopanned against PD-L1-Fc

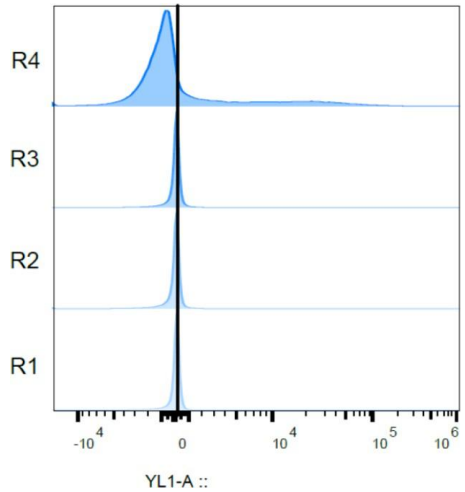

Figure 3.8: Binding analysis of R1-R4 PD-L1-Fc phage pools using flow cytometry. Binding analysis of the different rounds were tested against PD-L1-Fc bait, protein G beads (no target) and trimer bait shown respectively in A), B) and C). In A) other controls were also included such as no bait control with anti PD-L1-PE and a no library control with anti-M13-PE to check for background fluorescence; PD-L-Fc bait with anti-PD-L1-PE were also included to ensure proper immobilisation. As can be observed there is no shift in the fluorescent result with either target further confirming that biopanning failed

On the other hand, the different rounds of PD-L1-HT library and trimer-HT library shown in figure 3.9 A and D have a shift in fluorescence detected in R3 and R4. This shift remains present also in R3 and R4 of both libraries with only the magnetic beads and with their control baits. This indicates that the phages biopanned were not targeting specifically the baits but these may have targeted the magnetic beads.

A) PD-L1-HT bait with R1-R4 library biopanned against PD-L1-HT

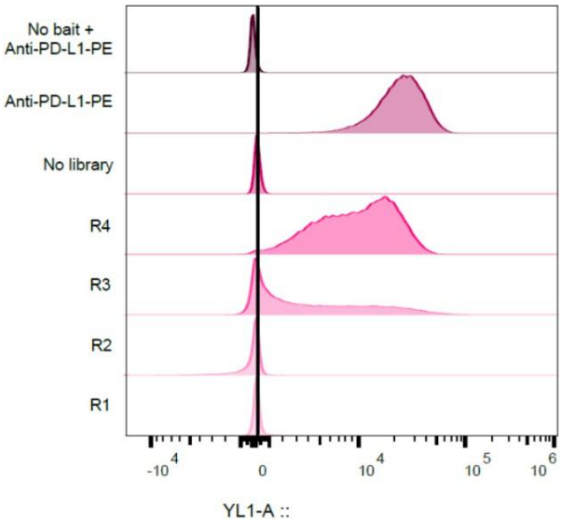

No bait bait with R1-R4 library biopanned against PD-L1-HT

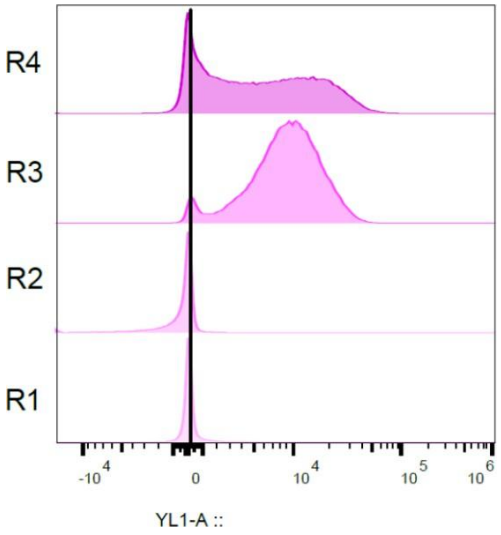

C) Trimer bait with R1-R4 library biopanned against PD-L1-HT

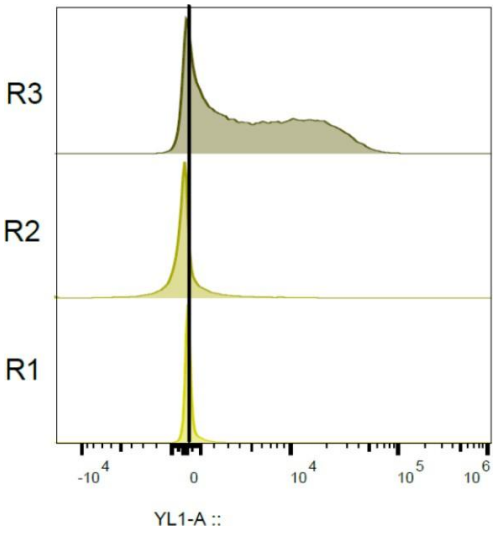

D) Trimer bait with R1-R4 library biopanned against Trimer-HT

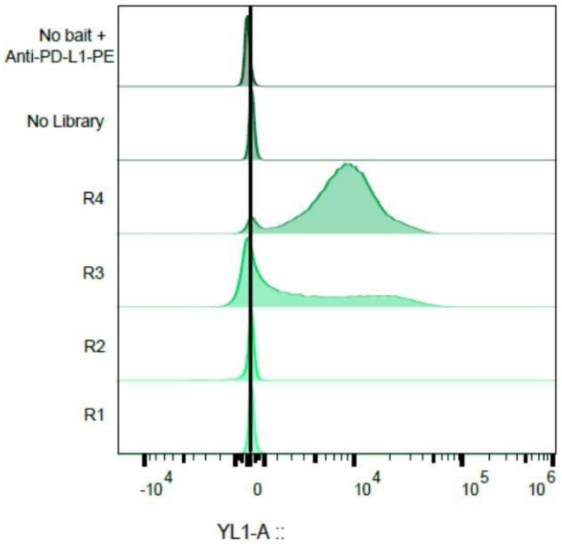

E) No bait with R1-R4 library biopanned against Trimer-HT

F) PD-L1-HT bait with R1-R4 library biopanned against Trimer-HT

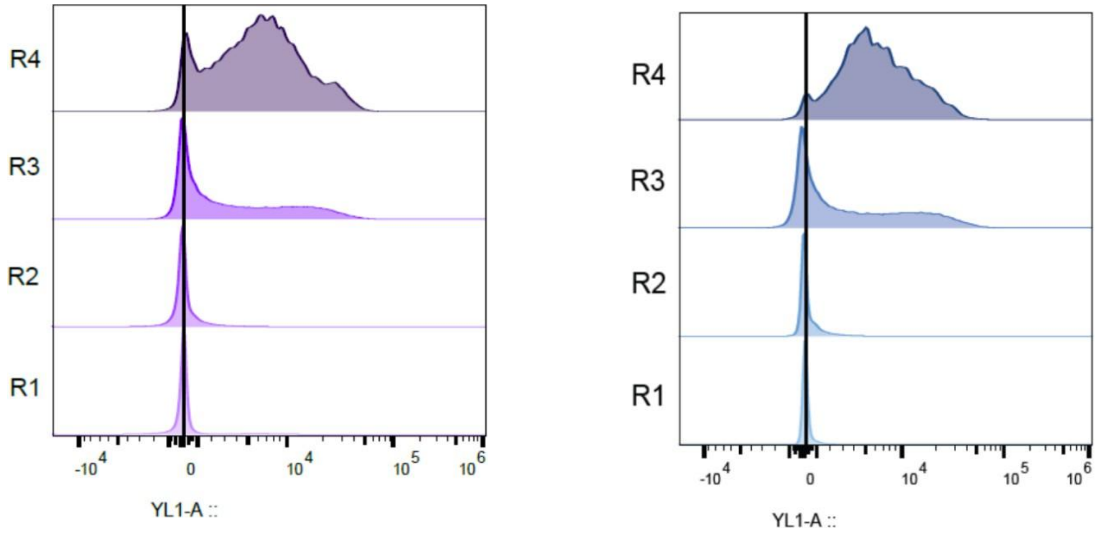

Figure 3.9: Binding analysis of R1-R4 PD-L1-HT & trimer-HT phage pools with flow cytometry. Binding analysis of the different rounds of PD-L1-HT was tested against PD-L1-HT bait, Co-NTA Magbeads and trimer bait shown respectively in A), B) and C). Whereas different rounds of trimer-HT was tested against trimer-HT, Co-NTA Mag beads and PD-L1-HT baits shown respectively shown in D)-F). In A) and D), additional controls include no bait with anti-PD-L1-PE and no library with anti-M13-PE to assess background fluorescence. A) also includes PD-L1-HT bait with anti-PD-L1-PE to confirm bait immobilization. A shift was observed between R3 & R4 with all targets of both libraries indicating that the phages were binding non-specifically potentially against the Co-NTA Mag beads instead of their target bait

3.5. ELISA analysis of monoclones

Monoclonal analysis of 30 candidate phage clones were obtained from the R4 VISTA library biopanned during the Spiteri 2022 study. These clones were isolated and their binding affinity was initially assessed with ELISA against its target bait and negative control bait which was the Fc portion of IgG to ensure that the clones were not cross-reacting with the Fc part of the VISTA-Fc chimera bait protein. A no clone control where PBS was added instead of a clone to act as a negative control and R4 1:100 VISTA polyclonal population were assessed with both VISTA-Fc and the Fc-part of IgG baits to respectively act as positive and negative controls.

Statistical analysis of this ELISA result was done by initially checking the normal distribution of each clone using the Shapiro-Wilk test. The statistical significance of those clones which were normally distributed with the two baits were assessed with the multiple unpaired T-test using Welch’s correction to not assume that the clones with the different baits have the same standard deviation. Whereas statistical significance of those clones which were not normally distributed with either baits were assessed by the Multiple Mann-Whitney test.

Statistical analysis was performed on those clones that had a higher binding affinity towards VISTA that is higher than the baseline. The baseline was determined by the clone which had the highest binding affinity towards the negative control bait. As can be observed from figure 3.10, clone 8 had the highest binding affinity towards the Fc bait thus the MFI of clone 8 with Fc part of IgG acted as the baseline and marked with a dotted line. Clones 9 and 12 were not included for statistical analysis as they had the weakest binding to VISTA, lower than the baseline. Statistical analysis of the ELISA result shown in figure 3.10 below shows that all clones had a statistically significant higher result with the VISTA-Fc when compared with Fc bait protein (p-value <0.000001) with clones 1, 15 and 22 having the highest fluorescent result towards VISTA bait.

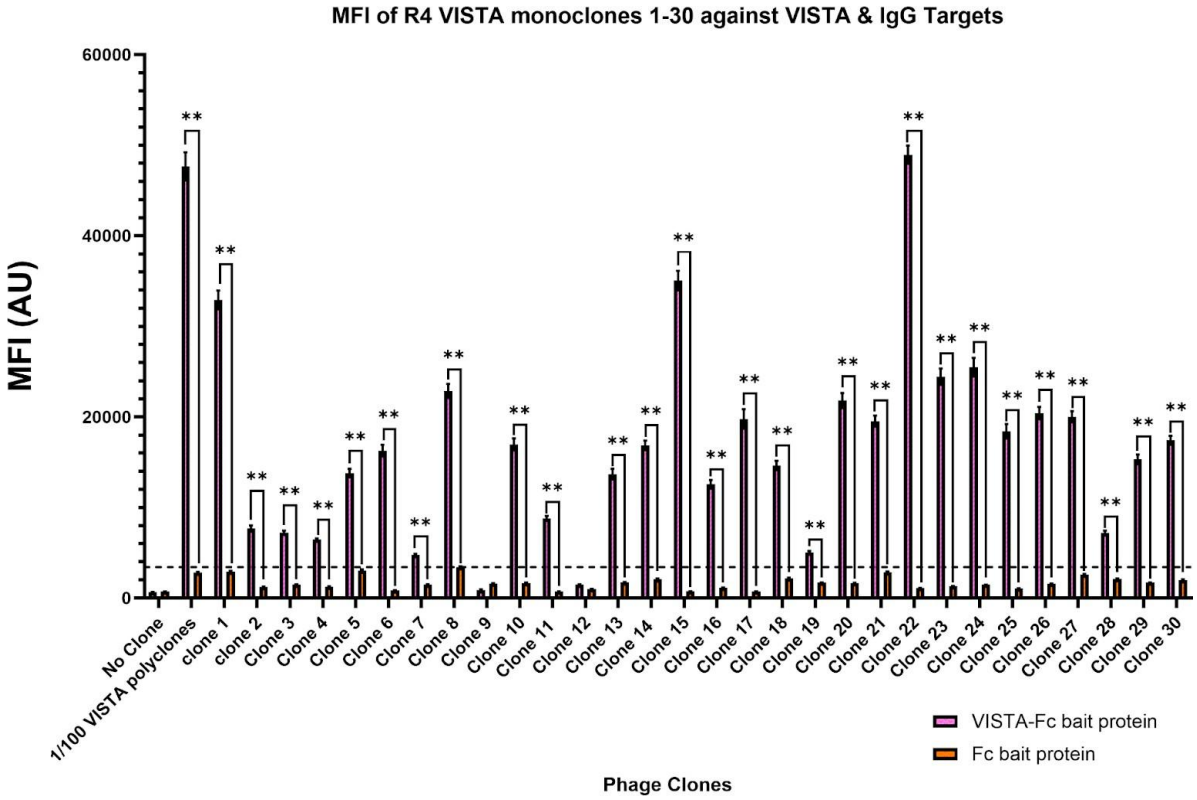

Figure 3.10: Specificity analysis of monoclones with VISTA-Fc and Fc bait protein. ELISA analysis of 30 clones with VISTA and Fc bait proteins was done. A no-clone control with PBS served as a negative control and R4 1:100 VISTA polyclonal population was assessed with VISTA-Fc to act as a positive control and with the Fc-part of IgG baits to ensure that there is no cross-reaction with the polyclonal library. All clones exhibited low binding affinity to Fc, with clone 8 showing the highest binding. This value was used as a baseline, and clones with binding affinities to VISTA higher than this baseline were included in statistical analysis. All clones except for clone 9 & 12 strongly bound to VISTA compared to the Fc bait protein. Statistical analysis of clones was done by using the multiple unpaired T-test using Welch's correction for those normally distributed and the Mann Whitney Test for non-normally distributed clones. These showed that all clones (excluding 9 & 12) were binding strongly in comparison to the Fc bait protein (p value <0.000001)

Following analysis of the binding of 30 clones with VISTA-Fc bait and Fc bait proteins, additional testing was conducted using a different bait protein, SARS-COV-2, to further assess the specificity of the clones. Binding against VISTA-Fc bait was done again to check for reproducibility of clone binding and a no clone control, where instead of phage clones, PBS was included to check for background fluorescence and a positive control of R4 1:100 VISTA polyclonal population against target were included. Analysis of 30 clones at once was found to be laborious and has an increased risk of errors during the procedure thus it was decided to divide this experiment into two. Initially clones 1-15 were analysed and as can be

observed from figure 3.11, all clones were binding weakly to SARS-COV-2. Clone 15 had the strongest binding towards SARS-COV-2 thus the MFI of clone 15 with SARS-COV-2 acted as the baseline and marked with a dotted line and statistical analysis was performed on all clones which had a higher binding with VISTA bait, higher than this baseline. All clones except for clones 9 and 12 were binding strongly to VISTA similar to binding produced in figure 3.10 and this binding was statistically significantly higher than binding with SARS-COV-2.

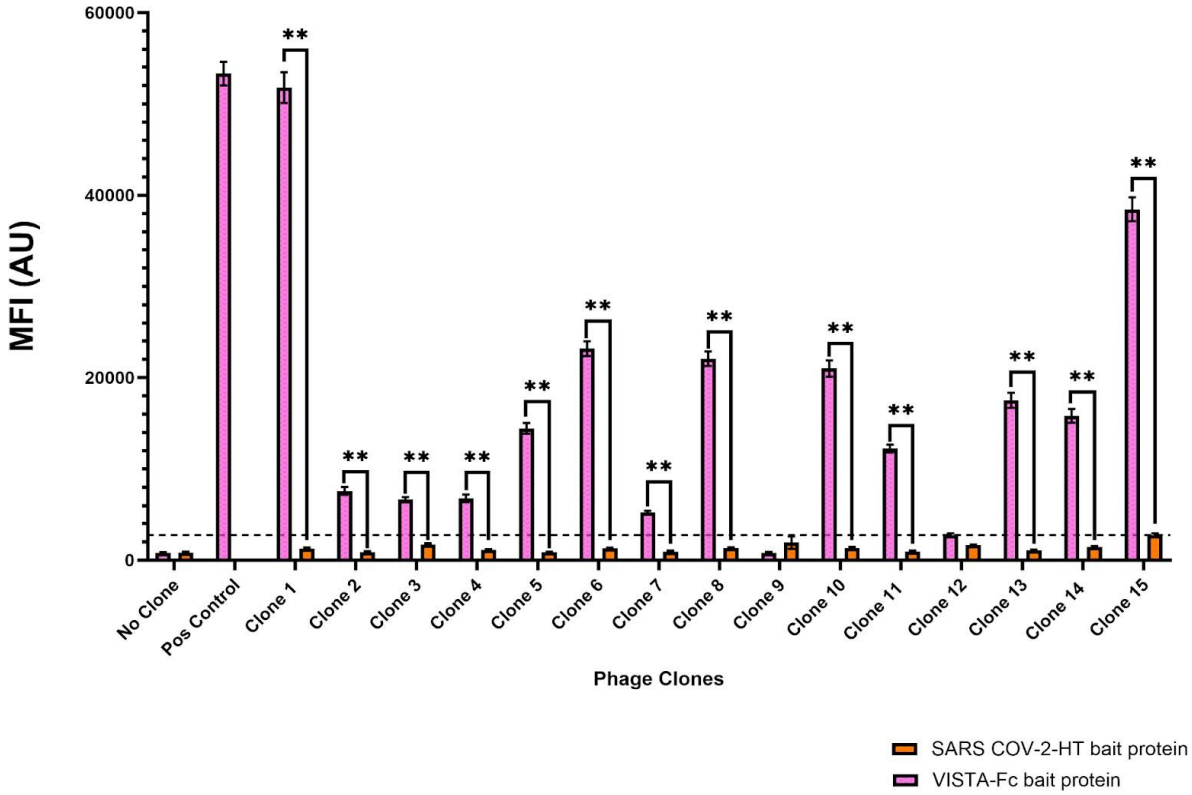

Figure 3.11: Specificity analysis of monoclones 1-15 with VISTA-Fc and SARS-COV-2-HT bait protein. ELISA testing of the first 15 clones with VISTA and SARS-COV-2 bait proteins was performed. A no-clone control with PBS served as a negative control and R4 1:100 VISTA polyclonal population was assessed with VISTA-Fc to act as a positive control. This ELISA revealed that all clones, except for clone 9 & 12 strongly bound stronger to VISTA compared to SARS-COV- 2 bait protein. All clones exhibited low binding affinity to SARS-COV-2, with clone 15 showing the highest binding. This value was used as a baseline, and clones with binding affinities to VISTA higher than this baseline were included in the statistical analysis. Statistical analysis of clones showed that all clones were binding strongly in comparison to the SARS-COV-2 bait protein with clones 1 and 15 having the highest binding to VISTA.

When clones 16-30 shown in figure 3.12 were assessed, binding towards SARS-COV-2 of all clones was significantly higher than the binding produced with clones 1-15. The no clone control towards VISTA was low however with SARS-COV-2 was relatively high indicating the presence of background fluorescence with SARS-COV-2. The positive control was also low which further questions the reliability of the results. The results of the clones binding towards VISTA bait show similarity to figure 3.10 however clones 20, 21 23 and 24 were binding weaker towards VISTA. Since clone 27 had the strongest binding towards SARS-COV-2, it acted as the baseline and marked with a dotted line and statistical analysis was performed on all clones which had a higher binding with VISTA bait than this baseline. Statistical analysis was performed on only clones 17, 22, 25 and 26 and these were found to be statistically significantly higher binding with VISTA than SARS-COV-2 with clone 22 having the highest binding towards VISTA.

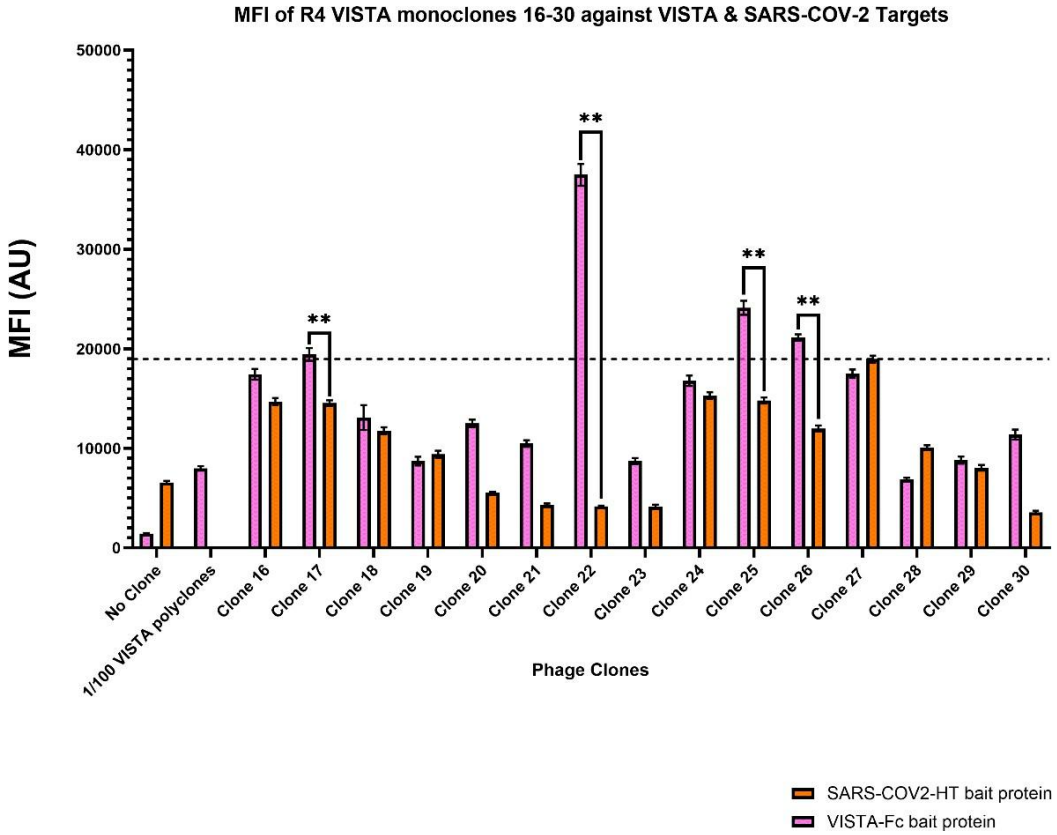

Figure 3.12: Specificity analysis of monoclones 16-30 with VISTA-Fc and SARS-COV-2-HT bait proteins. ELISA testing of the remaining 15 clones with VISTA and SARS-COV-2 bait proteins showed that there is an increase in background fluorescence with SARS-COV-2 which was confirmed by the no clone control and on the contrary the positive control produced a low fluorescent result. Clone 27 showed the highest binding with SARS-COV-2 thus this value was used as a baseline, and clones with binding affinities to VISTA higher than this baseline were included in the statistical analysis. Statistical analysis of clones 17, 22, 25 and 26 showed that they were binding strongly to VISTA in comparison to the SARS-COV-2 bait proteins however these results are not reliable as the controls used showed an increase in background fluorescence and the positive control did not work.

Since the results produced with clones 16-30 with SARS-COV-2 were uncertain, a repeat of this experiment was required. However, the volume of phage clones used for these analyses was depleted and only 15% glycerol stocks of the phagemid clones were present. Retrieval of phage clones from these glycerol stocks was not previously done in-house, thus it was attempted following Ph.D. Phage Display Biopanning Manual of New England Biolabs n.d. Along with assessing binding of clones 16-30, binding of clone 9 which was a weak binder to VISTA and clone 10 which was a strong binder to VISTA were included as

controls to ensure that similar binding pattern would be present when re-assessing with VISTA and SARS-COV-2. However, as can be observed from figure 3.13, the results produced from the phage clones retrieved from phagemids showed that the method used did not work and there were also issues with the ELISA procedure as the no clone control against both VISTA and SARS-COV-2 baits was again high and the positive control was also low. The binding pattern of clones 9, 10 were different from figure 3.11 as they both produced weak binding towards VISTA and had a higher binding with SARS-COV-2. The binding pattern towards either clone with VISTA was completely different from figure 3.10 and the majority of clones were shown to bind stronger with SARS-COV-2. It was concluded that erroneous results were produced and that retrieval of phage clones was not successful.

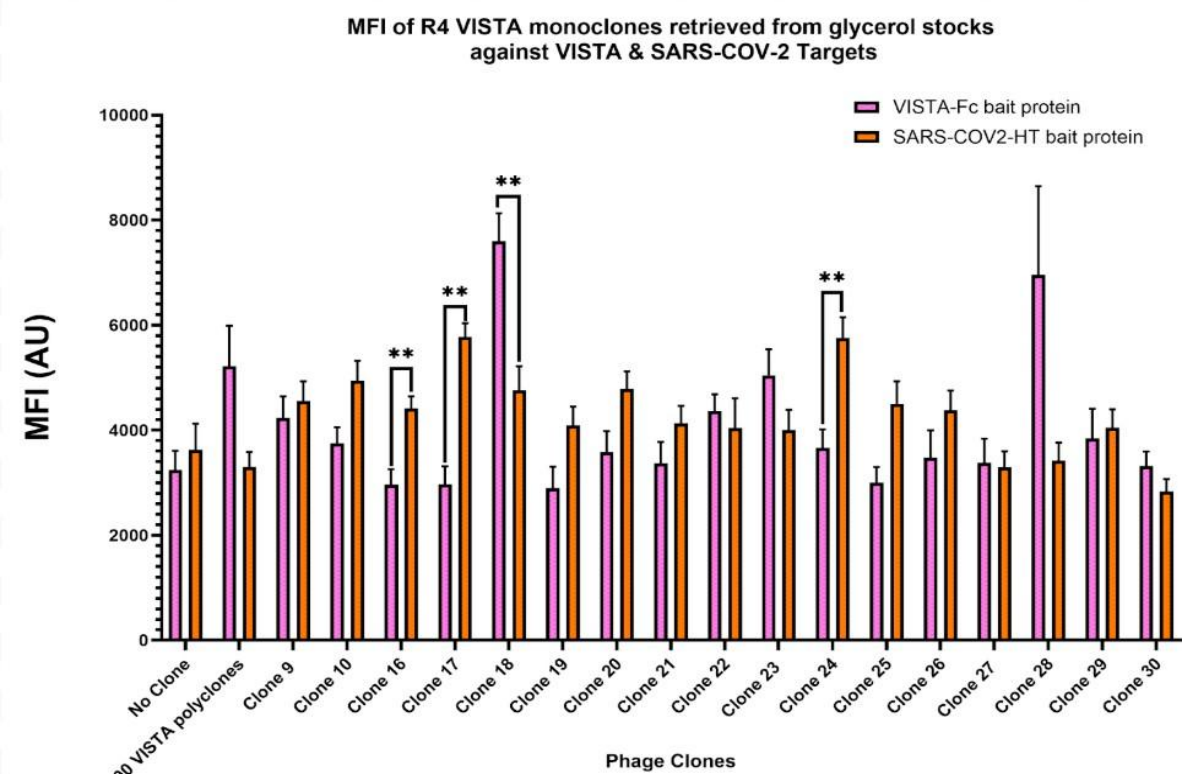

Figure 3.13: Specificity analysis of monoclones of 9,10,16-30 with VISTA-Fc and SARS-COV-2-HT bait protein. ELISA testing of clones 9,10, 16-30 retrieved from glycerol stocks show that binding to VISTA bait was low and different from the previous figures 3.10-3.12. The clones were binding similarly or stronger to SARS-COV-2 in comparison to VISTA thus this shows that retrieval of phage clones was unsuccessful. The positive control which was the 1:100 VISTA polyclones with VISTA bait was too low and the no clone controls was detecting an increase in background fluorescence which also indicates problems in the ELISA procedure.

Since retrieval of phage clones was unsuccessful, assessment of the specificity of phage clones was not continued any further. Plasmid extraction of these clones was done, and these were sent for Sanger sequencing to determine the DNA sequence of each clone Since no further analysis of clone specificity could be done, a further 30 candidate phage clones were picked and assessed. During this period, other researchers were obtaining erroneous results when conducting the same experiment which was expected to be due to helper phages being used. Thus, while performing this experiment, all 30 clones were generated using a new aliquot of helper phages and 15 from these 30 clones were tested using both helper and hyperphages which display up to 5 scFvs on the surface of phages to have higher avidity. Binding of clones was initially assessed with ELISA against VISTA and SARS-COV-2. The no clone control was used as a negative control to test for background fluorescence which as can be observed from figure 3.14 background fluorescence still remained high especially with SARS-COV-2. On the other hand, the 1:100 VISTA polyclones which was a positive control showed a high fluorescent result with VISTA bait. During preparation of phage clones for ELISA, a 1:100 dilution of the monoclones was mistakenly done. Consequently, as can be observed from the ELISA of all 30 clones with helper phages in figure 3.14, all clones had a weak fluorescent result with VISTA bait similar to the binding with SARS-COV-2. Statistical analysis was performed on all clones and only clones 36 and 60 had a significantly higher binding with VISTA than SARS-COV-2. Clones 31, 37 and 54 produced a high fluorescent result with SARS-COV-2 which was significantly higher than VISTA whereas the remaining clones were found to not have a significant difference between binding with VISTA and SARS– COV-2.

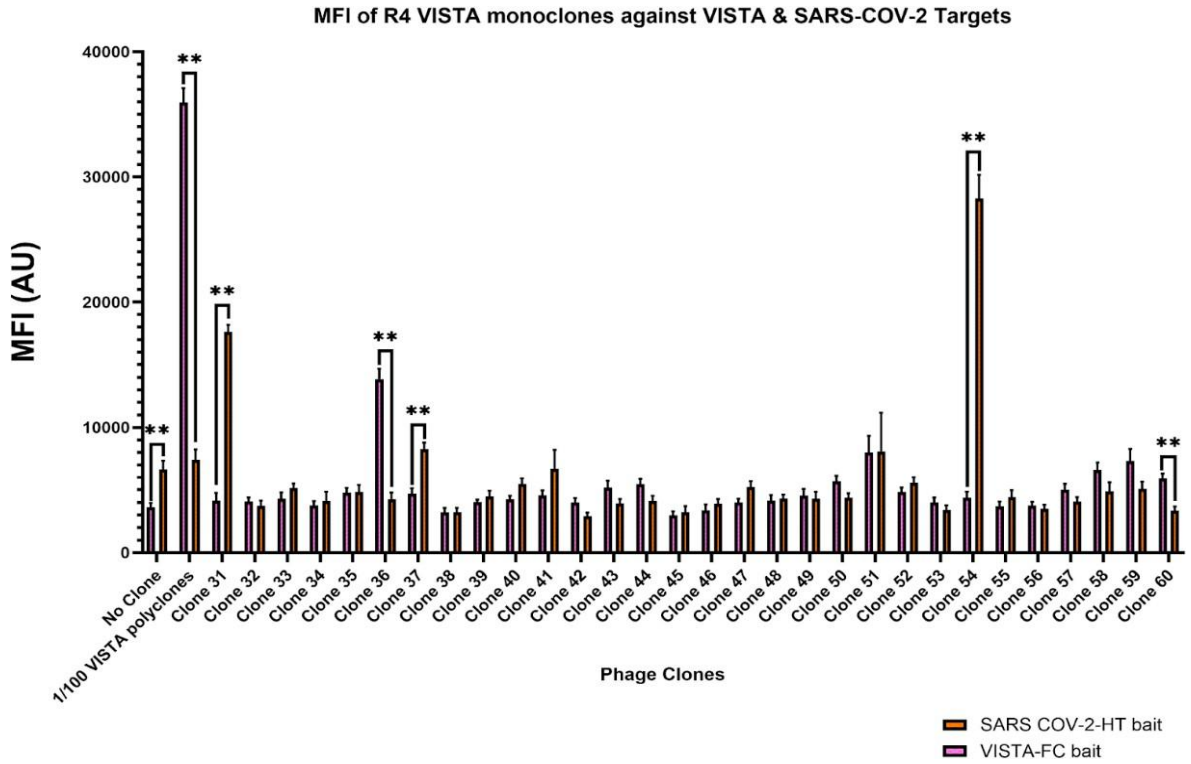

Figure 3.14: Specificity analysis of 31-60 monoclones with VISTA-Fc and SARS-COV-2-HT bait protein. ELISA testing of clones 31-60 which were produced using helper phages was done against VISTA and SARS-COV-2 bait proteins. During preparation of clones for ELISA, a 1:100 dilution of these clones was mistakenly done and due to this, all clones were binding weakly to VISTA in comparison SARS-COV-2. Whereas, clones 31, 37 and 54 were binding significantly stronger with SARS-COV-2. The no-clone control with PBS which served as a negative control with both VISTA and SARS-COV-2 bait still produced a significantly higher background fluorescence with SARS-COV-2. However, the R4 1:100 VISTA polyclonal population assessed with VISTA-Fc which acted as a positive control produced a very high fluorescent result.

When ELISA was performed on the 1:100 dilution of 15 clones that were produced using hyperphages shown in figure 3.15, it was found that most clones were binding stronger to VISTA bait compared to clones generated with helper phages. Statistical analysis was performed on all clones and as can be observed, clones 31, 37, 42, 44, 50, 51, 53, and 55 were binding strongly to VISTA bait in comparison to SARS-COV-2. Clones 33 and 39 also have a significantly higher binding to VISTA however it is not as strong as the other clones. Clones 35, 46 and 57 had no statistically significant binding between SARS-COV-2 and VISTA whereas clones 48 and 59 were found to be binding stronger to SARS-COV-2 than VISTA.

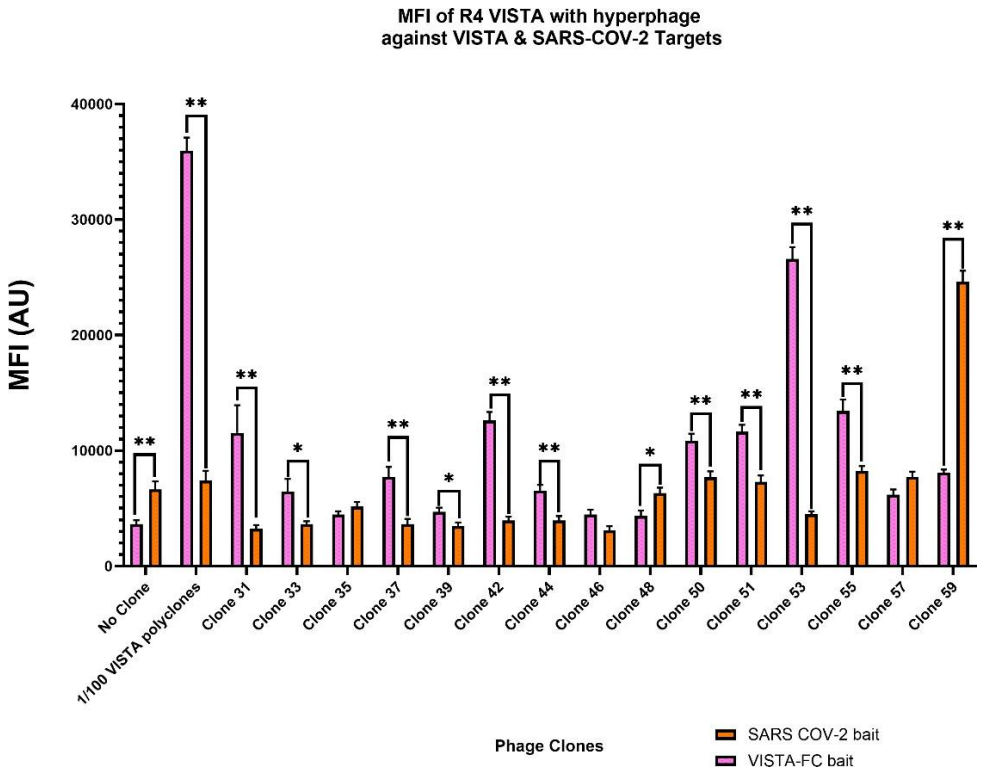

Figure 3.15: Specificity analysis of monoclones prepared with hyperphages against VISTA-Fc and SARS-COV-2-HT bait protein. ELISA testing on 15 clones produced using hyperphages was done against VISTA and SARS-COV-2 bait proteins. During preparation of these clones for ELISA, a 1:100 dilution of these clones was mistakenly done. Despite this, the majority of clones still showed significantly stronger binding with VISTA than SARS-COV-2 whereas clones 48 & 59 displayed significantly stronger binding with SARS-COV-2. The no-clone control with PBS which served as a negative control with both VISTA and SARS-COV-2 bait still produced a significantly higher background fluorescence with SARS-COV-2. However, the R4 1:100 VISTA polyclonal population assessed with VISTA-Fc which acted as a positive control produced a very high fluorescent result.

Since binding of monoclones towards VISTA was stronger with the clones generated using hyperphages in comparison to helper phages, further specificity analysis was done using only these 15 clones. Specificity analysis of monoclones against VISTA-Fc, SARS-COV-2- HT and PD-L1-Fc baits was done. PD-L1-Fc was used as a bait protein as significant sequence homology was shown to be present in the extracellular Ig domain with VISTA (Wang et al. 2011).

BLASTp analysis was conducted from the NCBI Blast® website between the human VISTA and PD-L1 protein sequences, both obtained from the UniProt: the Universal Protein Knowledgebase, to assess potential sequence homology. As shown in Table 3.1, only a

portion of the PD-L1 sequence aligned significantly with the VISTA sequence, with a query coverage of 42%. Among the aligned regions, only 24.81% of the residues were identical, indicating low sequence identity (Figure 3.16A). Despite this low identity, the E-value was low, suggesting that the observed alignment is statistically significant and unlikely to have occurred by chance.

To further explore potential similarity, a second BLASTp analysis was performed focusing specifically on the extracellular domains (ECDs) of both VISTA and PD-L1, as this is the domain accessible for scFv binding during phage display biopanning. As illustrated in Figure 3.16B, this analysis produced a higher query coverage of 72%, indicating that a larger portion of the VISTA ECD aligned with the PD-L1 ECD. However, the percentage identity remained low at 24.79%, again suggesting weak sequence homology between these domains. The pairwise alignments from both BLASTp analyses are presented in Figure 3.16.A.

A.

Protein	Organism	Max Score	Total Score	Query Cover	% Identity	E-value	Accession Length.	Accession Number
PD-L1	Homo sapiens	43.1	43.1	42%	24.81%	2e-09	20013	Query_3919085

B.

Protein	Organism	Max Score	Total Score	Query Cover	% Identity	E-value	Accession Length.	Accession Number
PD-L1 ECD	Homo sapiens	40.8	40.8	72%	24.79%	2e-09	220	Query_3980013

Table 3.1: BLASTp sequence alignment between VISTA and PD-L1. A presents the alignment of the full-length protein sequences, while B focuses on the alignment of their extracellular domains (ECDs). In the full-sequence alignment (Panel A), 42% of the VISTA sequence aligned with PD-L1, and the aligned region showed a high Max Score relative to the Total Score, indicating that the alignment was primarily composed of strong matches as the Total Score includes both strong and weak alignments, while the Max Score reflects the highest scoring aligned segment. Within the aligned region, 24.81% of the residues were identical. The low E-value suggests that this similarity is statistically significant and unlikely to have occurred by chance**.** When analysing only the ECDs (B), a similar pattern was observed; however, the query coverage increased to 72%, indicating that a larger portion of the VISTA ECD aligned with the PD-L1 ECD.

A.

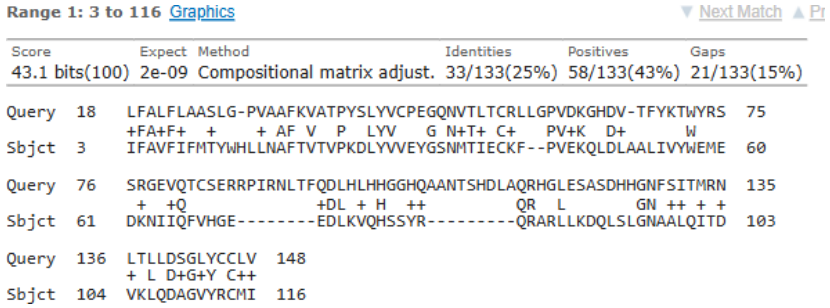

B.

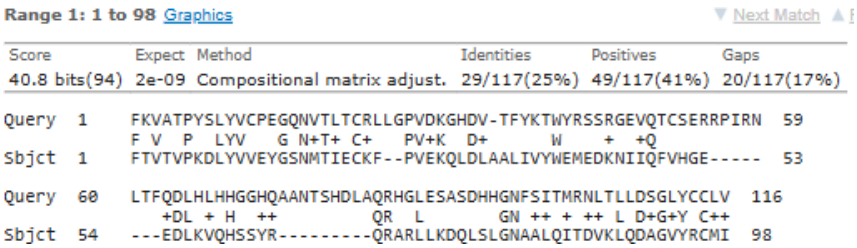

Figure 3.16: Pairwise sequence alignments of VISTA and PD-L1 obtained from BLASTp analysis. A shows the alignment of the full-length protein sequences of VISTA and PD-L1, while B presents the alignment of their extracellular domains (ECDs). In A, three distinct BLAST hits were identified from different regions of the PD-L1 sequence that show similarity to VISTA. In B, two BLAST hits were observed between the ECDs of PD-L1 and VISTA. For each alignment, the alignment score, E-value, and percentage identity are provided. These alignments were generated using the NCBI Blast® tool from the National Library of Medicine website.

As can be observed in figure 3.17, 1:10 and 1:100 VISTA polyclonal population with VISTA bait were used as a positive control and a no library control was used to detect background fluorescence. During the previous ELISA analysis, there was a markedly high background fluorescence especially with SARS-COV-2 bait. Therefore, for this experiment blocking was performed using a higher percentage of BSA (3% BSA in 0.1% tween 20) which was found to be effective to markedly reduce background fluorescence. In this case, 1:10 dilution of VISTA polyclones had the strongest binding towards SARS-COV-2, therefore used as the baseline for comparison. Statistical analysis was performed only on clones that exhibited stronger binding to the VISTA bait than this baseline, resulting in the exclusion of clones

31, 33, 35, 39, and 46 from statistical analysis. Statistical analysis of the clones binding stronger to VISTA than the baseline showed that all clones analysed were all binding strongly with VISTA in comparison to SARS-COV-2 and PD-L1 with a p-value <0.000001. The strongest binders to VISTA were clones 53 and 42.

With the remaining volume of clones 31-60, plasmid extraction was performed and sent abroad for Sanger sequencing.

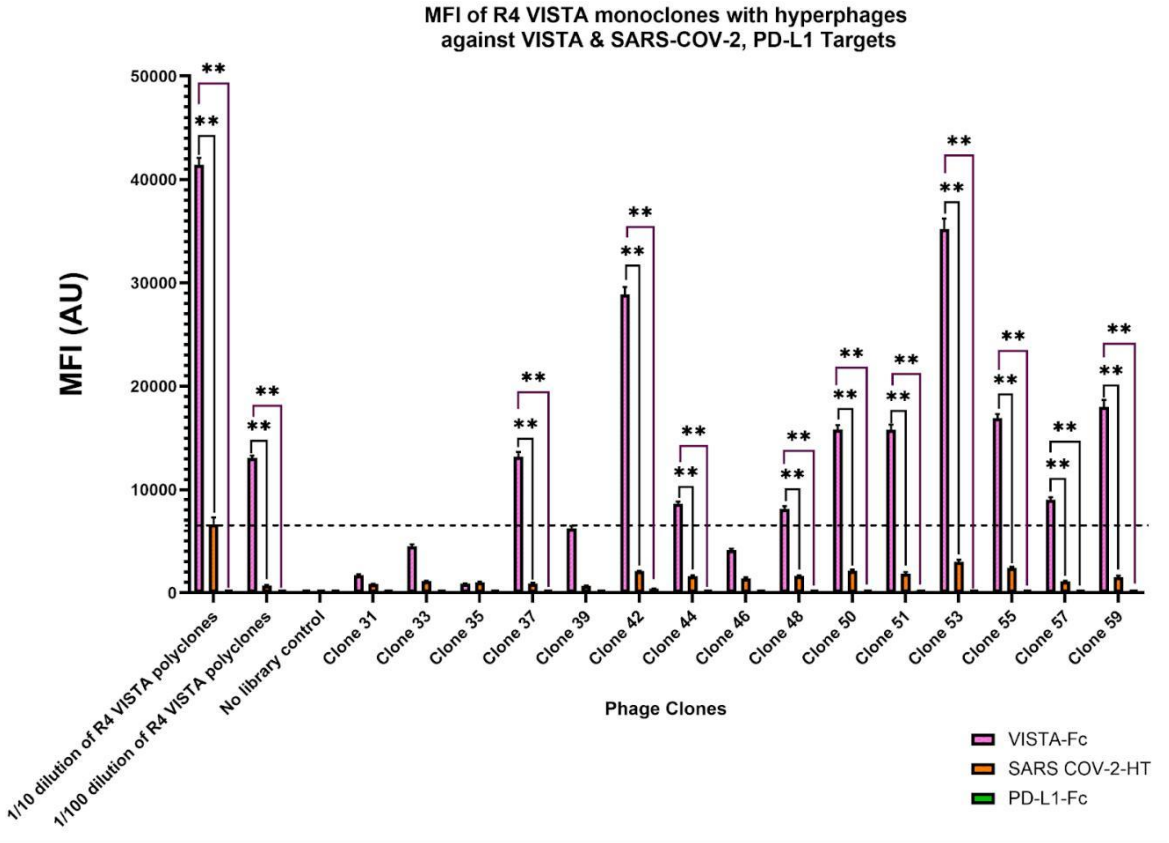

Figure 3.17: specificity analysis of monoclones prepared with hyperphages against VISTA, SARS-COV-2 and PD-L1. ELISA analysis on clones produced using hyperphages showed that most clones were binding strongly to VISTA except for clones 31, 33, 35, 39 & 46. The no-clone control with PBS which served as a negative control with both VISTA and SARS-COV-2 baits showed weak background fluorescence with both baits. A R4 1:10 and 1:100 VISTA polyclonal population were both assessed with VISTA-Fc to act as a positive controls. All clones exhibited low binding affinity to SARS-COV-2 however 1:10 dilution of polyclones showed the strongest binding towards SARS-COV-2. This value was used as a baseline, and clones with binding affinities to VISTA higher than this baseline were included in the statistical analysis. with PD-L1 was very low and it was barely visible on this graph. Statistical analysis of clones assessed had a p value <0.000001.

3.6. Analysis of Sanger sequencing results

Sanger sequencing was performed to determine the different scFv sequences of the strong binding and weak binding clones. This aids in determining the diversity of the sequencing following the final round. Prior to sending the DNA for Sanger sequencing, the concentration and purity of all clones was assessed by the Nanodrop spectrophotometer. The results are presented in Table 6.2 of the Appendix. DNA concentrations ranged from 101.3 to 273.2ng/ μ L, which was sufficient for Sanger sequencing. The 260/280 absorbance ratios were close to the expected value of ~1.8, indicating acceptable protein contamination levels. However, approximately half of the clones exhibited 260/230 ratios slightly above 2.2, suggesting the possible presence of impurities such as residual salts or organic compounds. From the Sanger sequencing analysis, the amino acid sequence of each clone was obtained and these were aligned for comparison. From the aligned sequences of clones 1–30, presented in figure 6.2 of the appendix, revealed that only clones 9 and 10 contained the full-length sequence. In most of these clones, only the variable heavy chain (VH) region was successfully sequenced. In contrast, sequencing of clones 31–60 successfully yielded full-length sequences for all clones. Analysis of the full-length sequences revealed that the majority of clones shared an identical sequence. However, sequence variations were observed in clones 9, 10, 34, 37, 39, 40, 42, 49, 53, and 60. The fact that only 10 out of 32 full-length sequence clones showed sequence variation suggests that R4 of VISTA biopanning led to the enrichment of a dominant clone during the selection process. Notably, clones 10 and 37 are highly similar to each other, differing by only two amino acids within the CDR3 region of the VL chain. However, both clones show distinct variations across all framework and CDR regions of both the VH and VL chains when compared to the sequence of the dominant clone. When compared to the dominant clone, clone 9 also

showed extensive variation across most framework and CDR regions of VH and VL. Clones 40, 42, 53, and 60 shared an identical sequence variation, primarily within the framework and CDR regions of the VL. Clone 34 displayed variation in framework regions 3 and 4 of the VL, while clone 39 contained 2–3 amino acid substitutions in framework regions 1 and 2 of the VH when compared to the dominant clone. Clone 49 differed by a single amino acid substitution in framework region 3 of the VL.

To assess the similarity amongst clones, a dendrogram was generated using the Complementarity-Determining Region3 (CDR3) protein sequences from both the heavy and light chains, for all clones where sequencing data was available. A CSV file containing the CDR3 sequences was created and uploaded to a dendrogram program developed by Ms Francesca Chircop in 2025. As shown in figure 3.18, the dendrogram for the heavy chain CDR3 (CDR3-VH) includes the majority of clones, excluding clones 1, 3, 5, 6, 8, 12, 16–19, 21, 22, 26, 28–30, and 39, for which sequencing data was unavailable. The variable light chain of CDR3 (CDR3-VL), dendrogram however, includes only clones 9, 10, 31–33, 35–38, and 40–60.

Both dendrograms display clone identity along the x-axis and linkage distance on the y-axis, using a logarithmic scale to enhance resolution of smaller distances. This distance is relative to show relationships between clones. The dendrogram program arranged each clone on the x-axis and grouped those clones that have an identical sequence or similar sequences together. When the clones are connected together they become a cluster. The point on the y-axis where these clones are connected together indicates the similarity between one clone and the other. If the values on the y-axis are close to 0, this indicates that the clones are highly similar. In contrast, the further the linkage distance is from 0, the

more dissimilar the clones are (Landau & Ster 2010). Overall, both dendrograms show that most clones have an identical CDR3 sequence.

In the CDR3-VH dendrogram, all clones except clones 2, 10 and 37 are clustered together with and orange line. This line is on the '0' showing that these sequences of the CD3-VH are identical. Clone 2 clusters closely with clones 10 and 37, indicating high sequence similarity. This cluster is distinct from the remaining clones, merging with them at a much greater linkage distance, signifying low similarity to the rest of the clones.

In contrast, the CDR3-VL dendrogram reveals a greater number of distinct clusters, reflecting increased variability in the light chain compared to the heavy chain. Nonetheless, all clones except 60,53,40,42,9,10,37 still share identical sequences as they are clustered with an orange line on the '0'. Clones 10 and 37 form a tightly clustered pair with a linkage distance of ~1, reflecting a high sequence similarity, followed by clone 9. These, in turn, are more distantly related to clones 60, 53, 40, and 42 which have an identical sequence to each other as they have a linkage distance of 0. This entire group (clones 10, 37, 9, 42, 40, 53, and 60) is markedly dissimilar from the remaining clones as they cluster together at a much higher linkage distance (~15).

A. Dendrogram of CDR3-VH

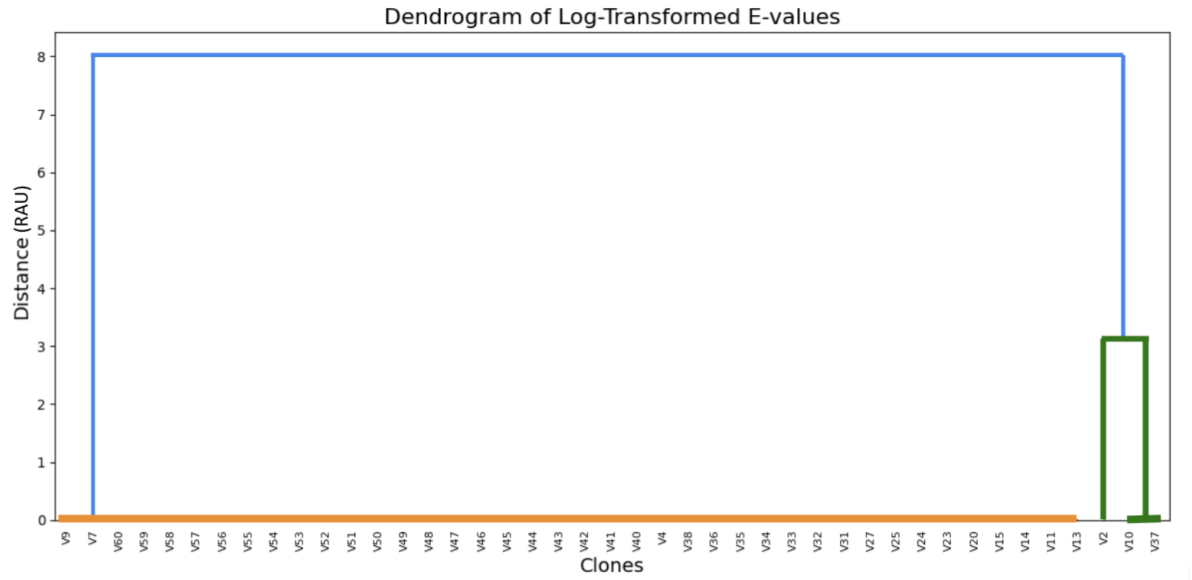

B. Dendrogram of CDR3-VL

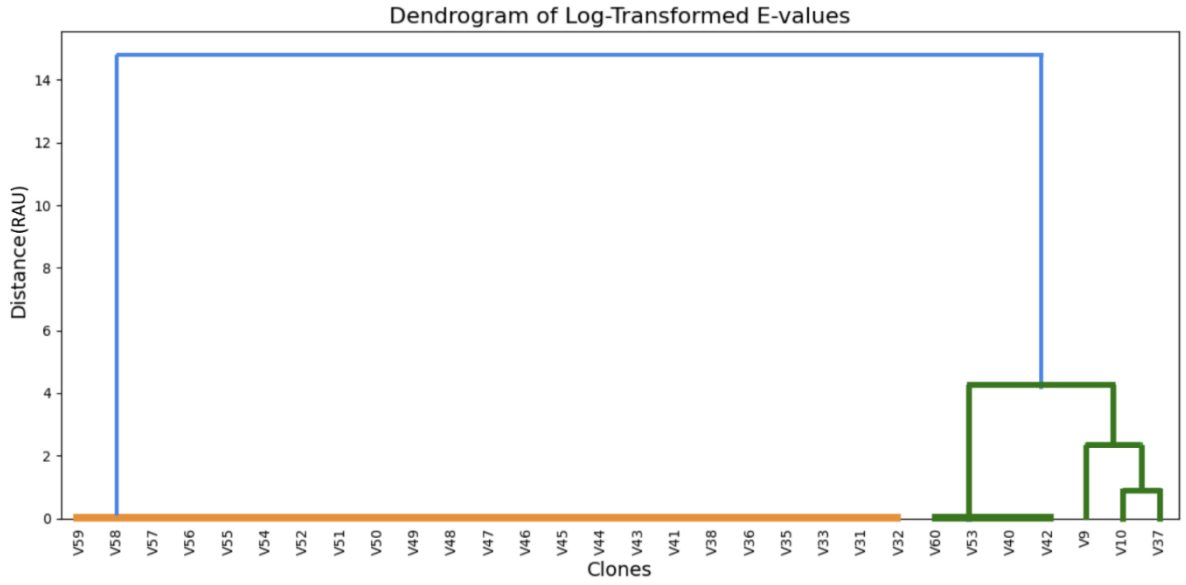

Figure 3.18: Dendrograms illustrating the hierarchical clustering of CDR3 sequences from the heavy chain (CDR3-VH) in A and the light chain (CDR3-VL) in B across different clones. Both dendrograms show the clones on the x-axis and the distance which has Relative Arbitrary Units (RAU) on the y axis. In both dendrograms, the majority of clones have an identical sequence as they have a linkage distance of 0. However, in the CDR3-VH dendrogram, a distinct cluster comprising clones 2, 10, and 37 stands out due to their significant divergence from the other clones which have a distance of 8. In the CDR3-VL dendrogram, while most clones still share identical sequences, there is greater structural complexity, reflecting increased variability compared to the heavy chain. Clones 10 and 37 form a tight cluster with a linkage distance of ~1 indicating strong sequence similarity. This cluster further groups with clone 9, followed by a broader cluster including clones 42, 40, 53, and 60, which have the same sequence as they cluster together at a linkage distance of 0. These clones are clearly distinct from the remaining group, merging at a higher linkage distance of ~15, indicating lower sequence similarity with the remaining clones.

The physicochemical properties including molecular weight, isoelectric point (pI) and instability index of all full-length sequence clones were analysed using the Expasy ProtParam tool, with the results summarized in the Table 3.2. The isoelectric point represents the pH at which a protein carries no net charge. At pH values above the pI, the protein will possess a net negative charge, while below the pI it will have a net positive charge (Tokmakov et al. 2021).

All clones, except clone 34, exhibit pI values between 4 and 5.05, indicating that at neutral pH, they would display a net negative charge. In contrast, clone 34, with a pI of 9, would carry a net positive charge under the same conditions. The instability index offers an estimate of a protein's stability, based on a computational formula derived from a statistical analysis of stable and unstable proteins. Typically, unstable proteins have a higher frequency of methionine, glutamine, proline, glutamate, and serine, while stable proteins are richer in asparagine, lysine, and glycine. An instability index below 40 suggests that the protein is stable, whereas a value above 40 indicates instability (Guriprasad et al. 1990). Accordingly, all proteins in this study, except for clone 34, are predicted to be stable.

Clone	MW	pI	Instability Index (II)
V9	29834	4.78	31.8
V10	26186.3	5.05	38.89
V31	26857.4	4.68	30.49
V32	29738.9	4.66	32.6
V33	29738.9	4.66	32.6
V34	29555.4	9.1	43.27
V35	29738.9	4.66	32.6

V36	29625.8	4.66	32.68
V37	28666.1	4.98	39.35
V38	29738.9	4.66	32.6
V40	29474.6	4.75	32.88
V41	29738.9	4.66	32.6
V42	29474.6	4.75	32.88
V43	29738.9	4.66	32.6
V44	29738.9	4.66	32.6
V45	29738.9	4.66	32.6
V46	29738.9	4.66	32.6
V47	29738.9	4.66	32.6
V48	29738.9	4.66	32.6
V49	27286.2	4.72	31.23
V50	28026.8	4.58	33.33
V51	28411.5	4.85	30.57
V52	29738.9	4.66	32.6
V53	29474.6	4.75	32.88
V54	29738.9	4.66	32.6
V55	29738.9	4.66	32.6
V56	29738.9	4.66	32.6
V57	29738.9	4.66	32.6
V58	29738.9	4.66	32.6
V59	29738.9	4.66	32.6
V60	29474.6	4.75	32.88

Table 3.2: Physicochemical properties of clones 9-10 and 31-60 predicted by Expasy ProtParam computational tool. The protein sequence of these clones were entered to predict the Molecular weight, isoelectric point (pI) and instability index and from these parameters it was noted that pI ranges between 4.00 to 5.05 except for clone 34 which has a pI of 9.1. All our clones have an instability index <40 suggesting these clones are stable. Clone 34 has an instability index of 43.27 showing that it is not a stable protein.

The sequence of the strongest binder; clone 53 and the weakest binder; clone 35 from the results identified in figure 3.17, were used to predict the 3D structure using SWISS-MODEL, shown in figure 3.19.

The protein sequences of these clones, formatted in FASTA, were submitted to the SWISS-MODEL server for analysis using the automated mode. This tool predicted the 3D model using homology modelling of proteins based on their amino acid sequence. SWISS-MODEL aligned the amino acid sequence provided with structurally characterized proteins in order to identify a suitable template for homology modelling. Template identification was carried out using sequence comparison tools such as BLAST and HHblits, which search for proteins with known 3D structures that share significant sequence similarity. Once an appropriate template was selected, the ProMod3 modelling engine was used to construct a comparative 3D model of the target protein, incorporating conserved structural features and optimizing variable regions. This automated pipeline enabled the generation of reliable structural models when no experimentally determined structure was available (SWISS-MODEL n.d).

For clones 53 and 35, scFv55 protein was used as the template sequence to create the 3D structure. The ideal template was selected based on the sequence similarity, coverage and the predicted model quality was assessed using the global model quality estimate (GMQE) and QMEAN Distance Constraint Score (QMEANDisCo) (SWISS-MODEL n.d). This template exhibited 71.54% sequence identity with clone 53 and 69.39% with clone 35.

The GMQE indicates the quality of both the template and its alignment with the clone sequences. This model quality measurement gives a value between 0 and 1 and values closer to 1 have a higher quality measurement. Both of our clones with the template sequence have a GMQE value of 0.71 which means both clones have a good predicted

model quality (SWISS-MODEL n.d). The QMEANDisCo measures the quality of the model generated using distance constraints and structural features where values greater than 0.70 indicate a good quality model generated (Guillon et al. 2024, SWISS-MODEL n.d). Clone 53 generated a QMEANDisCo of 0.75 ± 0.05 whereas clone 35 generated a value of 0.74 ± 0.05 which means that both models are of good quality.

Furthermore, model validation was performed using the MolProbity score. This score is based on multiple factors including steric clashes, Ramachandran statistics (favoured regions and outliers), rotamer outliers, deviations in C-β geometry by more than 0.25Å, as well as bad bonds and angles (Chen et al. 2009; SWISS-MODEL n.d). Lower MolProbity scores correlate with higher model quality. Clones 53 and 35 attained scores of 1.02 and 1.10, respectively, indicating a good model quality.

In the 3D model generated, the VH, VL, linker, and Myc tag regions were clearly annotated. Both the VH and VL domains adopt an immunoglobulin-like β-sheet structure, with the VH domain positioned near the N-terminal and the VL domain located towards the C-terminal. These domains are connected by a flexible linker which is rich in glycine and serine residues, which provides sufficient spatial separation to allow proper folding and orientation of the variable domains without introducing steric hindrance or interfering with their function. (Chen et al. 2014).

A.

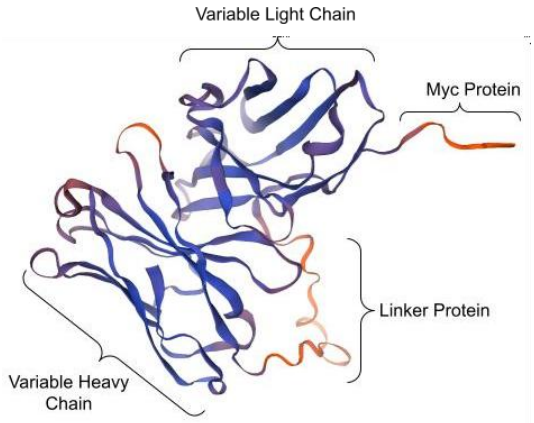

B.

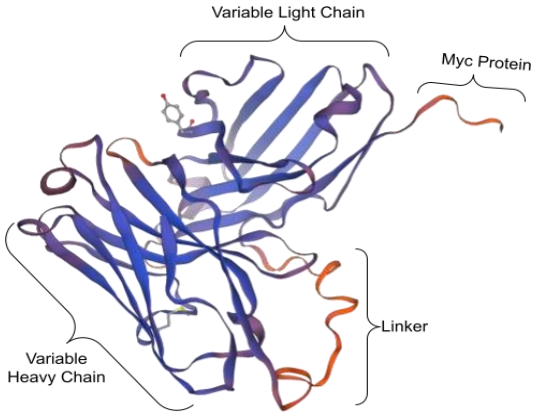

Figure 3.19: Predicted 3D protein structure of A. clone 53 and B clone 35. These models were generated based on homology modelling with scFv55 protein which had a sequence identity of 71.54% with clone 53 and 69.39% with clone 35. These structures show the variable heavy and variable light chain linked together with a linker protein along with a Myc tag at the C-terminus.

Ramachandran plots were generated with the 3D protein structure to visualize the feasibility of the torsion angles of the amino acid residues which can range from +180° to -180° . The Ramachandran plot is graph of the torsion angles of the amino nitrogen bonded with the α - carbon known as the phi (Φ) angle and the torsion angle of the α -carbon bonded with the carbonyl carbon known as the psi (ϕ) angle. These torsion angles depend greatly on steric hindrance caused when a polypeptide chain repels another when they are in proximity of each other due to overlapping electron clouds which form energetically unfavourable conformations (Clayden et al. 2012, Kumar & Arya 2019).

Figure 3.20 presents the Ramachandran plots for clones 53 and 35. In these plots, the dark green areas denote sterically favoured conformations, while the light green regions represent sterically allowed conformations where minimal steric interference is observed. The majority of amino acid residues in the predicted structures for both clones (indicated in red and blue) fall within these green zones, with residues outside considered as outliers as they have sterically disallowed conformations. Specifically, in clone 53, 90.98% of residues are located in the Ramachandran favoured regions, with only 0.82% classified as outliers.

Similarly, clone 35 shows 91.80% of its residues in the Ramachandran favored regions, with 1.23% as outliers. This Ramachandran plot excludes glycine and proline residues as glycine residues lack a side chain thus it is less sterically hindered and can form favourable conformations outside the Ramachandran favoured regions. On the other hand, proline has a cyclic side chain which makes it more sterically hindered which restricts conformation.

The plots feature different green regions corresponding to the characteristic torsion angle ranges of various secondary structures. For example, β-sheets generally adopt torsion angles around $\Phi \approx -139^{\circ}$ and $\phi \approx +135^{\circ}$, placing their allowed conformations in the upper left quadrant. Right-handed α-helices, with typical angles near $\Phi \approx -57^{\circ}$ and $\phi \approx -47^{\circ}$, are primarily found in the lower left quadrant, whereas left-handed α-helices, with angles around $\Phi \approx +57^{\circ}$ and $\phi \approx +47^{\circ}$, appear in the upper right quadrant (Kumar & Arya 2019).

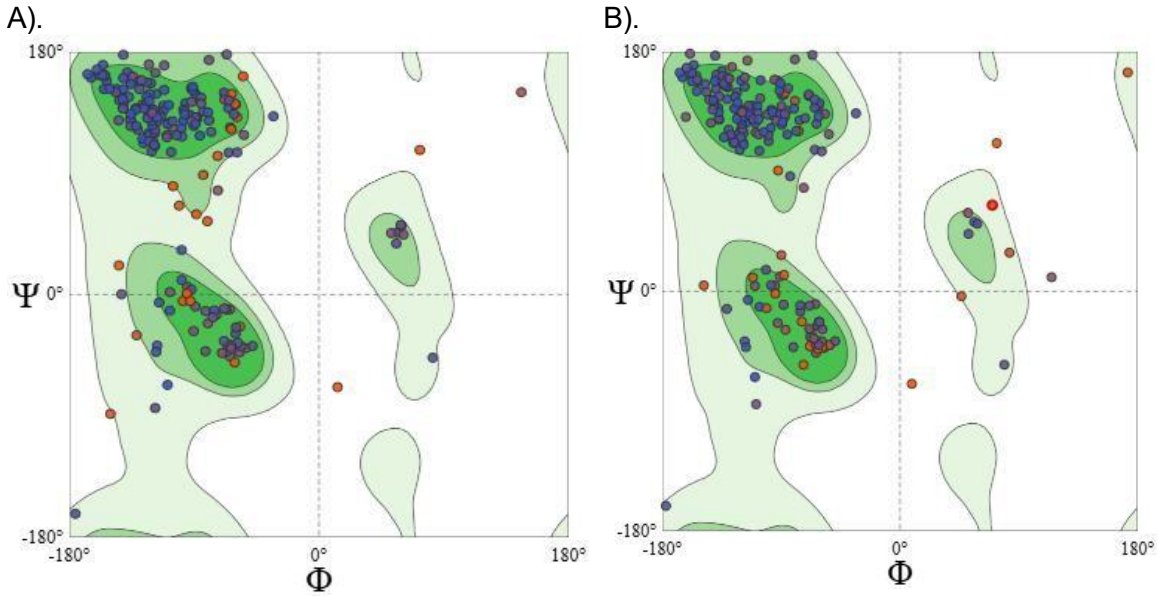

Figure 3.20: Ramachandran plots of predicted 3D models of clone 53 in A and 35 in B generated by Swiss-Model. These plots display the Φ and ψ torsion angles of all amino acid residues except for glycine and proline residues. The favoured regions are shown in different shades of green and the residues in darkest green have the most favourable conformations.

Chapter 4:

Discussion

In this project, a naïve canine scFv library was employed to target various epitopes on recombinant human PD-L1, which had been immobilized on magnetic beads. The use of a naïve library offers significant advantage over an immunized library, as it enables targeting of virtually any antigen without the need to construct a new library for each application. Moreover, it allows for targeting of antigens that are typically challenging to elicit an immune response against, such as self-antigens or antigens with low immunogenicity (Griffiths & Duncan, 1998). However, since the library was not pre-immunized against the target antigens, it must possess a high degree of diversity to ensure the presence of high-affinity binders. For this reason, a library with a diversity of 10^9 variants was utilized in this study. The scFv is a small fragment of the antibody composed of a variable heavy chain (VH) and variable light chain (VL) domains which are joined together by a peptide linker which has a single binding site. Using only this fragment produces a stable active library which is easier to handle and more efficiently expressed in *E.coli* in comparison to fragment antigen binding (Fab) and full antibody libraries which are more complex as they require more protein folding and interaction between different polypeptides (Ahmad et al. 2012)

The scFv library was produced by first extracting the mRNA from B cells of non-immunized canines and with PCR, amplifying only the VH and VL chain domains which are then fused together by a peptide linker to form scFv. With the help of restriction endonucleases, these were then ligated into vectors containing M13gIII gene and β -lactamase gene for ampicillin resistance. These recombinant vectors were transfected in *E.coli* containing M13KO7 helper phages to amplify and generate the primary library containing phages expressing scFv fused with the pIII protein on their surface (Di Pietro, 2020; Dong et al. 2020). The diversity and enrichment of the antibodies was assessed by Next generation short-read DNA sequencing and long-read DNA sequencing was performed to determine the

Immunoglobulin Heavy chain Variable region (IGHV), immunoglobulin lambda variable (IGLV) and immunoglobulin kappa variable (IGKV) subfamily distribution of our library (Lisowska et al.2025).

Even Though biopanning phage display has been shown to be a powerful and reproducible tool for mAb preparation (Alfaleh et al. 2020), in this project two attempts for biopanning phage display using the scFv antibodies did not yield antibodies with a high binding affinity against PD-L1.

Following the groundbreaking discovery of phage display by George P. Smith in 1985, the biopanning phage display technique has significantly transformed the field of Immunotherapeutics. It has been very successful in the production of specific proteins, peptides and antibodies which have a variety of clinical applications. This method has been proven to be highly effective in generating specific proteins, peptides, and monoclonal Antibodies (mAbs), all of which have wide-ranging clinical applications. Numerous studies have demonstrated the high success rate of phage display in antibody generation (Kalim et al., 2019, Rabinal et al., 2015, Sulong et al., 2021), positioning it as a robust alternative to the traditional hybridoma technology that has long been used for mAb production.

The use of these antibodies have also been FDA approved for clinical use. Currently, 14 mAbs derived from phage display have been approved such as Adalimumab, a fully human mAb targeting tumour necrosis factor (TNF), used to treat immune-mediated disorders such as rheumatoid arthritis and psoriasis. Necitumumab, a human mAb targeting the Epidermal Growth Factor Receptor (EGFR), approved for the treatment of metastatic non-small cell lung carcinoma (NSCLC). Atezolizumab and Avelumab, both targeting PD-L1, used in the treatment of urothelial carcinoma and metastatic Merkel cell carcinoma, respectively (Alfaleh et al., 2020).

During the initial biopanning phage display against PD-L1-HT, biopanning against VISTA- HT was done consequently to act as a positive control. The results of the phage ELISA presented in Figure 3.2 indicate that no binding was observed to the positive control target protein. One key difference between this unsuccessful biopanning experiment and the previously successful biopanning against VISTA was the use of a different immobilisation technique. To investigate whether this variation affected target protein immobilization, an experiment was designed to assess immobilization efficiency.

As shown in Figure 3.3, increased fluorescence was detected for both VISTA-Fc and trimer-HT proteins, confirming their effective immobilization and successful detection. In contrast, no significant difference in fluorescence was observed across varying titres of VISTA-HT, suggesting a failure in the immobilization of the VISTA-HT onto Co-NTA Magbeads.

The polyhistidine tag is a relatively small, uncharged peptide that typically causes minimal interference with the structure and function of the fused protein, while exhibiting strong affinity for metal ions (Bornhorst & Falke, 2010, Spriestersbach et al., 2015). In this study, the HT was fused to the C-terminus of VISTA. However, the protein was not being efficiently immobilized, possibly due to the HT becoming buried within the folded VISTA structure, thereby preventing its interaction with Co-NTA magnetic beads (Bornhorst & Falke, 2010, Spriestersbach et al., 2015). To overcome this, denaturation of the protein was required but this approach was ultimately not pursued, as biopanning with denatured VISTA could lead to the selection of antibodies that recognize epitopes not exposed in the native, functional conformation. In addition, the binding efficiency of the HT to metal ions can be adversely affected by acidic pH, as protonation of the histidine residues under low pH conditions reduces their affinity for metal ions. The presence of reducing agents, chelating

agents, or imidazole, can also disrupt polyhistidine-metal interactions (Bornhorst & Falke 2010) but contamination of these agents were unlikely present, since successful binding of the trimer-HT was still achieved under the same conditions.

This experiment showed that lack of VISTA presentation contributed to the failure of positive biopanning control however as can be observed in figure 3.4, PD-L1-HT was being efficiently immobilised to their respective beads and failure of this biopanning was not due to the lack of HT exposure which may indicate that other issues with biopanning were present. Nonetheless for the repeat biopanning, both PD-L1-HT and PD-L1-Fc were used to check whether different immobilisation techniques affect biopanning results.

During the initial biopanning, fresh in-house aliquots of helper-phages were prepared which had a working phage titre of $6.7x10^9$ PFU/mL which is more than the concentration used by the New England Biolabs manual which has a final working concentration of $1x10^8$ PFU/mL (*Use of M13KO7 Helper Phage for isolation of single-stranded phagemid DNA* n.d). Helper phages have a defective replication site to have a low replicative ability to allow for the packaging of the phagemid DNA containing the chimeric pIII-scFv protein. The pIII protein is an essential surface protein that aids in F-pilus binding thus expression of wild type pIII is favoured during phage assembly (Broders et al. 2003). Since a higher titre of helper phages were used which express a wild type pIII protein, it was speculated that there were not enough phagemids present to displace the helper phages and replication favoured helper phages to produce phages containing wild type pIII protein (Aripov et al. 2024). Thus a low binding affinity from the fourth round could be due to the favoured amplification of the wild type pIII protein. For the the second attempt of biopanning phage display, the working phage titre used was of $6.7x10^8$ PFU/mL to increase the likelihood of phages containing the pIII-scFv protein. Other than this, for the repeat biopanning an increased

concentration of phage library was added in each round to increase the volume of phages to bind to our target. A different positive biopanning control was used; trimer-HT protein as successful biopanning has been repeatedly achieved (Lisowska et al. 2025).

During the second attempt of biopanning, only a significant result was achieved against trimer-HT bait whereas no significant binding was observed against either PD-L1-HT and PD-L1-Fc bait even though efficient antigen presentation was shown to be done during each round by flow cytometry.

To examine the binding analysis of the phage pools with ELISA, the proteins were being coated directly on ELISA plates. This direct adsorption results in the proteins to randomly orient and may undergo conformational changes that could have been easily denatured during the various washing steps (Ledsgaard et al. 2018). Thus, binding analysis was checked using flow cytometry to use the same immobilisation technique as that of biopanning to ensure that lack of binding was not due to lack of antigen presentation during ELISA. As can be observed from figure 3.8, PD-L1-Fc did not show a difference in fluorescence result during the different rounds with either the target and control baits confirming the ELISA results obtained. On the other hand, as can be observed in figure 3.9, round 4 of both PD-L1-HT and trimer-HT phage libraries were showing a shift in the fluorescent signal with the target bait, control bait and no bait control. Since this shift is slightly evident in round 3 and becomes more pronounced during round 4 it is likely to be due to biopanning of phages against a non-specific target potentially against the Co-NTA Mag beads. This conclusion is supported by the observation that phages biopanned against the PD-L1-Fc bait did not exhibit a shift when tested with either PD-L1-Fc or trimer-HT bait proteins, suggesting a specific issue arises when HT bait proteins are used during biopanning. Despite this, the ELISA results for the PD-L1-HT and trimer-HT phage pools did

not show significant non-specific binding, likely because magnetic beads were not included during the ELISA, thereby eliminating bead-related interactions. These findings suggest that biopanning with HT proteins may yield ambiguous results, as phages might be selected based on binding to components other than the intended target producing selection-related, target-unrelated phages. This non-specific binding could result from interactions between certain amino acids and the magnetic bead matrix or the Co^{2+} ions present on the Co-NTA beads. A study by Barbas et al. (1993) demonstrated that approximately nine common amino acids, including histidine, serine, and tyrosine, can bind to bivalent metal ions. Such interactions are biologically relevant, as bivalent metal ions contribute to protein stability, structural assembly, and catalytic activity.

Based on these results, it was concluded that biopanning should ideally be performed using bait proteins fused with Fc tags. Additionally, incorporating a bead-only control during ELISA analysis is recommended to detect and account for any non-specific binding. Since the objective to generate antibodies with high binding affinity towards PD-L1 was not achieved, the aim of this project was shifted to retrieve monoclones from only the VISTA library. From this project 60 monoclones were successfully isolated and the scFv binding was assessed by ELISA.

The initial 30 monoclones were screened against VISTA and the Fc region of human IgG to confirm that binding was specific to the VISTA target and not the Fc portion of the bait protein. As shown in Figure 3.10, all clones, except clones 9 and 12, demonstrated strong binding to VISTA bait and only weak binding to the Fc region, indicating good specificity.

Additionally, binding to SARS-COV-2 antigens was assessed to exclude non-specific interactions. To perform this, the analysis was divided into two sets. The first set,

comprising clones 1‑15, is shown in Figure 3.11. These clones exhibited weak binding to SARS-COV-2 and maintained a similar binding profile to VISTA as seen in Figure 3.10. However, clones 16‑30 showed stronger binding to SARS-COV-2. Notably, the no-clone control in this set yielded higher than expected fluorescence, while the positive control showed relatively low signal, suggesting potential issues with the assay. Due to these ambiguous control results, it was deemed necessary to repeat the experiment. However, the volume of phage clones had been exhausted, and only 15% glycerol stocks of the corresponding phagemid clones remained. Attempts to rescue phages from these glycerol stocks were unsuccessful, as subsequent ELISA results were inconsistent and unreliable. Given these limitations and the time constraints of the project, it was ultimately decided not to proceed with further binding analysis of the 30 clones.

Due to the unreliable results obtained previously, a new set of 30 clones (numbered 31‑60) were selected for further binding analysis against VISTA-Fc, SARS-COV-2, and PD-L1- HT bait proteins. Both VISTA and PD-L1 contain an Immunoglobulin Variable (Ig-V) domain and a cytoplasmic domain. The Ig-V domain of VISTA has been shown to share a close evolutionary relationship with that of PD-L1 (Wang et al., 2011). To explore this relationship in more detail, a BLASTp sequence alignment was performed between the whole VISTA and PD-L1 proteins and another was performed on their ECDs. The analysis revealed that only 42% of the VISTA sequence aligned significantly with PD-L1, and this region exhibited a low sequence identity of 24.81%. Analysis of their ECDs was done since, *in vivo*, this is part of the protein that is present outside of the cell and it contains binding sites to interact with other proteins to initiate signalling pathways (Chen & Wu 2018). Alignment of the two ECDs show that 72% of VISTA sequence was aligned with PD-L1 and this region exhibited 24.79% sequence identity. Even though they have a low percentage identity, PD-L1 was still

included in the binding analysis as a control to evaluate potential cross-reactivity.

During this phase, both hyperphages and standard helper phages were used on 15 randomly selected clones to assess whether hyperphages offered more efficient phage recovery. Hyperphages are a specialized type of helper phage capable of displaying multiple scFv antibodies; up to five on each phage particle, thereby enhancing the overall avidity of the phage for its target (*Hyperphage n.d).* Hyperphages only expresses the phenotype of pIII to be able to infect *E.coli,* however it lacks a functional pIII gene required during phage assembly so that only the scFv-pIII protein is available for assembly into phages. Due to these factors a research study conducted by Rondot et al. 2001 found that antigen binding activity increased by 400-fold compared to normal helper phages. Figures 3.14 and 3.15 shows that the results obtained from this research study is concordant to literature as even though 1:100 dilution of clones was mistakenly done during analysis of monoclones against both VISTA and SARS-COV-2, majority of clones assembled by hyperphages produced a statistically significant stronger binding to VISTA than SARS-COV-2. In comparison, only 2 clones out of 60 that were assembled using helper phages produced a significantly stronger binding to VISTA than SARS-COV-2. Due to this remarkable difference, further binding analysis was assessed using only those clones assembled by hyperphages. Analysis of undiluted monoclones against VISTA, SARS COV- 2 and PD-L1 showed that these clones had a strong binding affinity towards VISTA and weak binding towards SARS-COV-2 and PD-L1 baits. Clones 31, 33, 35, 39 and 46 were excluded from statistical analysis as they had a very low binding result towards VISTA.

Sanger sequencing was then done with the remaining volume of the 60 monoclones to assess the protein sequence, from which the frameworks and CDRs were labelled. The length range of frameworks and CDRs were previously determined by Lisowska et al. 2025

using next generation long-read DNA sequencing on an aliquot of the scFv library. The sequences obtained were compared to a reference sequence with defined framework and CDR regions from the international ImMunoGeneTics information system® (IMGT®) database.

Each light and heavy chain consists of four framework regions and three CDRs. The framework regions form the structural scaffold of the scFv and are therefore expected to exhibit minimal variation (Birshtein, 2016). These regions are primarily composed of β-sheets, which provide stability and support to the CDRs. The CDRs, which are hypervariable loop structures, form the antigen-binding site and are critical for antigen specificity and affinity (Birshtein 2016, Mak & Saunders 2006). The CDR regions of the light chain are randomly assembled by the V and J genes whereas the CDR regions of the heavy chain are randomly assembled by the V,D,J genes (Dondelinger et al. 2018). The CDR3 of the heavy chain is shown to be the most diverse region as other than random assembly there are also nucleotide additions and losses between different segments (D' Angelo et al. 2018). From our library, it was estimated that $3.3x10^8$ unique FR3-CDR3 sequences were present in $1x10^9$heavy chain sequences (Lisowska et al. 2025) The CDR3 of the heavy chain can also exhibit conformational flexibility to be able to configure to bind with different targets (D' Angelo et al. 2018) and most of this region has been shown to form part of the specificity-determining residues which are the residues that make direct contact with the antigen (Padlan et al.1995).

Sanger sequencing results for the initial 30 clones revealed that only the heavy chain region was successfully sequenced, with full-length sequence obtained in just one clone (clone 10). Incomplete sequencing can arise from several factors, including the formation of secondary structures. Regions rich in G-C or A-T content can form stable hydrogen bonds,

resulting in hairpin structures that impede the sequencing process. Additionally, internal restriction enzyme sites may lead to partial digestion, yielding incomplete sequence reads. Repetitive sequences may also cause DNA polymerase slippage, further affecting sequencing accuracy (Sanger Sequencing Troubleshooting Guide, n.d.).

In contrast, clones 31‑60 yielded complete full-length sequences. Analysis of these sequences revealed that the majority of clones were identical, with sequence variation observed only in clones 9, 10, 37, 40, 42, 53, and 60, specifically within their complementarity-determining regions (CDRs). Notably, only clones 10 and 37 exhibited variation in the CDR3 of the heavy chain (CDR3-VH), suggesting that clonal overamplification occurred during biopanning. Dendrogram analysis further indicated greater sequence diversity in the CDR3 of the light chain (CDR3-VL) compared to the heavy chain, as additional variations were observed in clones 9, 34, 40, 42, 53, and 60. This finding contrasts literature findings where CDR3-VH typically exhibits higher diversity than CDR3-VL.

The overrepresentation of a single clone during phage display often results from a propagation advantage, whereby certain clones replicate more efficiently in *E.coli* due to higher infectivity and faster growth rates compared to others (Bakhshinejad et al., 2016). These clones do not necessarily exhibit high affinity or specificity for the target antigen. Instead, their abundance in the enriched phage pool arises from replication efficiency rather than selective binding, leading to an amplification-induced bias. As a consequence, slow-growing clones, including those with high affinity or unique epitope specificity, may be outcompeted and lost during amplification, ultimately reducing the diversity of the phage library (Matochko et al., 2013). This bias can occur due to the scFv sequence interfering with proper phage assembly, impairing replication (Thomas et al., 2011). In other instances,

mutations that enhance replication confer a biological advantage. For example, Brammer et al. (2008) identified a mutation in the M13 phage's gIIp regulatory protein that increased replication efficiency and led to clone overamplification. Since the amplified phage pool from each round is used as the input for subsequent biopanning cycles, clones with superior propagation rates accumulate disproportionately over time. With each round of amplification, these fast-replicating but potentially non-specific clones can outcompete high-affinity binders, especially as the number of rounds increases. This underscores a critical limitation; although amplification is essential to the success of phage display, excessive rounds may ultimately favour the selection of target-unrelated phages and result in the loss of genuinely high-affinity clones (Bakhshinejad et al., 2016).

Although, the majority of clones sequenced in this project were the same, as can be observed in figure 3.16, most clones tested had a strong binding affinity to VISTA and weak binding to other bait proteins showing that even though there was an amplification induced bias, the overamplified clone still had a strong binding affinity to the target. However, this ELISA result produced inconsistent results between binding of the same sequence clone with the target bait for example clones 31, 33, 35 and 48 which are considered to be weak binders have the same sequence as clones 44, 46, 50, 51, 55, 57 and 59 which are strong binders to VISTA. This inconsistent result can be attributed to various factors affecting ELISA. One of these factors includes antigen presentation on the plate which varies from one well to the other due to inconsistent coating, random orientation and conformational changes of the bait that may mask the epitope that binds to the clone (Alhajj et al. 2023). Another factor to consider was the concentration of the phage clone present following candidate phage clone preparation. The phage pellet produced following candidate phage clone preparation greatly varied from one clone to the other due to loss of phages during

centrifugation and transferring steps. Thus, the concentration of each candidate phage clone added to the ELISA with bait proteins greatly varied from one clone to another which would affect the fluorescent result produced. Since direct ELISA technique has a low sensitivity as there is no signal amplification of the bound phage, the antibody concentration of the weak binders may have been too low to be detected (Aydin et al. 2025, Mason 2021). The differences in the signal produced could also have been affected by bubbles in the wells, inconsistent pipetting, washing, or non homogenous reagents (*Surmodics* n.d).

To prevent the library from becoming devoid of high affinity binders and binders to different epitopes, it would have been ideal to identify strong binders from round 3 phage pools.

Using the SWISS-MODEL, a simulation of the 3D structure of the strongest and weakest binder was generated. This web-based program employs homology modelling by aligning the clone sequence with a template sequence that displays the highest sequence identity, as identified through BLAST and HHblits searches (Waterhouse et al. 2018). Predicting the 3D structure of these proteins provides a deep understanding of their molecular function and how they can form protein complexes. Furthermore, the use of homology modelling web server is an inexpensive and rapid technique to predict the protein structure in comparison to experimentally identifying the 3D structure by X-ray crystallography or nuclear magnetic resonance.

Limitation of the study

During this project, several limitations were encountered, with non-specific binding of phages representing a significant challenge. As previously discussed, the use of poly-histidine tags led to suboptimal target immobilization and non-specific interactions between phages and the cobalt magnetic beads. In contrast, baits fused with an Fc domain

proved more effective, as these issues were not observed when using Fc-tagged constructs. Therefore, Fc fusion proteins are recommended for future experiments to enhance binding specificity and reliability. Another limitation was the absence of a bead-only control during ELISA analysis of phage pool binding affinities. Including such control would have allowed for the identification of phages that bind non-specifically to the beads rather than the bait proteins.

The lack of a negative selection step in the biopanning process further contributed to non-specific binding. Negative selection involves pre-incubating phages with blocked beads (without bait proteins) that have undergone the same blocking and washing conditions. This step removes phages that bind to components other than the bait, enriching for specific binders. The inclusion of negative selection helps minimize false positives and enhances the specificity of phage-bait interactions (Ph.D. Phage Display Libraries, n.d.; McLaughlin, 2024).

The use of triethylamine (TEA) at pH 11 as an elution buffer represents another limitation in this study. While TEA is an effective non-specific elution agent capable of releasing even strong binders from the target, its high alkalinity poses a risk. If phages are not promptly neutralized following TEA incubation, the elevated pH can denature both the phage particles and the scFv proteins, potentially compromising their structural integrity and binding affinity. Moreover, the high pH environment of TEA elution may preferentially elute binders with a net negative charge. This is supported by data in Table 3.2, which show that all but one of the isolated clones possess a low isoelectric point (pI ≈ 4.66). At pH 11, these scFv proteins would carry a net negative charge, favouring their elution. Conversely, positively charged binders may have been underrepresented due to inefficient elution under these conditions, which might have affected the overall diversity of the phage library

(Thota et al., 2024). Given these drawbacks, more selective elution strategies that do not rely on extreme pH shifts are gaining preference such as trypsin elution. For trypsin elution to be possible, a trypsin cleavage site is present between the scFv protein and the pIII protein of the phage. During trypsin elution, this site is cleaved, releasing only those phages whose scFv domains are actively bound to the target (Ledsgaard et al., 2018). A comparative study by Zadeh et al. (2019) evaluated three elution techniques: TEA at pH 10, glycine-HCl at pH 2.2, and trypsin. The findings revealed that performing trypsin elution twice per panning round increased phage titres by 50-fold, demonstrating its superior efficiency.

During this project, the use of M13KO7 phages may have favoured the replication of wild type phages reducing amplification of scFv-pIII fused phages. The use of CM13K helper phages designed specifically for phage display offers further advantages over conventional M13KO7 phages. CM13K phages include a trypsin-sensitive linker between the wild-type pIII gene and the N2 domain. Upon trypsin treatment, this linker is cleaved, effectively removing phages displaying wild type pIII. This ensures that only phages presenting the scFv-pIII fusion survive and are amplified, enriching the pool for specific binders (CM13K Trypsin-Sensitive Helper Phage, n.d.).

Due to time constraints and limited resources, it was difficult to successfully troubleshoot biopanning phage display against PD-L1. In this project there was not enough time to validate the procedure for retrieval of phage clones from the glycerol stocks thus there was limited volume of phage clones that could be used for binding analysis and to send for Sanger sequencing.

The amplification bias is another limitation encountered in this project, as phage binding was not only dependent on target specificity but also by the replication efficiency of each

phage within *E.coli.* This results in overrepresentation of the same clone with reduced diversity, non-specific binders and strong binders may have been lost. There are various strategies to mitigate amplification bias such as performing stringent washing steps to ensure that any non-binders or weak binders are washed off prior to amplification. Reducing the number of amplification rounds to avoid the enrichment of phage clones which have a fast replication rate. The use of the T7 phage library instead of M13 library. The T7 library reduces amplification bias as this library has an efficient packaging system and following phage assembly, mature phages are released by cell lysis unlike M13 phages which require the displayed proteins to be secreted through the membrane of *E.coli* thus are constrained by the host secretory mechanism. The T7 library also has a fast replication rate where a plaque takes around 3 hours to form (Rosenberg et al. 1996 & Tan et al. 2016). Another promising approach is emulsion-based amplification, where individual phages are co-encapsulated with host cells in microdroplets. Each droplet acts as an isolated growth chamber, enabling uniform amplification and reducing competition among clones. However, the effectiveness of this technique depends heavily on achieving consistent droplet size. While highly effective, emulsion-based amplification is technically demanding and labour-intensive (Matochko et al., 2012).

Since ELISA technique was used to determine the success of biopanning phage display, several limitations were present mainly due to the way the target was immobilised on the plate which may have been due to differences in antigen presentation, low sensitivity and its inability to identify functional binders which are those scFv that when bound to the target would affect its biological activity (Hoogenboom 2005).

The use of Sanger sequencing to identify the clone sequences is very labour intensive and

has a very low throughput as only 60 clones were sequenced out of which only 31 clones had the full sequence. These 60 clones were picked from a phage pool that may potentially contain millions of clones thus stronger binding clones which are highly specific to our target that were present in low quantities were easily missed. Preferably next-generation sequencing (NGS) is utilized as it able to assess the full sequence of millions of diverse clones that bind to different epitopes of the target (Kohl et al. 2025) For example, the use of Illumina deep sequencing technology allows for 10^7 reads which would allow more sequence coverage of the enriched pool to identify diverse clones (Matochko et al. 2012).

Further work

Further validation of the scFv phage monoclones can be performed by assessing their binding towards antigens present on cells. Analysis by flow cytometry of purified clones binding to cell lines natively expressing VISTA can be done to determine if these phage clones can bind to antigens in their specific conformational state on the cell surface (Alfaleh et al. 2017). Affinity measurements can be done using biolayer interferometry (BLI) analysis to accurately measure the binding association and dissociation between the antigen and antibody (Dong et al. 2020). The phage clone with the ideal binding can be engineered to produce a full monoclonal antibody by introducing the scFv in a vector containing the constant region which can then transfect mammalian cell lines to produce full antibody proteins (Jones et al. 2010). These antibodies can also be humanized by using the constant region of a human antibody and incorporating CDR grafting where the CDRs of the scFv are grafted onto a human antibody framework however performing CDR grafting may affect the functionality and affinity of the antibody (Kerry 2024).

Bioinformatic tools offer valuable insights into the predicted interaction between scFv clones and the bait protein. For instance, paratope prediction tools can be used to identify

the specific residues on the scFv that are likely to interact with the antigen. Additionally, computational methods for predicting binding affinity and dissociation constants allow for the estimation of how strongly the scFv binds to the bait based on their intermolecular interactions. To further investigate structural compatibility, docking simulations can be conducted using web-based platforms. These tools allow for the generation of 3D models of scFv-antigen complexes, using the most accurate homology models available for both the scFv binder and the VISTA protein. Docking can also provide epitope predictions and can help to identify the specific region on VISTA that the scFv is likely targeting (Chorpunkul et al., 2024). An attempt was made to model the interaction of the scFv clone with the highest affinity. The scFv structure was obtained from SWISS-MODEL, while the extracellular domain of VISTA was sourced from the AlphaFold Protein Structure Database. However, as shown in Figure 6.4 of the Appendix, the docking simulation using HADDOCK 2.4 produced a positive HADDOCK score, indicating an unfavourable interaction between the two proteins (HADDOCK2.4 Scoring Function, n.d.). This result may be attributed to the lack of pre-processing of the PDB files prior to submission to HADDOCK. Specifically, extra structural data generated by SWISS-MODEL that can interfere with docking simulations was not removed, potentially skewing the results (Antibody-Antigen Modelling Tutorial Using a Local Version of HADDOCK3, n.d.).

Computer modeling and artificial intelligence (AI) can be utilised to predict various aspects of antibody behaviour in the human body, including pharmacokinetics, potential adverse events, and overall clinical outcome. These technologies enable simulation of antibody distribution, metabolism, and interaction with biological targets, helping to inform early-stage decision-making in therapeutic development. In addition to in silico approaches, advanced in vitro human-derived systems such as organoids and organ-on-chip platforms

offer powerful tools for evaluating antibody safety and efficacy. These engineered systems replicate the architecture and function of native human tissues, allowing for the assessment of immune-mediated adverse effects, tissue-specific toxicity, and therapeutic response in a more physiologically relevant context. Compared to traditional animal models, these human-based systems provide a more accurate prediction of clinical outcome. Animal studies often fail to reliably predict human responses due to significant physiological differences between species. Thus, integrating these cutting-edge technologies into testing may enhance translational accuracy and reduce reliance on animal testing (Roadmap to Reducing Animal Testing in Preclinical Safety Studies, n.d.).

Conclusion

In conclusion, scFv antibodies targeting immune checkpoints hold significant promise for advancing cancer immunotherapy. While this study initially aimed to develop novel anti-PD-L1 scFv antibodies, various challenges encountered during the biopanning process prevented their successful isolation. As a result, the focus of the study was redirected toward the generation of 60 monoclonal scFvs targeting the VISTA immune checkpoint. Monoclonal antibodies against VISTA were successfully produced, with the majority demonstrating strong binding affinity to VISTA and minimal cross-reactivity with control proteins. Full sequencing was completed for approximately half of the clones. Among these, many were found to share identical sequences, indicating a degree of amplification bias during the biopanning process. Further investigations are necessary to validate the functional activity of the scFv binders both in vitro and *in vivo*. Additionally, improvements to the biopanning methodology are essential, to enhance target-specific library generation and minimize amplification bias.

Chapter 5:

References

2022, Dec 28,. NCI clinical trial leads to atezolizumab approval for advanced alveolar soft part sarcoma. *Contify Life Science News*.

260/280 and 260/230 Ratios 2009-last update. Available: https://dna.uga.edu/wp-content/uploads/sites/51/2019/02/Note-on-the-260_280-and-260_230-Ratios.pdf [20th October, 2024].

AHMAD, Z.A., YEAP, S.K., ALI, A.M., HO, W.Y., ALITHEEN, N.B.M. and HAMID, M., 2012. scFv Antibody: Principles and Clinical Application. *Clinical and Developmental Immunology,* 2012, pp. 1.

AHMADZADEH, M., JOHNSON, L.A., HEEMSKERK, B., WUNDERLICH, J.R., DUDLEY, M.E., WHITE, D.E. and ROSENBERG, S.A., 2009. Tumor antigen–specific CD8 T cells infiltrating the tumor express high levels of PD-1 and are functionally impaired. *Blood,* **114**(8), pp. 1537-1544.

AI, L., CHEN, J., YAN, H., HE, Q., LUO, P., XU, Z. and YANG, X., 2020. Research Status and Outlook of PD-1/PD-L1 Inhibitors for Cancer Therapy. *Drug design, development and therapy,* **14**, pp. 3625-3649.

AKINLEYE, A. and RASOOL, Z., 2019. Immune checkpoint inhibitors of PD-L1 as cancer therapeutics. *Journal of Hematology & Oncology,* **12**(1), pp. 92.

ALFALEH, M.A., ALSAAB, H.O., MAHMOUD, A.B., ALKAYYAL, A.A., JONES, M.L., MAHLER, S.M. and HASHEM, A.M., 2020. Phage Display Derived Monoclonal Antibodies: From Bench to Bedside. *Frontiers in Immunology,* **11**.

ALFALEH, M.A., JONES, M.L., HOWARD, C.B. and MAHLER, S.M., 2017b. Strategies for Selecting Membrane Protein-Specific Antibodies using Phage Display with Cell-Based Panning. *Antibodies,* **6**(3),.

ALHAJJ, M., ZUBAI, FARHANA, AISHA, 2023. Enzyme Linked Immunosorbent Assay. *StatPearl,*.

ALTSCHUL, S.F., GISH, W., MILLER, W., MEYERS, E.W. and LIPMAN, D.J., 1990. Basic Local Alignment Search Tool. *Journal of molecular biology,* **215**(3), pp. 403-410.

ANDERSON, A., JOLLER, N. and KUCHROO, V., 2016. Lag-3, Tim-3, and TIGIT: Co-inhibitory Receptors with Specialized Functions in Immune Regulation. *Immunity,* **44**(5), pp. 989-1004.

Antibody-antigen modelling tutorial using a local version of HADDOCK3. Available: https://www.bonvinlab.org/education/HADDOCK3/HADDOCK3-antibody-antigen/ [5th March, 2025].

ARAS, S. and ZAIDI, M.R., 2017. TAMeless traitors: macrophages in cancer progression and metastasis. *British Journal of Cancer,* **117**(11), pp. 1583-1591.

ARDIZZONI, A., AZEVEDO, S., RUBIO-VIQUEIRA, B., RODRIGUEZ-ABREU, D., ALATORRE-ALEXANDER, J., SMIT, H.J.M., YU, J., SYRIGOS, K., HÖGLANDER, E., KAUL, M., TOLSON, J., HU, Y., VOLLAN, H.K. and NEWSOM-DAVIS, T., 2022. Final results from TAIL: updated long-term efficacy of atezolizumab in a diverse population of patients with previously treated advanced non-small cell lung cancer. *Journal for immunotherapy of cancer,* **10**(11), pp. e005581.

ARIPOV, V.S., VOLKOVA, N.V., ILYICHEV, A.A. and SHCHERBAKOV, D.N., 2024a. Problems of creating antibody phage libraries and their solutions. *Vavilov Journal of Genetics and Breeding,* **28**(2), pp. 249-257.

ASIF, P.J., LONGOBARDI, C., HAHNE, M. and MEDEMA, J.P., 2021. The role of cancer-associated fibroblasts in cancer invasion and metastasis. *Cancers,* **13**(18), pp. 4720.

AVERBUCH, I., STOFF, R., MIODOVNIK, M., FENNIG, S., BAR-SELA, G., YAKOBSON, A., DALIOT, J., ASHER, N. and FENIG, E., 2023. Avelumab for the treatment of locally advanced or metastatic Merkel cell carcinoma-A multicenter real-world experience in Israel. *Cancer medicine (Malden, MA),* .

AYDIN, S., EMRE, E., UGUR, K., AYDIN, M.A., SAHIN, İ, CINAR, V. and AKBULUT, T., 2025. *An overview of ELISA: a review and update on best laboratory practices for quantifying peptides and proteins in biological fluids.* SAGE Publications.

BABAN, B., LIU, J.Y., QIN, X., WEINTRAUB, N.L. and MOZAFFARI, M.S., 2015. Upregulation of programmed death-1 and its ligand in cardiac injury models: Interaction with GADD153. *PLoS ONE,* **10**(4), pp. e0124059.

BAI, R., LV, Z., XU, D. and CUI, J., 2020. Predictive biomarkers for cancer immunotherapy with immune checkpoint inhibitors. *Biomarker research,* **8**(1), pp. 34.

BAKHSHINEJAD, B., ZADE, H.M., SHEKARABI, H.S.Z. and NEMAN, S., 2016a. Phage display biopanning and isolation of target-unrelated peptides: in search of nonspecific binders hidden in a combinatorial library. *Amino Acids,* **48**(12), pp. 2699–2716.

BANG, A. and SCHOENFELD, J.D., 2019. Immunotherapy and radiotherapy for metastatic cancers. *Annals of palliative medicine,* **8**(3), pp. 312-325.

BARBAS III, C.F., ROSENBLUM, J.S. and LERNER, R.A., 1993a. *Direct selection of antibodies that coordinate metals from semisynthetic combinatorial libraries (metalproptens/catalytic antibodies/surface expression/magnetite).*

BASHIR, S. and PAESHUYSE, J., 2020. Construction of Antibody Phage Libraries and Their Application in Veterinary Immunovirology. Antibodies, **9**(2),.

BATLLE, E. and MASSAGUÉ, J., 2019. Transforming Grown Factor-β Signalling in Immunity and Cancer. *Immunity (Cambridge, Mass.),* **50**(4), pp. 924-940.

BATEMAN, A., MARTIN, M., ORCHARD, S., MAGRANE, M., ADESINA, A., AHMAD, S., BOWLER-BARNETT, E.H., BYE-A-JEE, H., CARPENTIER, D., DENNY, P., FAN, J., GARMIRI, P., GONZALES, L.J.D.C., HUSSEIN, A., IGNATCHENKO, A., INSANA, G., ISHTIAQ, R., JOSHI, V., JYOTHI, D., KANDASAAMY, S., LOCK, A., LUCIANI, A., LUO, J., LUSSI, Y., MARIN, J.S.M., RAPOSO, P., RICE, D.L., SANTOS, R., SPERETTA, E., STEPHENSON, J., TOTOO, P., TYAGI, N., URAKOVA, N., VASUDEV, P., WARNER, K., WIJERATHNE, S., YU, C.W., ZARU, R., BRIDGE, A.J., AIMO, L., ARGOUD-PUY, G., AUCHINCLOSS, A.H., AXELSEN, K.B., BANSAL, P., BARATIN, D., BATISTA NETO, T.M., BLATTER, M., BOLLEMAN, J.T., BOUTET, E., BREUZA, L., GIL, B.C., CASALS-CASAS, C., ECHIOUKH, K.C., COUDERT, E., CUCHE, B., DE CASTRO, E., ESTREICHER, A., FAMIGLIETTI, M.L., FEUERMANN, M., GASTEIGER, E., GAUDET, P., GEHANT, S., GERRITSEN, V., GOS, A., GRUAZ, N., HULO, C., HYKA-NOUSPIKEL, N., JUNGO, F., KERHORNOU, A., MERCIER, P.L., LIEBERHERR, D., MASSON, P., MORGAT, A., PAESANO, S., PEDRUZZI, I., PILBOUT, S., POURCEL, L., POUX, S., POZZATO, M., PRUESS, M., REDASCHI, N., RIVOIRE, C., SIGRIST, C.J.A., SONESSON, K., SUNDARAM, S., SVESHNIKOVA, A., WU, C.H., ARIGHI, C.N., CHEN, C., CHEN, Y., HUANG, H., LAIHO, K., LEHVASLAIHO, M., MCGARVEY, P., NATALE, D.A., ROSS, K., VINAYAKA, C.R., WANG, Y. and ZHANG, J., 2024. UniProt: the Universal Protein Knowledgebase in 2025. *Nucleic Acids Research,* **53**(D1), pp. D609.

BAZAN, J., CAŁKOSIŃSKI, I. and GAMIAN, A., 2012. Phage display-A powerful technique for immunotherapy. *Human vaccines & immunotherapeutics,* **8**(12), pp. 1817-1828.

BELLONE, M., CALCINOTTO, A., FILIPAZZI, P., DE MILITO, A., FAIS, S. and RIVOLTINI, L., 2013. The acidity of the tumor microenvironment is a mechanism of immune escape that can be overcome by proton pump inhibitors. *Oncoimmunology,* **2**(1), pp. 22-21.

BENJAMINI, B, Y., and KRIEGER, A.M., Adaptive linear step-up procedures that control the false discovery rate. *Biometrika,* **93**(3), pp. 491–507.

BENEFIELD, J., PETRUZZELLI, G.J., FOWLER, S., TAITZ, A., KALKANIS, J. and YOUNG, M.R., 1996. Regulation of the steps of angiogenesis by human head and neck squamous cell carcinomas. *Invasion and metastasis,* **16**(6), pp. 291-301.

BERTONI, M., KIEFER, F., BIASINI, M., BORDOLI, L. and SCHWEDE, T., 2017. Modeling protein quaternary structure of homo- and hetero-oligomers beyond binary interactions by homology. *Scientific Reports,* **7**(1),.

BIENERT, S., WATERHOUSE, A., DE BEER, T.A.P., TAURIELLO, G., STUDER, G., BORDOLI, L. and SCHWEDE, T., 2016. *The SWISS-MODEL Repository—new features and functionality.* Oxford University Press (OUP).

BINBAY, F.A., RATHOD, D.C., GEORGE, A.A.P. and IMHOF, D., 2023. Quality Assessment of Selected Protein Structures Derived from Homology Modeling and AlphaFold. *Pharmaceuticals,* **16**(12),.

BLACKBURN, S.D., SHIN, H., FREEMAN, G.J. and WHERRY, E.J., 2008b. Selective expansion of a subset of exhausted CD8 T cells by αPD-L1 blockade. *Proceedings of the National Academy of Sciences - PNAS,* **105**(39), pp. 15016-15021.

BLANKENSTEIN, T. and WILLIMSKY, G., 2005. Sporadic immunogenic tumours avoid destruction by inducing T-cell tolerance. *Nature,* **437**(7055), pp. 141-146.

BÖGER, C., BEHRENS, H., KRÜGER, S. and RÖCKEN, C., 2017. The novel negative checkpoint regulator VISTA is expressed in gastric carcinoma and associated with PD-L1/PD-1: A future perspective for a combined gastric cancer therapy? *Oncoimmunology,* **6**(4), pp. e1293215.

BORNHORST, J.A. and FALKE, J.J., 2010. *[16] Purification of Proteins Using Polyhistidine Affinity Tags.*

BOSTRÖM, T., NILVEBRANT, J., HOBER, S., 2012. Purification Systems Based on Bacterial Surface Proteins. In: R. AHMAD, ed, *Protein Purification.* Royal Institute of Technology, Stockholm, Sweden: Intechopen, pp. 89–118.

BOUSSIOTIS, V.A., TZACHANIS, D., FREEMAN, G.J., HIRANO, N., VAN PUIJENBROEK, A.A.F.L., DELFS, M.W., BEREZOVSKAYA, A. and NADLER, L.M., 2001. Tob is a negative regulator of activation that is expressed in anergic and quiescent T cells. *Nature immunology,* **2**(12), pp. 1174-1182.

BOYERO, L., SANCHEZ-GASTALDO, A., ALONSO, M., NOGUERO-UCLES, J.F., MOLINA-PINELO, S. and BERNABE-CARO, R., 2020. Primary and Acquired Resistance to Immunotherapy in lung cancer. *Cancer,* **12**(3279), pp. 1-36.

BRAMMER, L.A., BOLDUC, B., KASS, J.L., FELICE, K.M., NOREN, C.J. and HALL, M.F., 2007. A target-unrelated peptide in an M13 phage display library traced to an advantageous mutation in the gene II ribosome-binding site. *Analytical Biochemistry,* **373**(1), pp. 88.

BRODERS, O., BREITLING, F. and DÜBEL, S., b. Improving Antibody Presentation in Phage Display.

BROZ, M., BINNEWIES, M., BOLDAJIPOUR, B., NELSON, A., POLLACK, J., ERLE, D., BARCZAK, A., ROSENBLUM, M., DAUD, A., BARBER, D., AMIGORENA, S., VAN'T VEER, L., SPERLING, A., WOLF, D. and KRUMMEL, M., 2014. Dissecting the Tumor Myeloid Compartment Reveals Rare Activating Antigen-Presenting Cells Critical for T Cell Immunity. *Cancer Cell,* **26**(5), pp. 638-652.

BYRNE, E.H. and FISHER, D.E., 2017. *Correlates of metastatic melanoma response to checkpoint inhibition.*

CALCINOTTO, A., FILIPAZZI, P., HUBER, V., PARMIANI, G., GENEROSO, L., SANTINAMI, M., BORGHI, M., FAIS, S., BELLONE, M., RIVOLTINI, L., GRIONI, M., LERO, M., DE MILITO, A., RICUPITO, A., COVA, A., CANESE, R., JACHETTI, E. and ROSSETTI, M., 2012. Modulation of Microenvironment Acidity Reverses Anergy in Human and Murine Tumor-Infiltrating T Lymphocytes. *Cancer research (Chicago, Ill.),* **72**(11), pp. 2746-2756.

CASTELLI, M.S., MCGONIGLE, P. and HORNBY, P.J., 2019. The pharmacology and therapeutic applications of monoclonal antibodies. Wiley.

CATON, A.J., JORDAN, M.S., BOESTEANU, A., REED, A.J., PETRONE, A.L., HOLENBECK, A.E., LERMAN, M.A. and NAJI, A., 2001. Thymic selection of CD4 + CD25 + regulatory T cells induced by an agonist self-peptide. *Nature immunology,* **2**(4), pp. 301-306.

CD274 molecule [Homo sapiens (human)] 2025-last update. Available: https://www.ncbi.nlm.nih.gov/gene/29126 [5th December, 2025].

ČEMERSKI, S. and SHAW, A., 2006. Immune synapses in T-cell activation. *Current Opinion in Immunology,* **18**(3), pp. 298-304.

CHANG, R.B. and BEATTY, G.L., 2020a. The interplay between innate and adaptive immunity in cancer shapes the productivity of cancer immunosurveillance. *Journal of leukocyte biology,* **108**(1), pp. 363-376.

CHEN, J. and WU, Y., 2018. Understanding the Functional Roles of Multiple Extracellular Domains in Cell Adhesion Molecules with a Coarse-Grained Model. *Journal of Molecular Biology,* **429**(7), pp. 1081.

CHEN, L. and FLIES, D.B., 2013. Molecular mechanisms of T cell co-stimulation and co-inhibition. *Nature reviews. Immunology,* **13**(4), pp. 227-242.

CHEN, L., DONG, H., STROME, S.E., SALOMAO, D.R., TAMURA, H., HIRANO, F., FLIES, D.B., ROCHE, P.C., LU, J., ZHU, G., TAMADA, K., LENNON, V.A. and CELIS, E., 2002. Tumor-associated B7-H1 promotes T-cell apoptosis: A potential mechanism of immune evasion. *Nature medicine,* **8**(8), pp. 793-800.

CHEN, L., HARRISON, S.C., GLOVER, J.N.M., HOGAN, P.G. and RAO, A., 1998. Structure of the DNA-binding domains from NFAT, Fos and Jun bound specifically to DNA. *Nature (London),* **392**(6671), pp. 42-48.

CHEN, V.B., ARENDALL, W.B., HEADD, J.J., KEEDY, D.A., IMMORMINO, R.M., KAPRAL, G.J., MURRAY, L.W., RICHARDSON, J.S. and RICHARDSON, D.C., 2009. MolProbity: all-atom structure validation for macromolecular crystallography. *Acta Crystallographica Section D Biological Crystallography,* **66**(1), pp. 12.

CHEN, W., JIN, W., HARDEGEN, N., LEI, K., LI, L., MARINOS, N., MCGRADY, G. and WAHL, S.M., 2003. Conversion of peripheral CD4+CD25- naive T cells to CD4+CD25+ regulatory T cells by TGF-beta induction of transcription factor Foxp3. *The Journal of Experimental Medicine,* **198**(12), pp. 1875-1886.

CHEN, X., ZARO, J.L. and SHEN, W., 2014. *Fusion protein linkers: Property, design and functionality.* Elsevier BV.

CHEN, Z., ZHAO, S., WANG, Z., QIU, B., LI, B., ZHOU, F., TAN, X. and HE, J., 2011. Expression and unique functions of four nuclear factor of activated T cells isoforms in non-small cell lung cancer. *Ai zheng,* **30**(1), pp. 62-68.

CHIRCOP, F., 2025. *Exploring SARS-CoV-2 Antibody Data through Machine Learning Methods.* Unpublished research (M.Sc Data Science Dissertation), University of Malta.

CHOI, J. and LEE, S.Y., 2020. Clinical Characteristics and Treatment of Immune-Related Adverse Events of Immune Checkpoint Inhibitors. *Immune Network,* **20**(1), pp. e9.

CLARK, C.A., GUPTA, H.B., SAREDDY, G., PANDESWARA, S., LAO, S., YUAN, B., RUP, J.M., PAON, A., CONEJO-GARCIA, J., MURTHY, K., LIU, Y., TURK, M.J., THEDIECK, K., HUREZ, V., LI, R., VADLAMUDI, R. and CURIEL, T.J., 2016. Tumor-intrinsic PD-L1 signals regulate cell growth, pathogenesis and autophagy in ovarian cancer and melanoma. *Cancer research (Chicago, Ill.),* **76**(23), pp. 6964-6974.

CLAYDEN, J., GREEVES, N., WARREN, S., 2001. *Organic Chemistry.* New York, USA: Oxford University Press (OUP).

CM13K Trypsin-Sensitive Helper Phage. Available: https://www.abdesignlabs.com/store/index.php?dispatch=products.view&product_id=29817 [2nd March, 2025].

Comprehensive molecular profiling of lung adenocarcinoma. 2014. *Nature,* **511**(7511), pp. 543-550.

COOPER, G.M., 2000. *The cell.* 2nd edition. New York ; Oxford: Sinauer Associates, Oxford University Press.

CORREIA, D.V., LOPES, A.C. and SILVA-SANTOS, B., 2013b. Tumor cell recognition by γδ T lymphocytes. *Oncoimmunology,* **2**(1), pp. e22892.

CORZO, C.A., CONDAMINE, T., LU, L., COTTER, M.J., YOUN, J., CHENG, P., CHO, H., CELIS, E., QUICENO, D.G., PADHYA, T., MCCAFFREY, T.V., MCCAFFREY, J.C. and GABRILOVICH, D.I., 2010. HIF-1α regulates function and differentiation of myeloid-derived suppressor cells in the tumor microenvironment. *The Journal of Experimental Medicine,* **207**(11), pp. 2439-2453.

Coté, R.J. Aseptic Technique for Cell Culture. Current Protocols in Cell Biology. Chapter 1, Unit 1.3 (2001)COUSSENS, L.M. and WERB, Z., 2010. Inflammation and cancer. *Nature,* 420(6917), pp. 860-867.

CRESPO, J., SUN, H., WELLING, T.H., TIAN, Z. and ZOU, W., 2013. T cell anergy, exhaustion, senescence, and stemness in the tumor microenvironment. *Current opinion in immunology,* **25**(2), pp. 214-221.

D'ANGELO, S., FERRARA, F., NARANJO, L., ERASMUS, M.F., HRABER, P. and BRADBURY, A.R.M., 2018. Many Routes to an Antibody Heavy-Chain CDR3: Necessary, Yet Insufficient, for Specific Binding. *Frontiers in Immunology,* 9.

DAHLIN, A.M., HENRIKSSON, M.L., VAN GUELPEN, B., STENLING, R., OBERG, A., RUTEGÅRD, J. and PALMQVIST, R., 2011. Colorectal cancer prognosis depends on T-cell infiltration and molecular characteristics of the tumor. *Modern pathology,* **24**(5), pp. 671-682.

DAVIS, J., SMYTH, M. and TRAPANI, J., 2001. Granzyme A and B-deficient killer lymphocytes are defective in eliciting DNA fragmentation but retain potent in vivo anti-tumor capacity. *European journal of immunology,* **31**(1), pp. 39-47.

DAVIS, Z.B., VALLERA, D.A., MILLER, J.S. and FELICES, M., 2017. Natural killer cells unleashed: Checkpoint receptor blockade and BiKE/TriKE utilization in NK-mediated anti-tumor immunotherapy. *Seminars in immunology,* 31, pp. 64-75.

DE VISSER, K.E., KORETS, L.V. and COUSSENS, L.M., 2005. De novo carcinogenesis promoted by chronic inflammation is B lymphocyte dependent. *Cancer Cell,* **7**(5), pp. 411-423.

DENNIS, K., BLATNER, N., GOUNARI, F. and KHAZAIE, K., 2013. Current status of interleukin-10 and regulatory T-cells in cancer. *Current opinion in oncology,* **25**(6), pp. 637-645.

DI PIETRO,F.,2020. *The Development of Monoclonal Antibodies to IFITM1 Protein Using scFv-phage Display Libraries.*

DIVISION OF CANCER PREVENTION AND CONTROL, CENTERS FOR DISEASE CONTROL AND PREVENTION, 2019-last update, Melanoma Incidence and Mortality, United States–2012–2016. Available: https://www.cdc.gov/nccdphp/divisions-offices/about-the-division-of-cancer-prevention-and-control.html [1st of May, 2023].

DONDELINGER, M., FILÉE, P., SAUVAGE, E., QUINTING, B., MUYLDERMANS, S., GALLENI, M. and VANDEVENNE, M.S., 2018. Understanding the Significance and Implications of Antibody Numbering and Antigen-Binding Surface/Residue Definition. *Frontiers in Immunology,* **9**.

DONG, Y., MENG, F., WANG, Z., YU, T., CHEN, A., XU, S., WANG, J., YIN, M., TANG, L., HU, C., WANG, H. and CAI, J., 2020a. Construction and application of a human scFv phage display library based on Cre-LoxP recombination for anti-PCSK9 antibody selection. *International Journal of Molecular Medicine,* **47**(2), pp. 708.

Dotmatics (2012). *SnapGene* (Version 8.0.1) [software]. Available at: https://www.snapgene.com/ (Accessed: 7 October 2024).

ELTANBOULY, M.A., ZHAO, Y., NOWAK, E., LI, J., SCHAAFSMA, E., LE MERCIER, I., CEERAZ, S., LINES, J.L., PENG, C., CARRIERE, C., HUANG, X., DAY, M., KOEHN, B., LEE, S.W., SILVA MORALES, M., HOGQUIST, K.A., JAMESON, S.C., MUELLER, D., ROTHSTEIN, J., BLAZAR, B.R., CHENG, C. and NOELLE, R.J., 2020. VISTA is a checkpoint regulator for naïve T cell quiescence and peripheral tolerance. *Science (American Association for the Advancement of Science),* 367(6475).

FACCIABENE, A., PENG, X., HAGEMANN, I.S., BALINT, K., BARCHETTI, A., WANG, L., GIMOTTY, P.A., GILKS, C.B., LAL, P., ZHANG, L. and COUKOS, G., 2011. Tumour hypoxia promotes tolerance and angiogenesis via CCL28 and T(reg) cells. *Nature (London),* **475**(7355), pp. 226-230.

FAHIE-WILSON, M. and HALSALL, D., 2008. Polyethylene glycol precipitation: proceed with

care. Annals of Clinical Biochemistry: International Journal of Laboratory Medicine, **45**(3), pp. 233.

FARES, C.M., VAN ALLEN, E.M., DRAKE, C.G., ALLISON, J.P. and HU-LIESKOVAN, S., 2019. Mechanisms of Resistance to Immune Checkpoint Blockade: Why Does Checkpoint Inhibitor Immunotherapy Not Work for All Patients? *American Society of Clinical Oncology educational book,* **39**(39), pp. 147-164.

FEARON, E.R. and VOGELSTEIN, B., 1990. *A genetic model for colorectal tumorigenesis.* Cambridge, MA: Elsevier Inc.

FEGAN, J.E., YU, R., ISLAM, E.A. and SCHRYVERS, A.B., 2022. Development of a non-biased, high-throughput ELISA for the rapid evaluation of immunogenicity and cross-reactivity. *Journal of Immunological Methods,* **493**.

FELLNER, C., 2012. Ipilimumab (yervoy) prolongs survival in advanced melanoma: serious side effects and a hefty price tag may limit its use. *P&T (Lawrenceville, N.J.),* **37**(9), pp. 503-530.

First-In-Human (FIH) Study of W0180 as Single Agent and in Combination With Pembrolizumab in Adults With Locally Advanced or Metastatic Solid Tumors. Available: https://clinicaltrials.gov/ct2/show/NCT04564417 [10th May, 2023].

FLIES, D.B., HIGUCHI, T. and CHEN, L., 2015. *Mechanistic Assessment of PD-1H Coinhibitory Receptor-Induced T-Cell Tolerance to Allogeneic Antigens1.*

FLIES, D.B., WANG, S., XU, H. and CHEN, L., 2011. Cutting Edge: A Monoclonal Antibody Specific for the Programmed Death-1 Homolog Prevents Graft-versus-Host Disease in Mouse Models. *The Journal of immunology (1950),* **187**(4), pp. 1537-1541.

FRANCISCO, L.M., SALINAS, V.H., BROWN, K.E., VANGURI, V.K., FREEMAN, G.J., KUCHROO, V.K. and SHARPE, A.H., 2009. PD-L1 regulates the development, maintenance, and function of induced regulatory T cells. *The Journal of Experimental Medicine,* **206**(13), pp. 3015-3029.

FREEMAN, G.J., LONG, A.J., IWAI, Y., BOURQUE, K., CHERNOVA, T., NISHIMURA, H., FITZ, L.J., MALENKOVICH, N., OKAZAKI, T., BYRNE, M.C., HORTON, H.F., FOUSER, L., CARTER, L., LING, V., BOWMAN, M.R., CARRENO, B.M., COLLINS, M., WOOD, C.R. and HONJO, T., 2000. Engagement of the Pd-1 Immunoinhibitory Receptor by a Novel B7 Family Member Leads to Negative Regulation of Lymphocyte Activation. *The Journal of Experimental Medicine,* **192**(7), pp. 1027-1034.

FREI, J.C. and LAI, J.R., 2017. Protein and Antibody Engineering by Phage Display. *Methods in Enzymology,* , pp. 45.

FUCHS, C.S., ÖZGÜROĞLU, M., BANG, Y., DI BARTOLOMEO, M., MANDALA, M., RYU, M., FORNARO, L., OLESINSKI, T., CAGLEVIC, C., CHUNG, H.C., MURO, K., VAN CUTSEM, E., ELME, A., THUSS-PATIENCE, P., CHAU, I., OHTSU, A., BHAGIA, P., WANG, A., SHIH, C. and SHITARA, K., 2022. Pembrolizumab versus paclitaxel for previously treated PD-L1-positive advanced gastric or gastroesophageal junction cancer: 2-year update of the randomized phase 3 KEYNOTE-061 trial. *Gastric cancer : official journal of the International Gastric Cancer*

Association and the Japanese Gastric Cancer Association, **25**(1), pp. 197-206.

FUJITA, Y., YAGISHITA, S., HAGIWARA, K., YOSHIOKA, Y., KOSAKA, N., TAKESHITA, F., FUJIWARA, T., TSUTA, K., NOKIHARA, H., TAMURA, T., ASAMURA, H., KAWAISHI, M., KUWANO, K. and OCHIYA, T., 2015. The Clinical Relevance of the miR-197/CKS1B/STAT3-mediated PD-L1 Network in Chemoresistant Non-small-cell Lung Cancer. *Molecular Therapy,* **23**(4), pp. 717-727.

GAJEWSKI, T.F., CORRALES, L., WILLIAMS, J., HORTON, B., SIVAN, A. and SPRANGER, S., 2017. Cancer immunotherapy targets based on understanding the t cell-inflamed versus non-T Cell-inflamed tumor microenvironment. *Advances in Experimental Medicine and Biology,* **1036**, pp. 19-31.

GALLI, F., AGUILERA, J.V., PALERMO, B., MARKOVIC, S.N., NISTICÒ, P. and SIGNORE, A., 2020. Relevance of immune cell and tumor microenvironment imaging in the new era of immunotherapy. *Journal of experimental & clinical cancer research,* **39**(1), pp. 89.

GALLUZZI, L., HUMEAU, J., BUQUE, A., ZITVOGEL, L. and KROEMER, G., 2020. Immunostimulation with chemotherapy in the era of immune checkpoint inhibitors. *Nature Reviews Clinical Oncology,* **17**, pp. 725-741.

GAO, G.F. and JAKOBSEN, B.K., 2000. *Molecular interactions of coreceptor CD8 and MHC class I: the molecular basis for functional coordination with the T-cell receptor.* England: Elsevier B.V.

GAO, J., WARD, J.F., PETTAWAY, C.A., SHI, L.Z., SUBUDHI, S.K., VENCE, L.M., ZHAO, H., CHEN, J., CHEN, H., EFSTATHIOU, E., TRONCOSO, P., ALLISON, J.P., LOGOTHETIS, C.J., WISTUBA, I.I., SEPULVEDA, M.A., SUN, J., WARGO, J., BLANDO, J. and SHARMA, P., 2017. VISTA is an inhibitory immune checkpoint that is increased after ipilimumab therapy in patients with prostate cancer. *Nature medicine,* **23**(5), pp. 551-555.

GARDNER, A. and RUFFELL, B., 2016. Dendritic Cells and Cancer Immunity. *Trends in immunology,* **37**(12), pp. 855-865.

GARON, E.B., HELLMANN, M.D., RIZVI, N.A., CARCERENY, E., LEIGHL, N.B., AHN, M., EDER, J.P., BALMANOUKIAN, A.S., AGGARWAL, C., HORN, L., PATNAIK, A., GUBENS, M., RAMALINGAM, S.S., FELIP, E., GOLDMAN, J.W., SCALZO, C., JENSEN, E., KUSH, D.A. and HUI, R., 2019. Five-Year Overall Survival for Patients With Advanced Non–Small-Cell Lung Cancer Treated With Pembrolizumab: Results From the Phase I KEYNOTE-001 Study. *Journal of Clinical Oncology,* **37**(28), pp. 2518-2527.

GASTEIGER E., HOOGLAND C., GATTIKER A., DUVAUD S., WILKINS M.R., APPEL R.D., BAIROCH A., 2005. Protein Identification and Analysis Tools on the Expasy Server; In: J.M. WALKER, ed, *The Proteomics Protocols Handbook.* New Jersey, USA: Humana Press, pp. 571–607.

GIBBS, J., VESSELS, M. and ROTHENBERG, M., *Immobilization Principles – Selecting the Surface for ELISA Assays.*

GOEL, S., DUDA, D.G., XU, L., MUNN, L.L., BOUCHER, Y., FUKUMURA, D. and JAIN, R.K., 2011. Normalization of the Vasculature for Treatment of Cancer and Other Diseases.

Physiological Reviews, **91**(3), pp. 1071-1121.

GraphPad Statistics Guide. Available: https://www.graphpad.com/guides/prism/latest/statistics/index.htm [4th November, 2025].

GUEX, N., PEITSCH, M.C. and SCHWEDE, T., 2009. Automated comparative protein structure modeling with SWISS-MODEL and Swiss-PdbViewer: A historical perspective. *ELECTROPHORESIS,* 30(S1),.

GUILLON, C., ROBERT, X. and GOUET, P., 2024. "It's Only a Model": When Protein Structure Predictions Need Experimental Validation, the Case of the HTLV-1 Tax Protein. *Pathogens,* **13**(3),.

GURUPRASAD, K., REDDY, B.V.B., PANDIT, M.W. and CURUPRASAD, K., Correlation between stability of a protein and its dipeptide composition: a novel approach for predicting in vivo stability of a protein from its primary sequence.

HADDOCK2.4 scoring function. Available: https://www.bonvinlab.org/software/haddock2.4/scoring/?utm_source=chatgpt.com [5th March, 2025].

HAMID, O., ROBERT, C., DAUD, A., HODI, F.S., HWU, W., KEFFORD, R., WOLCHOK, J.D., HERSEY, P., JOSEPH, R.W., WEBER, J.S., DRONCA, R., GANGADHAR, T.C., PATNAIK, A., ZAROUR, H., JOSHUA, A.M., GERGICH, K., ELASSAISS-SCHAAP, J., ALGAZI, A., MATEUS, C., BOASBERG, P., TUMEH, P.C., CHMIELOWSKI, B., EBBINGHAUS, S.W., LI, X.N., KANG, S.P. and RIBAS, A., 2013. Safety and Tumor Responses with Lambrolizumab (Anti–PD-1) in Melanoma. The New England journal of medicine, **369**(2), pp. 134-144.

HANAHAN, D., 2022. Hallmarks of Cancer: New Dimensions. *Cancer discovery,* **12**(1), pp. 31-46.

HANSON, H.L., DONERMEYER, D.L., IKEDA, H., WHITE, J.M., SHANKARAN, V., OLD, L.J., SHIKU, H., SCHREIBER, R.D. and ALLEN, P.M., 2000. Eradication of Established Tumors by CD8 + T Cell Adoptive Immunotherapy. *Immunity,* **13**(2), pp. 265-276.

HE, M., CHAI, Y., QI, J., ZHANG, C.W.H., TONG, Z., SHI, Y., YAN, J., TAN, S. and GAO, G.F., 2017. Remarkably similar CTLA-4 binding properties of therapeutic ipilimumab and tremelimumab antibodies. Oncotarget, **8**(40), pp. 67129-67139.

HERBERMAN, R.B., NUNN, M.E. and LAVRIN, D.H., 1975. Natural cytotoxic reactivity of mouse lymphoid cells against syngeneic acid allogeneic tumors. I. Distribution of reactivity and specificity. *International journal of cancer,* **16**(2), pp. 216-229.

HERBST, R.S., Prof, BAAS, P., Prof, KIM, D., MD, FELIP, E., MD, PÉREZ-GRACIA, J.L., MD, HAN, J., Prof, MOLINA, J., MD, KIM, J., Prof, ARVIS, C.D., MD, AHN, M., Prof, MAJEM, M., MD, FIDLER, M.J., MD, DE CASTRO, G., MD, GARRIDO, M., MD, LUBINIECKI, G.M., MD, SHENTU, Y., PhD, IM, E., MD, DOLLED-FILHART, M., PhD and GARON, E.B., MD, 2016. Pembrolizumab versus docetaxel for previously treated, PD-L1-positive, advanced non-small-cell lung

cancer (KEYNOTE-010): a randomised controlled trial. *The Lancet (British edition),* **387**(10027), pp. 1540-1550.

HINO, R., KABASHIMA, K., KATO, Y., YAGI, H., NAKAMURA, M., HONJO, T., OKAZAKI, T. and TOKURA, Y., 2010. Tumor cell expression of programmed cell death-1 ligand 1 is a prognostic factor for malignant melanoma. *Cancer,* **116**(7), pp. 1757-1766.

HODGE, J., 2022-last update, Checkpoint Frenzy. Available: https://www.iqvia.com/blogs/2022/04/checkpoint-frenzy [15th May, 2023].

HODI, F.S., O'DAY, S.J., MCDERMOTT, D.F., WEBER, R.W., WEBER, J.S., SOSMAN, J.A., HAANEN, J.B., GONZALEZ, R., ROBERT, C., SCHADENDORF, D., HASSEL, J.C., AKERLEY, W., VAN DEN EERTWEGH, ALFONS J.M, LUTZKY, J., LORIGAN, P., VAUBEL, J.M., LINETTE, G.P., HOGG, D., OTTENSMEIER, C.H., LEBBÉ, C., PESCHEL, HUANG, X., ZHANG, X., LI, E., ZHANG, G., WANG, X., TANG, T., BAI, X. and LIANG, T., 2020. VISTA an immune regulatory protein checking tumour and immune cells in cancer immunotherapy. Journal of Haematology and Oncology, **13**(83), pp. 1-13.

HODI, F.S., O'DAY, S.J., MCDERMOTT, D.F., WEBER, R.W., WEBER, J.S., SOSMAN, J.A., HAANEN, J.B., GONZALEZ, R., ROBERT, C., SCHADENDORF, D., HASSEL, J.C., AKERLEY, W., VAN DEN EERTWEGH, A.J.M., LUTZKY, J., LORIGAN, P., VAUBEL, J.M., LINETTE, G.P., HOGG, D., OTTENSMEIER, C.H., LEBBÉ, C., PESCHEL, C., QUIRT, I., CLARK, J.I., WOLCHOK, J.D., TIAN, J., YELLIN, M.J., NICHOL, G.M., HOOS, A. and URBA, W.J., 2010. Improved Survival with Ipilimumab in Patients with Metastatic Melanoma. *The New England journal of medicine,* **363**(8), pp. 711-723.

HONORATO, R.V., KOUKOS, P.I., JIMÉNEZ-GARCÍA, B., TSAREGORODTSEV, A., VERLATO, M., GIACHETTI, A., ROSATO, A. and BONVIN, A.M.J.J., 2021. Structural Biology in the Clouds: The WeNMR-EOSC Ecosystem. *Frontiers in Molecular Biosciences,* **8**.

HONORATO, R.V., TRELLET, M.E., JIMÉNEZ-GARCÍA, B., SCHAARSCHMIDT, J.J., GIULINI, M., REYS, V., KOUKOS, P.I., RODRIGUES, J.P.G.L.M., KARACA, E., VAN ZUNDERT, G.C.P., ROEL-TOURIS, J., VAN NOORT, C.W., JANDOVÁ, Z., MELQUIOND, A.S.J. and BONVIN, A.M.J.J., 2024. The HADDOCK2.4 web server for integrative modeling of biomolecular complexes. *Nature protocols,* **19**(11), pp. 3219–3241.

HOOGENBOOM, H.R., 2005. Selecting and screening recombinant antibody libraries. *Nature Biotechnology,* **23**(9), pp. 1105.

HOY, M.A., 2013. *Some Additional Tools for the Molecular Biologist.* Elsevier.

HUGO, W., ZARETSKY, J.M., SUN, L., SONG, C., MORENO, B.H., HU-LIESKOVAN, S., BERENT-MAOZ, B., PANG, J., CHMIELOWSKI, B., CHERRY, G., SEJA, E., LOMELI, S., KONG, X., KELLEY, M.C., SOSMAN, J.A., JOHNSON, D.B., RIBAS, A. and LO, R.S., 2016. Genomic and Transcriptomic Features of Response to Anti-PD-1 Therapy in Metastatic Melanoma. *Cell,* **165**(1), pp. 35-44.

HUI, E., CHEUNG, J., ZHU, J., SU, X., TAYLOR, M.J., WALLWEBER, H.A., SASMAL, D.K., HUANG, J., KIM, J.M., MELLMAN, I. and VALE, R.D., 2017. T cell costimulatory receptor

CD28 is a primary target for PD-1–mediated inhibition. *Science (American Association for the Advancement of Science),* **355**(6332), pp. 1428-1433.

HWANG, J., BYEON, Y., KIM, D. and PARK, S., 2020. Recent insights of T cell receptor-mediated signalling pathways for T cell activation and development. *Experimental & molecular medicine,* **52**(5), pp. 750-761.

Hyperphage. Available: https://www.progen.com/Products/Antibodies/Related-Products/Hyperphage/ [31st October, 2024].

Inconsistent results and high coefficient of variation in ELISA. Available: https://www.abcam.com/en-us/technical-resources/troubleshooting/inconsistent-results-and-high-cv-elisa?srsltid=AfmBOorOVe3To2EXjNwUGnbhf1dShQ_qN8h03ICsA0unUUqwbo2tILt2 [20th January, 2025].

Introduction to SWISS-MODEL. Available: https://swissmodel.expasy.org/docs/help [15th December, 2024].

ISHII, G., SANGAI, T., ODA, T., AOYAGI, Y., HASEBE, T., KANOMATA, N., ENDOH, Y., OKUMURA, C., OKUHARA, Y., MAGAE, J., EMURA, M., OCHIYA, T. and OCHIAI, A., 2003. Bone-marrow-derived myofibroblasts contribute to the cancer-induced stromal reaction. *Biochemical and biophysical research communications,* **309**(1), pp. 232-240.

JAISWAL, M., LARUSSO, N.F., BURGART, L.J. and GORES, G.J., 2000. Inflammatory Cytokines Induce DNA damage and Inhibit DNA repair in Cholangiocarcinoma Cells by a Nitric Oxide-dependent Mechanism. *Cancer Research,* **60**(1), pp. 184-190.

JENKINS, R.W., BARBIE, D.A. and FLAHERTY, K.T., 2018. Mechanisms of resistance to immune checkpoint inhibitors. *British journal of cancer,* **118**(1), pp. 9-16.

JIA, X., XU, H., GENG, L., JIAO, M., WANG, W., JIANG, L. and GUO, H., 2020. Efficacy and safety of neoadjuvant immunotherapy in resectable nonsmall cell lung cancer: A meta-analysis. *Lung cancer (Amsterdam, Netherlands),* **147**, pp. 143-153.

JOHNSTON, R.J., SU, L.J., PINCKNEY, J., CRITTON, D., BOYER, E., KRISHNAKUMAR, A., CORBETT, M., RANKIN, A.L., DIBELLA, R., CAMPBELL, L., MARTIN, G.H., LEMAR, H., CAYTON, T., HUANG, R.Y., DENG, X., NAYEEM, A., CHEN, H., ERGEL, B., RIZZO, J.M., YAMNIUK, A.P., DUTTA, S., NGO, J., SHORTS, A.O., RAMAKRISHNAN, R., KOZHICH, A., HOLLOWAY, J., FANG, H., WANG, Y., YANG, Z., THIAM, K., RAKESTRAW, G., RAJPAL, A., SHEPPARD, P., QUIGLEY, M., BAHJAT, K.S. and KORMAN, A.J., 2019. VISTA is an acidic pH-selective ligand for PSGL-1. *Nature,* **574**(7779), pp. 565-570.

JONES, M.L., SELDON, T., SMEDE, M., LINVILLE, A., CHIN, D.Y., BARNARD, R., MAHLER, S.M., MUNSTER, D., HART, D., GRAY, P.P. and MUNRO, T.P., 2010. A method for rapid, ligation-independent reformatting of recombinant monoclonal antibodies. *Journal of Immunological Methods,* **354**(1-2), pp. 85.

JURASZEK, J., RUTTEN, L., BLOKLAND, S., BOUCHIER, P., VOORZAAT, R., RITSCHEL, T., BAKKERS, M.J.G., RENAULT, L.L.R. and LANGEDIJK, J.P.M., 2021. *Stabilizing the closed*

SARS-CoV-2 spike trimer. Springer Science and Business Media LLC.

KALLURI, R. and ZEISBERG, M., 2006. Fibroblasts in cancer. *Nature reviews. Cancer,* **6**(5), pp. 392-401.

KANE, L.P., ANDRES, P.G., HOWLAND, K.C., ABBAS, A.K. and WEISS, A., 2001. Akt provides the CD28 costimulatory signal for up-regulation of IL-2 and IFN-[gamma] but not TH2 cytokines. *Nature immunology,* **2**(1), pp. 37.

KANG, C., DUTTA, A., CHANG, L., MAHALINGAM, J., LIN, Y., CHIANG, J., HSU, C., HUANG, C., SU, W., CHU, Y. and LIN, C., 2015. Apoptosis of tumor infiltrating effector TIM-3+CD8+ T cells in colon cancer. *Scientific Reports,* **5**(1), pp. 15659.

KAPSENBERG, M.L., 2003. Dendritic-cell control of pathogen-driven T-cell polarization. *Nature reviews. Immunology,* **3**(12), pp. 984-993.

KATHER, J.N., SUAREZ-CARMONA, M., CHAROENTONG, P., WEIS, C., HIRSCH, D., BANKHEAD, P., HORNING, M., FERBER, D., KEL, I., HERPEL, E., SCHOTT, S., ZÖRNIG, I., UTIKAL, J., MARX, A., GAISER, T., BRENNER, H., CHANG-CLAUDE, J., HOFFMEISTER, M., JÄGER, D. and HALAMA, N., 2018. Topography of cancer-associated immune cells in human solid tumors. *eLife,* 7.

KEIR, M.E., BUTTE, M.J., FREEMAN, G.J. and SHARPE, A.H., 2008. PD-1 and Its Ligands in Tolerance and Immunity. *Annual review of immunology,* **26**(1), pp. 677-704.

KERRY, J., 2024-last update, Antibody Humanization Strategies, Challenges, and Innovations. Available: https://www.rapidnovor.com/antibody-humanization-strategies-challenges-innovations/#postsectionseven [5th March, 2025].

KEYING, M.K., SALEEM, L.M., KHAN, I.J., ZHAN, KALIM, M., LIANG, ÁK., KHAN, Á and ZHAN, ÁJ., 2019. Efficient development and expression of scFv recombinant proteins against PD-L1 surface domain and potency in cancer therapy.

KIM, J.W., CHO, A.H., SHIN, H.G., JANG, S.H., CHO, S.Y., LEE, Y.R. and LEE, S., 2023. Development and Characterization of Phage Display-Derived Monoclonal Antibodies to the S2 Domain of Spike Proteins of Wild-Type SARS-CoV-2 and Multiple Variants. MDPI AG.

KIM, S.K. and CHO, S.W., 2022. The Evasion Mechanisms of Cancer Immunity and Drug Intervention in the Tumor Microenvironment. *Frontiers in pharmacology,* **13**, pp. 868695.

KIMBARA, S., FUJIWARA, Y., IWAMA, S., OHASHI, K., KUCHIBA, A., ARIMA, H., YAMAZAKI, N., KITANO, S., YAMAMOTO, N. and OHE, Y., 2018. Association of antithyroglobulin antibodies with the development of thyroid dysfunction induced by nivolumab. *Cancer Science,* **109**(11), pp. 3583-3590.

KINZLER, K.W. and VOGELSTEIN, B., 1997. Cancer-susceptibility genes. Gatekeepers and caretakers. *Nature (London),* **386**(6627), pp. 761, 763.

KOHL, F., LAUFKÖTTER, O., FIRTH, M., KRIMPENFORT, L., MANGLA, P., ANSARIZADEH, M.,

GEYLAN, G., EKLUND, L., DE MARIA, L., JAKOBSSON, L. and WISEMAN, J., 2024a. Identification of cell type-specific cell-penetrating peptides through in vivo phage display leveraged by next generation sequencing. *Biomedicine & Pharmacotherapy,* **182**.

KUANG, D., ZHAO, Q., PENG, C., XU, J., ZHANG, J., WU, C. and ZHENG, L., 2009. Activated monocytes in peritumoral stroma of hepatocellular carcinoma foster immune privilege and disease progression through PD-L1. *The Journal of Experimental Medicine,* **206**(6), pp. 1327-1337.

KUIPERS, H., MUSKENS, A.M., WILLART, M., HIJA, D., VAN ASSEMA, F., COYLE, A.J., HOOGSTEDEN, H. and LAMBRECHT, B., 2006. Contribution of the PD-1 ligands/PD-1 signalling pathway to dendritic cell-mediated CD4(+) T cell activation. *European journal of immunology,* **36**(9), pp. 2472-2482.

KUMAR, P., ARYA, A., 2019. Ramachandran Plot : A simplified approach. *Research Gate,* pp. 1–6.

KUMAR, P., BHATTACHARYA, P. and PRABHAKAR, B.S., 2018. A comprehensive review on the role of co-signalling receptors and Treg homeostasis in autoimmunity and tumor immunity. *Journal of autoimmunity,* **95**, pp. 77-99

LANDAU, S. and CHIS STER, I., 2010. *Cluster Analysis: Overview.* Elsevier.

LAO, Y., SHEN, D., ZHANG, W., HE, R. and JIANG, M., 2022. Immune Checkpoint Inhibitors

in Cancer Therapy—How to Overcome Drug Resistance? *Cancers,* **14**(15), pp. 3575.

LE ROUZIC, E., 2006. Contamination-pipetting: relative efficiency of filter tips compared to Microman® positive displacement pipette. *Nature methods,* **3**(6), pp. III–IV.

LEACH, D.R., KRUMMEL, M.F. and ALLISON, J.P., 1996. Enhancement of Antitumor Immunity by CTLA-4 Blockade. *Science,* **271**(5256), pp. 1734-1736.

LEDSGAARD, L., KILSTRUP, M., KARATT-VELLATT, A., MCCAFFERTY, J. and LAUSTSEN, A.H., 2018. Basics of Antibody Phage Display Technology. Toxins, **10**(6),.

LEFRANÇOIS, L., SCHLUNS, K.S., KIEPER, W.C. and JAMESON, S.C., 2000. Interleukin-7 mediates the homeostasis of naïve and memory CD8 T cells in vivo. *Nature immunology,* **1**(5), pp. 426-432.

LEIDEN, J.M., BUCKLEY, A.F. and KUO, C.T., 2001. Transcription factor LKLF is sufficient to program T cell quiescence via a c-Myc-dependent pathway. *Nature immunology,* **2**(8), pp. 698-704.

LENSCHOW, D.J., WALUNAS, T.L. and BLUESTONE, J.A., 1996. CD28/B7 SYSTEM OF T CELL COSTIMULATION. *Annual review of immunology,* **14**(1), pp. 233-258.

LI, Y., LI, G., ZHANG, J., WU, X. and CHEN, X., 2021. The Dual Roles of Human γδ T Cells: Anti-Tumor or Tumor-Promoting. *Frontiers in immunology,* **11**, pp. 619954.

LIECHTENSTEIN, T., DUFAIT, I., LANNA, A., BRECKPOT, K. and ESCORS, D., 2012. Modulating Co-Stimulation During Antigen Presentation to Enhance Cancer Immunotherapy. *Immunology, endocrine & metabolic agents in medicinal chemistry,* **12**(3), pp. 224-235.

LINES, J.L., PANTAZI, E., NOELLE, R., MAK, J., SEMPERE, L.F., LI WANG, O'CONNELL, S., CEERAZ, S., SURIAWINATA, A.A., SHAOFENG YAN and ERNSTOFF, M.S., 2014. VISTA Is an Immune Checkpoint Molecule for Human T Cells. *Cancer research (Chicago, Ill.),* **74**(7), pp. 1924-1932.

LIPMAN, N.S., JACKSON, L.R., TRUDEL, L.J. and WEIS-GARCIA, F., Monoclonal Versus Polyclonal Antibodies: Distinguishing Characteristics, Applications, and Information Resources.

LIU, J., HAMROUNI, A., WOLOWIEC, D., COITEUX, V., KULICZKOWSKI, K., HETUIN, D., SAUDEMONT, A. and QUESNEL, B., 2007. Plasma cells from multiple myeloma patients express B7-H1 (PD-L1) and increase expression after stimulation with IFN-γ and TLR ligands via a MyD88-, TRAF6-, and MEK-dependent pathway. *Blood,* **110**(1), pp. 296-304.

LIU, Z., GUO, Y., TANG, S., ZHOU, L., HUANG, C., CAO, Y., HUANG, H., WU, X., MENG, D., YE, L., HE, H., XIE, Z., WU, Y., LIU, X. and ZHOU, X., 2019. Cutting Edge: Transcription Factor BCL6 Is Required for the Generation, but Not Maintenance, of Memory CD8+ T Cells in Acute Viral Infection. *The Journal of immunology (1950),* **203**(2), pp. 323-327.

LIU, Z., KIM, D., KANG, S. and JUNG, J.U., 2024. A Detailed Protocol for Constructing a Human Single-Chain Variable Fragment (scFv) Library and Downstream Screening via Phage Display. MDPI AG.

LIU, Z., KIM, D., KANG, S. and JUNG, J.U., 2024. A Detailed Protocol for Constructing a Human Single-Chain Variable Fragment (scFv) Library and Downstream Screening via Phage Display. *Methods and Protocols,* **7**(1),.

LYNCH, T.J., BONDARENKO, I., RECK, M., LUFT, A., SERWATOWSKI, P., BARLESI, F., CHACKO, R., SEBASTIAN, M., NEAL, J., HAOLAN LU and CUILLEROT, J., 2012. Ipilimumab in Combination With Paclitaxel and Carboplatin As First-Line Treatment in Stage IIIB/IV Non–Small-Cell Lung Cancer: Results From a Randomized, Double-Blind, Multicenter Phase II Study. *Journal of clinical oncology,* **30**(17), pp. 2046-2054.

MA, Y., SHURIN, G.V., PEIYUAN, Z. and SHURIN, M.R., 2013. Dendritic Cells in the Cancer Microenvironment. *Journal of Cancer,* **4**(1), pp. 36-44.

MACIÁN, F., GARCÍA-RODRÍGUEZ, C. and RAO, A., 2000. Gene expression elicited by NFAT in the presence or absence of cooperative recruitment of Fos and Jun. *The EMBO journal,* **19**(17), pp. 4783-4795.

MADDEN, T. and CAMACHO, C., 2008. User Manual. *BLAST® Command Line Applications User Manual [Internet].* Bethesda, Maryland (MD), USA: National Center for Biotechnology Information, pp. 1–58.

MAK, T.W., CAIRNS, R.A. and HARRIS, I.S., 2011. Regulation of cancer cell metabolism.

Nature reviews. Cancer, **11**(2), pp. 85-95.

MALHOTRA CONTENTS, A., 2009. *Chapter 16 Tagging for Protein Expression.* Elsevier.

MALHOTRA, A., 2009. Methods in Enzymology. USA: Elsevier.

MANIAR, A., ZHANG, X., LIN, W., GASTMAN, B.R., PAUZA, C.D., STROME, S.E. and CHAPOVAL, A.I., 2010. Human gammadelta T lymphocytes induce robust NK cell-mediated antitumor cytotoxicity through CD137 engagement. *Blood,* **116**(10), pp. 1726-1733.

MANTOVANI, A., 2005. Inflammation by remote contro. *Nature,* **435**(7043), pp. 752-753.

MANTOVANI, A., SICA, A. and LOCATI, M., 2005. Macrophage Polarization Comes of Age. *Immunity,* **23**(4), pp. 344-346.

MARANGONI, F., MUROOKA, T., MANZO, T., KIM, E., CARRIZOSA, E., ELPEK, N. and MEMPEL, T., 2013. The Transcription Factor NFAT Exhibits Signal Memory during Serial T Cell Interactions with Antigen-Presenting Cells. *Immunity,* **38**(2), pp. 237-249.

MARCUS, A., GOWEN, B.G., THOMPSON, T.W., IANNELLO, A., ARDOLINO, M., DENG, W., WANG, L., SHIFRIN, N. and RAULET, D.H., 2014. Recognition of Tumors by the Innate Immune System and Natural Killer Cells. *Advances in Immunology.* United States: Elsevier Science & Technology, pp. 91-128.

MARTINEZ, G.J., PEREIRA, R.M., ÄIJÖ, T., KIM, E.Y., MARANGONI, F., PIPKIN, M.E., TOGHER, S., HEISSMEYER, V., ZHANG, Y.C., CROTTY, S., LAMPERTI, E.D., ANSEL, K.M., MEMPEL, T.R., LÄHDESMÄKI, H., HOGAN, P.G. and RAO, A., 2015. The Transcription Factor NFAT Promotes Exhaustion of Activated CD8 + T Cells. *Immunity,* **42**(2), pp. 265-278.

MASON, E., 2021-last update, ELISA Troubleshooting Guide. Available: https://www.biocompare.com/579531-ELISA-Troubleshooting/ [20th February, 2025].

MATOCHKO, W.L., CHU, K., JIN, B., LEE, S.W., WHITESIDES, G.M. and DERDA, R., 2012. Deep sequencing analysis of phage libraries using Illumina platform. *Methods,* **58**(1), pp. 47.

MATOCHKO, W.L., CORY LI, S., TANG, S.K.Y. and DERDA, R., 2013. Prospective identification of parasitic sequences in phage display screens. *Nucleic Acids Research,* **42**(3), pp. 1784.

MATOCHKO, W.L., NG, S., JAFARI, M.R., ROMANIUK, J., TANG, S.K.Y. and DERDA, R., 2012a. Uniform amplification of phage display libraries in monodisperse emulsions. *Methods,* **58**(1), pp. 18.

MCCONNELL, S.J., DINH, T., LE, M. and SPINELLA, D.G., 2018. Biopanning Phage Display Libraries Using Magnetic Beads Vs. Polystyrene Plates. BioTechniques, **26**(2), pp. 208.

MCLAUGHLIN, L., 2024-last update, Tiny Viruses, Big Impact: The Science and Future of Phage Display [20th February, 2025].

Most Popular Antibody Fragment: Single Domain Antibody vs. ScFv2023-last update. Available: https://www.creative-biolabs.com/blog/sdab/biological-knowledge/most-

popular-antibody-fragment-single-domain-antibody-vs-scfv/#:~:text=CDRs%20are%20responsible%20for%20antigen,in%20antigen%20binding%20is%20different. [20th January, 2025].

MULATI, K., HAMANISHI, J., MATSUMURA, N., CHAMOTO, K., MISE, N., ABIKO, K., BABA, T., YAMAGUCHI, K., HORIKAWA, N., MURAKAMI, R., TAKI, M., BUDIMAN, K., ZENG, X., HOSOE, Y., AZUMA, M., KONISHI, I. and MANDAI, M., 2019. VISTA expressed in tumour cells regulates T cell function. *British Journal of Cancer,* **120**(1), pp. 115-127.

MURRAY, P., ALLEN, J., BISWAS, S., FISHER, E., GILROY, D., GOERDT, S., GORDON, S., HAMILTON, J., IVASHKIV, L., LAWRENCE, T., LOCATI, M., MANTOVANI, A., MARTINEZ, F., MEGE, J., MOSSER, D., NATOLI, G., SAEIJ, J., SCHULTZE, J., SHIREY, K., SICA, A., SUTTLES, J., UDALOVA, I., VAN GINDERACHTER, J., VOGEL, S. and WYNN, T., 2014. Macrophage Activation and Polarization: Nomenclature and Experimental Guidelines. *Immunity,* **41**(1), pp. 14-20.

MURRAY, P., ALLEN, J., BISWAS, S., FISHER, E., GILROY, D., GOERDT, S., GORDON, S., HAMILTON, J., IVASHKIV, L., LAWRENCE, T., LOCATI, M., MANTOVANI, A., MARTINEZ, F., MEGE, J., MOSSER, D., NATOLI, G., SAEIJ, J., SCHULTZE, J., SHIREY, K., SICA, A., SUTTLES, J., UDALOVA, I., VAN GINDERACHTER, J., VOGEL, S. and WYNN, T., 2014. Macrophage Activation and Polarization: Nomenclature and Experimental Guidelines. *Immunity,* **41**(1), pp. 14-20.

NA, J., JOO, M., LEE, W., SHIM, H., LIM, S., JUNG, S.T. and YU, Y.G., 2013. Development of a Single Chain Antibody Using a Phage Display Cloning Method for the Detection of 2,4-Dinitrotoluene. Bulletin of the Korean Chemical Society, **34**(2), pp. 460.

NanoDrop Microvolume Spectrophotometers Resources. Available: https://www.thermofisher.com/mt/en/home/industrial/spectroscopy-elemental-isotope-analysis/molecular-spectroscopy/uv-vis-spectrophotometry/instruments/nanodrop/resources.htmL#:~:text=NanoDrop%20spectrophotometers%20work%20on%20the,a%20peak%20of%20205%20nm. [2nd November, 2024].

NanoDrop Spectrophotometer Resources. Available: https://www.thermofisher.com/mt/en/home/industrial/spectroscopy-elemental-isotope-analysis/molecular-spectroscopy/uv-vis-spectrophotometry/instruments/nanodrop.html [22nd October, 2024].

NIH clinical trial leads to atezolizumab approval for advanced alveolar soft part sarcoma2022-last update. Available: https://www.nih.gov/news-events/news-releases/nih-clinical-trial-leads-atezolizumab-approval-advanced-alveolar-soft-part-sarcoma [20th May, 2023].

NILSSON, N., MALMBORG, A.C. and BORREBAECK, C.A., 2000. The Phage Infection Process: a Functional Role for the Distal Linker Region of Bacteriophage Protein 3. Journal of Virology, **74**(9), pp. 4229-4235.

NOVITSKIY, S.V., RYZHOV, S., ZAYNAGETDINOV, R., GOLDSTEIN, A.E., HUANG, Y.,

TIKHOMIROV, O.Y., BLACKBURN, M.R., BIAGGIONI, I., CARBONE, D.P., FEOKTISTOV, I. and DIKOV, M.M., 2008. Adenosine receptors in regulation of dendritic cell differentiation and function. *Blood,* **112**(5), pp. 1822-1831.

O'DONNELL, J.S., TENG, M.W.L. and SMYTH, M.J., 2019. Cancer immunoediting and resistance to T cell-based immunotherapy. *Nature reviews. Clinical oncology,* **16**(3), pp. 151-167.

OSTRAND-ROSENBERG, S., SINHA, P., CHORNOGUZ, O. and ECKER, C., 2012. Regulating the suppressors: apoptosis and inflammation govern the survival of tumor-induced myeloid-derived suppressor cells (MDSC). *Cancer Immunology, Immunotherapy,* **61**(8), pp. 1319-1325.

OSWALD, N., 2024-last update, What's The Problem With Ampicillin Selection?. Available: https://bitesizebio.com/10188/whats-the-problem-with-ampicillin-selection/ [20th March, 2025].

OVERMAN, M.J., LONARDI, S., WONG, K.Y.M., LENZ, H., GELSOMINO, F., AGLIETTA, M., MORSE, M.A., VAN CUTSEM, E., MCDERMOTT, R., HILL, A., SAWYER, M.B., HENDLISZ, A., NEYNS, B., SVRCEK, M., MOSS, R.A., LEDEINE, J., CAO, Z.A., KAMBLE, S., KOPETZ, S. and ANDRÉ, T., 2018. Durable Clinical Benefit With Nivolumab Plus Ipilimumab in DNA Mismatch Repair–Deficient/Microsatellite Instability–High Metastatic Colorectal Cancer. *Journal of clinical oncology,* **36**(8), pp. 773-779.

PALEY, M.A., KROY, D.C., ODORIZZI, P.M., JOHNNIDIS, J.B., DOLFI, D.V., BARNETT, B.E., BIKOFF, E.K., ROBERTSON, E.J., LAUER, G.M., REINER, S.L. and WHERRY, E.J., 2012. Progenitor and Terminal Subsets of $CD8^+$ T Cells Cooperate to Contain Chronic Viral Infection. *Science (American Association for the Advancement of Science),* **338**(6111), pp. 1220-1225.

PARDOLL, D., 2015. Cancer and the Immune System: Basic Concepts and Targets for Intervention. *Seminars in oncology,* **42**(4), pp. 523-538.

PEGGS, K.S., QUEZADA, S.A., CHAMBERS, C.A., KORMAN, A.J. and ALLISON, J.P., 2009. Blockade of CTLA-4 on both effector and regulatory T cell compartments contributes to the antitumor activity of anti–CTLA-4 antibodies. *The Journal of Experimental Medicine,* **206**(8), pp. 1717-1725.

PENG, W., CHEN, J.Q., LIU, C., MALU, S., CREASY, C., TETZLAFF, M.T., XU, C., MCKENZIE, J.A., ZHANG, C., LIANG, X., WILLIAMS, L.J., DENG, W., CHEN, G., MBOFUNG, R., LAZAR, A.J., TORRES-CABALA, C.A., COOPER, Z.A., CHEN, P., TIEU, T.N., SPRANGER, S., YU, X., BERNATCHEZ, C., FORGET, M., HAYMAKER, C., AMARIA, R., MCQUADE, J.L., GLITZA, I.C., CASCONE, T., LI, H.S., KWONG, L.N., HEFFERNAN, T.P., HU, J., BASSETT, J., Roland L, BOSENBERG, M.W., WOODMAN, S.E., OVERWIJK, W.W., LIZÉE, G., ROSZIK, J., GAJEWSKI, T.F., WARGO, J.A., GERSHENWALD, J.E., RADVANYI, L., DAVIES, M.A. and HWU, P., 2016. Loss of PTEN Promotes Resistance to T Cell–Mediated Immunotherapy. *Cancer discovery,* **6**(2), pp. 202-216.

Ph.D. Phage Display Libraries. Available: chrome-extension: https://www.neb.com/en/-

/media/nebus/files/manuals/manuale8100_e8101_e8110_e8111_e8120.pdf?rev=b9782324ddd14d489da1db10e9240e60&sc_lang=en&hash=5CB7FEC5412FD9E047BB53E3FD120547&srsltid=AfmBOopfW0hpuMVhiOafwGANp9GHfmaNLPN1bqdw98YAXNXodQSyoD5w [22nd October, 2024].

Phase 1 study of CI-8993 anti-VISTA antibody in patients with advanced solid tumor malignancies. Available: https://clinicaltrials.gov/ct2/show/NCT04475523 [10th May, 2023].

PITT, J., VÉTIZOU, M., DAILLÈRE, R., ROBERTI, M., YAMAZAKI, T., ROUTY, B., LEPAGE, P., BONECA, I., CHAMAILLARD, M., KROEMER, G. and ZITVOGEL, L., 2016. Resistance Mechanisms to Immune-Checkpoint Blockade in Cancer: Tumor-Intrinsic and -Extrinsic Factors. *Immunity (Cambridge, Mass.),* **44**(6), pp. 1255-1269.

PORTA, C., RIMOLDI, M., RAES, G., BRYS, L., GHEZZI, P., DI LIBERTO, D., DIELI, F., GHISLETTI, S., NATOLI, G., DE BAETSELIER, P., MANTOVANI, A. and SICA, A., 2009. Tolerance and M2 (alternative) macrophage polarization are related processes orchestrated by p50 nuclear factor κB. *Proceedings of the National Academy of Sciences - PNAS,* **106**(35), pp. 14978-14983.

POSTOW, M.A., CALLAHAN, M.K. and WOLCHOK, J.D., 2015. Immune Checkpoint Blockade in Cancer Therapy. *Journal of clinical oncology,* **33**(17), pp. 1974-1982.

POSTOW, M.A., SIDLOW, R. and HELLMANN, M.D., 2018. Immune-Related Adverse Events Associated with Immune Checkpoint Blockade. *The New England journal of medicine,* **378**(2), pp. 158-168.

QIAN, B., JIUFENG LI, HUI ZHANG, KITAMURA, T., JINGHANG ZHANG, CAMPION, L.R., KAISER, E.A., SNYDER, L.A. and POLLARD, J.W., 2011. Ccl2 Recruits Inflammatory Monocytes to Facilitate Breast-Tumour Metastasis. *Nature,* **475**(7355), pp. 222-225.

QIN, S., XU, L., YI, M., YU, S., WU, K. and LUO, S., 2019. Novel immune checkpoint targets: moving beyond PD-1 and CTLA-4. Molecular Cancer, 18(1), pp. 155.
QIU, X.Y., HU, D.X., CHEN, W., CHEN, R.Q., QIAN, S.R., LI, C.Y., LI, Y.J., XIONG, X.X., LIU, D., PAN, F., YU, S.B. and CHEN, X.Q., 2018. PD-L1 confers glioblastoma multiforme malignancy via Ras binding and Ras/Erk/EMT activation. *Biochimica et biophysica acta,* **1864**(5), pp. 1754-1769.

RABINAL, C.A., MOGER, N., VERMA, S., KRISHNARAJ, P.U. and CHANDRASHEKARA, K.N., *Production of Single Chain Fragment Variable (scFv) Monoclonal Antibody against Cry2B through Phage Display Technology.*

RAO, A., LUO, C. and HOGAN, P.G., 1997. TRANSCRIPTION FACTORS OF THE NFAT FAMILY:Regulation and Function. *Annual review of immunology,* **15**(1), pp. 707-747.

RAVETCH, J.V. and LANIER, L.L., 2000. Immune Inhibitory Receptors. *Science,* **290**(5489), pp. 84-89.

RESTIFO, N.P., MARINCOLA, F.M., KAWAKAMI, Y., TAUBENBERGER, J., YANNELLI, J.R. and ROSENBERG, S.A., 1996. Loss of Functional Beta2-Microglobulin in Metastatic Melanomas From Five Patients Receiving Immunotherapy. *JNCI : Journal of the National Cancer*

Institute, **88**(2), pp. 100-108.

RIBAS, A., SHIN, D.S., ZARETSKY, J., FREDERIKSEN, J., CORNISH, A., AVRAMIS, E., SEJA, E., KIVORK, C., SIEBERT, J., KAPLAN-LEFKO, P., WANG, X., CHMIELOWSKI, B., GLASPY, J.A., TUMEH, P.C., CHODON, T., PE'ER, D. and COMIN-ANDUIX, B., 2016. PD-1 Blockade Expands Intratumoral Memory T Cells. *Cancer immunology research,* **4**(3), pp. 194-203.

RIHA, P. and RUDD, C.E., 2010. CD28 co-signalling in the adaptive immune response. *Self/nonself,* **1**(3), pp. 231-240.

RIZVI, N.A., HELLMANN, M.D., SNYDER, A., KVISTBORG, P., MAKAROV, V., HAVEL, J.J., LEE, W., YUAN, J., WONG, P., HO, T.S., MILLER, M.L., REKHTMAN, N., MOREIRA, A.L., IBRAHIM, F., BRUGGEMAN, C., GASMI, B., ZAPPASODI, R., MAEDA, Y., SANDER, C., GARON, E.B., MERGHOUB, T., WOLCHOK, J.D., SCHUMACHER, T.N. and CHAN, T.A., 2015. Mutational landscape determines sensitivity to PD-1 blockade in non–small cell lung cancer. *Science (American Association for the Advancement of Science),* **348**(6230), pp. 124-128.

Roadmap to Reducing Animal Testing in Preclinical Safety Studies. Available: chrome-extension://efaidnbmnnnibpcajpcglclefindmkaj/https://www.fda.gov/media/186092/download [27th March, 2025].

ROBBINS, P.F., LU, Y., EL-GAMIL, M., LI, Y.F., GROSS, C., GARTNER, J., LIN, J.C., TEER, J.K., CLIFTEN, P., TYCKSEN, E., SAMUELS, Y. and ROSENBERG, S.A., 2013. Mining exomic sequencing data to identify mutated antigens recognized by adoptively transferred tumor-reactive T cells. *Nature medicine,* **19**(6), pp. 747-752.

ROBERTS, E.W., BROZ, M.L., BINNEWIES, M., HEADLEY, M.B., NELSON, A.E., WOLF, D.M., KAISHO, T., BOGUNOVIC, D., BHARDWAJ, N. and KRUMMEL, M.F., 2016. Critical Role for CD103+/CD141+ Dendritic Cells Bearing CCR7 for Tumor Antigen Trafficking and Priming of T Cell Immunity in Melanoma. *Cancer cell,* **30**(2), pp. 324-336.

RONDOT, S., KOCH, J., BREITLING, F. and DÜBEL, S., A helper phage to improve single-chain antibody presentation in phage display.

ROSENBERG, A., GRIFFIN, K., STUDIER, W., MCCORMICK, M., BERG, J., NOVY R. and MIERENDOF, R., 1996. T7Select Phage Display System: A Powerful New Protein Display System Based on Bacteriophage T7. *Innovations,* **6**, pp. 1–6.

RUMPRET, M., DRYLEWICZ, J., ACKERMANS, L.J.E., BORGHANS, J.A.M., MEDZHITOV, R. and MEYAARD, L., 2020. Functional categories of immune inhibitory receptors. *Nature reviews. Immunology,* **20**(12), pp. 771-780.

SAITO, T., YOKOSUKA, T. and HASHIMOTO-TANE, A., 2010. Dynamic regulation of T cell activation and co-stimulation through TCR-microclusters. *FEBS letters,* **584**(24), pp. 4865-4871.

SAKAGUCHI, S., 2004. Naturally Arising CD4+ Regulatory T Cells for Immunologic Self-Tolerance and Negative Control of Immune Responses. *Annual review of immunology,* **22**, pp. 531-562.

SANDERS, E.R., 2012a. Aseptic Laboratory Techniques: Plating Methods. Journal of

Visualized Experiments, (63), pp. E3064

SANDRU, A., VOINEA, S., PANAITESCU, E. and BLIDARU, A., 2014. Survival rates of patients with metastatic malignant melanoma. *Journal of Medicine and Life,* **7**(4), pp. 572-576.

SAVELYEVA, L. and SCHWAB, M., 2001. *Amplification of oncogenes revisited: from expression profiling to clinical application.* Shannon: Elsevier Ireland Ltd.

SAYERS, E.W., BECK, J., BOLTON, E.E., BRISTER, J.R., CHAN, J., CONNOR, R., FELDGARDEN, M., FINE, A.M., FUNK, K., HOFFMAN, J., KANNAN, S., KELLY, C., KLIMKE, W., KIM, S., LATHROP, S., MARCHLER-BAUER, A., MURPHY, T.D., O'SULLIVAN, C., SCHMIEDER, E., SKRIPCHENKO, Y., STINE, A., THIBAUD-NISSEN, F., WANG, J., YE, J., ZELLERS, E., SCHNEIDER, V.A. and PRUITT, K.D., 2024. Database resources of the National Center for Biotechnology Information in 2025. *Nucleic Acids Research,* **53**(D1), pp. D20.

SCHADENDORF, D., HODI, F.S., ROBERT, C., WEBER, J.S., MARGOLIN, K., HAMID, O., PATT, D., CHEN, T., BERMAN, D.M. and WOLCHOK, J.D., 2015. Pooled Analysis of Long-Term Survival Data From Phase II and Phase III Trials of Ipilimumab in Unresectable or Metastatic Melanoma. *Journal of clinical oncology,* **33**(17), pp. 1889-1894.

SCHIETINGER, A., PHILIP, M., KRISNAWAN, V.E., CHIU, E.Y., DELROW, J.J., BASOM, R.S., LAUER, P., BROCKSTEDT, D.G., KNOBLAUGH, S.E., HÄMMERLING, G.J., SCHELL, T.D., GARBI, N. and GREENBERG, P.D., 2016. Tumor-Specific T Cell Dysfunction Is a Dynamic Antigen-Driven Differentiation Program Initiated Early during Tumorigenesis. *Immunity (Cambridge, Mass.),* **45**(2), pp. 389-401.

SCHNELL, A., BOD, L., MADI, A. and KUCHROO, V.K., 2020. The yin and yang of co-inhibitory receptors: toward anti-tumor immunity without autoimmunity. *Cell Research,* **30**(4), pp. 285-299.

SCHOALES, J., 2015-last update, How Does Sanger Sequencing Work?. Available: https://www.thermofisher.com/blog/behindthebench/how-does-sanger-sequencing-work/#:~:text=Sanger%20sequencing%20results%20in%20the,filled%20with%20a%20gel%20polymer [4th November, .

SCHREIBER, R.D., DUNN, G.P., BRUCE, A.T., IKEDA, H. and OLD, L.J., 2002. Cancer immunoediting: from immunosurveillance to tumor escape. *Nature immunology,* **3**(11), pp. 991-998.

SCHRIJVER, R.S. and KRAMPS, J.A., Critical factors affecting the diagnostic reliability of enzyme-linked immunosorbent assay formats.

Sequencing troubleshooting. Available: chrome-extension://efaidnbmnnnibpcajpcglclefindmkaj/https://genomique.iric.ca/resources/files/Guide_Troubleshooting_Data.pdf [20th February, 2025].

SETHI, S., ALI, S., PHILIP, P.A. and SARKAR, F.H., 2013. Clinical Advances in Molecular Biomarkers for Cancer Diagnosis and Therapy. *International Journal of Molecular Sciences,* **14**(7), pp. 14771-14784.

SEZER, A., KILICKAP, S., GÜMÜŞ, M., BONDARENKO, I., ÖZGÜROĞLU, M., GOGISHVILI, M., TURK, H.M., CICIN, I., BENTSION, D., GLADKOV, O., CLINGAN, P., SRIURANPONG, V., RIZVI, N., GAO, B., LI, S., LEE, S., MCGUIRE, K., CHEN, C., MAKHARADZE, T., PAYDAS, S., NECHAEVA, M., SEEBACH, F., WEINREICH, D.M., YANCOPOULOS, G.D., GULLO, G., LOWY, I. and RIETSCHEL, P., 2021. Cemiplimab monotherapy for first-line treatment of advanced non-small-cell lung cancer with PD-L1 of at least 50%: a multicentre, open-label, global, phase 3, randomised, controlled trial. *The Lancet (British edition),* **397**(10274), pp. 592- 604.

SHANKARAN, V., IKEDA, H., BRUCE, A.T., WHITE, J.M., SWANSON, P.E., OLD, L.J. and SCHREIBER, R.D., 2001. IFNgamma and lymphocytes prevent primary tumour development and shape tumour immunogenicity. *Nature (London),* **410**(6832), pp. 1107-1111.

SHARPE, A.H. and PAUKEN, K.E., 2018. The diverse functions of the PD1 inhibitory pathway. *Nature reviews. Immunology,* **18**(3), pp. 153-167.

SHEPPARD, K., FITZ, L.J., LEE, J.M., BENANDER, C., GEORGE, J.A., WOOTERS, J., QIU, Y., JUSSIF, J.M., CARTER, L.L., WOOD, C.R. and CHAUDHARY, D., 2004. PD-1 inhibits T-cell receptor induced phosphorylation of the ZAP70/CD3ζ signalosome and downstream signalling to PKCθ. *FEBS letters,* **574**(1), pp. 37-41.

SHI, F., SHI, M., ZENG, Z., QI, R., LIU, Z., ZHANG, J., YANG, Y., TIEN, P. and WANG, F., 2011. PD-1 and PD-L1 upregulation promotes CD8+ T-cell apoptosis and postoperative recurrence in hepatocellular carcinoma patients. *International journal of cancer,* **128**(4), pp. 887-896.

SHIN, D.S., ZARETSKY, J.M., ESCUIN-ORDINAS, H., GARCIA-DIAZ, A., HU-LIESKOVAN, S., KALBASI, A., GRASSO, C.S., HUGO, W., SANDOVAL, S., TORREJON, D.Y., PALASKAS, N., RODRIGUEZ, G.A., PARISI, G., AZHDAM, A., CHMIELOWSKI, B., CHERRY, G., SEJA, E., BERENT-MAOZ, B., SHINTAKU, I.P., LE, D.T., PARDOLL, D.M., DIAZ, J., Luis A, TUMEH, P.C., GRAEBER, T.G., LO, R.S., COMIN-ANDUIX, B. and RIBAS, A., 2017. Primary Resistance to PD-1 Blockade Mediated by JAK1/2 Mutations. *Cancer discovery,* **7**(2), pp. 188-201.

SINGH, N., BABY D., PRASAD RAJGURU, J., PATIL, P.B., THAKKANNAVAR, S.S. and BHOJARAJ PUJARI, V., 2019. Inflammation and Cancer. *Annals of African Medicine,* **18**(3), pp. 121-126.

SLATER, B.T., HAN, X., CHEN, L. and XIONG, Y., 2020. Structural insight into T cell coinhibition by PD-1H (VISTA). *Proceedings of the National Academy of Sciences - PNAS,* **117**(3), pp. 1648-1667.

SMYTH, M.J., DUNN, G.P. and SCHREIBER, R.D., 2006. Cancer Immunosurveillance and Immunoediting: The Roles of Immunity in Suppressing Tumor Development and Shaping Tumor Immunogenicity. *Advances in Immunology.* United States: Elsevier Science & Technology, pp. 1-50.

SOENDERGAARD, M., 2022-last update, Biopanning of Phage Display Libraries. Available: https://www.cellorigins.com/biopanning?utm [10th March, 2025].

SOLEMANI ZADEH, A., GRÄSSER, A., DINTER, H., HERMES, M. and SCHINDOWSKI, K., 2019. Efficient Construction and Effective Screening of Synthetic Domain Antibody Libraries. *Methods and Protocols,* **2**(1),.

SPRANGER, S., DAI, D., HORTON, B. and GAJEWSKI, T.F., 2017. Tumor-Residing Batf3 Dendritic Cells Are Required for Effector T Cell Trafficking and Adoptive T Cell Therapy. *Cancer cell,* **31**(5), pp. 711-723.e4.

SPRIESTERSBACH, A., KUBICEK, J., SCHÄFER, F., BLOCK, H. and MAERTENS, B., 2015. Purification of His-Tagged Proteins. *Methods in Enzymology,* , pp. 1.

SPROUFFSKE, K., AGUILAR-RODRÍGUEZ, J. and WAGNER, A., 2016. How Archiving by Freezing Affects the Genome-Scale Diversity ofEscherichia coliPopulations. *Genome Biology and Evolution,* **8**(5), pp. 1290.

STARON, M., GRAY, S., MARSHALL, H., PARISH, I., CHEN, J., PERRY, C., CUI, G., LI, M. and KAECH, S., 2014. The Transcription Factor FoxO1 Sustains Expression of the Inhibitory Receptor PD-1 and Survival of Antiviral CD8+ T Cells during Chronic Infection. *Immunity,* **41**(5), pp. 802-814.

STEWART, J., 2021-last update, Keytruda FDA Approval History. Available: https://www.drugs.com/history/keytruda.html [3rd of May, 2023].

STONE, J.C., DOWER, N.A., STANG, S.L., BOTTORFF, D.A., EBINU, J.O., DICKIE, P. and OSTERGAARD, H.L., 2000. RasGRP is essential for mouse thymocyte differentiation and TCR signalling. *Nature immunology,* **1**(4), pp. 317-321.

STUDER, G., REMPFER, C., WATERHOUSE, A.M., GUMIENNY, R., HAAS, J. and SCHWEDE, T., 2020. QMEANDisCo—distance constraints applied on model quality estimation. *Bioinformatics,* **36**(6), pp. 1765–1771.

SULONG, P., ANUDIT, N., NUANUALSUWAN, S., MARIELA, S. and KHANTASUP, K., 2021. Application of phage display technology for the production of antibodies against Streptococcus suis serotype **2**. *PLOS ONE,* **16**(10),.

TAGLIAMENTO, M., AGOSTINETTO, E., BOREA, R., BRANDÃO, M., POGGIO, F., ADDEO, A. and LAMBERTINI, M., 2021. VISTA: A Promising Target for Cancer Immunotherapy? ImmunoTargets and therapy, **10**, pp. 185-200.

TAN, S., DAY, D., NICHOLLS, S.J. and SEGELOV, E., 2022. Immune Checkpoint Inhibitor Therapy in Oncology: Current Uses and Future Directions: JACC: CardioOncology State-of-the-Art Review. *JACC CardioOncology,* **4**(5), pp. 579-597.

TAN, Y., TIAN, T., LIU, W., ZHU, Z. and J. YANG, C., 2016. Advance in phage display technology for bioanalysis. *Biotechnology journal,* **11**(6), pp. 732–745.

THOMPSON, R.H., KUNTZ, S.M., LEIBOVICH, B.C., DONG, H., LOHSE, C.M., WEBSTER, W.S., SENGUPTA, S., FRANK, I., PARKER, A.S., ZINCKE, H., BLUTE, M.L., SEBO, T.J., CHEVILLE, J.C. and KWON, E.D., 2006. Tumor B7-H1 Is Associated with Poor Prognosis in Renal Cell Carcinoma Patients with Long-term Follow-up. *Cancer Research,* **66**(7), pp. 3381-3385.

TOKMAKOV, A.A., KUROTANI, A. and SATO, K., 2021. Protein pI and Intracellular Localization. *Frontiers in Molecular Biosciences,* **8**.

TOPALIAN, S.L., SZNOL, M., LEMING, P.D., LIPSON, E.J., PUZANOV, I., SMITH, D.C., TAUBE, J.M., WIGGINTON, J.M., KOLLIA, G.D., GUPTA, A., PARDOLL, D.M., SOSMAN, J.A., MCDERMOTT, D.F., STEPHEN HODI, F., KLUGER, H.M., CARVAJAL, R.D., SHARFMAN, W.H., BRAHMER, J.R., LAWRENCE, D.P., ATKINS, M.B. and POWDERLY, J.D., 2014. Survival, Durable Tumor Remission, and Long-Term Safety in Patients With Advanced Melanoma Receiving Nivolumab. *Journal of clinical oncology,* **32**(10), pp. 1020-1030.

Troubleshooting His-Tagged Protein Binding to Ni-NTA Columns2024-last update. Available: https://blog.interchim.com/troubleshooting-his-protein-ni-nta-columns/ [20th January, 2025].

TSKVITARIA-FULLER, I., ROZELLE, A.L., YIN, H.L. and WULFING, C., 2003. Regulation of Sustained Actin Dynamics by the TCR and Costimulation as a Mechanism of Receptor Localization. *The Journal of immunology (1950),* **171**(5), pp. 2287-2295.

TU, J., DING, Y., YING, X., WU, F., ZHOU, X., ZHANG, D., ZOU, H. and JI, J., 2016. Regulatory T cells, especially ICOS+ FOXP3+ regulatory T cells, are increased in the hepatocellular carcinoma microenvironment and predict reduced survival. *Scientific Reports,* **6**(1), pp. 35056.

TUTTLE, A.R., TRAHAN, N.D. and SON, M.S., 2022. Growth and Maintenance of Escherichia coli Laboratory Strains. *Current Protocols,* **1**(1),.

Universal validations. Available: http://molprobity.manchester.ac.uk/help/validation_options/validation_options.html#:~:text=Rotamer%20evaluation,-Overview&text=Protein%20sidechain%20geometry%20generally%20exhibits,rotamer%20definition%20are%20considered%20outliers [15th December, 2024].

URZAINQUI, A., MARTINEZ DEL HOYO, G., LAMANA, A., DE LA FUENTE, H., BARREIRO, O., OLAZABAL, I.M., MARTIN, P., WILD, M.K., VESTWEBER, D., GONZALEZ-AMARO, R. and SANCHEZ-MADRID, F., 2007. Functional Role of P-Selectin Glycoprotein Ligand 1/P-Selectin Interaction in the Generation of Tolerogenic Dendritic Cells. *The Journal of immunology (1950),* **179**(11), pp. 7457-7465.

Use of M13KO7 Helper Phage for isolation of single-stranded phagemid DNA. Available: https://www.neb.com/en/protocols/0001/01/01/use-of-m13ko7-helper-phage-for-isolation-of-single-stranded-phagemid-dna [5th January, 2025].

VAN SANDICK, J.W., BOERMEESTER, M.A., GISBERTZ, S.S., TEN BERGE, I.J.M., OUT, T.A., VAN DER POUW KRAAN, TINEKE C. T. M and VAN LANSCHOT, J.J.B., 2003. Lymphocyte subsets and T(h)1/T(h)2 immune responses in patients with adenocarcinoma of the oesophagus or oesophagogastric junction: relation to pTNM stage and clinical outcome. *Cancer immunology, immunotherapy,* **52**(10), pp. 617-624.

VAN SANDICK, J.W., GISBERTZ, S.S., TEN BERGE, I.J.M., BOERMEESTER, M.A., VAN DER POUW KRAAN, TINEKE C. T. M, OUT, T.A., OBERTOP, H. and VAN LANSCHOT, J.J.B., 2003. Immune responses and prediction of major infection in patients undergoing transhiatal or transthoracic esophagectomy for cancer. *Annals of surgery,* **237**(1), pp. 35-43.

VANIO, H., MAGEE, P.N., MCGREGOR, D.B. and MCMICHAEK, A.J., 1992. *Mechanisms of Carcinogenesis in Risk Identification.* No. 116 edn. Lyon, France: IARC Scientific Publication.

VAUPEL, P., HÖCKEL, M. and MAYER, A., 2007. Detection and characterization of tumor hypoxia using pO2 histography. *Antioxidants & redox signalling,* **9**(8), pp. 1221-1235.

VELAZQUEZ-SOTO, H., REAL, F. and JIMÉNEZ-MARTÍNEZ, M.C., 2022. Historical evolution, overview, and therapeutic manipulation of co-stimulatory molecules. *World journal of immunology,* **12**(1), pp. 1-8.

VIEIRA, J. and MESSING, J., a. *[1] PRODUCTION OF SINGLE-STRANDED PLASMID DNA 3 [1] Production of Single-Stranded Plasmid DNA.*

VODNIK, M., ZAGER, U., STRUKELJ, B. and LUNDER, M., 2011. Phage Display: Selecting Straws Instead of a Needle from a Haystack. *Molecules,* **16**(1), pp. 790.

VSIR V-set immunoregulatory receptor [Homo sapiens (human)]2025-last update. Available: https://www.ncbi.nlm.nih.gov/gene?Db=gene&Cmd=DetailsSearch&Term=64115 [5th December, 2025].

WANG, G., TAI, R., WU, Y., YANG, S., WANG, J., YU, X., LEI, L., SHAN, Z. and LI, N., 2020. The expression and immunoregulation of immune checkpoint molecule VISTA in autoimmune diseases and cancers. *Cytokine & growth factor reviews,* **52**, pp. 1-14.

WANG, J., WU, G., MANICK, B., HERNANDEZ, V., RENELT, M., ERICKSON, C., GUAN, J., SINGH, R., ROLLINS, S., SOLORZ, A., BI, M., LI, J., GRABOWSKI, D., DIRKX, J., TRACY, C., STUART, T., ELLINGHUYSEN, C., DESMOND, D., FOSTER, C. and KALABOKIS, V., 2019. VSIG-3 as a ligand of VISTA inhibits human T-cell function. *Immunology,* **156**(1), pp. 74-85.

WANG, L., RUBINSTEIN, R., LINES, J.L., WASIUK, A., AHONEN, C., GUO, Y., LU, L., GONDEK, D., WANG, Y., FAVA, R.A., FISER, A., ALMO, S. and NOELLE, R.J., 2011. VISTA, a novel mouse Ig superfamily ligand that negatively regulates T cell responses. *The Journal of Experimental Medicine,* **208**(3), pp. 577-592.

WANG, M., ZHAO, J., ZHANG, L., WEI, F., LIAN, Y., WU, Y., GONG, Z., ZHANG, S., ZHOU, J., CAO, K., LI, X., XIONG, W., LI, G., ZENG, Z. and GUO, C., 2017. Role of tumor microenvironment in tumorigenesis. *Journal of Cancer,* **8**(5), pp. 761-773.

Ward's Method (Minimum variance method) [Statistics How To], [Online]. Available: https://www.statisticshowto.com/wards-method/

WATERHOUSE, A., BERTONI, M., BIENERT, S., STUDER, G., TAURIELLO, G., GUMIENNY, R., HEER, F.T., DE BEER, T.A.P., REMPFER, C., BORDOLI, L., LEPORE, R. and SCHWEDE, T., 2018. SWISS-MODEL: homology modelling of protein structures and complexes. *Nucleic Acids Research,* **46**(W1), pp. W296.

WELSH, R.M., 2001. Assessing Cd8 T Cell Number and Dysfunction in the Presence of Antigen. *The Journal of Experimental Medicine,* **193**(5), pp. F19-F22.

What is the Difference Between Direct and Indirect ELISA?. Available: https://shop.surmodics.com/what-is-the-difference-between-direct-and-indirect-elisa#:~:text=The%20advantage%20of%20a%20direct,binding%20to%20the%20target%20protein. [25th January, 2025].

What light wavelength regions are used?. Available: https://www.ssi.shimadzu.com/service-support/faq/uv-vis/light-and-theory/4/index.html [5th October, 2024].

When your his-tagged constructs don't bind—troubleshooting your protein purification woes2018-last update. Available: https://www.takarabio.com/about/bioview-blog/tips-and-troubleshooting/when-your-his-tagged-constructs-dont-bind [2nd November, 2024].

WHERRY, E.J. and KURACHI, M., 2015. Molecular and cellular insights into T cell exhaustion. *Nature reviews. Immunology,* **15**(8), pp. 486-499.

WHERRY, E.J., BLATTMAN, J.N., MURALI-KRISHNA, K., VAN DER MOST, R. and AHMED, R., 2003. Viral Persistence Alters CD8 T-Cell Immunodominance and Tissue Distribution and Results in Distinct Stages of Functional Impairment. *Journal of Virology,* **77**(8), pp. 4911-4927.

WHERRY, J.E., 2011. T cell exhaustion. *Nature,* **12**, pp. 492-499.

WING, K., ONISHI, Y., PRIETO-MARTIN, P., YAMAGUCHI, T., MIYARA, M., FEHERVARI, Z., NOMURA, T. and SAKAGUCHI, S., 2008. CTLA-4 Control over Foxp3^{+} Regulatory T Cell Function. *Science,* **322**(5899), pp. 271-275.

WISEMAN, B.S. and WERB, Z., 2002. Stromal Effects on Mammary Gland Development and Breast Cancer. *Science,* **296**(5570), pp. 1046-1049.

WOLCHOK, J.D., CHIARION-SILENI, V., GONZALEZ, R., GROB, J., RUTKOWSKI, P., LAO, C.D., COWEY, C.L., SCHADENDORF, D., WAGSTAFF, J., DUMMER, R., FERRUCCI, P.F., SMYLIE, M., BUTLER, M.O., HILL, A., MÁRQUEZ-RODAS, I., HAANEN, J.B.A.G., GUIDOBONI, M., MAIO, M., SCHÖFFSKI, P., CARLINO, M.S., LEBBÉ, C., MCARTHUR, G., ASCIERTO, P.A., DANIELS, G.A., LONG, G.V., BAS, T., RITCHINGS, C., LARKIN, J. and HODI, F.S., 2022. Long-Term Outcomes With Nivolumab Plus Ipilimumab or Nivolumab Alone Versus Ipilimumab in Patients With Advanced Melanoma. *Journal of Clinical Oncology,* **10** (2) pp. 127-137

WOLF, A., STRATMANN, J.A., SHAID, S., NIKLAS, N., CALLEJA, A., UBHI, H., MUNRO, R., WALDENBERGER, D., CARROLL, R., DAUMONT, M.J., PENROD, J.R., LACOIN, L. and ROHDE, G., 2023. Evolution of treatment patterns and survival outcomes in patients with advanced non-small cell lung cancer treated at Frankfurt University Hospital in 2012-2018. *BMC pulmonary medicine,* **23**(1), pp. 16.

WOODS, M.L., CABAÑAS, C. and SHIMIZU, Y., 2000. Activation-dependent changes in soluble fibronectin binding and expression of β1 integrin activation epitopes in T cells: relationship to T cell adhesion and migration. *European journal of immunology,* **30**(1), pp. 38-49.

WU, C., CAO, X. and ZHANG, X., 2021. VISTA inhibitors in cancer immunotherapy: a short perspective on recent progresses. *RSC Medicinal Chemistry,* **12**(10), pp. 1672-1679.

XIAO, T., CHEN, W., WANG, S., HUANG, S., CHIANG, C., ZOU, Y., ZHAO, Y. and ZHENG, D., 2020. Tacrolimus and ascomycin inhibit melanoma cell growth, migration and invasion via targeting nuclear factor of activated T-cell 3. *Melanoma research,* **30**(4), pp. 325-335.

XIONG, X., QU, K., CIAZYNSKA, K.A., HOSMILLO, M., CARTER, A.P., EBRAHIMI, S., KE, Z., SCHERES, S.H.W., BERGAMASCHI, L., GRICE, G.L., ZHANG, Y., BRADLEY, J., LYONS, P.A., SMITH, K.G.C., TOSHNER, M., ELMER, A., RIBEIRO, C., KOURAMPA, J., JOSE, S., KENNET, J., ROWLANDS, J., MEADOWS, A., O'BRIEN, C., RASTALL, R., CRUCUSIO, C., HEWITT, S., PRICE, J., CALDER, J., CANNA, L., BUCKE, A., TORDESILLAS, H., HARRIS, J., RUFFOLO, V., DOMINGO, J., GRAVES, B., BUTCHER, H., CAPUTO, D., LE GRESLEY, E., DUNMORE, B.J., MARTIN, J., LEGCHENKO, E., TREACY, C., HUANG, C., WOOD, J., SUTCLIFFE, R., HODGSON, J., SHIH, J., GRAF, S., TONG, Z., MESCIA, F., TILLY, T., O'DONNELL, C., HUNTER, K., POINTON, L., POND, N., WYLOT, M., JONES, E., FAWKE, S., BULLMAN, B., BERGAMASCHI, L., TURNER, L., JARVIS, I., OMARJEE, O., DE SA, A., MARSDEN, J., BETANCOURT, A., PERERA, M., EPPING, M., RICHOZ, N., BOWER, G., SHARMA, R., NICE, F., HUHN, O., STARK, H., WALKER, N., STIRRUPS, K., OVINGTON, N., DEWHUST, E., LI, E., PAPADIA, S., NATHAN, J.A., BAKER, S., JAMES, L.C., BAXENDALE, H.E., GOODFELLOW, I., DOFFINGER, R. and BRIGGS, J.A.G., 2021. *A thermostable, closed SARS-CoV-2 spike protein trimer.* Springer Science and Business Media LLC.

YAMAMOTO, K.R., ALBERTS, B.M., BENZINGER, R., LAWHORNE, L. and TREIBER, G., 1970. Rapid Bacteriophage Sedimentation in the Presence of Polyethylene Glycol and Its Application to Large-Scale Virus Purification. *Virology,* **40**(3), pp. 734-744

YAMAZAKI, T., AKIBA, H., IWAI, H., MATSUDA, H., AOKI, M., TANNO, Y., SHIN, T., TSUCHIYA, H., PARDOLL, D.M., OKUMURA, K., AZUMA, M. and YAGITA, H., 2002. Expression of Programmed Death 1 Ligands by Murine T Cells and APC. *The Journal of immunology (1950),* **169**(10), pp. 5538-5545.

YASINSKA, I.M., MEYER, N.H., SCHLICHTNER, S., HUSSAIN, R., SILIGARDI, G., CASELY-HAYFORD, M., FIEDLER, W., WELLBROCK, J., DESMET, C., CALZOLAI, L., VARANI, L., BERGER, S.M., RAAP, U., GIBBS, B.F., FASLER-KAN, E. and SUMBAYEV, V.V., 2020. Ligand-Receptor Interactions of Galectin-9 and VISTA Suppress Human T Lymphocyte Cytotoxic Activity. *Frontiers in immunology,* **11**, pp. 580557.

YUAN, L., TATINENI, J., MAHONEY, K.M. and FREEMAN, G.J., 2021. VISTA: A Mediator of Quiescence and a Promising Target in Cancer Immunotherapy. *Trends in immunology,* **42**(3), pp. 209-227.

YUM, J.I. and HONG, Y., 2021. Terminating Cancer by Blocking VISTA as a Novel Immunotherapy: Hasta la vista, baby. *Frontiers in oncology,* **11**, pp. 658488.

ZAJAC, A.J., BLATTMAN, J.N., MURALI-KRISHNA, K., SOURDIVE, D.J., SURESH, M., ALTMAN, J.D. and AHMED, R., 1998. Viral Immune Evasion Due to Persistence of Activated T Cells Without Effector Function. *The Journal of Experimental Medicine,* **188**(12), pp. 2205-2213.

ZHANG, H., XIE, X., ZHU, X., ZHU, J., HAO, C., LU, Q., DING, L., LIU, Y., ZHOU, L., LIU, Y., HUANG, C., WEN, C. and YE, Q., 2005. Stimulatory Cross-talk between NFAT3 and Estrogen Receptor in Breast Cancer Cells. *The Journal of biological chemistry,* **280**(52), pp. 43188-43197.

ZHU, J., LIANG, L., JIAO, Y. and LIU, L., 2015. Enhanced Invasion of Metastatic Cancer Cells via Extracellular Matrix Interface. *PLoS ONE,* **10**(2), pp. e0118058.

ZHU, X., YAO, Y., LIANG, H., XU, S., DONG, N., YU, Y. and SHENG, Z., 2009. The Effect of High Mobility Group Box-1 Protein on Splenic Dendritic Cell Maturation in Rats. *Journal of interferon & cytokine research,* **29**(10), pp. 677-686.

Chapter 6:

Appendix

6.1. Infecteion of *E.coli* with phage pools streaked on ampicillin plates

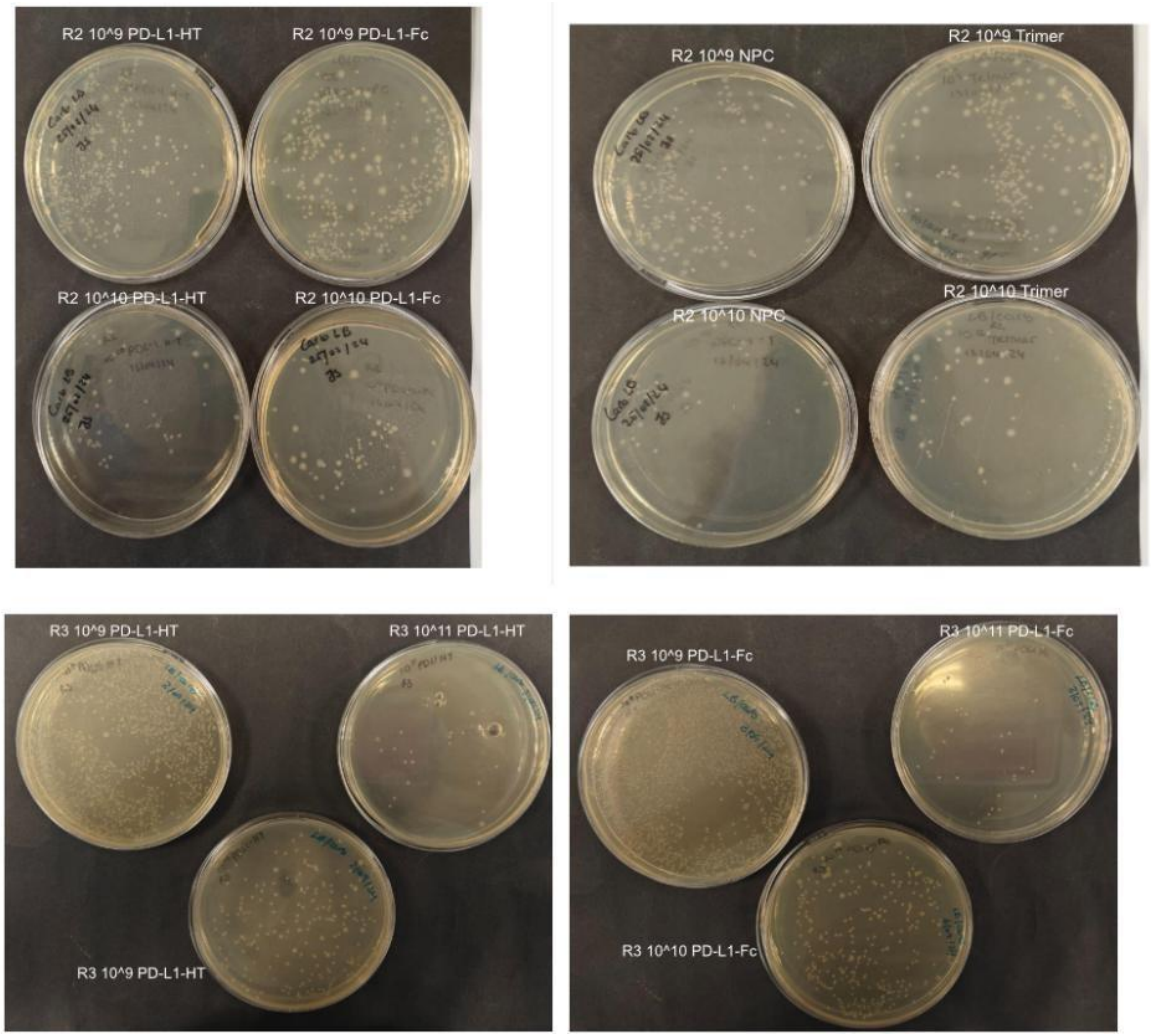

Figure 6.1: Growth of E.coli infected with phage pools from biopanning rounds 2–4 against various baits: PD-L1-HT, PD-L1-Fc, Trimer, and No Protein Control (NPC). Phage pools from rounds 2–4 were diluted to 10^9 and 10^{10} (with an additional 10^{11} dilution in round 3) and incubated for 5 minutes with mid-log phase *E.coli* to allow for single-phage infection events. Following incubation, the mixtures were evenly spread onto LB agar plates containing ampicillin and incubated overnight at 37 °C. The next day, plates with 30–300 colonies were counted to calculate colony-forming units per milliliter (CFU/mL). The round no, dilution and the bait used for biopanning of phage pools were written on top of or next to the plate image.

Round no. of phage pools biopanned against different baits	Colony Count	Dilution	CFU/ml (phage dilution Colony Count) 0.5
R2 phage pools biopanned against PD-L1-Fc	51	10^{10}	1.02×10^{12}
R2 phage pools biopanned against PD-L1-HT	41	10^{10}	8.20×10^{11}
R2 phage pools biopanned against trimer	31	10^{10}	6.20×10^{11}
R3 phage pools biopanned against PD-L1-Fc	31	10^{11}	6.20×10^{12}
R3 phage pools biopanned against PD-L1-HT	31	10^{11}	6.20×10^{12}
R3 phage pools biopanned against trimer	139	10^{10}	2.78×10^{12}
R4 phage pools biopanned against PD-L1-Fc	301	10^{10}	6.02×10^{12}
R4 phage pools biopanned against PD-L1-HT	35	10^{10}	7.00×10^{11}
R4 phage pools biopanned against trimer	111	10^{10}	2.22×10^{12}

Table 6.1: The measurement of the CFU/ml phage pools from biopanning rounds 2–4 against various baits: PD-L1-HT, PD-L1-Fc, trimer. The measurement of the CFU/ml was done on Rounds 2-4 biopanned against different baits. The CFU/ml was calculated by multiplying the number of colonies by the phage dilution and dividing by the constant 0.5. This was done to ensure that the phage titre remained equivalent during different rounds.

6.2. Checking the quality of DNA using Nanodrop

Clone no.	Conc. ng/µl	260/280	260/230
1	140.5	1.86	1.96
2	139.7	1.86	2.24
3	151.0	1.86	2.21
4	101.3	1.85	2.15
5	111.3	1.84	2.18
6	135.7	1.86	2.13
7	126.6	1.87	2.28
8	129.5	1.86	2.10
9	108.1	1.83	2.06
10	129.5	1.88	2.23
11	129.3	1.86	2.25
12	110.8	1.84	2.09
13	167.7	1.82	1.72
14	128.3	1.85	2.19
15	147.2	1.86	2.16
16			
17	174.6	1.86	2.10
18	150.1	1.83	2.23
19			
20	180.9	1.85	2.19
21	149.8	1.83	2.09
22	135.3	1.82	2.11
23	151.6	1.83	2.15
24	181.9	1.81	1.97
25	165.0	1.85	2.25

26			
27	201.1	1.95	2.34
28	143.1	1.84	2.14
29	172.4	1.84	2.18
30	133.1	1.83	2.15

Clone no.	**Conc. ng/µl**	**260/280**	**260/230**
31	192.2	1.86	2.27
32	236.6	1.86	2.16
33	245.3	1.87	2.24
34	248.3	1.86	2.20
35	235.4	1.86	2.12
36	232.6	1.86	2.08
37	273.2	1.87	2.13
38	264.7	1.88	2.20
39	267.4	1.87	2.15
40	273.2	1.86	2.13
41	223.7	1.86	2.12
42	233.2	1.87	2.15
43	169.9	1.85	2.15
44	197.6	1.87	2.19
45	195.2	1.87	2.24
46	201.8	1.88	2.25
47	203.8	1.88	2.26
48	198.5	1.88	2.25
49	224.1	1.87	2.25

50	225.4	1.87	2.21
51	266.0	1.88	2.27
52	159.6	1.88	2.28
53	224.1	1.87	2.24
54	200.6	1.87	2.28
55	243.1	1.88	2.20
56	239.7	1.88	2.25
57	238.2	1.87	2.18
58	226.7	1.87	2.15
59	227.5	1.87	2.20
60	231.3	1.87	2.25

Table 6.2: Assessment of DNA concentration and purity of clones 1-60 using Nanodrop spectrophotometry. DNA purity was evaluated by measuring absorbance at 260/280 and 260/230 nm ratios. DNA concentrations ranged from 101.3 to 273.2 ng/µL. The 260/280 ratios were close to the expected value of ~1.8 for pure DNA, with clone 27 showing the highest deviation at 1.95. Approximately half of the samples had 260/230 ratios within the ideal range of 2.0–2.2, suggesting that some clones may contain impurities.

6.3. Protein sequence of clones 1-60

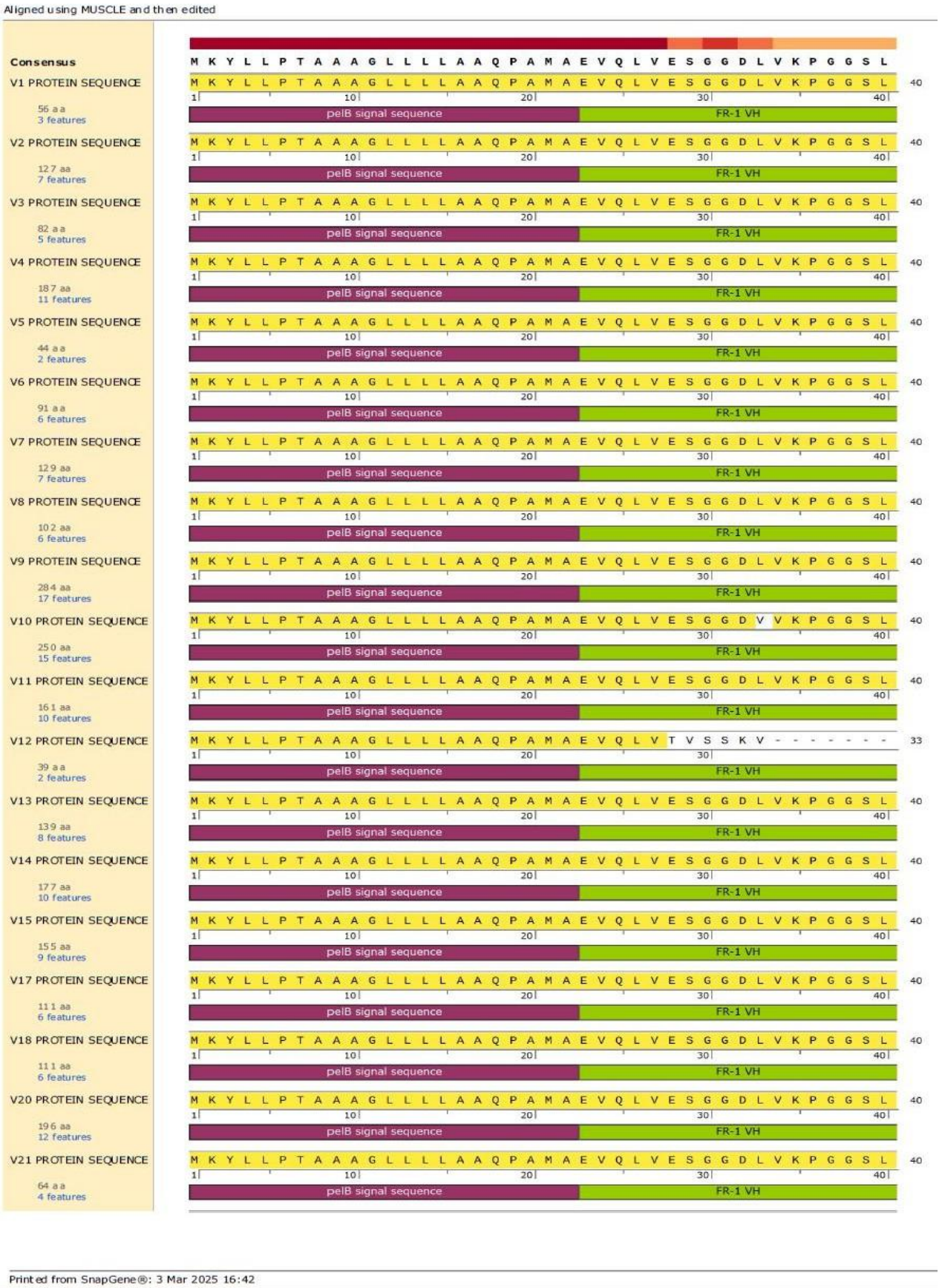

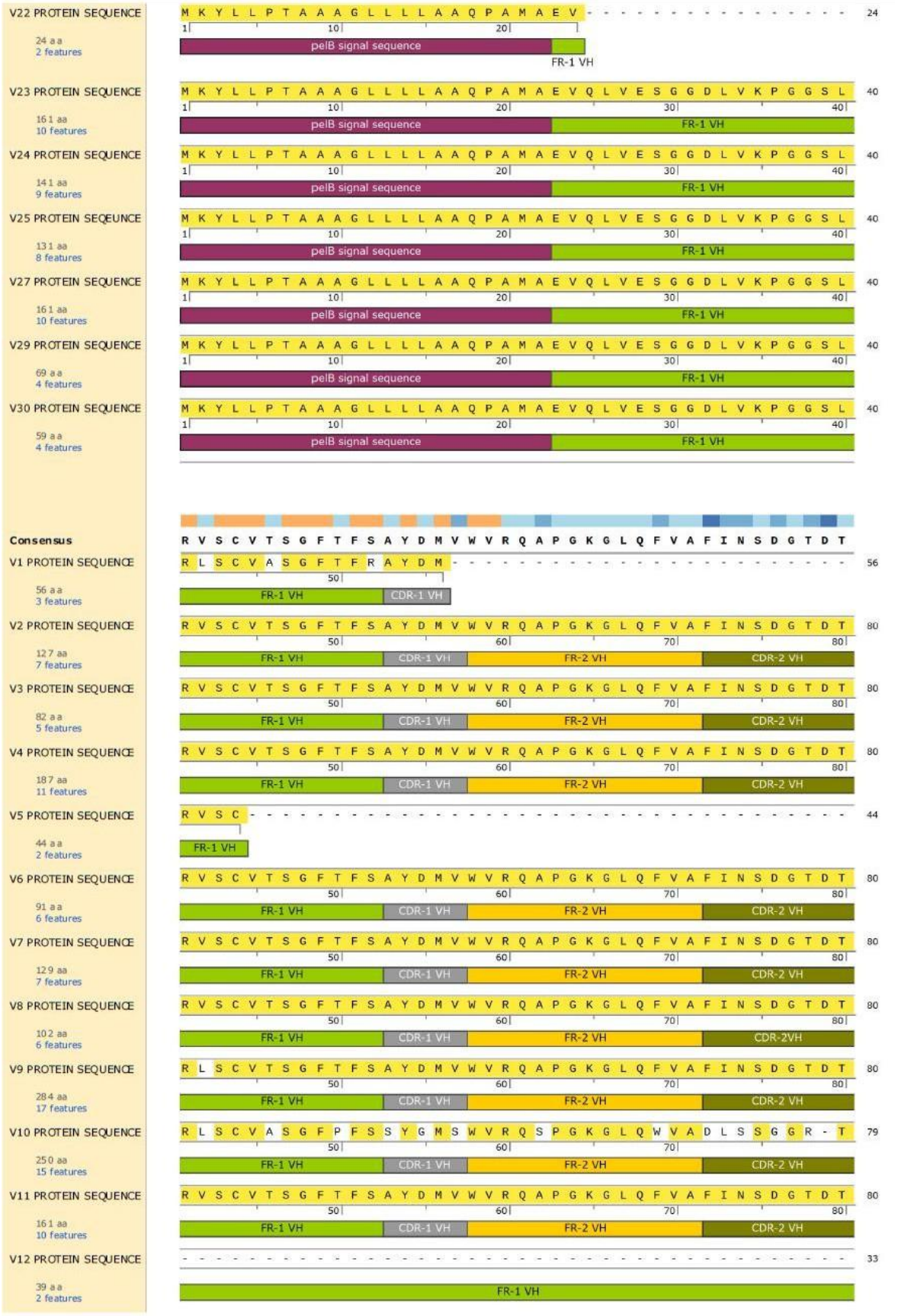
V22 PROTEIN SEQUENCE
M K Y L L P T A A A G L L L L A A Q P A M A E V - 24
24 a a
2 features
pelB signal sequence
FR-1 VH
V23 PROTEIN SEQUENCE
M K Y L L P T A A A G L L L L A A Q P A M A E V Q L V E S G G D L V K P G G S L 40
161 aa
10 features
pelB signal sequence
FR-1 VH
V24 PROTEIN SEQUENCE
M K Y L L P T A A A G L L L L A A Q P A M A E V Q L V E S G G D L V K P G G S L 40
141 aa
9 features
pelB signal sequence
FR-1 VH
V25 PROTEIN SEQEUNCE
M K Y L L P T A A A G L L L L A A Q P A M A E V Q L V E S G G D L V K P G G S L 40
131 aa
8 features
pelB signal sequence
FR-1 VH
V27 PROTEIN SEQUENCE
M K Y L L P T A A A G L L L L A A Q P A M A E V Q L V E S G G D L V K P G G S L 40
161 aa
10 features
pelB signal sequence
FR-1 VH
V29 PROTEIN SEQUENCE
M K Y L L P T A A A G L L L L A A Q P A M A E V Q L V E S G G D L V K P G G S L 40
69 a a
4 features
pelB signal sequence
FR-1 VH
V30 PROTEIN SEQUENCE
M K Y L L P T A A A G L L L L A A Q P A M A E V Q L V E S G G D L V K P G G S L 40
59 a a
4 features
pelB signal sequence
FR-1 VH
Consensus
R V S C V T S G F T F S A Y D M V W V R Q A P G K G L Q F V A F I N S D G T D T
V1 PROTEIN SEQUENCE
R L S C V A S G F T F R A Y D M - 56
56 a a
3 features
FR-1 VH
CDR-1 VH
V2 PROTEIN SEQUENCE
R V S C V T S G F T F S A Y D M V W V R Q A P G K G L Q F V A F I N S D G T D T 80
127 aa
7 features
FR-1 VH
CDR-1 VH
FR-2 VH
CDR-2 VH
V3 PROTEIN SEQUENCE
R V S C V T S G F T F S A Y D M V W V R Q A P G K G L Q F V A F I N S D G T D T 80
82 a a
5 features
FR-1 VH
CDR-1 VH
FR-2 VH
CDR-2 VH
V4 PROTEIN SEQUENCE
R V S C V T S G F T F S A Y D M V W V R Q A P G K G L Q F V A F I N S D G T D T 80
187 aa
11 features
FR-1 VH
CDR-1 VH
FR-2 VH
CDR-2 VH
V5 PROTEIN SEQUENCE
R V S C - 44
44 a a
2 features
FR-1 VH
V6 PROTEIN SEQUENCE
R V S C V T S G F T F S A Y D M V W V R Q A P G K G L Q F V A F I N S D G T D T 80
91 a a
6 features
FR-1 VH
CDR-1 VH
FR-2 VH
CDR-2 VH
V7 PROTEIN SEQUENCE
R V S C V T S G F T F S A Y D M V W V R Q A P G K G L Q F V A F I N S D G T D T 80
129 aa
7 features
FR-1 VH
CDR-1 VH
FR-2 VH
CDR-2 VH
V8 PROTEIN SEQUENCE
R V S C V T S G F T F S A Y D M V W V R Q A P G K G L Q F V A F I N S D G T D T 80
102 aa
6 features
FR-1 VH
CDR-1 VH
FR-2 VH
CDR-2VH
V9 PROTEIN SEQUENCE
R L S C V T S G F T F S A Y D M V W V R Q A P G K G L Q F V A F I N S D G T D T 80
284 aa
17 features
FR-1 VH
CDR-1 VH
FR-2 VH
CDR-2 VH
V10 PROTEIN SEQUENCE
R L S C V A S G F P F S S Y G M S W V R Q S P G K G L Q W V A D L S S G G R - T 79
250 aa
15 features
FR-1 VH
CDR-1 VH
FR-2 VH
CDR-2 VH
V11 PROTEIN SEQUENCE
R V S C V T S G F T F S A Y D M V W V R Q A P G K G L Q F V A F I N S D G T D T 80
161 aa
10 features
FR-1 VH
CDR-1 VH
FR-2 VH
CDR-2 VH
V12 PROTEIN SEQUENCE
- 33
39 a a
2 features
FR-1 VH

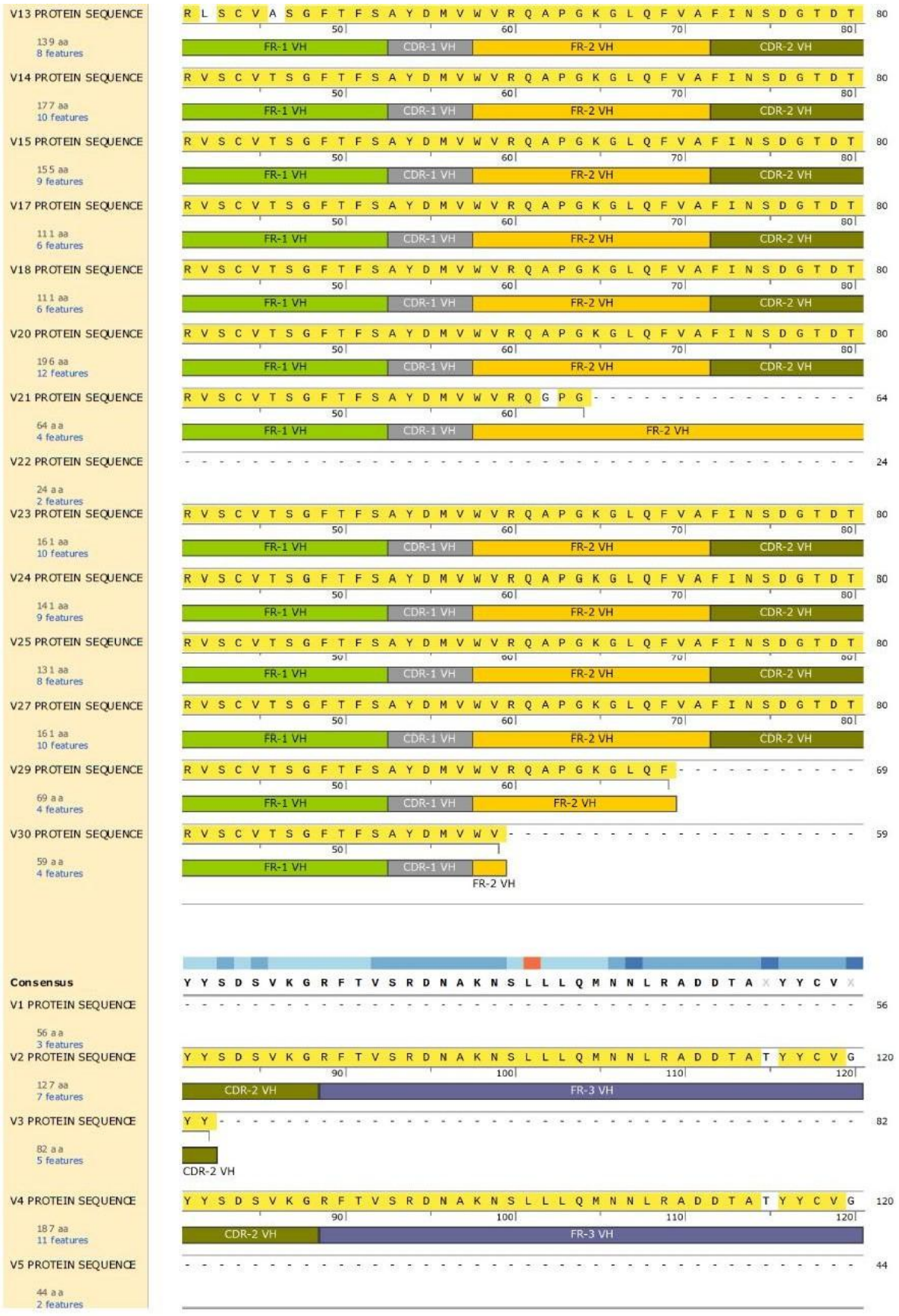
V13 PROTEIN SEQUENCE
R L S C V A S G F T F S A Y D M V W V R Q A P G K G L Q F V A F I N S D G T D T 80
50 60 70 80
139 aa
8 features
FR-1 VH CDR-1 VH FR-2 VH CDR-2 VH
V14 PROTEIN SEQUENCE
R V S C V T S G F T F S A Y D M V W V R Q A P G K G L Q F V A F I N S D G T D T 80
50 60 70 80
177 aa
10 features
FR-1 VH CDR-1 VH FR-2 VH CDR-2 VH
V15 PROTEIN SEQUENCE
R V S C V T S G F T F S A Y D M V W V R Q A P G K G L Q F V A F I N S D G T D T 80
50 60 70 80
155 aa
9 features
FR-1 VH CDR-1 VH FR-2 VH CDR-2 VH
V17 PROTEIN SEQUENCE
R V S C V T S G F T F S A Y D M V W V R Q A P G K G L Q F V A F I N S D G T D T 80
50 60 70 80
111 aa
6 features
FR-1 VH CDR-1 VH FR-2 VH CDR-2 VH
V18 PROTEIN SEQUENCE
R V S C V T S G F T F S A Y D M V W V R Q A P G K G L Q F V A F I N S D G T D T 80
50 60 70 80
111 aa
6 features
FR-1 VH CDR-1 VH FR-2 VH CDR-2 VH
V20 PROTEIN SEQUENCE
R V S C V T S G F T F S A Y D M V W V R Q A P G K G L Q F V A F I N S D G T D T 80
50 60 70 80
196 aa
12 features
FR-1 VH CDR-1 VH FR-2 VH CDR-2 VH
V21 PROTEIN SEQUENCE
R V S C V T S G F T F S A Y D M V W V R Q G P G - - - - - - - - - - - - - - - - 64
50 60
64 aa
4 features
FR-1 VH CDR-1 VH FR-2 VH
V22 PROTEIN SEQUENCE
- 24
24 aa
2 features
V23 PROTEIN SEQUENCE
R V S C V T S G F T F S A Y D M V W V R Q A P G K G L Q F V A F I N S D G T D T 80
50 60 70 80
161 aa
10 features
FR-1 VH CDR-1 VH FR-2 VH CDR-2 VH
V24 PROTEIN SEQUENCE
R V S C V T S G F T F S A Y D M V W V R Q A P G K G L Q F V A F I N S D G T D T 80
50 60 70 80
141 aa
9 features
FR-1 VH CDR-1 VH FR-2 VH CDR-2 VH
V25 PROTEIN SEQEUNCE
R V S C V T S G F T F S A Y D M V W V R Q A P G K G L Q F V A F I N S D G T D T 80
50 60 70 80
131 aa
8 features
FR-1 VH CDR-1 VH FR-2 VH CDR-2 VH
V27 PROTEIN SEQUENCE
R V S C V T S G F T F S A Y D M V W V R Q A P G K G L Q F V A F I N S D G T D T 80
50 60 70 80
161 aa
10 features
FR-1 VH CDR-1 VH FR-2 VH CDR-2 VH
V29 PROTEIN SEQUENCE
R V S C V T S G F T F S A Y D M V W V R Q A P G K G L Q F - - - - - - - - - - - 69
50 60
69 aa
4 features
FR-1 VH CDR-1 VH FR-2 VH
V30 PROTEIN SEQUENCE
R V S C V T S G F T F S A Y D M V W V - 59
50
59 aa
4 features
FR-1 VH CDR-1 VH
FR-2 VH
Consensus
Y Y S D S V K G R F T V S R D N A K N S L L L Q M N N L R A D D T A X Y Y C V X
V1 PROTEIN SEQUENCE
- 56
56 aa
3 features
V2 PROTEIN SEQUENCE
Y Y S D S V K G R F T V S R D N A K N S L L L Q M N N L R A D D T A T Y Y C V G 120
90 100 110 120
127 aa
7 features
CDR-2 VH FR-3 VH
V3 PROTEIN SEQUENCE
Y Y - 82
82 aa
5 features
CDR-2 VH
V4 PROTEIN SEQUENCE
Y Y S D S V K G R F T V S R D N A K N S L L L Q M N N L R A D D T A T Y Y C V G 120
90 100 110 120
187 aa
11 features
CDR-2 VH FR-3 VH
V5 PROTEIN SEQUENCE
- 44
44 aa
2 features

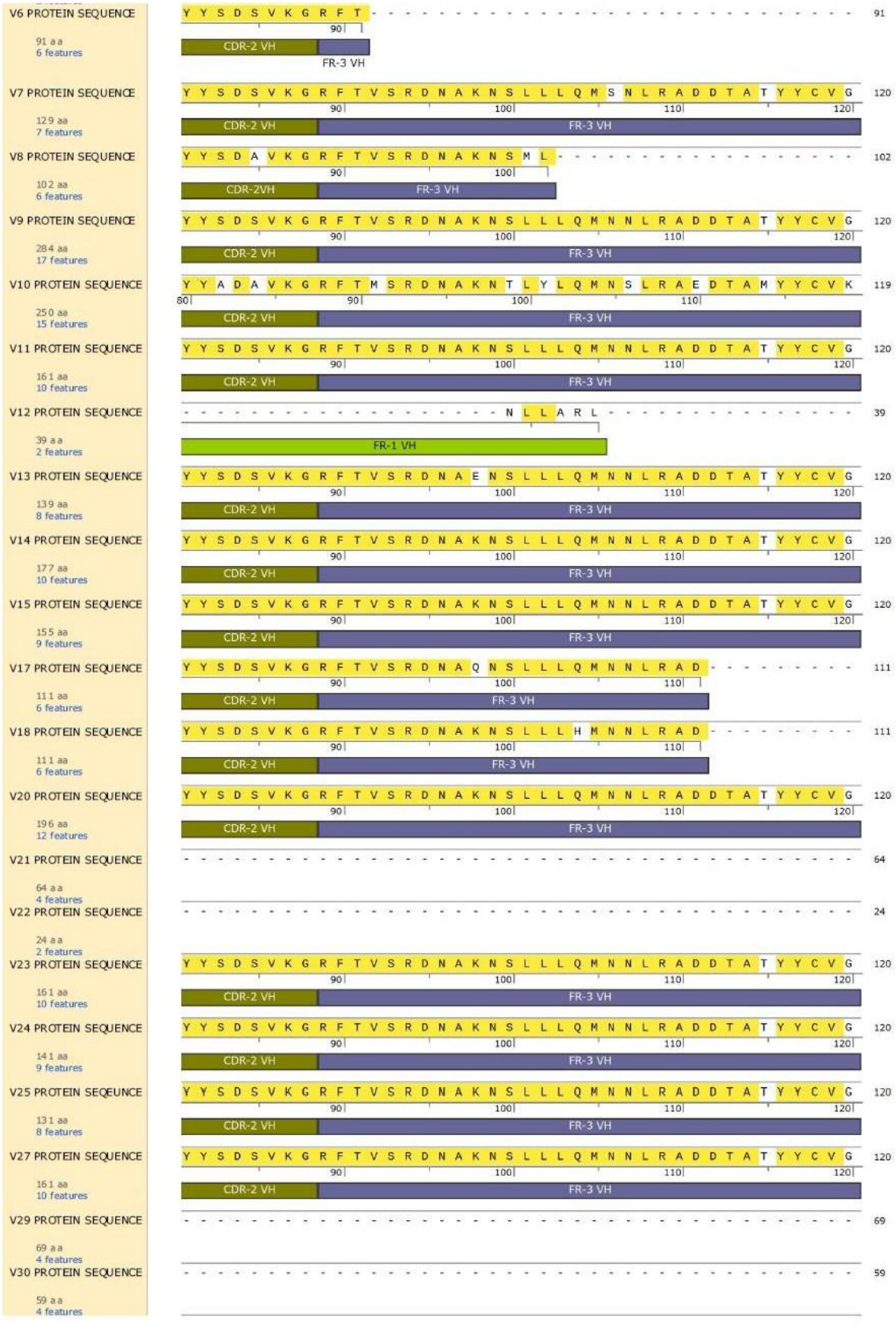
V6 PROTEIN SEQUENCE
Y Y S D S V K G R F T
91
91 a a
6 features
CDR-2 VH
FR-3 VH
V7 PROTEIN SEQUENCE
Y Y S D S V K G R F T V S R D N A K N S L L L Q M S N L R A D D T A T Y Y C V G
120
129 aa
7 features
CDR-2 VH
FR-3 VH
V8 PROTEIN SEQUENCE
Y Y S D A V K G R F T V S R D N A K N S M L
102
102 aa
6 features
CDR-2VH
FR-3 VH
V9 PROTEIN SEQUENCE
Y Y S D S V K G R F T V S R D N A K N S L L L Q M N N L R A D D T A T Y Y C V G
120
284 aa
17 features
CDR-2 VH
FR-3 VH
V10 PROTEIN SEQUENCE
Y Y A D A V K G R F T M S R D N A K N T L Y L Q M N S L R A E D T A M Y Y C V K
119
250 aa
15 features
CDR-2 VH
FR-3 VH
V11 PROTEIN SEQUENCE
Y Y S D S V K G R F T V S R D N A K N S L L L Q M N N L R A D D T A T Y Y C V G
120
161 aa
10 features
CDR-2 VH
FR-3 VH
V12 PROTEIN SEQUENCE
N L L A R L
39
39 a a
2 features
FR-1 VH
V13 PROTEIN SEQUENCE
Y Y S D S V K G R F T V S R D N A E N S L L L Q M N N L R A D D T A T Y Y C V G
120
139 aa
8 features
CDR-2 VH
FR-3 VH
V14 PROTEIN SEQUENCE
Y Y S D S V K G R F T V S R D N A K N S L L L Q M N N L R A D D T A T Y Y C V G
120
177 aa
10 features
CDR-2 VH
FR-3 VH
V15 PROTEIN SEQUENCE
Y Y S D S V K G R F T V S R D N A K N S L L L Q M N N L R A D D T A T Y Y C V G
120
155 aa
9 features
CDR-2 VH
FR-3 VH
V17 PROTEIN SEQUENCE
Y Y S D S V K G R F T V S R D N A Q N S L L L Q M N N L R A D
111
111 aa
6 features
CDR-2 VH
FR-3 VH
V18 PROTEIN SEQUENCE
Y Y S D S V K G R F T V S R D N A K N S L L L H M N N L R A D
111
111 aa
6 features
CDR-2 VH
FR-3 VH
V20 PROTEIN SEQUENCE
Y Y S D S V K G R F T V S R D N A K N S L L L Q M N N L R A D D T A T Y Y C V G
120
196 aa
12 features
CDR-2 VH
FR-3 VH
V21 PROTEIN SEQUENCE
64
64 a a
4 features
V22 PROTEIN SEQUENCE
24
24 a a
2 features
V23 PROTEIN SEQUENCE
Y Y S D S V K G R F T V S R D N A K N S L L L Q M N N L R A D D T A T Y Y C V G
120
161 aa
10 features
CDR-2 VH
FR-3 VH
V24 PROTEIN SEQUENCE
Y Y S D S V K G R F T V S R D N A K N S L L L Q M N N L R A D D T A T Y Y C V G
120
141 aa
9 features
CDR-2 VH
FR-3 VH
V25 PROTEIN SEQEUNCE
Y Y S D S V K G R F T V S R D N A K N S L L L Q M N N L R A D D T A T Y Y C V G
120
131 aa
8 features
CDR-2 VH
FR-3 VH
V27 PROTEIN SEQUENCE
Y Y S D S V K G R F T V S R D N A K N S L L L Q M N N L R A D D T A T Y Y C V G
120
161 aa
10 features
CDR-2 VH
FR-3 VH
V29 PROTEIN SEQUENCE
69
69 a a
4 features
V30 PROTEIN SEQUENCE
59
59 a a
4 features

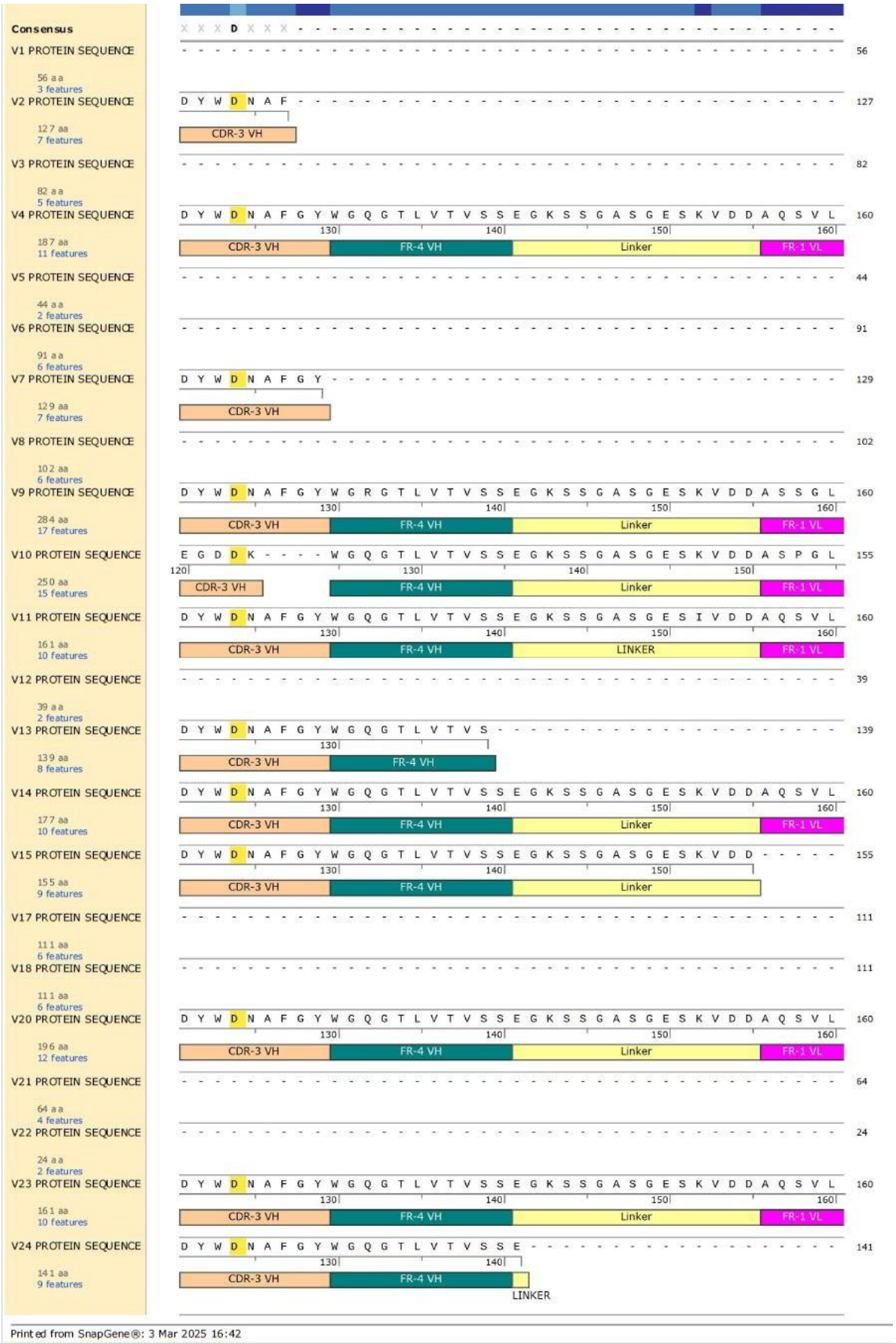
Consensus
V1 PROTEIN SEQUENCE
56 a a
3 features
V2 PROTEIN SEQUENCE
127 aa
7 features
CDR-3 VH
V3 PROTEIN SEQUENCE
82 a a
5 features
V4 PROTEIN SEQUENCE
187 aa
11 features
CDR-3 VH
FR-4 VH
Linker
FR-1 VL
V5 PROTEIN SEQUENCE
44 a a
2 features
V6 PROTEIN SEQUENCE
91 a a
6 features
V7 PROTEIN SEQUENCE
129 aa
7 features
CDR-3 VH
V8 PROTEIN SEQUENCE
102 aa
6 features
V9 PROTEIN SEQUENCE
284 aa
17 features
CDR-3 VH
FR-4 VH
Linker
FR-1 VL
V10 PROTEIN SEQUENCE
250 aa
15 features
CDR-3 VH
FR-4 VH
Linker
FR-1 VL
V11 PROTEIN SEQUENCE
161 aa
10 features
CDR-3 VH
FR-4 VH
LINKER
FR-1 VL
V12 PROTEIN SEQUENCE
39 a a
2 features
V13 PROTEIN SEQUENCE
139 aa
8 features
CDR-3 VH
FR-4 VH
V14 PROTEIN SEQUENCE
177 aa
10 features
CDR-3 VH
FR-4 VH
Linker
FR-1 VL
V15 PROTEIN SEQUENCE
155 aa
9 features
CDR-3 VH
FR-4 VH
Linker
V17 PROTEIN SEQUENCE
111 aa
6 features
V18 PROTEIN SEQUENCE
111 aa
6 features
V20 PROTEIN SEQUENCE
196 aa
12 features
CDR-3 VH
FR-4 VH
Linker
FR-1 VL
V21 PROTEIN SEQUENCE
64 a a
4 features
V22 PROTEIN SEQUENCE
24 a a
2 features
V23 PROTEIN SEQUENCE
161 aa
10 features
CDR-3 VH
FR-4 VH
Linker
FR-1 VL
V24 PROTEIN SEQUENCE
141 aa
9 features
CDR-3 VH
FR-4 VH
LINKER
Printed from SnapGene®: 3 Mar 2025 16:42

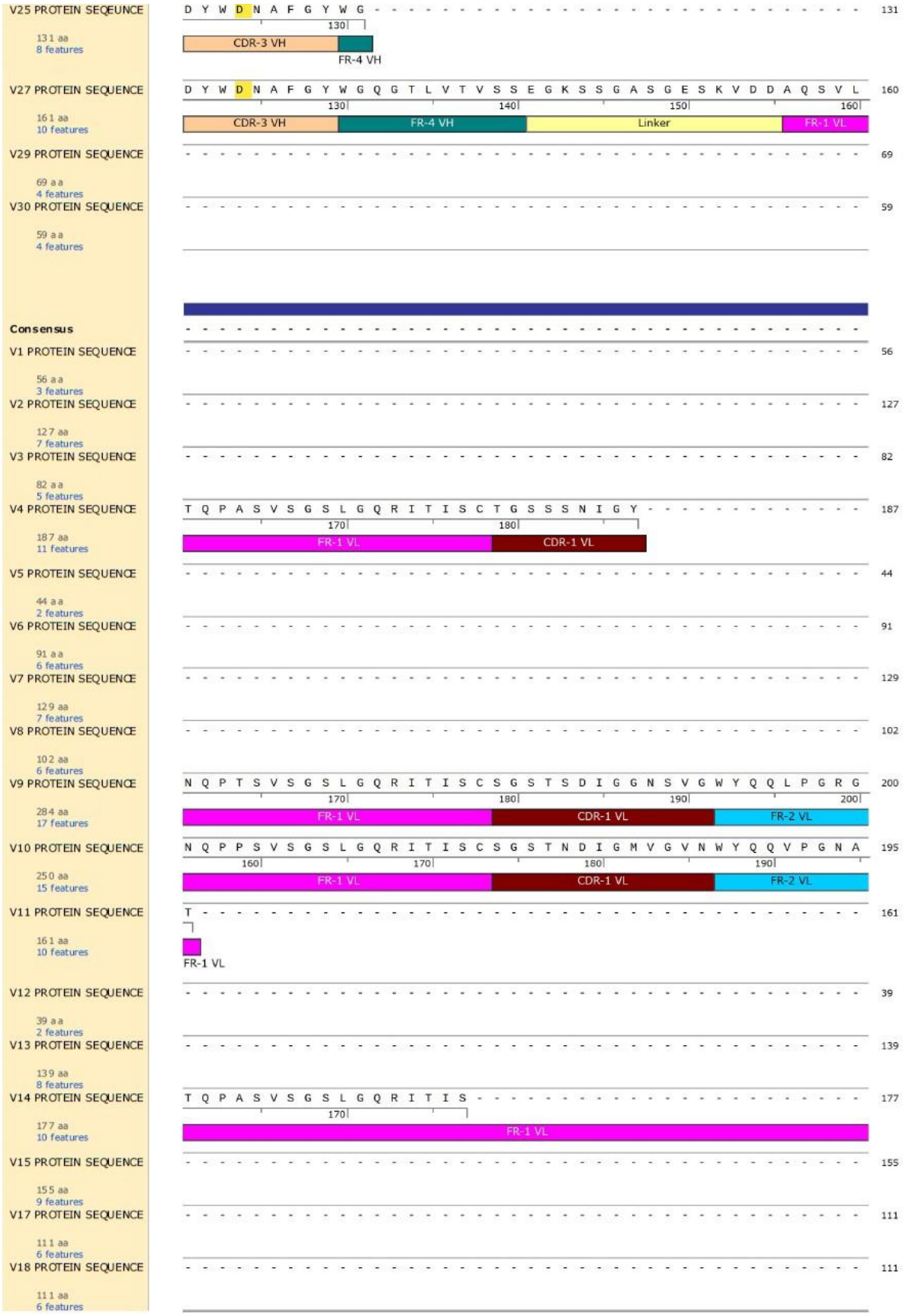
V25 PROTEIN SEQEUNCE
131 aa
8 features
D Y W D N A F G Y W G
130
CDR-3 VH
FR-4 VH
131
V27 PROTEIN SEQUENCE
161 aa
10 features
D Y W D N A F G Y W G Q G T L V T V S S E G K S S G A S G E S K V D D A Q S V L
130
140
150
160
CDR-3 VH
FR-4 VH
Linker
FR-1 VL
160
V29 PROTEIN SEQUENCE
69 aa
4 features
69
V30 PROTEIN SEQUENCE
59 aa
4 features
59
Consensus
V1 PROTEIN SEQUENCE
56 aa
3 features
56
V2 PROTEIN SEQUENCE
127 aa
7 features
127
V3 PROTEIN SEQUENCE
82 aa
5 features
82
V4 PROTEIN SEQUENCE
187 aa
11 features
T Q P A S V S G S L G Q R I T I S C T G S S S N I G Y
170
180
FR-1 VL
CDR-1 VL
187
V5 PROTEIN SEQUENCE
44 aa
2 features
44
V6 PROTEIN SEQUENCE
91 aa
6 features
91
V7 PROTEIN SEQUENCE
129 aa
7 features
129
V8 PROTEIN SEQUENCE
102 aa
6 features
102
V9 PROTEIN SEQUENCE
284 aa
17 features
N Q P T S V S G S L G Q R I T I S C S G S T S D I G G N S V G W Y Q Q L P G R G
170
180
190
200
FR-1 VL
CDR-1 VL
FR-2 VL
200
V10 PROTEIN SEQUENCE
250 aa
15 features
N Q P P S V S G S L G Q R I T I S C S G S T N D I G M V G V N W Y Q Q V P G N A
160
170
180
190
FR-1 VL
CDR-1 VL
FR-2 VL
195
V11 PROTEIN SEQUENCE
161 aa
10 features
T
FR-1 VL
161
V12 PROTEIN SEQUENCE
39 aa
2 features
39
V13 PROTEIN SEQUENCE
139 aa
8 features
139
V14 PROTEIN SEQUENCE
177 aa
10 features
T Q P A S V S G S L G Q R I T I S
170
FR-1 VL
177
V15 PROTEIN SEQUENCE
155 aa
9 features
155
V17 PROTEIN SEQUENCE
111 aa
6 features
111
V18 PROTEIN SEQUENCE
111 aa
6 features
111

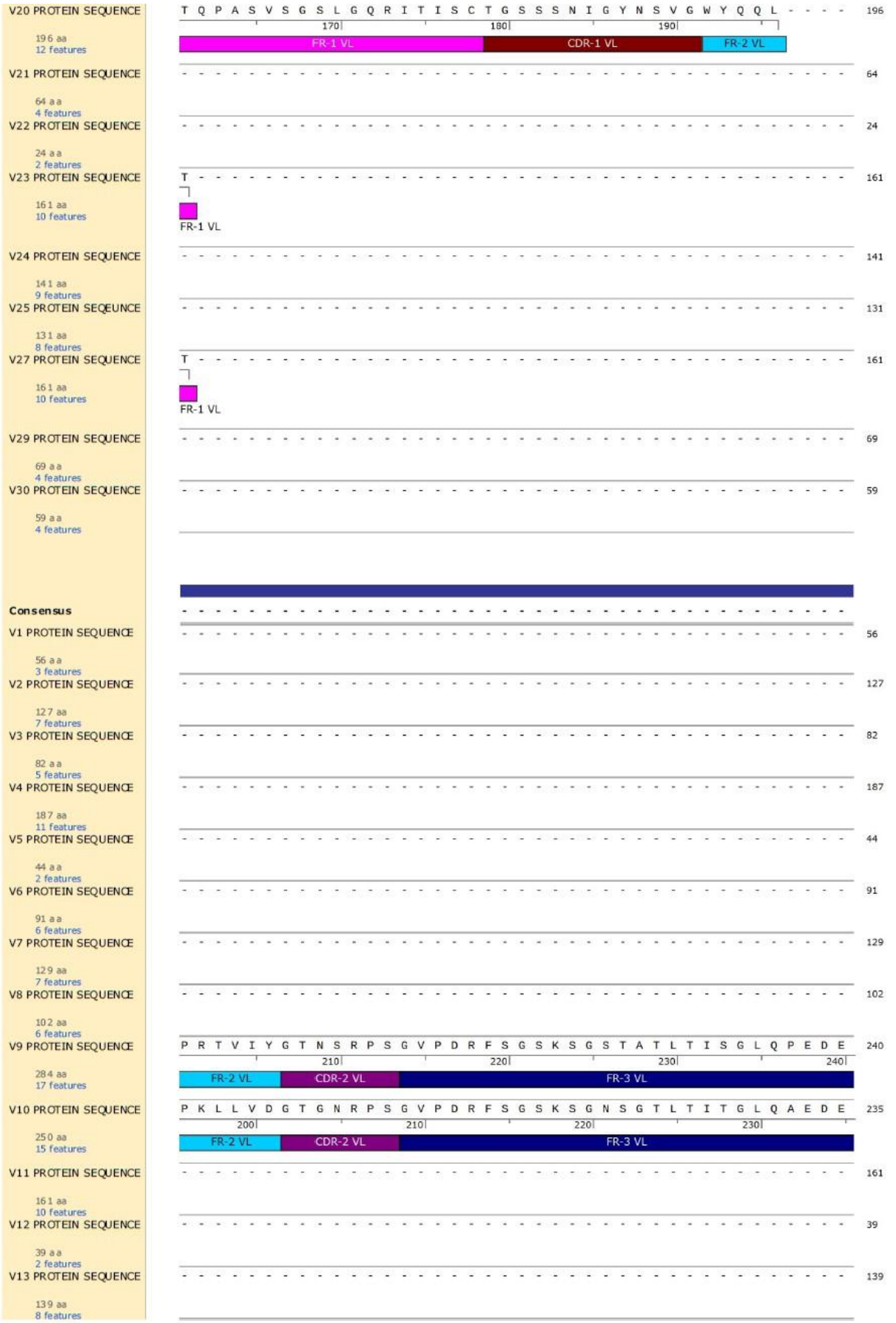
V20 PROTEIN SEQUENCE
T Q P A S V S G S L G Q R I T I S C T G S S S N I G Y N S V G W Y Q Q L
196
170
180
190
196 aa
12 features
FR-1 VL
CDR-1 VL
FR-2 VL
V21 PROTEIN SEQUENCE
64
64 aa
4 features
V22 PROTEIN SEQUENCE
24
24 aa
2 features
V23 PROTEIN SEQUENCE
T
161
161 aa
10 features
FR-1 VL
V24 PROTEIN SEQUENCE
141
141 aa
9 features
V25 PROTEIN SEQEUNCE
131
131 aa
8 features
V27 PROTEIN SEQUENCE
T
161
161 aa
10 features
FR-1 VL
V29 PROTEIN SEQUENCE
69
69 aa
4 features
V30 PROTEIN SEQUENCE
59
59 aa
4 features
Consensus
V1 PROTEIN SEQUENCE
56
56 aa
3 features
V2 PROTEIN SEQUENCE
127
127 aa
7 features
V3 PROTEIN SEQUENCE
82
82 aa
5 features
V4 PROTEIN SEQUENCE
187
187 aa
11 features
V5 PROTEIN SEQUENCE
44
44 aa
2 features
V6 PROTEIN SEQUENCE
91
91 aa
6 features
V7 PROTEIN SEQUENCE
129
129 aa
7 features
V8 PROTEIN SEQUENCE
102
102 aa
6 features
V9 PROTEIN SEQUENCE
P R T V I Y G T N S R P S G V P D R F S G S K S G S T A T L T I S G L Q P E D E
240
210
220
230
240
284 aa
17 features
FR-2 VL
CDR-2 VL
FR-3 VL
V10 PROTEIN SEQUENCE
P K L L V D G T G N R P S G V P D R F S G S K S G N S G T L T I T G L Q A E D E
235
200
210
220
230
250 aa
15 features
FR-2 VL
CDR-2 VL
FR-3 VL
V11 PROTEIN SEQUENCE
161
161 aa
10 features
V12 PROTEIN SEQUENCE
39
39 aa
2 features
V13 PROTEIN SEQUENCE
139
139 aa
8 features

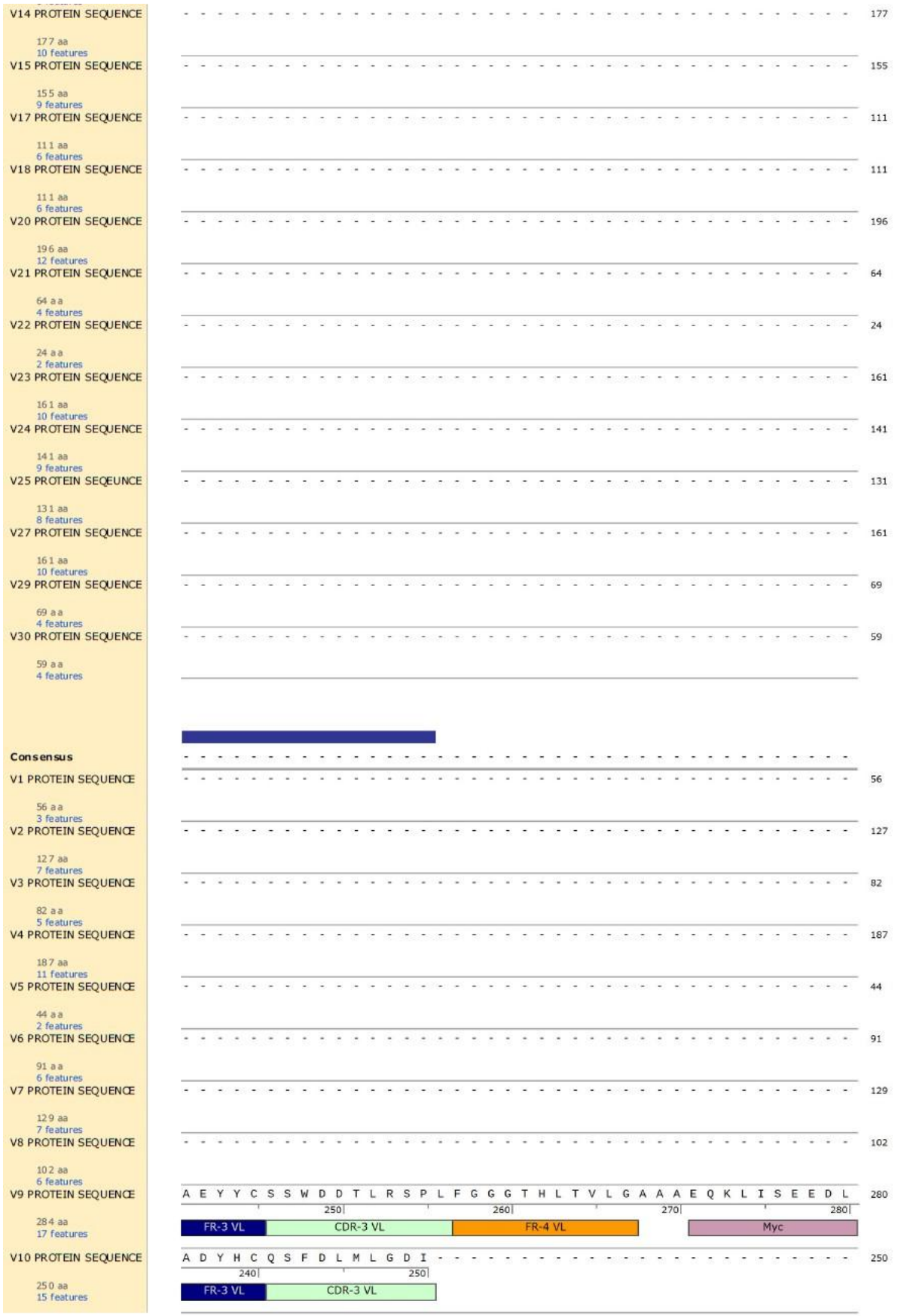

Printed from SnapGene®: 3 Mar 2025 16:42

Aligned using Clustal Omega and then edited

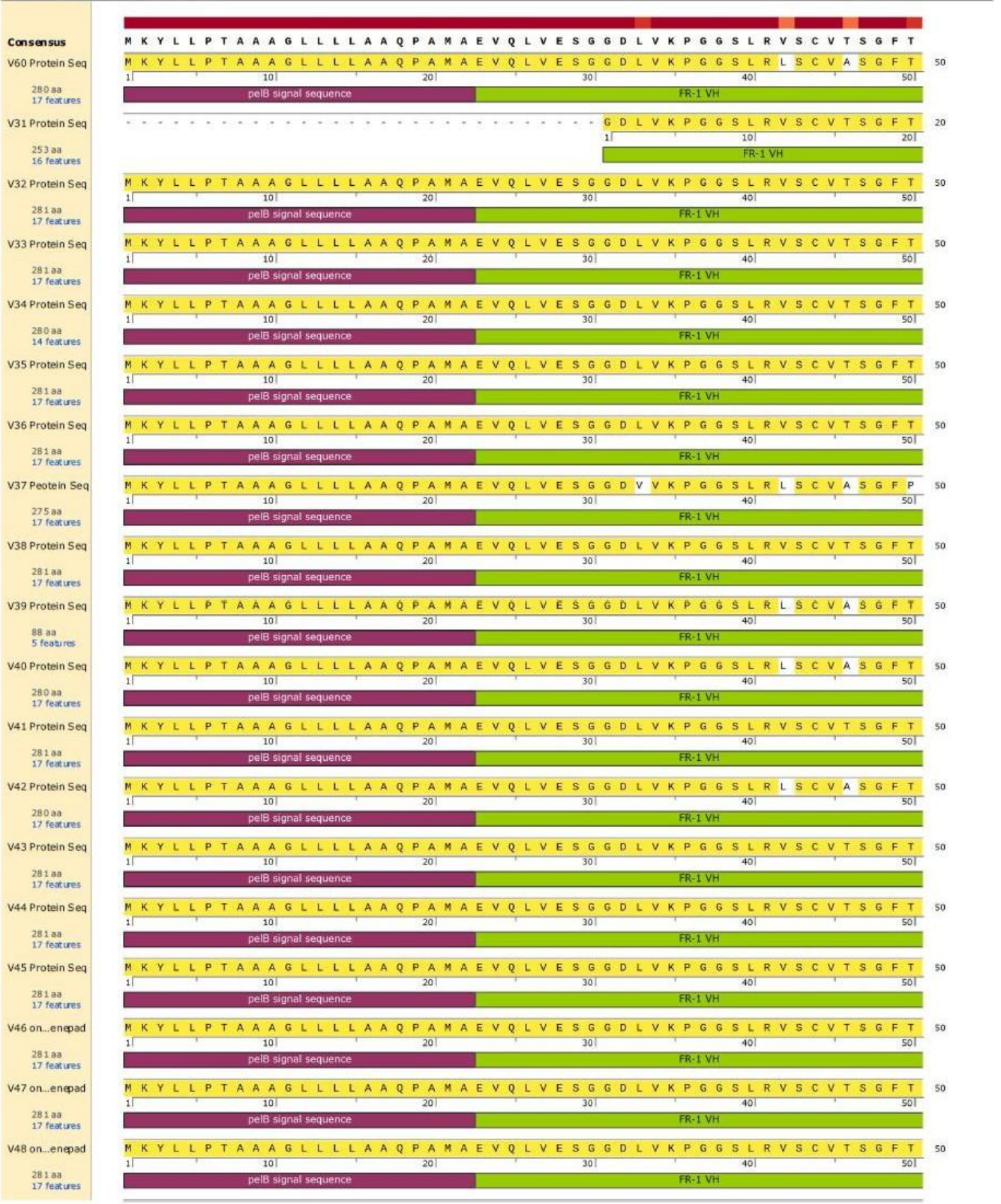

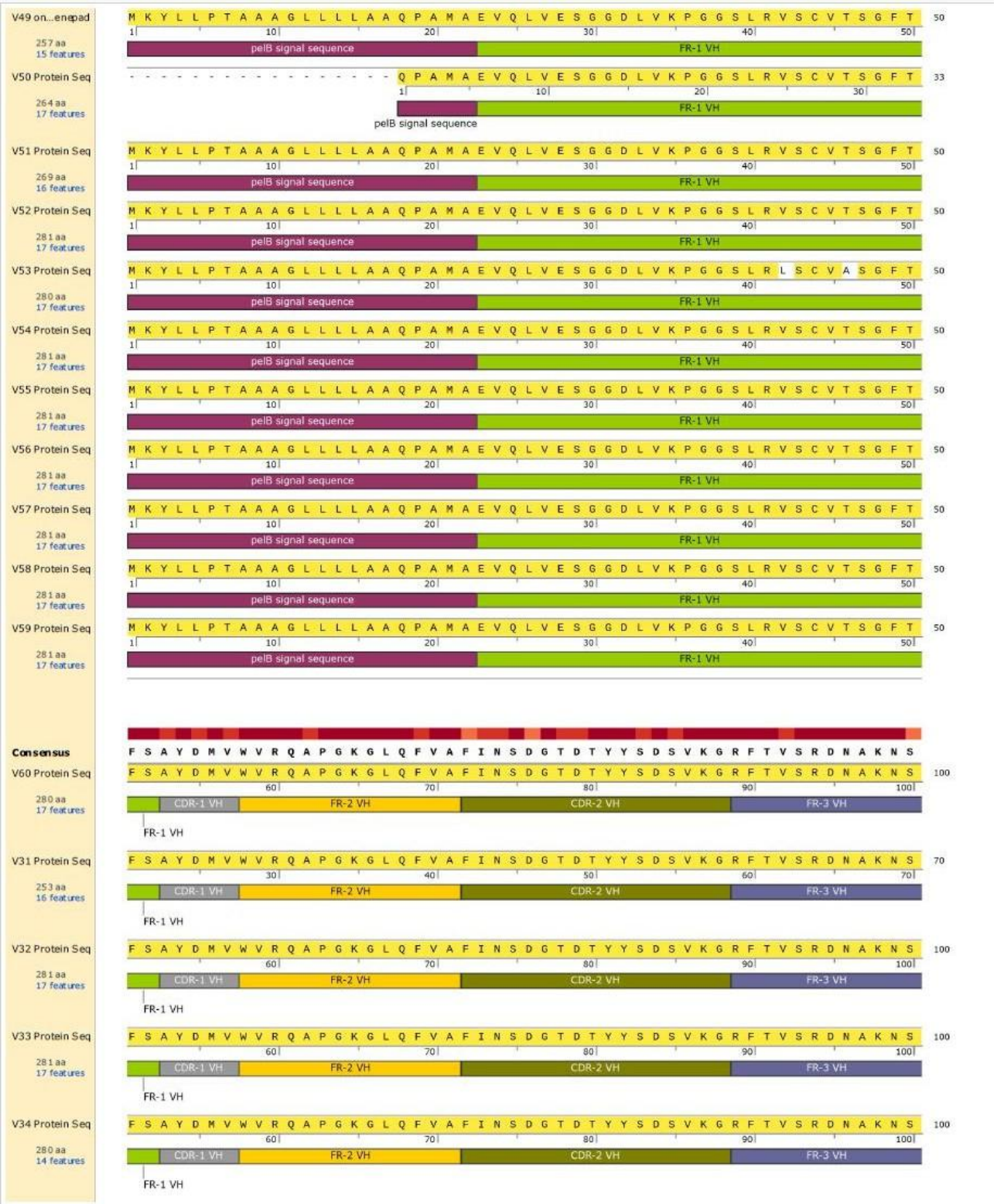
V49 on...enepad
257 aa
15 features
V50 Protein Seq
264 aa
17 features
V51 Protein Seq
269 aa
16 features
V52 Protein Seq
281 aa
17 features
V53 Protein Seq
280 aa
17 features
V54 Protein Seq
281 aa
17 features
V55 Protein Seq
281 aa
17 features
V56 Protein Seq
281 aa
17 features
V57 Protein Seq
281 aa
17 features
V58 Protein Seq
281 aa
17 features
V59 Protein Seq
281 aa
17 features
M K Y L L P T A A A G L L L L A A Q P A M A E V Q L V E S G G D L V K P G G S L R V S C V T S G F T
pelB signal sequence
FR-1 VH
Consensus
F S A Y D M V W V R Q A P G K G L Q F V A F I N S D G T D T Y Y S D S V K G R F T V S R D N A K N S
V60 Protein Seq
V31 Protein Seq
V32 Protein Seq
V33 Protein Seq
V34 Protein Seq
280 aa
17 features
253 aa
16 features
281 aa
17 features
281 aa
17 features
280 aa
14 features
CDR-1 VH
FR-2 VH
CDR-2 VH
FR-3 VH
FR-1 VH

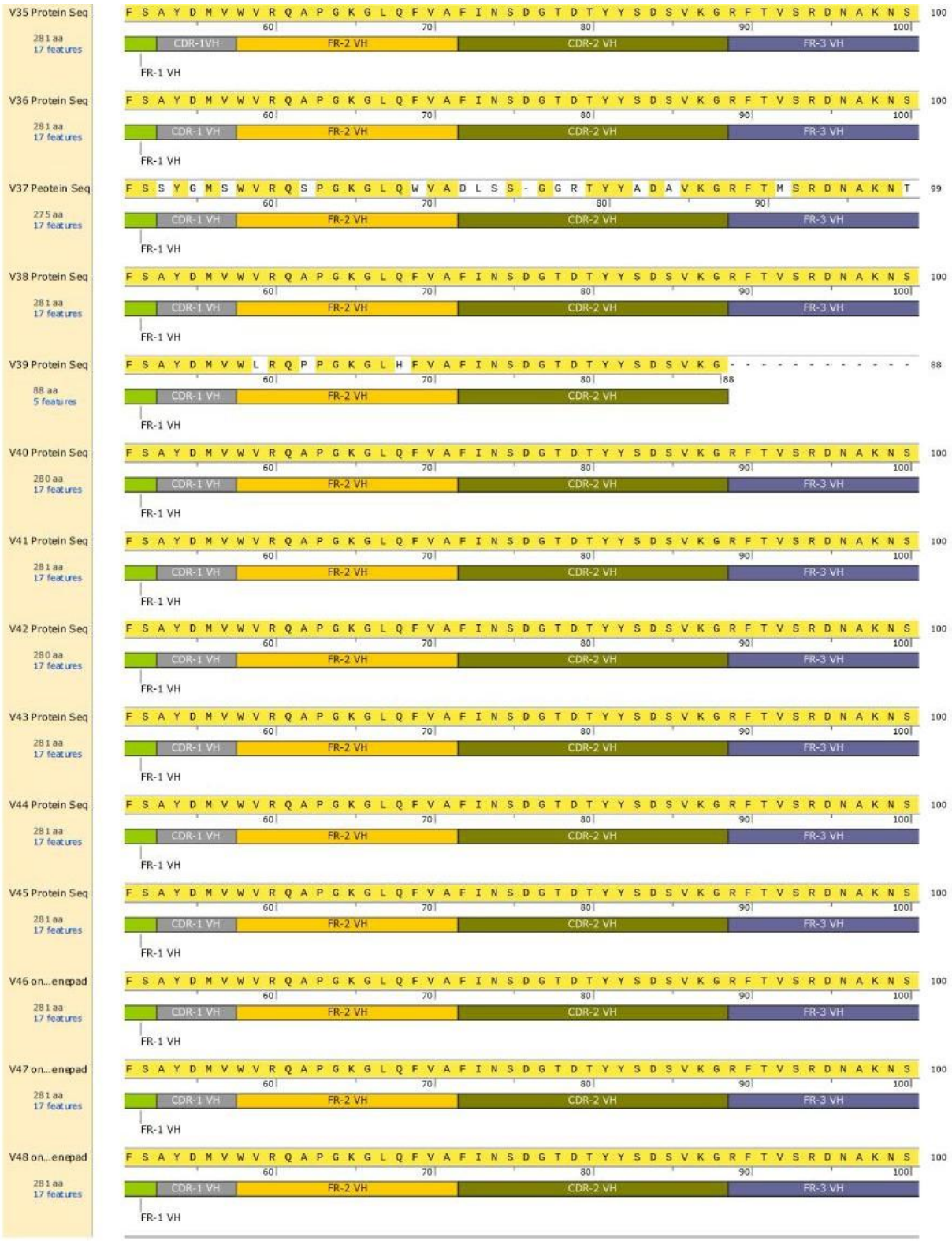
V35 Protein Seq
281 aa
17 features
F S A Y D M V W V R Q A P G K G L Q F V A F I N S D G T D T Y Y S D S V K G R F T V S R D N A K N S
100
60
70
80
90
100
CDR-1VH
FR-2 VH
CDR-2 VH
FR-3 VH
FR-1 VH
V36 Protein Seq
281 aa
17 features
F S A Y D M V W V R Q A P G K G L Q F V A F I N S D G T D T Y Y S D S V K G R F T V S R D N A K N S
100
CDR-1 VH
FR-2 VH
CDR-2 VH
FR-3 VH
FR-1 VH
V37 Peotein Seq
275 aa
17 features
F S S Y G M S W V R Q S P G K G L Q W V A D L S S - G G R T Y Y A D A V K G R F T M S R D N A K N T
99
CDR-1 VH
FR-2 VH
CDR-2 VH
FR-3 VH
FR-1 VH
V38 Protein Seq
281 aa
17 features
F S A Y D M V W V R Q A P G K G L Q F V A F I N S D G T D T Y Y S D S V K G R F T V S R D N A K N S
100
CDR-1 VH
FR-2 VH
CDR-2 VH
FR-3 VH
FR-1 VH
V39 Protein Seq
88 aa
5 features
F S A Y D M V W L R Q P P G K G L H F V A F I N S D G T D T Y Y S D S V K G - - - - - - - - - - - -
88
CDR-1 VH
FR-2 VH
CDR-2 VH
FR-1 VH
V40 Protein Seq
280 aa
17 features
F S A Y D M V W V R Q A P G K G L Q F V A F I N S D G T D T Y Y S D S V K G R F T V S R D N A K N S
100
CDR-1 VH
FR-2 VH
CDR-2 VH
FR-3 VH
FR-1 VH
V41 Protein Seq
281 aa
17 features
F S A Y D M V W V R Q A P G K G L Q F V A F I N S D G T D T Y Y S D S V K G R F T V S R D N A K N S
100
CDR-1 VH
FR-2 VH
CDR-2 VH
FR-3 VH
FR-1 VH
V42 Protein Seq
280 aa
17 features
F S A Y D M V W V R Q A P G K G L Q F V A F I N S D G T D T Y Y S D S V K G R F T V S R D N A K N S
100
CDR-1 VH
FR-2 VH
CDR-2 VH
FR-3 VH
FR-1 VH
V43 Protein Seq
281 aa
17 features
F S A Y D M V W V R Q A P G K G L Q F V A F I N S D G T D T Y Y S D S V K G R F T V S R D N A K N S
100
CDR-1 VH
FR-2 VH
CDR-2 VH
FR-3 VH
FR-1 VH
V44 Protein Seq
281 aa
17 features
F S A Y D M V W V R Q A P G K G L Q F V A F I N S D G T D T Y Y S D S V K G R F T V S R D N A K N S
100
CDR-1 VH
FR-2 VH
CDR-2 VH
FR-3 VH
FR-1 VH
V45 Protein Seq
281 aa
17 features
F S A Y D M V W V R Q A P G K G L Q F V A F I N S D G T D T Y Y S D S V K G R F T V S R D N A K N S
100
CDR-1 VH
FR-2 VH
CDR-2 VH
FR-3 VH
FR-1 VH
V46 on...enepad
281 aa
17 features
F S A Y D M V W V R Q A P G K G L Q F V A F I N S D G T D T Y Y S D S V K G R F T V S R D N A K N S
100
CDR-1 VH
FR-2 VH
CDR-2 VH
FR-3 VH
FR-1 VH
V47 on...enepad
281 aa
17 features
F S A Y D M V W V R Q A P G K G L Q F V A F I N S D G T D T Y Y S D S V K G R F T V S R D N A K N S
100
CDR-1 VH
FR-2 VH
CDR-2 VH
FR-3 VH
FR-1 VH
V48 on...enepad
281 aa
17 features
F S A Y D M V W V R Q A P G K G L Q F V A F I N S D G T D T Y Y S D S V K G R F T V S R D N A K N S
100
CDR-1 VH
FR-2 VH
CDR-2 VH
FR-3 VH
FR-1 VH

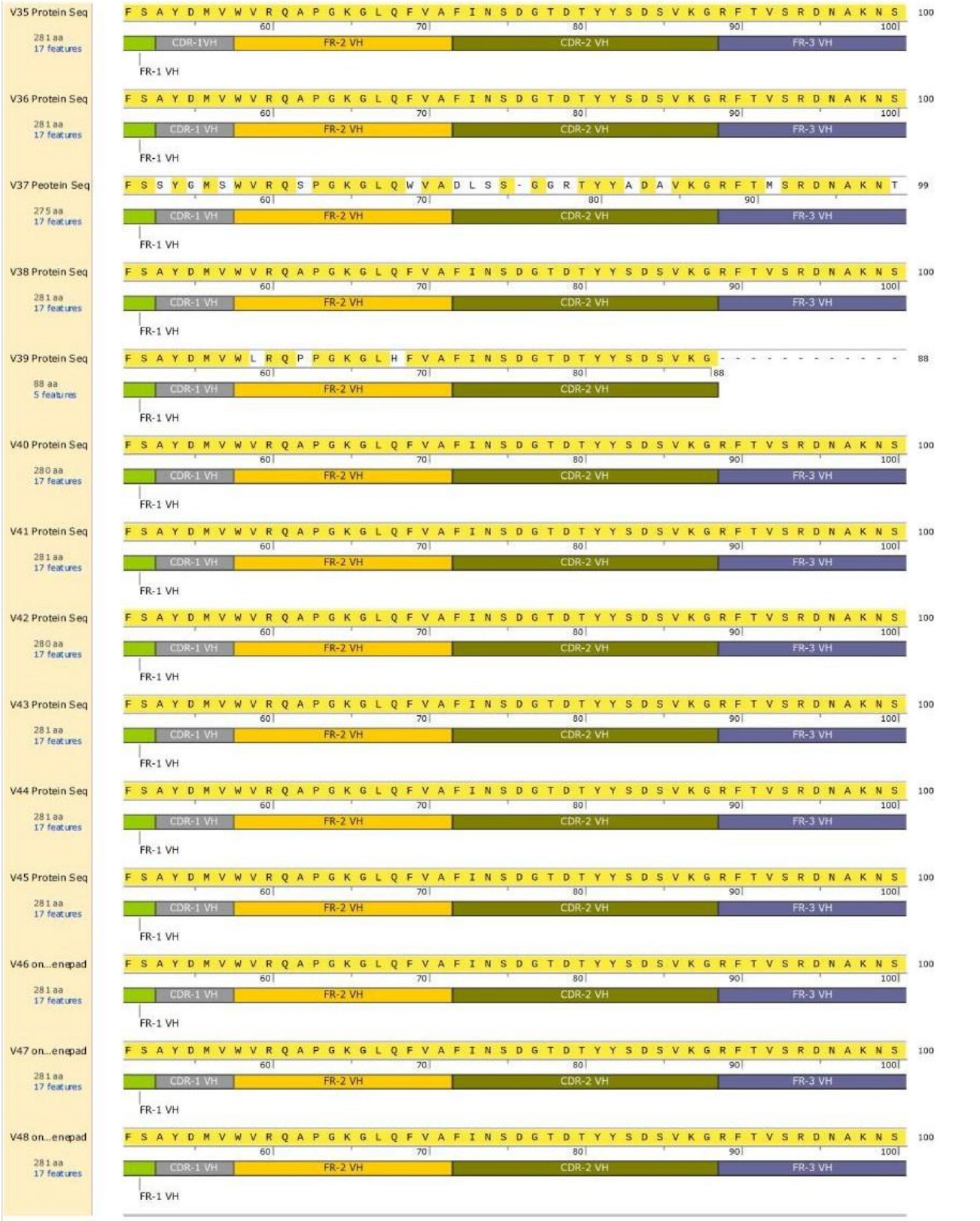
V35 Protein Seq
281 aa
17 features
F S A Y D M V W V R Q A P G K G L Q F V A F I N S D G T D T Y Y S D S V K G R F T V S R D N A K N S
100
60
70
80
90
100
CDR-1 VH
FR-2 VH
CDR-2 VH
FR-3 VH
FR-1 VH
V36 Protein Seq
281 aa
17 features
F S A Y D M V W V R Q A P G K G L Q F V A F I N S D G T D T Y Y S D S V K G R F T V S R D N A K N S
100
CDR-1 VH
FR-2 VH
CDR-2 VH
FR-3 VH
FR-1 VH
V37 Peotein Seq
275 aa
17 features
F S S Y G M S W V R Q S P G K G L Q W V A D L S S - G G R T Y Y A D A V K G R F T M S R D N A K N T
99
60
70
80
90
CDR-1 VH
FR-2 VH
CDR-2 VH
FR-3 VH
FR-1 VH
V38 Protein Seq
281 aa
17 features
F S A Y D M V W V R Q A P G K G L Q F V A F I N S D G T D T Y Y S D S V K G R F T V S R D N A K N S
100
CDR-1 VH
FR-2 VH
CDR-2 VH
FR-3 VH
FR-1 VH
V39 Protein Seq
88 aa
5 features
F S A Y D M V W L R Q P P G K G L H F V A F I N S D G T D T Y Y S D S V K G - - - - - - - - - - - -
88
60
70
80
88
CDR-1 VH
FR-2 VH
CDR-2 VH
FR-1 VH
V40 Protein Seq
280 aa
17 features
F S A Y D M V W V R Q A P G K G L Q F V A F I N S D G T D T Y Y S D S V K G R F T V S R D N A K N S
100
CDR-1 VH
FR-2 VH
CDR-2 VH
FR-3 VH
FR-1 VH
V41 Protein Seq
281 aa
17 features
F S A Y D M V W V R Q A P G K G L Q F V A F I N S D G T D T Y Y S D S V K G R F T V S R D N A K N S
100
CDR-1 VH
FR-2 VH
CDR-2 VH
FR-3 VH
FR-1 VH
V42 Protein Seq
280 aa
17 features
F S A Y D M V W V R Q A P G K G L Q F V A F I N S D G T D T Y Y S D S V K G R F T V S R D N A K N S
100
CDR-1 VH
FR-2 VH
CDR-2 VH
FR-3 VH
FR-1 VH
V43 Protein Seq
281 aa
17 features
F S A Y D M V W V R Q A P G K G L Q F V A F I N S D G T D T Y Y S D S V K G R F T V S R D N A K N S
100
CDR-1 VH
FR-2 VH
CDR-2 VH
FR-3 VH
FR-1 VH
V44 Protein Seq
281 aa
17 features
F S A Y D M V W V R Q A P G K G L Q F V A F I N S D G T D T Y Y S D S V K G R F T V S R D N A K N S
100
CDR-1 VH
FR-2 VH
CDR-2 VH
FR-3 VH
FR-1 VH
V45 Protein Seq
281 aa
17 features
F S A Y D M V W V R Q A P G K G L Q F V A F I N S D G T D T Y Y S D S V K G R F T V S R D N A K N S
100
CDR-1 VH
FR-2 VH
CDR-2 VH
FR-3 VH
FR-1 VH
V46 on...enepad
281 aa
17 features
F S A Y D M V W V R Q A P G K G L Q F V A F I N S D G T D T Y Y S D S V K G R F T V S R D N A K N S
100
CDR-1 VH
FR-2 VH
CDR-2 VH
FR-3 VH
FR-1 VH
V47 on...enepad
281 aa
17 features
F S A Y D M V W V R Q A P G K G L Q F V A F I N S D G T D T Y Y S D S V K G R F T V S R D N A K N S
100
CDR-1 VH
FR-2 VH
CDR-2 VH
FR-3 VH
FR-1 VH
V48 on...enepad
281 aa
17 features
F S A Y D M V W V R Q A P G K G L Q F V A F I N S D G T D T Y Y S D S V K G R F T V S R D N A K N S
100
CDR-1 VH
FR-2 VH
CDR-2 VH
FR-3 VH
FR-1 VH

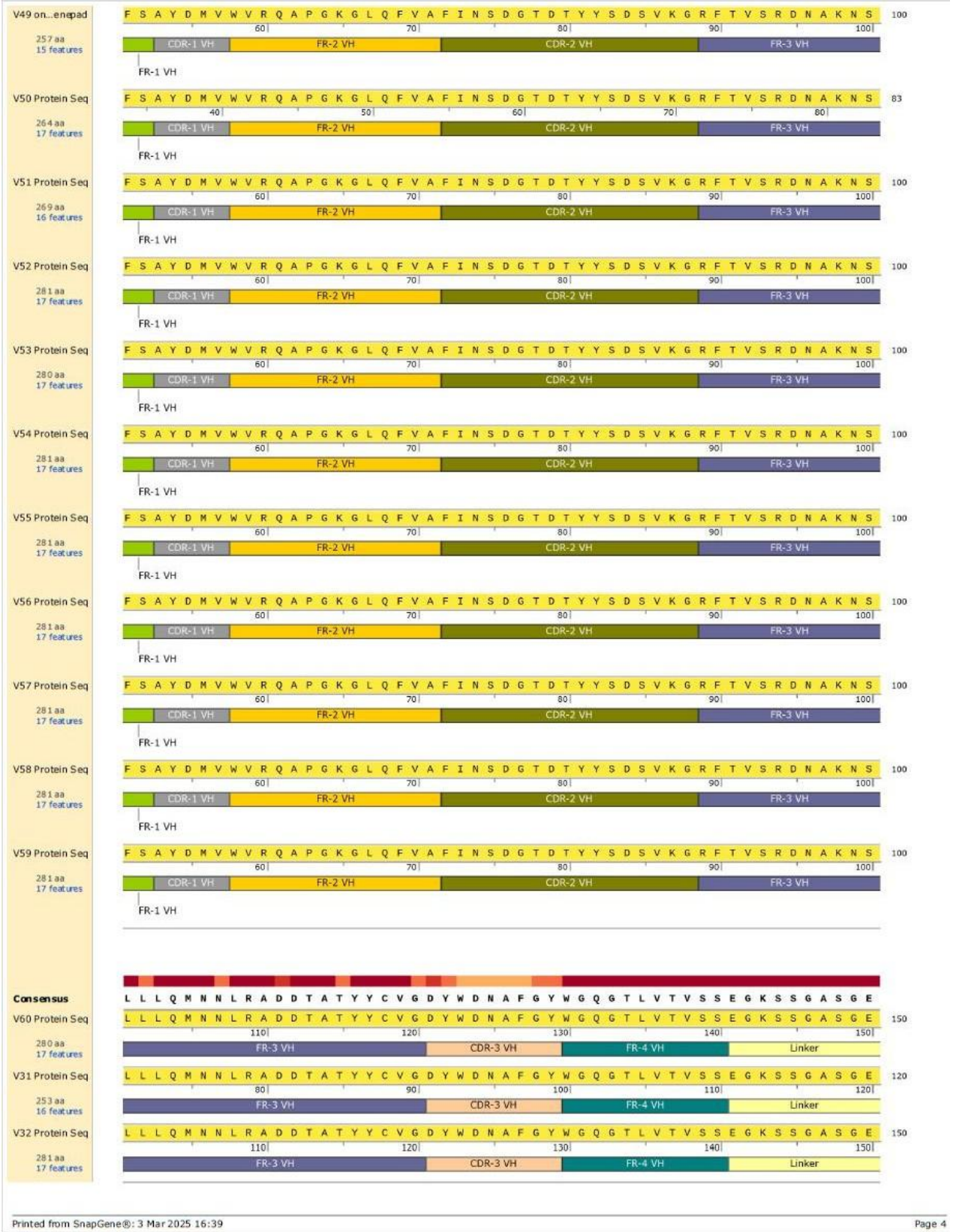
V49 on...enepad
257 aa
15 features
F S A Y D M V W V R Q A P G K G L Q F V A F I N S D G T D T Y Y S D S V K G R F T V S R D N A K N S
100
60
70
80
90
100
CDR-1 VH
FR-2 VH
CDR-2 VH
FR-3 VH
FR-1 VH
V50 Protein Seq
264 aa
17 features
F S A Y D M V W V R Q A P G K G L Q F V A F I N S D G T D T Y Y S D S V K G R F T V S R D N A K N S
83
40
50
60
70
80
CDR-1 VH
FR-2 VH
CDR-2 VH
FR-3 VH
FR-1 VH
V51 Protein Seq
269 aa
16 features
F S A Y D M V W V R Q A P G K G L Q F V A F I N S D G T D T Y Y S D S V K G R F T V S R D N A K N S
100
60
70
80
90
100
CDR-1 VH
FR-2 VH
CDR-2 VH
FR-3 VH
FR-1 VH
V52 Protein Seq
281 aa
17 features
F S A Y D M V W V R Q A P G K G L Q F V A F I N S D G T D T Y Y S D S V K G R F T V S R D N A K N S
100
60
70
80
90
100
CDR-1 VH
FR-2 VH
CDR-2 VH
FR-3 VH
FR-1 VH
V53 Protein Seq
280 aa
17 features
F S A Y D M V W V R Q A P G K G L Q F V A F I N S D G T D T Y Y S D S V K G R F T V S R D N A K N S
100
60
70
80
90
100
CDR-1 VH
FR-2 VH
CDR-2 VH
FR-3 VH
FR-1 VH
V54 Protein Seq
281 aa
17 features
F S A Y D M V W V R Q A P G K G L Q F V A F I N S D G T D T Y Y S D S V K G R F T V S R D N A K N S
100
60
70
80
90
100
CDR-1 VH
FR-2 VH
CDR-2 VH
FR-3 VH
FR-1 VH
V55 Protein Seq
281 aa
17 features
F S A Y D M V W V R Q A P G K G L Q F V A F I N S D G T D T Y Y S D S V K G R F T V S R D N A K N S
100
60
70
80
90
100
CDR-1 VH
FR-2 VH
CDR-2 VH
FR-3 VH
FR-1 VH
V56 Protein Seq
281 aa
17 features
F S A Y D M V W V R Q A P G K G L Q F V A F I N S D G T D T Y Y S D S V K G R F T V S R D N A K N S
100
60
70
80
90
100
CDR-1 VH
FR-2 VH
CDR-2 VH
FR-3 VH
FR-1 VH
V57 Protein Seq
281 aa
17 features
F S A Y D M V W V R Q A P G K G L Q F V A F I N S D G T D T Y Y S D S V K G R F T V S R D N A K N S
100
60
70
80
90
100
CDR-1 VH
FR-2 VH
CDR-2 VH
FR-3 VH
FR-1 VH
V58 Protein Seq
281 aa
17 features
F S A Y D M V W V R Q A P G K G L Q F V A F I N S D G T D T Y Y S D S V K G R F T V S R D N A K N S
100
60
70
80
90
100
CDR-1 VH
FR-2 VH
CDR-2 VH
FR-3 VH
FR-1 VH
V59 Protein Seq
281 aa
17 features
F S A Y D M V W V R Q A P G K G L Q F V A F I N S D G T D T Y Y S D S V K G R F T V S R D N A K N S
100
60
70
80
90
100
CDR-1 VH
FR-2 VH
CDR-2 VH
FR-3 VH
FR-1 VH
Consensus
L L L Q M N N L R A D D T A T Y Y C V G D Y W D N A F G Y W G Q G T L V T V S S E G K S S G A S G E
V60 Protein Seq
280 aa
17 features
L L L Q M N N L R A D D T A T Y Y C V G D Y W D N A F G Y W G Q G T L V T V S S E G K S S G A S G E
150
110
120
130
140
150
FR-3 VH
CDR-3 VH
FR-4 VH
Linker
V31 Protein Seq
253 aa
16 features
L L L Q M N N L R A D D T A T Y Y C V G D Y W D N A F G Y W G Q G T L V T V S S E G K S S G A S G E
120
80
90
100
110
120
FR-3 VH
CDR-3 VH
FR-4 VH
Linker
V32 Protein Seq
281 aa
17 features
L L L Q M N N L R A D D T A T Y Y C V G D Y W D N A F G Y W G Q G T L V T V S S E G K S S G A S G E
150
110
120
130
140
150
FR-3 VH
CDR-3 VH
FR-4 VH
Linker

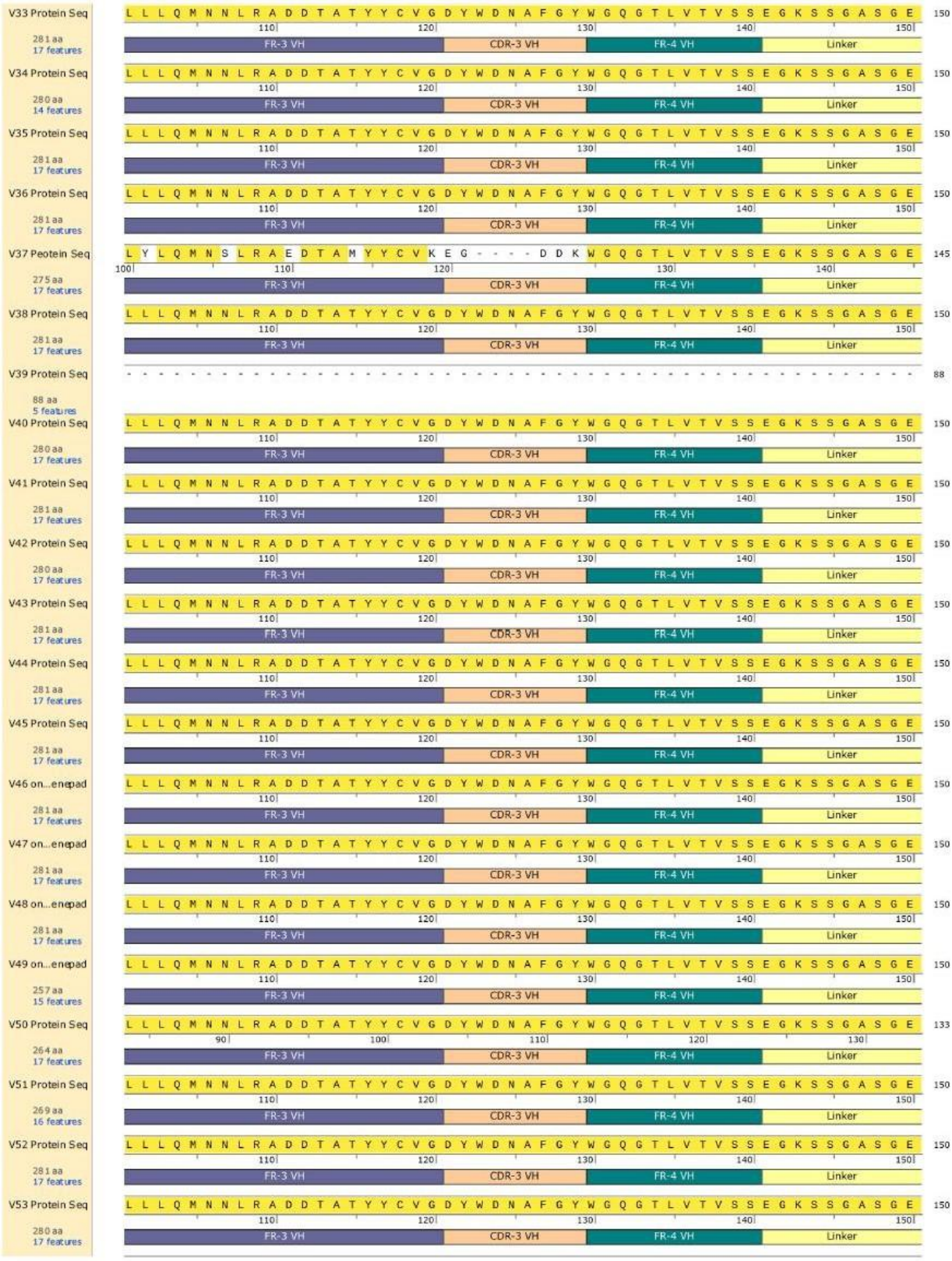
V33 Protein Seq
281 aa
17 features
V34 Protein Seq
280 aa
14 features
V35 Protein Seq
281 aa
17 features
V36 Protein Seq
281 aa
17 features
V37 Peotein Seq
275 aa
17 features
V38 Protein Seq
281 aa
17 features
V39 Protein Seq
88 aa
5 features
V40 Protein Seq
280 aa
17 features
V41 Protein Seq
281 aa
17 features
V42 Protein Seq
280 aa
17 features
V43 Protein Seq
281 aa
17 features
V44 Protein Seq
281 aa
17 features
V45 Protein Seq
281 aa
17 features
V46 on...enepad
281 aa
17 features
V47 on...enepad
281 aa
17 features
V48 on...enepad
281 aa
17 features
V49 on...enepad
257 aa
15 features
V50 Protein Seq
264 aa
17 features
V51 Protein Seq
269 aa
16 features
V52 Protein Seq
281 aa
17 features
V53 Protein Seq
280 aa
17 features
FR-3 VH
CDR-3 VH
FR-4 VH
Linker

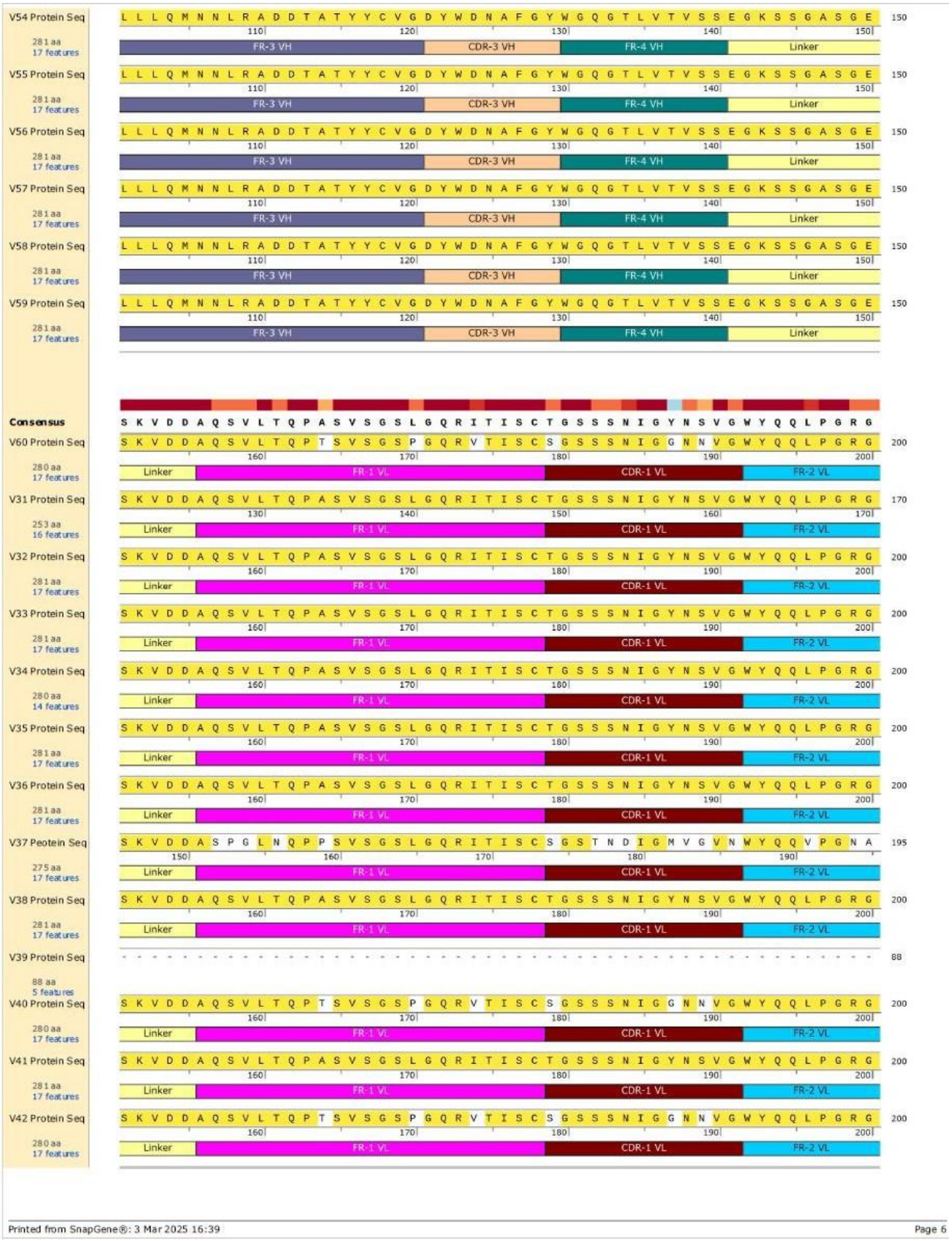
V54 Protein Seq
281 aa
17 features
V55 Protein Seq
281 aa
17 features
V56 Protein Seq
281 aa
17 features
V57 Protein Seq
281 aa
17 features
V58 Protein Seq
281 aa
17 features
V59 Protein Seq
281 aa
17 features
FR-3 VH
CDR-3 VH
FR-4 VH
Linker
Consensus
V60 Protein Seq
280 aa
17 features
V31 Protein Seq
253 aa
16 features
V32 Protein Seq
281 aa
17 features
V33 Protein Seq
281 aa
17 features
V34 Protein Seq
280 aa
14 features
V35 Protein Seq
281 aa
17 features
V36 Protein Seq
281 aa
17 features
V37 Peotein Seq
275 aa
17 features
V38 Protein Seq
281 aa
17 features
V39 Protein Seq
88 aa
5 features
V40 Protein Seq
280 aa
17 features
V41 Protein Seq
281 aa
17 features
V42 Protein Seq
280 aa
17 features
FR-1 VL
CDR-1 VL
FR-2 VL

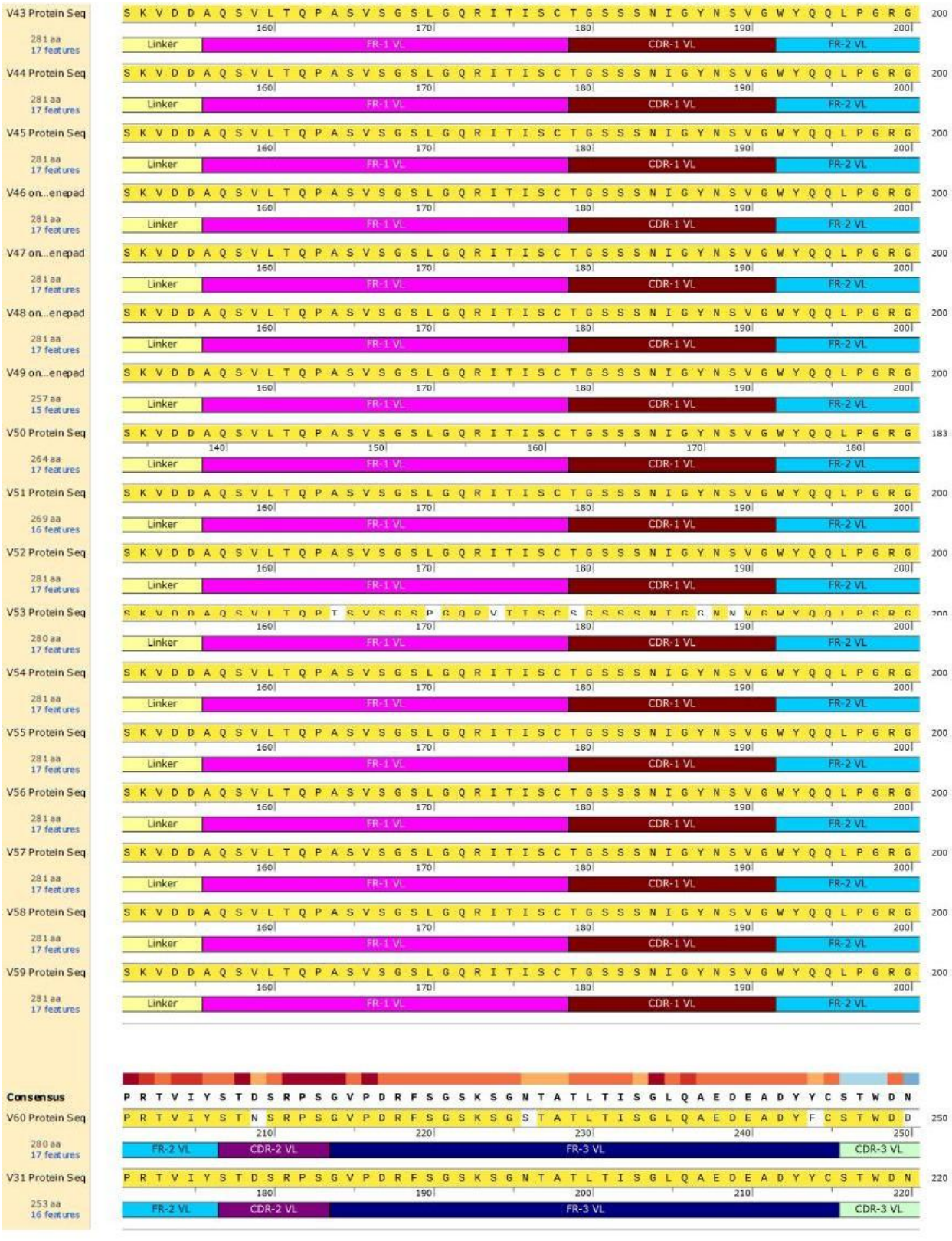
V43 Protein Seq
281 aa
17 features
V44 Protein Seq
281 aa
17 features
V45 Protein Seq
281 aa
17 features
V46 on...enepad
281 aa
17 features
V47 on...enepad
281 aa
17 features
V48 on...enepad
281 aa
17 features
V49 on...enepad
257 aa
15 features
V50 Protein Seq
264 aa
17 features
V51 Protein Seq
269 aa
16 features
V52 Protein Seq
281 aa
17 features
V53 Protein Seq
280 aa
17 features
V54 Protein Seq
281 aa
17 features
V55 Protein Seq
281 aa
17 features
V56 Protein Seq
281 aa
17 features
V57 Protein Seq
281 aa
17 features
V58 Protein Seq
281 aa
17 features
V59 Protein Seq
281 aa
17 features
Linker
FR-1 VL
CDR-1 VL
FR-2 VL
Consensus
V60 Protein Seq
280 aa
17 features
V31 Protein Seq
253 aa
16 features
CDR-2 VL
FR-3 VL
CDR-3 VL

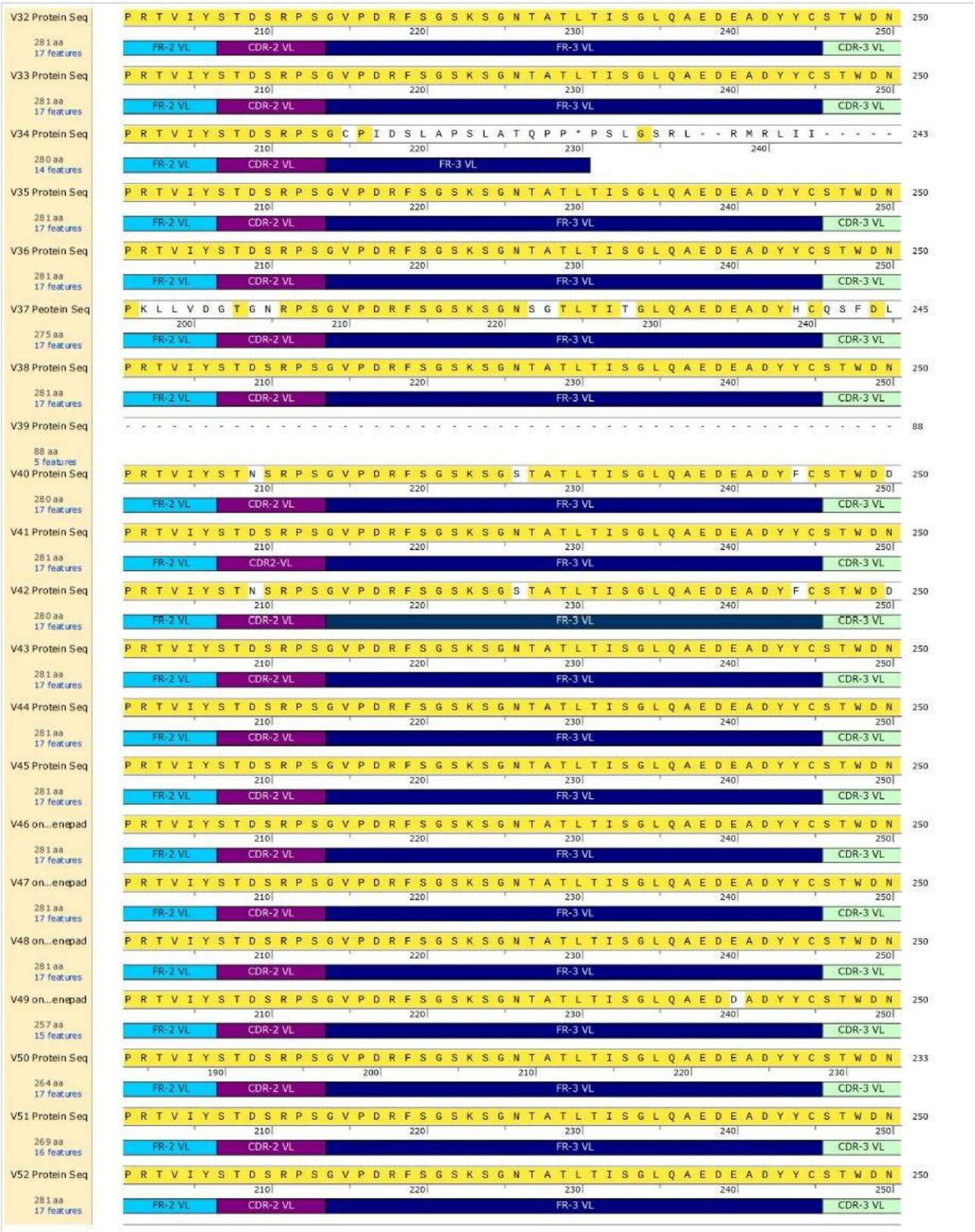
V32 Protein Seq
P R T V I Y S T D S R P S G V P D R F S G S K S G N T A T L T I S G L Q A E D E A D Y Y C S T W D N
250
281 aa
17 features
FR-2 VL
CDR-2 VL
FR-3 VL
CDR-3 VL
V33 Protein Seq
P R T V I Y S T D S R P S G V P D R F S G S K S G N T A T L T I S G L Q A E D E A D Y Y C S T W D N
250
281 aa
17 features
FR-2 VL
CDR-2 VL
FR-3 VL
CDR-3 VL
V34 Protein Seq
P R T V I Y S T D S R P S G C P I D S L A P S L A T Q P P * P S L G S R L - - R M R L I I - - - - -
243
280 aa
14 features
FR-2 VL
CDR-2 VL
FR-3 VL
V35 Protein Seq
P R T V I Y S T D S R P S G V P D R F S G S K S G N T A T L T I S G L Q A E D E A D Y Y C S T W D N
250
281 aa
17 features
FR-2 VL
CDR-2 VL
FR-3 VL
CDR-3 VL
V36 Protein Seq
P R T V I Y S T D S R P S G V P D R F S G S K S G N T A T L T I S G L Q A E D E A D Y Y C S T W D N
250
281 aa
17 features
FR-2 VL
CDR-2 VL
FR-3 VL
CDR-3 VL
V37 Peotein Seq
P K L L V D G T G N R P S G V P D R F S G S K S G N S G T L T I T G L Q A E D E A D Y H C Q S F D L
245
275 aa
17 features
FR-2 VL
CDR-2 VL
FR-3 VL
CDR-3 VL
V38 Protein Seq
P R T V I Y S T D S R P S G V P D R F S G S K S G N T A T L T I S G L Q A E D E A D Y Y C S T W D N
250
281 aa
17 features
FR-2 VL
CDR-2 VL
FR-3 VL
CDR-3 VL
V39 Protein Seq
88
88 aa
5 features
V40 Protein Seq
P R T V I Y S T N S R P S G V P D R F S G S K S G S T A T L T I S G L Q A E D E A D Y F C S T W D D
250
280 aa
17 features
FR-2 VL
CDR-2 VL
FR-3 VL
CDR-3 VL
V41 Protein Seq
P R T V I Y S T D S R P S G V P D R F S G S K S G N T A T L T I S G L Q A E D E A D Y Y C S T W D N
250
281 aa
17 features
FR-2 VL
CDR2-VL
FR-3 VL
CDR-3 VL
V42 Protein Seq
P R T V I Y S T N S R P S G V P D R F S G S K S G S T A T L T I S G L Q A E D E A D Y F C S T W D D
250
280 aa
17 features
FR-2 VL
CDR-2 VL
FR-3 VL
CDR-3 VL
V43 Protein Seq
P R T V I Y S T D S R P S G V P D R F S G S K S G N T A T L T I S G L Q A E D E A D Y Y C S T W D N
250
281 aa
17 features
FR-2 VL
CDR-2 VL
FR-3 VL
CDR-3 VL
V44 Protein Seq
P R T V I Y S T D S R P S G V P D R F S G S K S G N T A T L T I S G L Q A E D E A D Y Y C S T W D N
250
281 aa
17 features
FR-2 VL
CDR-2 VL
FR-3 VL
CDR-3 VL
V45 Protein Seq
P R T V I Y S T D S R P S G V P D R F S G S K S G N T A T L T I S G L Q A E D E A D Y Y C S T W D N
250
281 aa
17 features
FR-2 VL
CDR-2 VL
FR-3 VL
CDR-3 VL
V46 on...enepad
P R T V I Y S T D S R P S G V P D R F S G S K S G N T A T L T I S G L Q A E D E A D Y Y C S T W D N
250
281 aa
17 features
FR-2 VL
CDR-2 VL
FR-3 VL
CDR-3 VL
V47 on...enepad
P R T V I Y S T D S R P S G V P D R F S G S K S G N T A T L T I S G L Q A E D E A D Y Y C S T W D N
250
281 aa
17 features
FR-2 VL
CDR-2 VL
FR-3 VL
CDR-3 VL
V48 on...enepad
P R T V I Y S T D S R P S G V P D R F S G S K S G N T A T L T I S G L Q A E D E A D Y Y C S T W D N
250
281 aa
17 features
FR-2 VL
CDR-2 VL
FR-3 VL
CDR-3 VL
V49 on...enepad
P R T V I Y S T D S R P S G V P D R F S G S K S G N T A T L T I S G L Q A E D D A D Y Y C S T W D N
250
257 aa
15 features
FR-2 VL
CDR-2 VL
FR-3 VL
CDR-3 VL
V50 Protein Seq
P R T V I Y S T D S R P S G V P D R F S G S K S G N T A T L T I S G L Q A E D E A D Y Y C S T W D N
233
264 aa
17 features
FR-2 VL
CDR-2 VL
FR-3 VL
CDR-3 VL
V51 Protein Seq
P R T V I Y S T D S R P S G V P D R F S G S K S G N T A T L T I S G L Q A E D E A D Y Y C S T W D N
250
269 aa
16 features
FR-2 VL
CDR-2 VL
FR-3 VL
CDR-3 VL
V52 Protein Seq
P R T V I Y S T D S R P S G V P D R F S G S K S G N T A T L T I S G L Q A E D E A D Y Y C S T W D N
250
281 aa
17 features
FR-2 VL
CDR-2 VL
FR-3 VL
CDR-3 VL

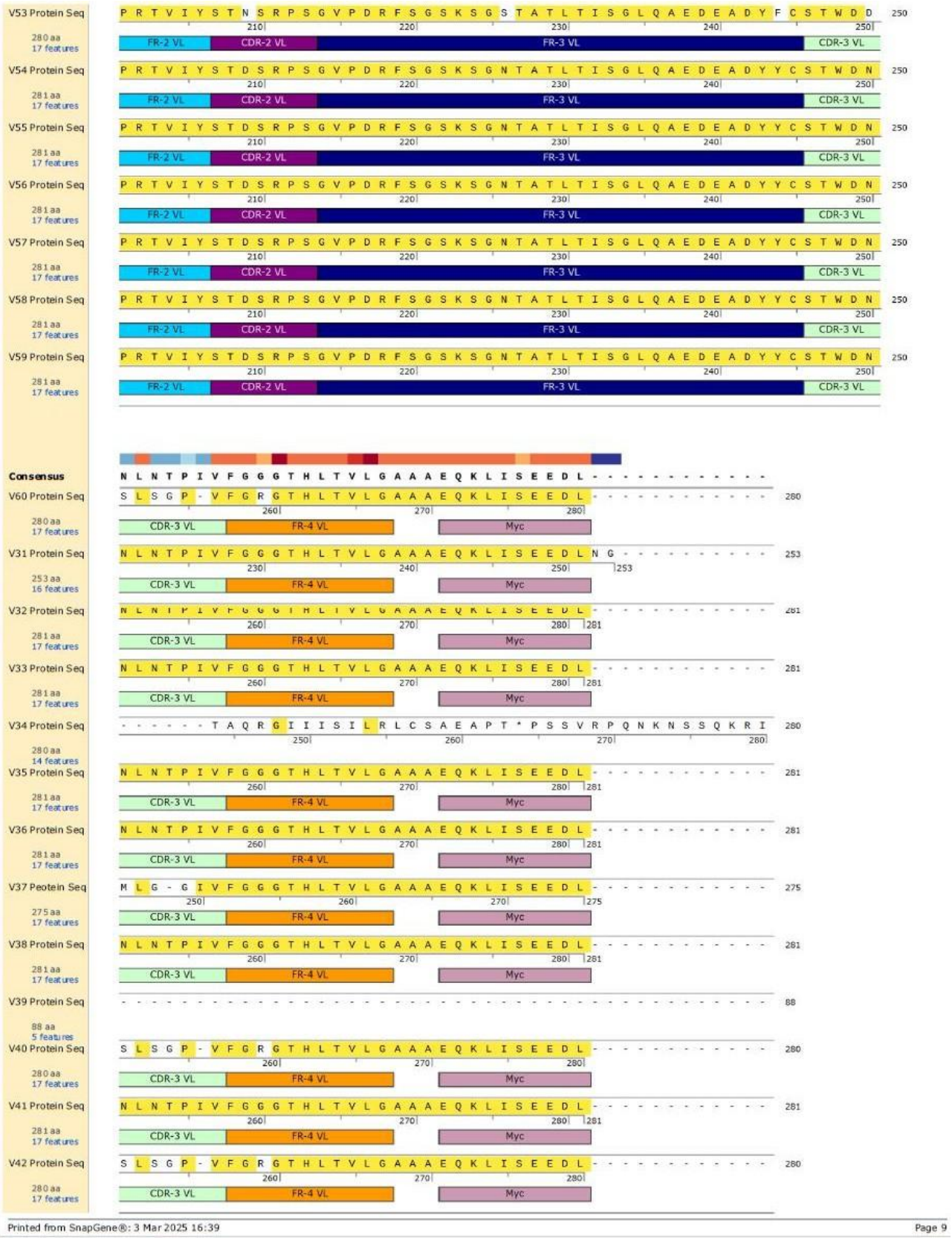
V53 Protein Seq
P R T V I Y S T N S R P S G V P D R F S G S K S G S T A T L T I S G L Q A E D E A D Y F C S T W D D
210 220 230 240 250
250
280 aa
17 features
FR-2 VL
CDR-2 VL
FR-3 VL
CDR-3 VL
V54 Protein Seq
P R T V I Y S T D S R P S G V P D R F S G S K S G N T A T L T I S G L Q A E D E A D Y Y C S T W D N
210 220 230 240 250
250
281 aa
17 features
FR-2 VL
CDR-2 VL
FR-3 VL
CDR-3 VL
V55 Protein Seq
P R T V I Y S T D S R P S G V P D R F S G S K S G N T A T L T I S G L Q A E D E A D Y Y C S T W D N
210 220 230 240 250
250
281 aa
17 features
FR-2 VL
CDR-2 VL
FR-3 VL
CDR-3 VL
V56 Protein Seq
P R T V I Y S T D S R P S G V P D R F S G S K S G N T A T L T I S G L Q A E D E A D Y Y C S T W D N
210 220 230 240 250
250
281 aa
17 features
FR-2 VL
CDR-2 VL
FR-3 VL
CDR-3 VL
V57 Protein Seq
P R T V I Y S T D S R P S G V P D R F S G S K S G N T A T L T I S G L Q A E D E A D Y Y C S T W D N
210 220 230 240 250
250
281 aa
17 features
FR-2 VL
CDR-2 VL
FR-3 VL
CDR-3 VL
V58 Protein Seq
P R T V I Y S T D S R P S G V P D R F S G S K S G N T A T L T I S G L Q A E D E A D Y Y C S T W D N
210 220 230 240 250
250
281 aa
17 features
FR-2 VL
CDR-2 VL
FR-3 VL
CDR-3 VL
V59 Protein Seq
P R T V I Y S T D S R P S G V P D R F S G S K S G N T A T L T I S G L Q A E D E A D Y Y C S T W D N
210 220 230 240 250
250
281 aa
17 features
FR-2 VL
CDR-2 VL
FR-3 VL
CDR-3 VL
Consensus
N L N T P I V F G G G T H L T V L G A A A A E Q K L I S E E D L - - - - - - - - - - - -
V60 Protein Seq
S L S G P - V F G R G T H L T V L G A A A A E Q K L I S E E D L - - - - - - - - - - - -
260 270 280
280
280 aa
17 features
CDR-3 VL
FR-4 VL
Myc
V31 Protein Seq
N L N T P I V F G G G T H L T V L G A A A A E Q K L I S E E D L N G - - - - - - - - - -
230 240 250 253
253
253 aa
16 features
CDR-3 VL
FR-4 VL
Myc
V32 Protein Seq
N L N T P I V F G G G T H L T V L G A A A A E Q K L I S E E D L - - - - - - - - - - - -
260 270 280 281
281
281 aa
17 features
CDR-3 VL
FR-4 VL
Myc
V33 Protein Seq
N L N T P I V F G G G T H L T V L G A A A A E Q K L I S E E D L - - - - - - - - - - - -
260 270 280 281
281
281 aa
17 features
CDR-3 VL
FR-4 VL
Myc
V34 Protein Seq
- - - - - - T A Q R G I I I S I L R L C S A E A P T * P S S V R P Q N K N S S Q K R I
250 260 270 280
280
280 aa
14 features
V35 Protein Seq
N L N T P I V F G G G T H L T V L G A A A A E Q K L I S E E D L - - - - - - - - - - - -
260 270 280 281
281
281 aa
17 features
CDR-3 VL
FR-4 VL
Myc
V36 Protein Seq
N L N T P I V F G G G T H L T V L G A A A A E Q K L I S E E D L - - - - - - - - - - - -
260 270 280 281
281
281 aa
17 features
CDR-3 VL
FR-4 VL
Myc
V37 Peotein Seq
M L G - G I V F G G G T H L T V L G A A A A E Q K L I S E E D L - - - - - - - - - - - -
250 260 270 275
275
275 aa
17 features
CDR-3 VL
FR-4 VL
Myc
V38 Protein Seq
N L N T P I V F G G G T H L T V L G A A A A E Q K L I S E E D L - - - - - - - - - - - -
260 270 280 281
281
281 aa
17 features
CDR-3 VL
FR-4 VL
Myc
V39 Protein Seq
- -
88
88 aa
5 features
V40 Protein Seq
S L S G P - V F G R G T H L T V L G A A A A E Q K L I S E E D L - - - - - - - - - - - -
260 270 280
280
280 aa
17 features
CDR-3 VL
FR-4 VL
Myc
V41 Protein Seq
N L N T P I V F G G G T H L T V L G A A A A E Q K L I S E E D L - - - - - - - - - - - -
260 270 280 281
281
281 aa
17 features
CDR-3 VL
FR-4 VL
Myc
V42 Protein Seq
S L S G P - V F G R G T H L T V L G A A A A E Q K L I S E E D L - - - - - - - - - - - -
260 270 280
280
280 aa
17 features
CDR-3 VL
FR-4 VL
Myc

Figure 6.2: Protein sequences of clones 1–60 obtained by Sanger sequencing. Sanger sequencing was used to determine the protein sequences of clones 1–60. For clones 1–30, only the heavy chain was sequenced, with complete sequence coverage achieved for clones 9 and 10. In contrast, full- length sequences were successfully obtained for all clones from 31–60. Annotated features indicate the framework regions (FRs) and complementarity-determining regions (CDRs) within each sequence.

6.4. SWISS-Model Report

A. Clone 53

Results

The SWISS-MODEL template library (SMTL version 2025-03-19, PDB release 2025-03-14) was searched with BLAST (Camacho et al.) and HHblits (Steinegger et al.) for evolutionary related structures matching the target sequence in Table T1. For details on the template search, see Materials and Methods. Overall 16999 templates were found (Table T2).

Models

The following model was built (see Materials and Methods "Model Building"):

Model #01	File	Built with	Oligo-State	Ligands	GMQE	QMEANDisCo Global
	PDB	ProMod3 3.4.1	monomer	None	0.72	0.75 ± 0.05

Template	Seq Identity	Oligo-state	QSQE	Found by	Method	Resolution	Seq Similarity	Range	Coverage	Description
6qb9.1.A	71.54	monomer	0.00	HHblits	X-ray	1.85Å	0.51	27 - 272	0.88	scFv55

The template contained no ligands.

```
Target    MKYLLPTAAAGLLLLAAQPAMAEVQLVESGGDLVKPGGSLRLSCVASGFTFSAYDMVWVRQAPGKGLQFVAFINSDGTDT
6qb9.1.A  ----------------------------KESGGGLVKPGGSLRLSCAASGFTFSSYSMNWVRQAPGKGLEWVSSISSSSSYI

Target    YYSDSVKGRFTVSRDNAKNSLLLQMNNLRADDTATYYCVGDYWDNA-FGYWGQGTLVTVSSEGKSSGASGESKVDDAQSV
6qb9.1.A  YYADSVKGRFTISRDNAKNSLYLQMNSLRAEDTAVYYCARQVGATWAFDIWGQGTLVTVSSGGGGSGGGGSGGGGSAQSV

Target    LTQPTSVSGSPGQRVTISCSGSSSNIGGNNVGWYQQLPGRGPRTVIYSTNSRPSGVPDRFSGSKSGSTATLTISGLQAED
6qb9.1.A  LTQPPSASGTPGQRVTISCSGSSSNIGSNTVNWYQQLPGTAPKLLIYSNNQRPSGVPDRFSGSKSGTSASLAISGLQSED

Target    EADYFCSTWDDSLSGPVFGRGTHLTVLGAAAEQKLISEEDL
6qb9.1.A  EADYYCAAWDDSLNAWVFGGGTKLTVLGAAAEN--------
```

B. Clone 35

Results

The SWISS-MODEL template library (SMTL version 2025-03-19, PDB release 2025-03-14) was searched with BLAST (Camacho et al.) and HHblits (Steinegger et al.) for evolutionary related structures matching the target sequence in Table T1. For details on the template search, see Materials and Methods. Overall 17067 templates were found (Table T2).

Models

The following model was built (see Materials and Methods "Model Building"):

Model #01	File	Built with	Oligo-State	Ligands	GMQE	QMEANDisCo Global
	PDB	ProMod3 3.4.1	monomer	None	0.71	0.75 ± 0.05

Template	Seq Identity	Oligo-state	QSQE	Found by	Method	Resolution	Seq Similarity	Range	Coverage	Description
6qb9.1.A	69.39	monomer	0.00	HHblits	X-ray	1.85Å	0.51	27 - 272	0.87	scFv55

The template contained no ligands.

```
Target    MKYLLPTAAAGLLLLAAQPAMAEVQLVESGGDLVKPGGSLRVSCVTSGFTFSAYDMVWVRQAPGKGLQFVAFINSDGTDT
6qb9.1.A  ----------------------------KESGGGLVKPGGSLRLSCAASGFTFSSYSMNWVRQAPGKGLEWVSSISSSSSYI

Target    YYSDSVKGRFTVSRDNAKNSLLLQMNNLRADDTATYYCVGDYWDN-AFGYWGQGTLVTVSSEGKSSGASGESKVDDAQSV
6qb9.1.A  YYADSVKGRFTISRDNAKNSLYLQMNSLRAEDTAVYYCARQVGATWAFDIWGQGTLVTVSSGGGGSGGGGSGGGGSAQSV

Target    LTQPASVSGSLGQRITISCTGSSSNIGYNSVGWYQQLPGRGPRTVIYSTDSRPSGVPDRFSGSKSGNTATLTISGLQAED
6qb9.1.A  LTQPPSASGTPGQRVTISCSGSSSNIGSNTVNWYQQLPGTAPKLLIYSNNQRPSGVPDRFSGSKSGTSASLAISGLQSED

Target    EADYYCSTWDNNLNTPIVFGGGTHLTVLGAAAEQKLISEEDL
6qb9.1.A  EADYYCAAWDDS-LNAWVFGGGTKLTVLGAAAE---------
```

Figure 6.3: Modelling Report of clone 53 in A. and 35 in B. generated by SWISS Model. Detailed summary of a protein structure prediction of clone 53 in A. and 35 in B. It includes all the essential information needed to evaluate the quality and reliability of the 3D structure that was built based on a known template.

6.5. HADDOCK

Cluster 4

HADDOCK score	57.3 +/- 5.3
Cluster size	11
RMSD from the overall lowest-energy structure	22.2 +/- 0.0
Van der Waals energy	-94.0 +/- 3.6
Electrostatic energy	-246.9 +/- 9.3
Desolvation energy	0.6 +/- 1.0
Restraints violation energy	2000.8 +/- 50.4
Buried Surface Area	2631.8 +/- 81.9
Z-Score	-1.4

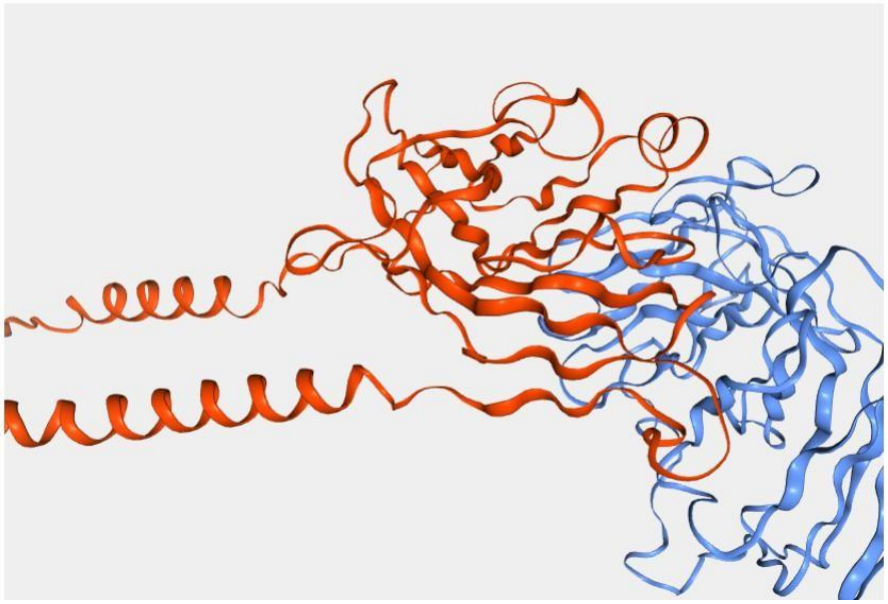

Figure 6.4: Protein Docking using HADDOCK 2.4. An attempt to perform protein docking was done to predict the protein interaction between clone 53 with the extracellular domain of VISTA. However the HADDOCK Score generated shows that there is an unfavourable interaction between clone 53 and VISTA. This high HADDOCK score may likely be due to the lack of pre-processing of the PDB files prior to analysis by HADDOCK 2.4